2005-10-12

Specific Heat and Thermodynamic Properties of Metallic Systems: Instrumentation and Analysis

Brian E. Lang
Brigham Young University - Provo

SPECIFIC HEAT AND THERMODYNAMIC PROPERTIES OF METALLIC SYSTEMS: INSTRUMENTATION AND ANALYSIS

by

Brian Edward Lang

A dissertation submitted to the faculty of

Brigham Young University

in partial fulfillment of the requirements for the degree of

Doctor of Philosophy

Department of Chemistry and Biochemistry

Brigham Young University

December 2005

BRIGHAM YOUNG UNIVERSITY

GRADUATE COMMITTEE APPROVAL

of a dissertation submitted by

Brian Edward Lang

This dissertation has been read by each member of the following graduate committee and by a majority vote has been found satisfactory.

Date	Brian F. Woodfield, Chair
Date	Juliana Boerio-Goates
Date	David V. Dearden
Date	Roger Harrison
Date	Gerald D. Watt

BRIGHAM YOUNG UNIVERSITY

As chair of the candidate's graduate committee, I have read the disseration of Brian E. Lang in its final form and have found that (1) its format, citations, and bibliographical style are consistant and acceptable and fulfill university and department style requirements; (2) its illustrative materials including figures, tables, and charts are in place; and (3) the final manuscript is satifactory to the graduate committee and is ready for submission to the university library.

Date

Brian F. Woodfield
Chair, Graduate Committee

Accepted for the Department

David V. Dearden
Graduate Coordinator

Accepted for the College

G. Rex Bryce
Associate Dean, College of Physical
and Mathematical Sciences

ABSTRACT

SPECIFIC HEAT AND THERMODYNAMIC PROPERTIES OF METALLIC SYSTEMS: INSTRUMENTATION AND ANALYSIS

Brian Edward Lang

Department of Chemistry and Biochemistry

Doctor of Philosophy

A small-scale adiabatic calorimeter has been constructed as part of a larger project to study nano-particles and to facilitate specific heat measurements on samples where it is difficult to obtain enough material to run on the current large-scale adiabatic apparatus. This calorimeter is designed to measure sample sizes of less than 0.8 cm^3 over a temperature range from 13 K to 350 K. Specific heat results on copper, sapphire, and benzoic acid show the accuracy of the measurements to be better than $\pm 0.4\%$ for temperatures higher than 50 K. The reproducibility of these measurements is generally better than ± 0.25 %.

Experimental specific heat data was collected on this new apparatus for synthetic akaganéite, β-FeOOH, for samples with varying degrees of hydration. Our results yield values for $\Delta_0^{298.15} S_m^\circ$ of 79.94 ± 0.20 $J \cdot K^{-1} \cdot mol^{-1}$ and 85.33 ± 0.021 $J \cdot K^{-1} \cdot mol^{-1}$ for samples of β-$FeOOH \cdot 0.551H_2O$ and β-$FeOOH \cdot 0.652H_2O$, respectively. From this data, we were able to determine the standard molar entropy for bare β-FeOOH, as

$\Delta_0^{298.15} S_m^\circ$ = 53.8 ±3.3 J·K^{-1}·mol^{-1}, based on subtractions of the estimated contribution of water from the hydrated species.

Additionally, the specific heats of α-uranium, titanium diboride, and lithium flouride have been measured on a low-temperature, semi-adiabatic calorimeter down to 0.5 K. For the α-uranium, the specific heat of a polycrystalline sample was compared to that of a single crystal, and it was found that there was a significant difference in the specific heats, which has been attributed to microstrain in the polycrystal. The third law entropy for the polycrystal at 298.15 K, $\Delta_0^{298.15} S_m^\circ$, calculated from these heat capacities is 50.21 ±0.1 J·K^{-1}·mol^{-1}, which is good in agreement with previously published values of polycrystal samples. For the single crystal $\Delta_0^{298.15} S_m^\circ$, calculated using the thermodynamic microstrain model, is 49.02 ± 0.2 J·K^{-1}·mol^{-1}.

The low-temperature specific heats of titanium diboride and lithium fluoride have been measured from 0.5 K to 30 K as part of a larger project in the construction of a neutron spectrometer. For this application, the measured specific heats were used to extrapolate the specific heats down to 0.1 K with lattice, electronic, and Schottky equations for the respective samples. The resultant specific heat values at 0.1 K for TiB_2 and ^{6}LiF are 4.08×10^{-4} ±0.27×10^{-4} J·K^{-1}·mol^{-1} and 9.19×10^{-9} ±0.15 ×10^{-9} J·K^{-1}·mol^{-1}, respectively.

ACKNOWLEDGEMENTS

During my studies at Brigham Young University, I have been assisted and guided by many people, and I owe them my gratitude. To Brian Woodfield, I offer my thanks for his endless hours of direction, editing, and the occasional push in the right direction. I also thank Juliana Boerio-Goates for her continual encouragement, mentorship, and willingness to share her theoretical and practical expertise. I would also like to thank all of the members of my graduate committee for their willingness to participate in the many review sessions that have accompanied my graduate studies.

Special thanks is also owed to the other graduate and undergraduate students I have worked with over the past several years in the Woodfield/Boerio-Goates lab group. Jason Lashley has been a strong collaborator since his graduation, and he has provided many samples for us to work with. Rebecca Stevens provided a lot of insight, knowledge, and skill around the lab, and she helped tremendously with data collection. I have also been assisted by Marcus Donaldson, Jamon Holzhouser, Sarah Hopkins, Tyler Meldrum, Tom Parry, and Trent Walker, and I owe them my great appreciation for their many hours of data collection and assistance.

I wish to thank Bart Whitehead for his help in designing many of the electronics used in our new apparatus. I would also like to thank the Precision Machine Shop for their excellent craftsmanship in producing the parts necessary in completing the apparatus. I also need to thank Dr. Matthew Asplund and Lonette Stoddard for their help in troubleshooting LaTeX during the process of writing this dissertation.

Finally, I wish to thank my wife, Renee, for her love and support over the past several years, for helping me get through my graduate program, and for her patience

through the long nights while I was working late at the laboratory. I also thank my children, Kylie and Jaden, for endless hours of entertainment and distraction, and for their understanding when I couldn't be home to play with them because I needed to be at school and work. My family and friends have been my biggest cheerleaders throughout the graduate school process, and I owe them my undying gratitude.

Contents

List of Figures

List of Tables

Chapter 1

Introduction

Since the beginning of the twentieth century, specific heat measurements have been a useful tool for studying the physical and thermodynamic properties of materials. While the specific heat and other thermodynamic properties of many compounds are already known, specific heat measurements continue to provide new insights into the properties of matter, and these insights help us to think about materials in new ways. Unlike the vibrational information provided by methods such as Raman or infrared spectroscopy, where the molecular vibrations yield discrete lines in a spectrum, specific heat measurements make no distinction between the energies, thus the values of these vibrational energies must be obtained through indirect means, often with the aid of other physical properties derived from other methods. The specific heat arises directly from the vibrational modes of any given system, and it is a sum total of all the energy available in the system, whether it be vibrational, magnetic, or otherwise. Furthermore, the specific heat yields the entropy and enthalpy of a system, and this can be used in conjunction with other data to calculate the free energy landscape. Specific heat is a bulk measurement that is affected very little at high temperatures by surface phenomenon, crystal defects, and differences in crystal

domains. Yet, specific heat measurements are extremely sensitive to magnetic and structural changes present in a given system as well as to sample impurities down to the part per million range depending on the impurity.[1,2] For these reasons, specific heat measurements are a useful tool in understanding the chemistry and physics of systems, since from thermodynamics and quantum theory, it is possible to relate the specific heat to lattice vibrations, free electrons (in metals), and a variety of other phenomenon.[1]

Since this work is concerned with specific heat measurements, it is essential to discuss several elements that relate directly to specific heat. First there will be a discourse on some of the basic relationships of the specific heat with other thermodynamic properties, followed by a descriptions of the various microscopic behaviors that give rise to the total specific heat. Finally, there will be a discussion of the various techniques used for measuring the specific heat, along with important experimental factors that influence these measurements.

1.1 Specific Heat Contributions to Thermodynamic Properties

In general, in this work, we are concerned with the specific heat at constant pressure, C_p, as opposed to the specific heat at constant volume, C_V. These two terms can be expressed by the thermodynamic relationships:

$$C_p = \left(\frac{\partial H}{\partial T}\right)_p , \quad C_V = \left(\frac{\partial U}{\partial T}\right)_V \tag{1.1}$$

where H is the enthalpy and U is the internal energy.[2] Most often, what is experimentally measured is C_p, but corrections from C_V can be easily made using the

relation:

$$C_p = C_V + T\left(\frac{\partial p}{\partial T}\right)_V \left(\frac{\partial V}{\partial T}\right)_p \tag{1.2}$$

which is particularly useful if the equation of state for a system is known. The specific heat is expressed most often in terms of molar quantities, which is denoted by $C_{p,m}$ (this notation extends to other thermodynamic variables as well).

Measurement of the specific heat of a system is often not an end unto itself; rather, the specific heat gives direct information on the absolute entropy and relative changes to the enthalpy and Gibbs free energy. The molar entropy, S_m, is related to the specific heat at constant pressure by the equation:

$$\left(\frac{\partial S_m}{\partial T}\right)_p = \frac{C_{p,m}}{T} \tag{1.3}$$

which by separation of variables and integration will give:

$$\int_{S_{m,1}}^{S_{m,2}} dS = \int_{T_1}^{T_2} \frac{C_{p,m}}{T} dT \tag{1.4}$$

or

$$\Delta S_m = \int_{T_1}^{T_2} \frac{C_{p,m}}{T} dT \tag{1.5}$$

where T_1 and T_2 are the bounds of the integration and ΔS_m is the change in entropy.[3] If the lower limit of the temperature integral is set to absolute zero, then by the third law of thermodynamics the lower limit of the entropy is also zero, and the relation becomes:

$$S_{m,T} = \int_0^T \frac{C_{p,m}}{T} dT. \tag{1.6}$$

An additional contribution to the total entropy of a system arises from equilibrium phase changes in the system (i.e. melting and boiling), where the entropy of each can be calculated using the molar enthalpy of the phase change, $\Delta_{pc}H_m$. Thus, the expression for the molar entropy becomes:

$$S_{m,T} = \int_0^T \frac{C_{p,m}}{T} dT + \sum \frac{\Delta_{pc}H_m}{T_{pc}} \tag{1.7}$$

which allows one to determine the absolute entropy of a substance at any given temperature.[3][a] Typically, the molar entropy is given at standard state conditions, S°_m, which by international convention is defined as 0.1 MPa or 1 bar.[4][b]

Unlike entropy, the enthalpy and Gibbs free energy cannot be found as absolute values, but this does not mean the expressions derived from the specific heat are not useful. The enthalpy can be related to the specific heat at constant pressure from the equation:

$$\left(\frac{\partial H_m}{\partial T}\right) = C_{p,m} \, . \tag{1.8}$$

This can be rearranged and integrated to give:

$$\int_{H_{m,0}}^{H_{m,T}} dH_m = \int_0^T C_{p,m} dT \tag{1.9}$$

or:

$$H_{m,T} - H_{m,0} = \int_0^T C_{p,m} dT + \sum \Delta_{pc} H_m \tag{1.10}$$

where $H_{m,0}$ is the enthalpy at 0 K, and the equation has been adjusted to include the enthalpies of any phase transitions ($\Delta_{pc} H_m$).[3] At standard state conditions, this can be expressed as $H^\circ_{m,T} - H^\circ_{m,0}$ and of particular interest is the enthalpy difference at $T = 298.15$ K, or $H^\circ_{m,298.15} - H^\circ_{m,0}$, since 298.15 K is the reference temperature for most thermodynamic data.[c]

The Gibbs free energy can be related to the entropy using the equation:

$$\left(\frac{\partial G_m}{\partial T}\right)_p = -S_m \tag{1.11}$$

[a] According to the third law the entropy at 0 K for a perfect crystal is zero, or $S_0 = 0$. However some materials (particularly glasses) exhibit a non-zero entropy (or residual entropy) at 0 K, thus the total entropy at a temperature, T, would be given by $S_T = S_0 + \int_0^T \frac{C_p}{T} dT + \sum \frac{\Delta_{pc} H}{T_{pc}}$.

[b] In 1982 the International Union of Pure and Applied Chemistry (IUPAC) recommended that the standard pressure, p°, be defined as 0.1 MPa. Prior to this date a value of 0.101325 MPa or 1 atm was defined as the standard pressure.[4] For solids, this difference in standard state pressure makes no appreciable difference to the specific heat.

[c] The enthalpy difference listed in many tables (such as the JANAF thermochemical tables) is between the enthalpy at a given temperature and the enthalpy at 298.15 K or $H^\circ_{m,T} - H^\circ_{m,298.15}$. This is easily found by $H^\circ_{m,T} - H^\circ_{m,289.15} = (H^\circ_{m,T} - H^\circ_{m,0}) - (H^\circ_{m,298.15} - H^\circ_{m,0})$

and integration gives:

$$\int_{G_{m,0}}^{G_{m,T}} dG_m = -\int_0^T S_m dT \tag{1.12}$$

or:

$$G_{m,T} - G_{m,0} = -\int_0^T S_m dT\,. \tag{1.13}$$

where, like as above, $G_{m,0}$ is the enthalpy at 0 K. When these functions are taken at the standard state, then $G^\circ_{m,0} = H^\circ_{m,0}$ and the equation can be expressed as:[3][d]

$$G^\circ_{m,T} - H^\circ_{m,0} = -\int_0^T S_m dT\,. \tag{1.14}$$

However, as a matter of practicality, this relation is usually calculated directly from the specific heat using:

$$G^\circ_{m,T} - H^\circ_{m,0} = \int_0^T C_{p,m} dT - T\int_0^T \frac{C_{p,m}}{T} dT\,. \tag{1.15}$$

Thus we have found relationships for the entropy, enthalpy and Gibbs free energy as some direct or indirect function of the specific heat. The expressions discussed above allow us to make calculations of thermodynamic data at any temperatures for which we have data and not just at the standard reference temperature (298.15 K) listed in basic thermodynamic tables. This, of course, is an important factor in determining the spontaneity and equilibrium conditions of reactions under different circumstances.

1.2 Physical Origins of the Specific Heat

In addition to the contributions of the specific heat to thermodynamic properties, the specific heat is also able to give insights into the microscopic behavior of

[d] As in the case of the enthalpy function, the Gibbs free energy function is often expressed in relation to enthalpy values at 298.15 K, where $G^\circ_{m,T} - H^\circ_{m,298.15} = G^\circ_{m,T} - H^\circ_{m,0} - (H^\circ_{m,298.15} - H^\circ_{m,0})$.

systems. As previously mentioned, the specific heat arises from a combination of several different types of atomic interactions, thus the specific heat is able to yield distinct information about each of these phenomenon. The specific heat comes from atomic displacement energetics as well as electrons in metals, splitting of electronic and nuclear energy levels (Schottky specific heat), and magnetic alignment phase transitions[e], each of which produce characteristic behavior in the specific heat.

1.2.1 Specific Heat from Degrees of Freedom

The major contributor to the specific heat of any substance comes from the atomic and molecular displacements (degrees of freedom), and by applying statistical mechanics and thermodynamics one can calculate how these modes contribute to the heat capacity at constant volume, C_V (though this can be quite easily adjusted to find C_p; i.e. equation 1.2). For gases, the specific heat comes from the translational, rotational, and vibrational motions of the atoms and molecules. Using classical mechanics, the equipartition theorem states that each degree of freedom adds $\frac{1}{2}RT$ per mole to the internal energy of the gas or $\frac{1}{2}R$ to the specific heat. For example, the translational motion of gas particles have three degrees of freedom, essentially one for each dimension of movement, which gives a contribution to C_V as $\frac{3}{2}R$.[1] Likewise, the contributions to C_V from the molecular rotations and vibrations of molecules can be calculated based on the molecular configuration and number of atoms per molecule, n. For a linear molecule the contributions to C_V are R and $(3n-5)R$ for rotations and vibrations, respectively, and $\frac{3}{2}R$ and $(3n-6)R$ for a non-linear molecule.[f] However, the equipartition theorem does not adequately calculate these specific heat contribu-

[e] There are other types of phase transitions besides magnetic transitions, such as structural and superconducting transitions, that make distinct contributions to specific heat as well. Further details can be found elsewhere.[1]

[f] For a mono-atomic gas, such as argon, there is only a translational component to the specific heat, since it has no vibrational or rotational modes.

tions because it does not account for the quantization of rotational and vibrational modes. For this reason, quantum mechanics is able to better model these systems, and one result from quantum mechanics is that the vibrational contribution to the specific heat, $C_{V,vib.}$, for each vibrational mode is:

$$C_{V,vib.} = R\left(\frac{\theta_v}{T}\right)^2 \frac{e^{\theta_v/T}}{\left(e^{\theta_v/T}-1\right)^2} \tag{1.16}$$

where $\theta_v = h\nu/k$ with h being Plank's constant, k is Boltzmann's constant, and ν is a fundamental vibrational frequency. The rotational specific heat can also be calculated, but this is generally done numerically, as the exact answer is the solution to a Schrödinger equation.[1] Regardless of the values of C_V, the specific heat at constant pressure can be calculated by the expression $C_p = C_V + R$ for gases behaving ideally (i.e. high temperature, low pressure).

As in the case of gases, liquids possess translational, rotational, and vibrational degrees of freedom, however the increased intermolecular interactions between the liquid molecules make it difficult to model their behavior. In gases the molecules are completely free to move about with little interaction with other molecules, but in liquids, translational movement is restricted, and the translational, vibrational, and rotational energies are more often interchanged because of the increased number of collisions. On the other extreme, solids are very well ordered and the atomic interactions are very limited, and thus easier to model. Because of this, much less is known about the liquid phase than the other two phases, and the models used to describe liquids and their specific heat contributions have varying degrees of success. That being said, the one relation that is true for all liquids is the relation between the specific heats at constant volume and constant pressure:

$$C_p = C_V + \frac{TV\beta^2}{k_T} \tag{1.17}$$

where β is the volume expansion coefficient and k_T is the isothermal compressibility.[3]

Unlike liquids and gases, the only contributor to the specific heat of simple solids (such as non-magnetic insulators) is the vibrational motion of the atoms, and it is commonly referred to as the lattice specific heat. From classical mechanics, each atom is seen as a three dimensional oscillator that would have six degrees of freedom, and from the equipartition theorem the molar specific heat should be $3nR$ or $n{\cdot}24.9$ $\mathrm{J{\cdot}K^{-1}{\cdot}mol^{-1}}$, where n is the number of atoms per molecule. For many solids at room temperature, this result agrees quite well with experiment, however for many materials, the specific heat only begins to approach $3nR$ at very high temperatures, referred to as the Dulong-Petit limit. Also, at low temperatures the specific heat of *all* materials will drop relatively sharply and approach zero as the temperature approaches 0 K. Again, it is quantum mechanics, by assuming that there are only certain allowable vibrational energy states, that is able to resolve the problems that the equipartition theorem cannot address. Thus, at thermal energies, k_bT, below an energy state, only a small fraction of the vibrational modes are populated as given by Maxwell-Boltzmann statistics, and the specific heat is relatively small, increasing sharply as the thermal energy approaches the energy of the vibrational modes. As the thermal energy becomes greater than the vibrational energy modes, all of the energy levels begin to be completely filled and the specific heat approaches the Dulong-Petit limit. From this basic quantum mechanical viewpoint, there are three major ways of modelling the lattice specific specific heat: the Einstein model, the Debye model, and direct calculation from known density of states.

The Einstein Model

The Einstein model was the first to qualitatively describe the features of a specific heat curve and is representative of a substance where every atom has the same environment as every other atom. In some ways this model is very simplistic in that

it assumes that all of the atoms vibrate independently of each other at the same fundamental frequency, ν_E.[1] Applying Maxwell-Boltzmann statistics, one can find that the specific heat for a substance with n atoms per mole from this model is:

$$C_V = 3nR \left(\frac{h\nu_E}{kT}\right)^2 \frac{e^{h\nu_E/kT}}{\left(e^{h\nu_E/kT}-1\right)^2}\,, \tag{1.18}$$

which is analogous to equation 1.16 that describes the vibrational component of a gas. Often, the Einstein function is expressed in terms of an Einstein temperature, $\theta_E = h\nu_E/k$, that allows one to interpret the vibrational frequency in terms of the thermal energy required to populate the vibrational modes, where the Einstein function takes the form:

$$C_V = 3nR \left(\frac{\theta_E}{T}\right)^2 \frac{e^{\theta_E/T}}{\left(e^{\theta_E/T}-1\right)^2}\,. \tag{1.19}$$

Unfortunately, the Einstein function does not adequately represent the lattice vibrations of all substances, since even for simple substances such as aluminum or copper there is not good quantitative agreement with experimental specific heats. This is due to the oversimplification of this model, since in a coupled system, like a lattice, the vibrations of one atom are affected by its neighbors, thus every atom can vibrate with several frequencies. While the Einstein model has its limitations, its is still a good approximation to use on a variety of systems, and is most often used in combination with other lattice models.

The Debye Model

The Debye approach to the specific heat differs from the Einstein model in that there is a finite range of vibrational frequencies, ν, that are allowed in the crystal where the range of frequencies is expressed in terms of a vibrational density of states $g(\nu)$. By this we mean the number of states (modes) between any two frequencies is given by the integral of $g(\nu)$ evaluated over the range of the frequencies.[5, 6] Debye

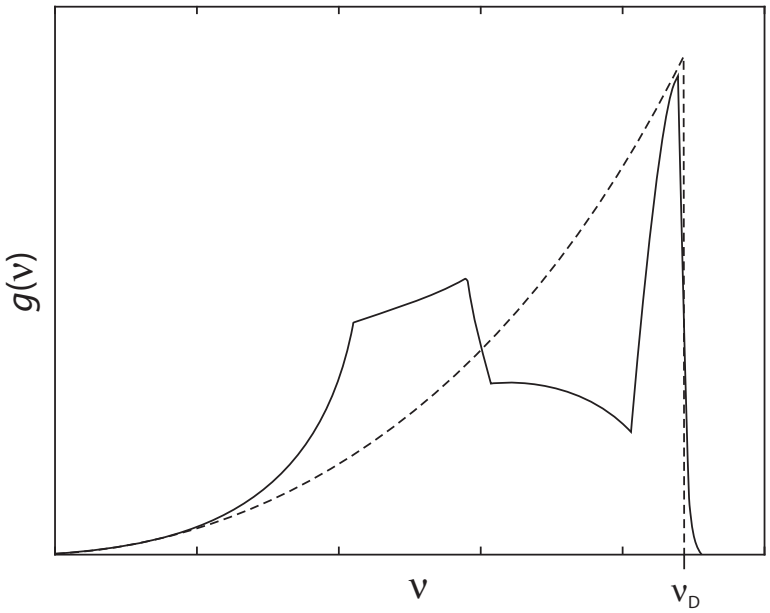

Figure 1.1. The vibrational density of states of copper as represented by the Debye model (dashed line) and from experimentally derived values (solid line). Taken from Kittel[5] and Stokes[6].

assumes the density of states follows a quadratic distribution up to a characteristic frequency, ν_D, at which point the density of states drops to zero (see figure 1.1).[1] Like the Einstein function, this characteristic frequency can be expressed in terms of a temperature, $\theta_D = h\nu_D/k$, known as the Debye temperature. From this approximation, the specific heat can be derived from statistical mechanics and is given by the expression:

$$C_V = 9nN_Ak\left(\frac{T}{\theta_D}\right)^3 \int_0^{\theta/T} \frac{x^4e^x}{\left(e^x-1\right)^2}dx \tag{1.20}$$

where N_A is Avagadro's number.[1]

In the low temperature limit, when $T \ll \theta_D$, the integral in equation 1.20 can be simplified, and the expression for the specific heat at low temperatures reduces to:

$$C_V = \frac{12\pi^4nN_AkT^3}{5\theta_D^3} \tag{1.21}$$

thus at low temperatures, the specific heat should obey a T^3-law, although at progres-

sively higher temperatures the specific heat tends to follow an odd power expansion, such that:

$$C = \beta_3 T^3 + \beta_5 T^5 + \beta_7 T^7 + \cdots . \tag{1.22}$$

In the low-temperature limit, assuming the T^3-law, the specific heat is traditionally evaluated as a plot of C/T versus T^2, and the low-temperature Debye expansion becomes an equation of the form $C/T = \beta_3 T^2$. Thus, the slope of the line, β_3, can be used to evaluate the Debye temperature as T approaches zero K with the expression:

$$\theta_D = \sqrt[3]{\frac{12\pi^4 n N_A k}{5\beta_3}} . \tag{1.23}$$

Evaluating the Debye temperature for various materials allows one to semi-quantitatively measure the stiffness of the bonds between atoms in different materials, and allows one to compare the nature of the bonding between similar materials.

While the Debye model does a much better job representing specific heat data than the Einstein function, it falls short of being a perfect model for all real systems. The Debye function works best when $T < \theta/50$ and $T > \theta/2$, but between these temperatures the Debye model often does not fit experimental results well. The main deficiency of the Debye model is that it does not take into account that the velocities of lattice waves (phonons) propagating through the system are a function of the frequency. Nonetheless, the Debye model continues to be a useful tool in modelling the specific heat, especially at low temperatures.

Specific heat from the density of states

A more exact calculation of the lattice specific heat can be made if the phonon density of states for a material is known (see figure 1.1). From statistical mechanics, the specific heat can be found by integrating the density of states over all vibrational

energies, ν, and yields the following relation:

$$C_V = 3\int_0^\infty g_0(\nu)\frac{\nu^2}{k_bT^2}\frac{e^{\nu/k_bT}}{\left(e^{\nu/k_bT}-1\right)^2}d\nu \tag{1.24}$$

where $g_0(\nu)$ is the density of states at 0 K.[5] While this relation is able to yield an exact and accurate value of the lattice specific heat, the difficulty in using this expression is in obtaining the density of states. Ideally, the phonon density of states is calculated from inelastic neutron scattering data, but this requires the use of a high energy neutron source, and these are only available at a limited number of facilities around the world. Conversely, the phonon density of states can be approximated using computer modelling, or by combinations of Debye and Einstein terms to approximate the various features of the true density of states.

Lattice C_p/C_V corrections

For the previous models, the specific heat has been described in terms of C_V, however what is experimentally measured for solids is C_p. At low temperatures, typically $T < 20$ K, the difference between C_p and C_V is almost insignificant, thus the difference is ignored, and more importantly C_p can be modelled with the functions used to describe C_V. At higher temperatures the C_p/C_V difference becomes increasingly larger, thus it becomes important to correct for the difference using a more practical form of equation 1.2, which is:

$$C_p = C_V + BV_m\alpha^2T \tag{1.25}$$

where B is the bulk modulus, V_m is the molar volume, and α is the coefficient of thermal expansion.[2, 5] In some situations, it is sufficient to approximate the $BV_m\alpha^2T$ term with a quadratic function.[7]

1.2.2 Electronic Specific Heat

In metals, the conduction electrons are often seen as moving freely through the lattice, and that is responsible for the high thermal and electrical conductivity. In this model, electrons should behave like an ideal gas, and from the equipartition theorem, contribute $\frac{3}{2}R$ per mole of conduction electrons to the total specific heat of the metal.[1] However, the actual specific heat attributed to the conduction electrons is much smaller than what is predicted by classical mechanics; it is only by applying quantum mechanics to the system that one correctly determines the electronic specific heat. In the quantum mechanical picture, all of the conduction electrons must occupy different energy states as expressed by the Pauli exclusion principle, and to accommodate all of the conduction electrons, there must be a wide distribution of the energies, up to some maximum energy state. At lower energies, there is zero probability of the electron transitioning to a higher state.[6] It is only electrons at the highest energies that are able to move to higher states, and at some energy, E_F, there is a 50 % probability of transitioning to a higher state, referred to as the Fermi energy. It is the electrons that are able to change energy states that contribute to the specific heat, which from Fermi-Dirac statistics can be expressed by:

$$C_{elec} = \frac{\pi^2 N_A k_b^2 T}{2E_F}\,. \tag{1.26}$$

At higher temperatures, the electronic specific heat is only a small fraction of the overall specific heat, but at low temperatures, the electronic specific heat becomes a larger fraction of the total since the electronic contribution follows T, but the lattice follows T^3, which approaches zero faster. In the low-temperature limit, the specific heat is observed as $C = \gamma T + \beta T^3$, where γT is the electronic contribution. Traditionally, the low-temperature value of the electronic specific heat is found by generating a plot of C/T against T^2 and fitting the data to a straight line, where

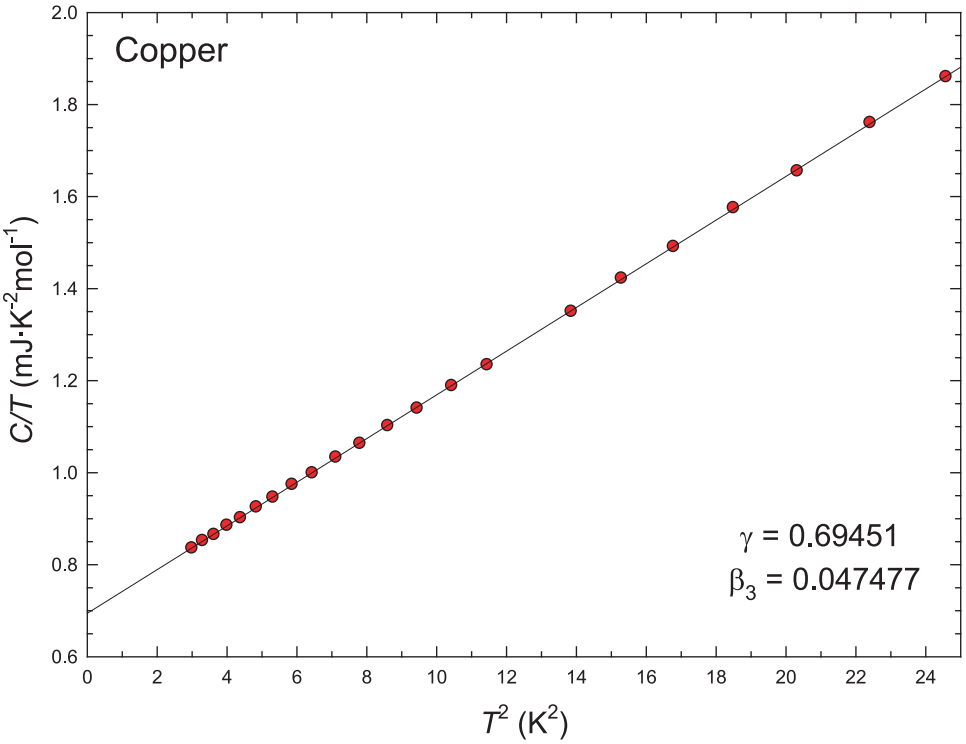

Figure 1.2. Debye low-temperature extrapolation of copper plotted as C/T vs. T^2. A fit of the data to a line is shown as well. The intercept (electronic term) is 0.69451 and the slope (lattice term) is 0.047477

γ is found from the intercept and β is the slope (as discussed in section 1.2.1). An example of the low-temperature extrapolation is given in figure 1.2.

1.2.3 Schottky Specific Heats

A Schottky system is a set of non-interacting particles with n available energy levels each separated from the ground state energy by $\epsilon_1, \epsilon_2, \ldots, \epsilon_n$, where each level has a specific degeneracy, $g_0, g_1, g_2, \ldots, g_n$.[1, 2] At the minimum thermal energy, $kT = 0$, all of the particles are in the ground state. As the thermal energy increases, the higher energy states begin to be populated. From Boltzmann statistics the probability

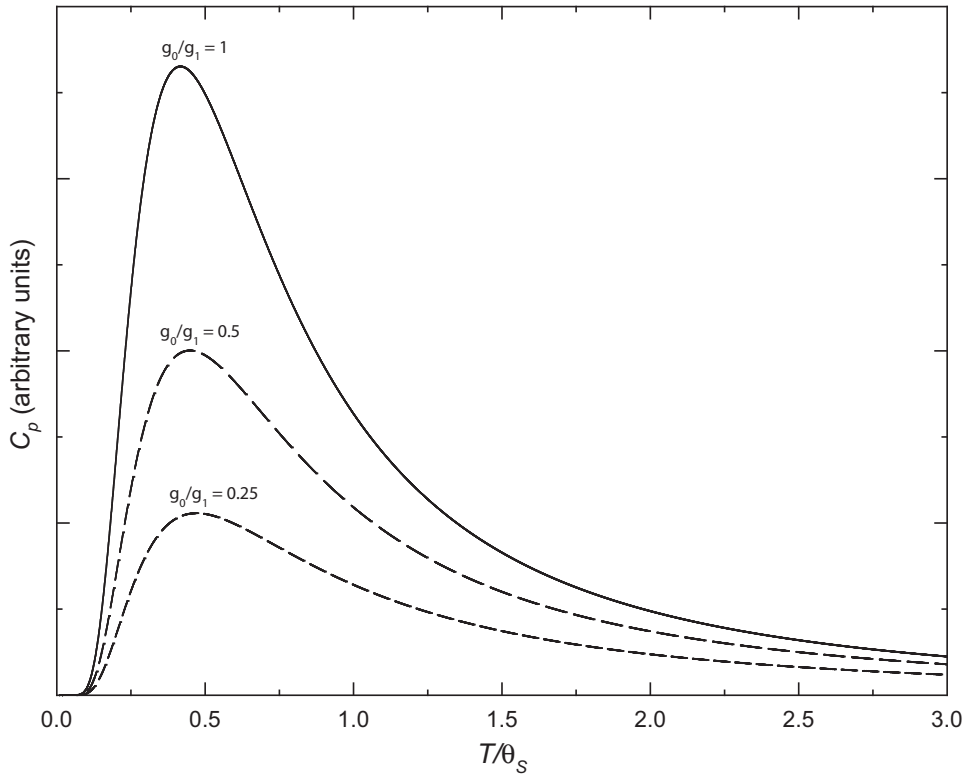

Figure 1.3. Representative Schottky specific heats showing the effects of different degeneracy ratios.

of a particle residing in an ith energy state is:

$$P_i = \frac{g_i e^{-\epsilon_i/kT}}{\sum_{j=1}^{n} g_j e^{-\epsilon_j/kT}} \,. \tag{1.27}$$

When a particle moves from the ground state to one of these higher energy states the internal energy of the system changes, and this results in a change in the overall specific heat. For a two-level system, the specific heat can be derived from the probability relationship in equation 1.27 as:

$$C_{Sch} = R \left(\frac{\theta_S}{T}\right)^2 \frac{g_0}{g_1} \frac{e^{-\theta_S/T}}{\left(1 - (g_0/g_1)e^{-\theta_S/T}\right)^2} \tag{1.28}$$

where θ_S is the Schottky temperature, or the energy separation expressed in temperature, $\theta_S = \epsilon/k$.

A representative Schottky specific heat function is shown in figure 1.3, and as seen, the specific heat is zero at 0 K, then rises quickly to a maximum value and then decays asymptotically to zero. At low temperatures, $T \ll \theta_S$, the specific heat rises exponentially, while at the upper end of the Schottky function, the specific heat is proportional to T^{-2}.

The Schottky specific heat in solid materials is arises from thermal population of electronic and nuclear energy levels. In electronic systems, one type of atom in the lattice, usually a transition metal, has undergone a splitting of electronic orbitals by neighboring atoms. Thus, in the case of a transition metal, the five normally degenerate d-orbitals can be split into two different energy levels with degeneracies of 2 and 3. Since there are no co-operative interactions between the electrons of neighboring atoms, the distribution of the electrons between the energy levels can be described by a Boltzmann distribution, and thus fits the criterion for a Schottky system.[1]

In nuclear systems, energy levels in atomic nuclei with a magnetic moment and a non-zero spin are split in the presence of a magnetic field. This is often referred to as the nuclear hyperfine. The magnetic field in question can be externally applied, inherent to the material, as in the case of Fe_3O_4, or there may be small local magnetic fields in the material caused by defects. In any case, all of the nuclear energy levels a populated independently, thus it can also be modelled with a Schottky function. Generally, the nuclear alignment is only observable below 2 K due to the size of the nuclear moments, and it is only the high-temperature side of the Schottky function that is usually observed, so the specific heat of the Schottky can be modelled by $C_{Schot} = XAT^{-2}$, where A is a factor determined by the hyperfine splitting and X is the mole fraction of the nuclei with magnetic moments.[1, 8] Conversely, with electronic Schottky contributions, electronic moments are appreciably larger,

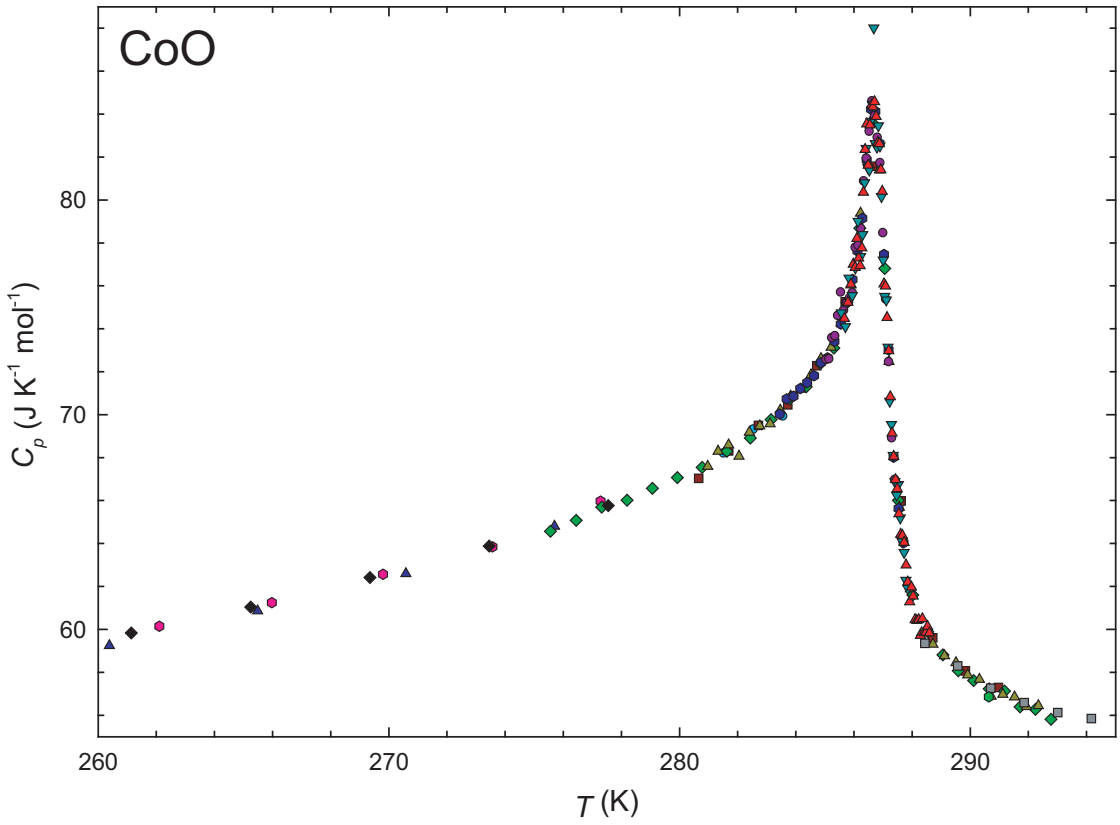

Figure 1.4. Specific heat of the magnetic transition in CoO

are observed at higher temperatures, and can generally be modelled using an entire Schottky function.

1.2.4 Magnetic Specific heat

Magnetism in solids arises from the alignment of magnetic dipoles (spins) in a system, of which there are four basic types: paramagnetism – disordered spins that can align with an applied field; ferromagnetism – alignment of all the spins in the same direction creating a net magnetic moment; antiferromagnetism – alignment of neighboring spins in opposite directions resulting in no net magnetic moment; and ferrimagnetism – alignment of neighboring spins of different magnitudes in opposite directions giving the system a net magnetization. For ordered magnetic systems there

is some critical temperature, T_c, below which there is magnetic ordering and above which the sample is paramagnetic.[g] As a magnetic material is heated up through the region of the critical temperature the spins transform cooperatively (one spin will influence the orientation of its neighbors) from an ordered state to a disordered state. The specific heat reflects the onset of this disorder (see figure 1.4).

The magnetic specific heat can be described using a variety of models, such as the Ising model, that depend on the geometry of the spin alignment and the interaction that couples spins. A simplistic description of the magnetic specific heat near the critical temperature is that the transition has a characteristic lambda shape where the specific heat on the high side of T_c rises sharply as $T \rightarrow T_c$, and decays more slowly below T_c. In many models, the specific heat approaches infinity at the critical temperature. Regardless of the model used, quantum mechanics predicts that the entropy per mole for a cooperative order-disorder transition should be:

$$S_M = R \ln(2s + 1) \tag{1.29}$$

where s is the magnetic spin quantum number.[1] Thus for a system with atoms having a spin of $\frac{1}{2}$, the entropy change from the magnetic transition should be $R \ln 2$ or ~ 9.7 $\mathrm{J \cdot K^{-1} \cdot mol^{-1}}$. If the magnetic specific heat can be isolated by subtracting the lattice and other specific heat contributions, then the entropy due to the order-disorder change in the spin alignments can be calculated and compared to the theoretical value.

In addition to the specific heat associated with the transition, magnetic materials display unique properties that contribute to the specific heat at low temperatures due to periodicity in the magnetic spins in the lattice (spin waves or magnons). For ferromagnetic and ferrimagnetic materials, the low temperature specific heat due to

[g]For ferromagnetic materials T_c is the Curie temperature, and for antiferromagnetic and ferrimagnetic materials the critical temperature is the Néel temperature, T_N.

the magnons is proportional to $T^{3/2}$. Thus the low-temperature specific heat should have the form $C = \delta T^{3/2} + \beta T^3$ for an insulator and $C = \gamma T + \delta T^{3/2} + \beta T^3$ for a conductor. Likewise, antiferromagnetic materials have low-temperature contributions from the magnons. However the specific heat contribution is proportional to T^3 and is therefore difficult to separate from the lattice contribution.

Specific heat investigations of magnetism are important in that they can provide information about a magnetic material better than many other techniques. Magnetism in materials is typically investigated using magnetic susceptibility measurements. However, specific heat measurements are often more sensitive to the magnetic ordering, especially with regard to antiferromagnetic transitions where there is a change in the ordering of the system but no drastic change in the net magnetic field of the material. Also, calorimetric devices generally have better thermometry and temperature control, so the magnetic transition temperatures can be determined with higher accuracy.

1.3 Principles of Specific Heat Measurements

The science of specific heat measurements, or calorimetry, is essentially the study of the heat flow into a system and the resultant temperature change. One can measure the specific heat on a variety of systems, but the discussion here will be limited to principles used for calorimetric studies of solids, although most of these procedures can be easily modified for other types of systems.

The basic design for a calorimetric system consists of a sample that is isolated from the surroundings, so that a controlled quantity of heat can be input into the sample (this is illustrated in figure 1.5). However, it is impossible to completely isolate the sample from the surroundings, since there is always some kind of connection or

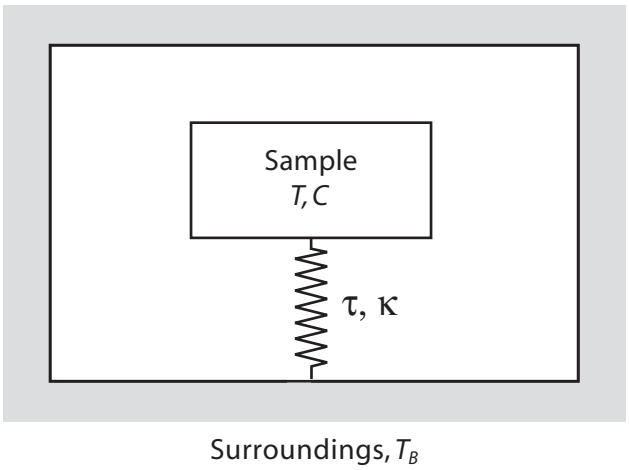

Figure 1.5. A schematic representation of calorimetric systems with the sample separated from the surroundings. The heat flow between the sample and surroundings is regulated by resistivity of the thermal link, κ, and the relaxation time of the thermal link to the surroundings, τ.

thermal link between the sample and the surroundings. Thus, there is the potential for heat flow between the two. The heat flow through the thermal link is regulated by its thermal resistivity, κ, and is often expressed in terms of a relaxation time, τ, where the thermal isolation of heat flow is dependent on the experimental technique. Additionally, because of the thermal isolation, the sample temperature, T, may not be the same as the temperature of the surroundings, T_B (or the bath temperature). In practice, specific heat measurements are made with the sample thermally attached to a sample platform or in a calorimeter vessel, referred to as the addenda. In addition to being a sample holder, the addenda consists of a thermometer, a resistive heater, and the associated wiring. The specific heat of the addenda must be measured (preferably before the sample is run), so the addenda specific heat can be subtracted from the total specific heat (addenda and sample), which gives the specific heat for the sample. While the nature of the thermal link varies with the specific experimental design, the heat flow through the thermal link should be reproducible so that it can be appropriately accounted for in the calculation of the sample specific heat.

Quite a variety of experimental techniques for measuring low-temperature specific heat (below 300 K) have been developed over the past century. The first modern calorimeter at low-temperatures was developed by Nernst near the beginning of the twentieth century. The experimental cell was simply a sample that was sealed in a vacuum chamber (along with a platinum wire that served as a thermometer and heater) that was immersed in a cryogenic bath. Since that time there have been a number of modifications to this basic design. Presently there are a number of experimental designs for measuring the specific heat, but they are all variations of four basic methods: adiabatic, semi-adiabatic or isothermal pulse, AC, relaxation, and continuous heating. Thus, there will be a discussion of the fundamentals of each of these techniques, with emphasis on the pulse method since this is the technique referred to in the subsequent chapters of this work. In addition, other factors affecting specific heat measurements such as temperature, power measurements, and curvature corrections will be discussed.

1.3.1 The Pulse Method

The pulse technique is generally regarded as one of the most accurate and precise methods for determining the specific heat, although the trade off is that it is often more time consuming and generally requires more sample than other methods.[2] In principle, the pulse method operates by performing the following on the sample: the sample is brought to an equilibrium condition at some initial temperature, T_i, and then a known quantity of heat is applied to the system resulting in a temperature change, ΔT, after which the sample is again allowed to equilibrate to a new temperature, T_f. Since the quantity of heat is known, the specific heat can be found at the median temperature, $(T_m = (T_i - T_f)/2)$, based on the thermodynamic definition of

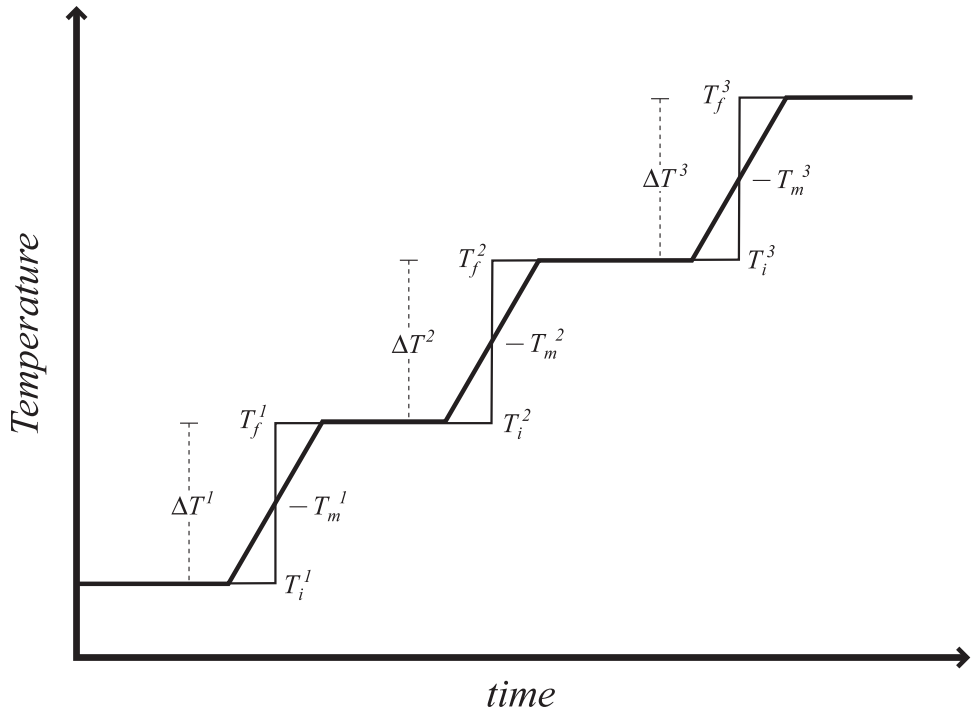

Figure 1.6. The adiabatic pulse method showing the temperature as a function of time. In the equilibrium or drift phase the temperature remains relatively constant, while the temperature changes quickly during the addition of heat or pulse. T_i and T_f are calculated by extrapolating the drift forward (or backwards) to the midpoint of the pulse. The superscript numbers denote which T values belong together.

specific heat (C_p, see equation 1.1). This can be expressed as:

$$C_p = \lim_{\Delta T \to 0} \left(\frac{Q}{\Delta T} \right) \tag{1.30}$$

where Q is an amount of heat energy that results in a discrete temperature change, ΔT, of the system (). From this relation, we are able to measure the specific heat of any given system, and the step process can then be repeated to allow for efficient specific heat measurement over a large temperature range (see figure 1.6). The pulse method may be performed using either an adiabatic, semi-adiabatic, or isothermal method, which shall be discussed subsequently.

The Adiabatic Technique

For a system to be considered adiabatic, there must be no heat flow into or out of the system from the surroundings. For calorimetry, this is accomplished by the use of an adiabatic shield that is maintained at the same temperature as the calorimeter, so there is no heat gradient between the system and the surroundings ($T = T_B$, refer to figure 1.5, κ is also very small). Thus, during the equilibrium step (or drift) the sample maintains a constant temperature, and during the pulse the only heat added to the calorimeter is from the resistive heater. Strictly speaking, there are no truly adiabatic calorimeters, since there will inevitably be some heat leak into or out of the system. However, we can approximate adiabatic conditions (quasi-adiabatic) with the use of thermal (adiabatic) shielding, and by minimizing the heat leak by ensuring that there is a large thermal resistance between the calorimeter and the shield.[2]

The thermal or adiabatic shields are kept at the same temperature as the calorimeter through the use of thermocouples wired in series between the calorimeter and the shield. This creates a highly sensitive detector of thermal gradients, and in this way, there can be compensation for any changes in the temperature between the calorimeter and the shield (See chapter 3 for further specifics on the various aspects of shield control). Although this shielding does not keep the temperature perfectly constant during a drift, it does establish a steady state condition with a minimal rate of heating or cooling, typically on the order of ± 0.1 mK/min or less.[9, 10] To further approximate adiabatic conditions, a set of radiation shields surround the calorimeter and the adiabatic shield to minimize the effects of blackbody radiation from outside sources, especially above 20 K where the effects of radiation become important. With careful measurements, the adiabatic technique can achieve accuracies of better than 0.1 %.[2, 9] The adiabatic technique begins to fail below 20 K, since this method

is designed to compensate for radiation as the primary source of heat loss, whereas conductivity becomes the more important factor in heat loss at these lower temperatures. Additionally, the platinum resistance thermometers typically used in this technique begin to loose sensitivity below 20 K, increasing the overall uncertainty in the temperature measurements.

The Semi-Adiabatic Technique

The semi-adiabatic pulse technique differs from the adiabatic technique in that the sample/calorimeter and the surroundings are not kept at the same temperature. In general, the surroundings (often a large constant temperature block that surrounds the sample) are kept at a lower temperature than the sample. Thus, there is a thermal gradient and subsequent heat loss from the sample to the surroundings ($T > T_B$, and the thermal conductivity, κ, should be small, see figure 1.5). However, the heat loss is compensated for by adding a known amount of heat back into the sample across the resistive heater during the drift portion of the specific heat measurement. Ideally, the heat input into the sample (background heat) equals the heat lost to the surroundings so there is no net heat loss into or out of the sample. This emulates an adiabatic system, thus the term semi-adiabatic. In practice, there is almost always some net heating or cooling during the drift for semi-adiabatic measurements. The technique will still produce good results if the change in temperature during the drift is less than 0.1 % of the pulse ΔT, and if there is sufficient thermal isolation between the system and surroundings.

Typically, the semi-adiabatic technique is used for temperature measurements below 20 K, since there is minimal loss of heat from the sample via blackbody radiation. Above 20 K, heat loss from blackbody radiation starts to become significant. This can contribute to large errors in the measurements, but results from measurements

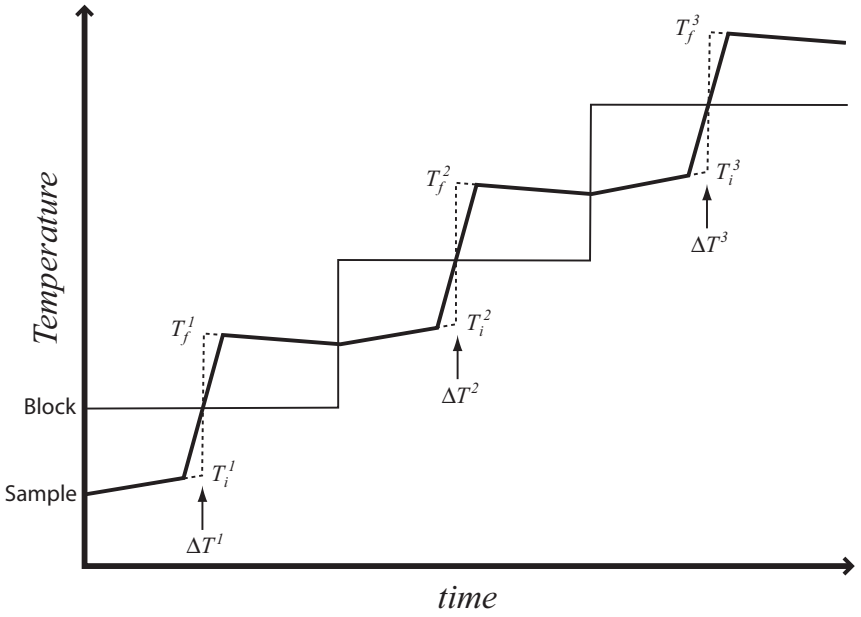

Figure 1.7. The isothermal technique illustrating the temperatures of the sample and the surroundings (block) with respect to time

above 20 K can give satisfactory results if care is taken during the experimental procedure. Because there is some heat flow in the system, the semi-adiabatic measurement tends to be less accurate than the adiabatic measurement. However, with care this technique can yield results with an accuracy of 0.25 % and a precision of 0.1 %.

The Isothermal Technique

In the isothermal technique, the surroundings are kept at a constant temperature that is different from the sample, and there is no attempt to control the heat flow in or out of the sample (in some regards, it may be more accurate to refer to it as an isoperibol technique). Initially, the surroundings (usually a constant temperature block) are set at a temperature, T_B, that is higher than the sample (refer back to figure 1.5). Thus the sample will slowly heat at a nearly constant rate that is some function of the overall mass of the sample, the total specific heat of the sample,

the sample thermal conductivity, and the thermal conductivity between the sample and the constant temperature block. The time/temperature drift (foredrift) of the sample is measured for a set length of time. Then a known quantity of heat is put into the system, raising the temperature of the sample above the temperature of the block. After the pulse, the temperature of the sample will begin to fall exponentially toward the temperature of the block (afterdrift), and after a set amount of time the temperature of the block is adjusted to be higher than the sample, so the process can be repeated to cover a large temperature range (see figure 1.7). The initial and final temperatures can be found by extrapolating the foredrift and afterdrift to the midpoint of the pulse. Ideally these temperatures are such that the median temperature, T_m, is the temperature of the block.

In practice, this technique is used sparingly because of several experimental limitations. First, above 100 K, radiative losses from the sample to the block become significant. Second, this technique requires that samples have a relatively high thermal conductivity. Samples with low thermal conductivity do not tend to equilibrate completely; this can dramatically increase the error in these samples. However, this technique can be highly useful for measuring metallic samples, and can be used in conjunction with the semi-adiabatic technique.

1.3.2 The AC method

The AC technique was developed in 1968 by Sullivan and Seidel as a method for measuring the specific heat of small samples of less than 200 mg. In this method, the sample is heated with an AC current of angular frequency $\omega/2$ passing through the sample resistive heater. This results in the sample temperature oscillating periodically over time, as shown in figure 1.8. Utilizing a lock-in amplifier, the frequency response

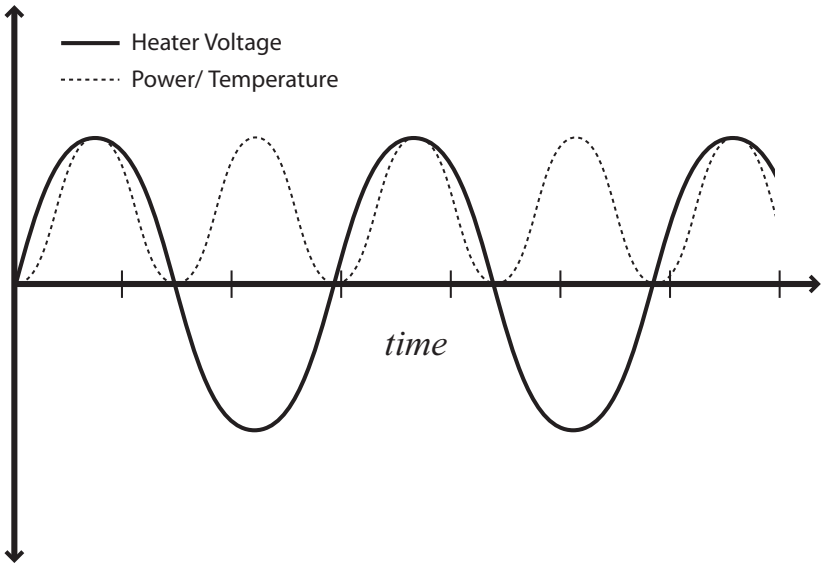

Figure 1.8. The AC technique showing the heater voltage, heater power and temperature change with respect to time

of the sample temperature, T_{ac}, can be determined with respect to the total heat input into the system at a frequency of ω.[2] Since the heat input from the AC current results in an oscillating heater power, the heat input into the sample, Q, is determined as a function of the amplitude of the current, i_0, or $\dot{Q}_0 = i_0^2 R$ where R is the resistance of the sample heater. The specific heat can then be calculated from the expression:

$$T_{ac} = \frac{\dot{Q}_0}{2\omega C_p}\left[1 + \frac{1}{\omega^2\tau_1^2} + \omega^2\tau_2^2 + const.\right]^{-1/2} \tag{1.31}$$

where τ_1 is the relaxation time of the thermal link of the sample to the surroundings, τ_2 is the net relaxation time of the various components of the addenda, and the constant is dependent on the thermal conductivity between the sample and the bath, and the thermal conductivity of the sample to the addenda.

In principle, the AC technique is run with the surroundings at a constant temperature and the thermal conductivity between the sample and surroundings is small, resulting in a relatively large relaxation time (τ_1 is on the order of a few seconds; refer to figure 1.5). Ideally, to achieve the best measurements the reciprocal square-root

term in equation 1.31 should be minimized, which is accomplished by ensuring that the thermal conductivity of the sample to the addenda is much greater than that of the thermal conductivity from the sample to the surroundings, and that $\tau_1 \ll 1/\omega$ and $\tau_2 \gg 1/\omega$.[2] In practice, the true values for all of the constants in equation 1.31 are determined experimentally. First, the appropriate sampling frequency, ω, can be determined by adjusting the frequency until T_{ac} varies linearly with respect to $1/\omega$. Also, for each new sample the values of τ_1 and the constant must be determined in the course of the experiment.[11]

The AC technique is an extremely sensitive method that can detect changes in the specific heat as small as 10^{-8} to 10^{-12} J·K^{-1}, and for this reason, it is particularly useful in measuring small samples.[2] Additionally, because the system uses a lock-in amplifier, it is able to filter out the background noise. However, as sensitive as this technique is, because of the small sample size and because of assumptions made in the derivation of equation 1.31, this method only has an absolute accuracy between 1% and 8%.[2, 11] This technique also assumes that the sample has a high thermal conductivity, and thus a small thermal relaxation time with respect to the addenda, so for samples with low thermal conductivity, the effectiveness of this method diminishes.

1.3.3 The Relaxation Technique

In the relaxation technique, the sample is connected to a constant temperature bath (surroundings) by a thermal link with a relatively high thermal conductivity, κ (as compared to the AC or pulse methods). Initially, the bath and the sample are at equilibrium, thus $T_{sample} = T_B$ (refer to figure 1.5). Then, a certain amount of heat, Q_{in}, is input into the sample heater, so that the sample reaches a steady state temperature, T_0. The heat input is abruptly turned off, and the sample is allowed

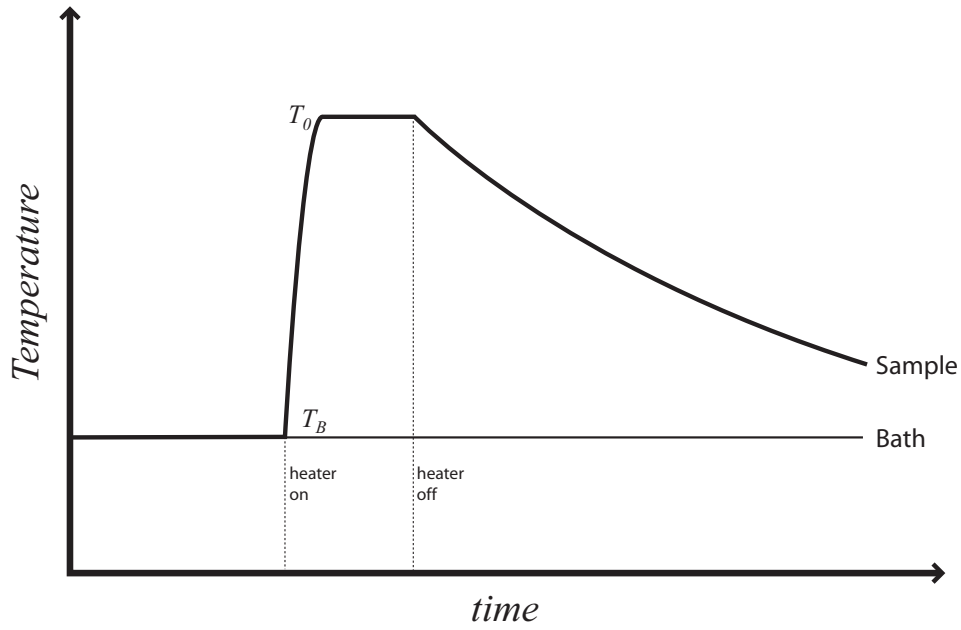

Figure 1.9. The relaxation technique

to decay back to T_B, while the temperature is constantly being monitored (see figure 1.9).[11] From basic heat flow equations, the specific heat can be found using $C = \kappa\tau_1$, where κ is dependent on the materials of the thermal link and relaxation time, τ_1, can be found by fitting the temperature decay of the sample to the relation:

$$(T - T_B) \cdot t = (T_0 - T_B)e^{-t/\tau_1} \,. \tag{1.32}$$

These equations work well when there is a small response time between the sample and the addenda (τ_2 from the discussion on the AC method), otherwise these thermal effects must be included in the heat flow equations which produce different solutions.[11] Typically, the temperature increase for this technique is relatively small ($\Delta T/T \approx 1\%$), thus to get specific heat over an extended temperature range the bath temperature must be changed for each new point.[2]

A variation of this basic relaxation technique allows the bath/sample temperature difference to be much larger, so that the bath temperature does not need to be

adjusted for every single data point. This method begins by stepwise increasing the power across the sample heater so that at each power increment a new sample temperature is maintained, thus the heater power can be expressed as a function of the sample temperature. Ideally, there will be enough temperature points so that the function, $\dot{Q}_{in}(T)$, will be a smooth curve. At the highest temperature point, T_0, the heater is turned off and the sample will begin to relax back to the bath temperature, and the specific heat is then:

$$C(T) = \left(\frac{dT}{dt}\right)^{-1} \dot{Q}_{in}(T) \tag{1.33}$$

where the differential is calculated form the decay of the sample temperature.

Like the AC technique, the relaxation technique is suited for use on small samples and is often used preferentially over the AC method because of its more simple experimental design and the simplicity of the heat flow equations. The relaxation technique tends to be more accurate than the AC technique (about 1% or so), however it is still not as accurate as the pulse method.[2] It is important to note that this method generally requires a new experimental set-up for each new sample. Also, this method may not be able to measure slowly equilibrating processes well (i.e. some phase transitions) if the relaxation time is too fast.[11]

1.3.4 The Continuous Heating Method

The continuous heating method is different from the other three methods in that the specific heat is measured as a function of the dynamic heating of the sample, instead of allowing the system to come to equilibrium or to a steady state condition. The heat flow in the continuous heating system can be expressed as:

$$\dot{Q}_{in} = \dot{Q}_{HL} + C\frac{dT}{dt} \tag{1.34}$$

where $\dot{Q}_{in}$ is the heat flow into the sample, which is balanced by the heat leak out of the sample, $\dot{Q}_{HL}$, and the absorption of the heat by the sample, $C\frac{dT}{dt}$.[11] Thus, the specific heat can be determined by a simple rearrangement of equation 1.34. Then C is function of the heat flow and the change in sample temperature over time.

There are a variety of experimental designs for implementing the continuous heating technique, but currently one of the most common methods is Differential Scanning Calorimetry (DSC).[12] While the actual solution for finding the specific heat is more complex than equation 1.34, and is too involved to be adequately discussed in this setting, the fundamental relation in equation 1.34 is still valid. The DSC technique uses two sample holders, one for the sample and one that serves as a reference (often it is left empty). During an experiment, the sample and the reference are both heated at the same rate, but the sample will have a higher specific heat than the reference, and thus the sample will change temperature at a different rate than the reference. The temperature difference itself is often measured as a voltage differential between thermocouples on the sample and the reference. Comparison of the voltage/temperature differentials of an unknown sample to those of a standard with known specific heat, such as sapphire, allows the calculation of the specific heat of the unknown sample.

One of the main advantages of the continuous heating method is that it allows for the measurement of the specific heat over a large temperature range, with a high density of data points, in a relatively short amount of time. Additionally the DSC technique is a relatively simple method to use, generally requiring only small amounts of sample, and there are a variety of commercial units available with automatic data collection and analysis programs. Unfortunately, since the continuous heating method does not allow the sample to come to equilibrium, thermal gradients may arise in the sample, and care must be taken to ensure that the heat flow in the system adequately represents the thermodynamics of the sample. Additionally, even the most careful

DSC measurements are typically accurate to only 2 or 3 percent, and it is important to make sure that the standard has similar heat flow characteristics as that of the sample.

1.3.5 Temperature

One of the most critical components of specific heat measurements is the accurate and reproducible determination of temperature. The accuracy and precision of the specific heat is determined in large part by the overall accuracy of temperature measurements and the sensitivity in determining the value of ΔT. Both of these factors are accomplished by having a smooth temperature scale and a reliable thermometer with sensitive instrumentation.

The subject of temperature is quite involved and cannot be adequately covered in this setting, however a few basic principles should be discussed, specifically temperature scales and thermometry. For thermodynamics, an absolute temperature scale is used to describe changes of state, and this scale is based on the Carnot cycle and establishes the lower limit of temperature, or absolute zero.[13] Thermodynamics is also able to define temperature in terms of the expansion of an ideal gas, and this is equivalent to the absolute temperature scale. The absolute temperature scale is based on fundamental physical laws, but there is no satisfactory relationship that relates the measured temperatures from thermometers used in everyday applications to the absolute temperature scale.[14] Therefore, a practical temperature scale is used that is based on a set of fixed points – such as the melting points of various metals and the triple point of water. The temperatures at these fixed points have been determined using a gas thermometer (at equilibrium with the fixed points) that relates the temperature to the pressure and volume of the gas through equations of state.

The assigned values for these fixed points were agreed upon at the Seventh General Conference on Weights and Measures in 1927 and became the International Temperature Scale.[13] Since its inception, refinements to the assigned values have been made and new fixed points have been added, and the current practical temperature scale is the International Temperature Scale of 1990 (ITS-90) that defines temperatures from 0.65 K to 1357 K.[15] From the ITS-90 fixed points, one can calibrate a practical thermometer for use in everyday applications.

For most applications of specific heat measurements, resistance thermometers are used as the working thermometers. These, like all resistance thermometers, operate on the principle that the electrical resistance of a material is dependent on temperature, thus a measurement of the thermometer resistance will yield the temperature. This type of thermometer can be constructed from a variety of materials (platinum being one of the most common) and the most important criterion is that the resistance of the thermometer be consistent at any given temperature and will not change with thermal cycling. Thermometers calibrated against the fixed points of ITS-90 are referred to as primary standards, and for the temperature range between 13.8 K and 505 K, a primary standard must be a Standard Platinum Resistance Thermometer (SPRT) that is made from pure, strain-free platinum with a nominal resistance of 25.5 Ω at 273.16 K[15]. In between the fixed points on the ITS-90 scale, the temperature is related to the resistance of the SPRT by a reference function that is defined by ITS-90.[15] Thermometers that have been calibrated against one of these primary standards are referred to as secondary standards.

Ideally, one would use a primary standard thermometer for specific heat measurement; however, it is cheaper and often more practical because of size and mass considerations to use a secondary standard. For these types of thermometers, it is best to use the ITS-90 reference function; however, due to the particular manufacturing

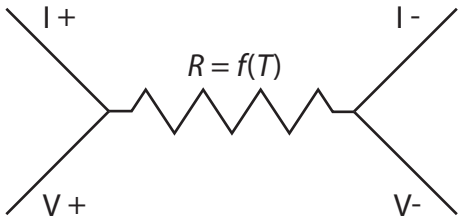

Figure 1.10. Schematic diagram for a resistance thermometer where the resistance is some function of temperature. The resistance is measured using the current leads, I, and the voltage leads V.

design of the thermometers or the calibration points used, the temperature-resistance function for these thermometers is often a polynomial of the type $T = \sum_{i=-j}^{k} n_i \cdot R^i$, where $-j$ and k are determined from a best fit of the T vs. R data.[h] This is not a function defined by ITS-90, and the R-T data is often known better than a polynomial can adequately represent. However, a smoothed function of the data can be found by fitting the deviation from the polynomial fit (residuals) with a spline function and adding the spline function to the R-T fit.

No matter what type of thermometer calibration is used, it is important that the temperature scale is a smooth representation of the temperature with respect to the resistance, since the resolution of ΔT (and of T) is determined by the resolution of the resistance measurements and the change of the thermometer's resistance with the change in temperature. The latter depends on the material from which the thermometer is constructed and the temperature range that is being measured. The former is determined by the sensitivity of the instrumentation and how the resistance is measured.

Resistance measurements for thermometers are generally made via a four lead method. Current, I, flows across the thermometer though one set of leads while

[h] Thermometers that meet the specifications for primary standards but have not been calibrated as such, can use the ITS-90 reference function to represent the R-T curve.

potential, V, is measured across the second set of leads. From the current and the potential, the resistance can be calculated from Ohm's law, $R = V/I$, using either a DC or AC measurement technique.

In the DC technique, a highly stable DC current is put through the sample thermometer, and the voltage potential across the thermometer is measured with a digital voltmeter or potentiometer. In this regard, the DC method is relatively simple for measuring the resistance, but several factors must be considered to obtain the best resistance measurements. These factors include: compensation for thermal EMF's in the thermometer circuit (this can be compensated for by switching polarity across the circuit); ensuring that the current is accurately known for each potential measurement; and adjusting the current so that it is high enough to maximize the sensitivity of the resistance measurement but not high enough to induce self heating. The AC technique works by passing an AC current through the thermometer at a selected frequency, and then measuring the potential across the thermometer with a bridge after the potential signal has been conditioned by a lock-in amplifier or a chopper that is synchronous with the AC current. This technique has a few advantages over the DC method, namely there is no need to compensate for thermal EMF's and the same sensitivity as the DC method can be achieved with a smaller current. The electronic circuitry required for this method is more complex than for the DC technique, but commercial units for measuring resistance with the AC technique are available.

1.3.6 Power Measurements

Equally important to the temperature measurement is the accurate determination of heat input into the system, since calculation of the specific heat is also dependent on the heat input. To accomplish this, the heater must be designed to efficiently

transfer heat, the power input into the heater must be measured accurately, and all sources of heat loss must be known and accounted for in the specific heat calculations.

The main criterion for the heater itself is that it be designed to distribute the heat quickly into the sample to help minimize heat loss.[10] This is accomplished by ensuring that the heater is in good thermal contact with the addenda, and there is good thermal conductivity between the addenda and the sample. Additionally, the heater should be constructed of a material with a low thermal resistance coefficient, such as Manganin or Constantan. Thus, as the temperature increases over the course of the specific heat measurement, the heater resistance remains relatively constant, making the power input and measurement more consistent.

The accurate and precise measurement of the power input across the heater begins with the design of the heater circuit. Generally, the calorimeter heater is wired in series with a standard resistor in which the current is supplied by a highly stable source – often a battery or a precision electronic device (see figure 1.11). The resistive heating power, P, from the calorimeter heater is $P = I^2R$, where I is the current and R is the heater resistance. If the current can be accurately determined, then an accurate resistance can be obtained using Ohm's law by measuring the potential across the calorimeter heater, V_{heat}. The current is the same at every point along the circuit loop, so it does not matter where the current is measured, but to obtain the best current measurement, the current is measured at the standard resistor by evaluating the potential across the standard resistor, V_{std}. Since the standard resistor has a known, constant resistance, Ohm's law is used to solve for the current and the power expression becomes $P = V_{std}V_{heat}/R_{std}$, where R_{std} is the resistance of the standard resistor. Therefore, to obtain the best power measurements, the voltage potentials must be measured with as much accuracy as possible and the resistance of the standard should be known with a high degree of certainty.

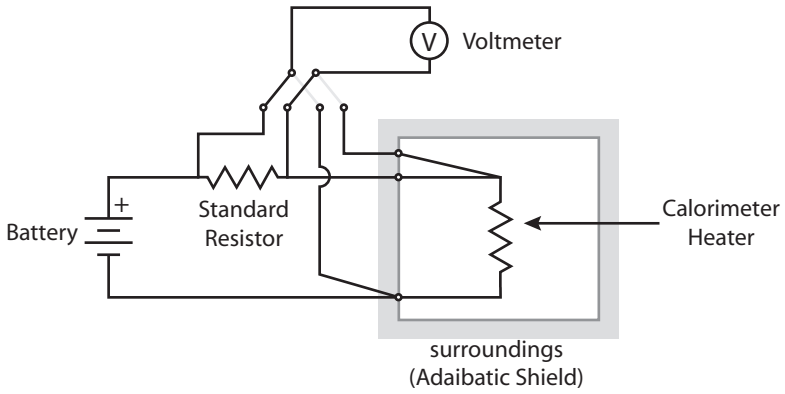

Figure 1.11. Schematic diagram of a basic calorimeter heater circuit.

The most exacting part of the power measurements is identifying and accounting for all heat losses associated with the power input. The main source of heat loss for the calorimeter heater during the pulse phase is through the heater leads extending from the addenda to the surroundings. To help minimize this loss, the calorimeter heater has three leads (one current lead, one potential lead, and one shared current/potential lead) with a four lead takeoff on the surroundings, instead of the traditional four leads typically used in resistance measurements (two current leads and two potential leads). Compare the current and potential leads in the heater circuit in figure 1.11 to the simple resistance measurement of a thermometer in figure 1.10. Although this results in measuring the lead resistance along with the heater resistance, a well designed system ensures that the heater resistance is very large compared to that of the lead, so that the resistance of the lead is a negligible fraction of the total resistance. The heat loss from the leads is often calculated by assuming that half of the resistive heating from the leads goes into the calorimeter and half goes out to the surroundings. Thus, the heat losses can be determined by knowing the temperature dependent thermal conductivity and resistivity of the leads. One difficulty with this correction is that the assumptions are not always completely valid, so there are often adjustments to the heat loss based on experiment.

1.3.7 Curvature Corrections

As discussed previously, the specific heat is the derivative of energy with respect to temperature, but in many of the experimental techniques (i.e. the pulse technique) this expression is simplified as $\lim_{\Delta T \to 0}(Q/\Delta T)$ (equation 1.30). This form of the expression actually calculates the mean specific heat, C_{mean}, at the median temperature of the ΔT range, but since the specific heat is defined by a derivative, there is some deviation from the true specific heat, C_{true}, that increases as the specific heat departs from linearity or as the value of ΔT becomes large.[10] Therefore, a curvature correction is applied to the mean specific heat to compensate for the deviation from the true specific heat. Essentially, it is assumed that the true specific heat and the mean specific heat can be represented by cubic functions over a limited range, then the difference between the true and mean heat capacities can be expressed by:

$$C_{true} - C_{mean} = \frac{(T_2 - T_1)^2}{24}\left(\frac{\partial^2 C_{true}}{\partial T^2}\right) \tag{1.35}$$

where the value of $\partial^2 C_{true}/\partial T^2$ can be approximated by assuming the mean specific heat is close enough to the true specific heat that the second derivative of the mean specific heat can be used instead.[10][i] The curvature correction is only a small fraction of the overall specific heat, but as the accuracy and precision of specific heat measurements is increased, it becomes an important factor in the overall uncertainty of the measured values.

1.4 Scope

This work will cover a variety of topics related to the study of specific heat including a discussion on the design, testing, and implementation of a new experimental

[i] A more descriptive derivation of the curvature correction has been presented by Westrum *et al.*[10]

apparatus, and the detailed and critical study of the thermodynamic and physical properties of various metallic systems.

As with any area of science, researchers in the area of calorimetry are continually refining instrumentation and techniques while simultaneously attempting to improve the overall accuracy and precision of the measurements. It is in this spirit and frame of mind that much of the work for this thesis has originated. As discussed above, the adiabatic pulse technique is generally regarded as the most accurate and precise of all of the calorimetric techniques, however it is not without its limitations, one of the main ones being the quantity of sample required to obtain accurate measurements. Typically, the current adiabatic calorimeter requires around 8 to 10 cm^3 of material for the specific heat measurements to ensure the desired accuracy and precision (ideally this is between 10 and 30 g). If the amount of sample available for study is less than 2 or 3 cm^3 (and less than a few grams), the sample will contribute only a small fraction to the overall specific heat of the system (the sample plus addenda or calorimeter vessel). This leads to an overall increase in the experimental uncertainty. Apart from obtaining more sample, the only way to improve the uncertainty of the measurement is to decrease the contribution from the addenda by minimizing the mass of the calorimeter. Thus, we have assembled a new adiabatic calorimetric instrument that is well suited to measure samples of less than 1 cm^3, which would have been previously considered too small to be measured on the current adiabatic equipment. Therefore, a critical part of this work focuses on this new apparatus that includes a detailed description of the new instrument including its construction, physical layout, and electronic circuitry. Along with this will be a discussion of shield control and its implementation on this apparatus, as well as an overview of the data collection and analysis programs used for obtaining the specific heat. Equally important to this discussion are the experimental results of standard reference materials measured on

the instrument; copper, sapphire, and benzoic acid. These materials allow one to asses the performance and overall uncertainty for the instrument. There will also be experimental results and discussions for measurements of materials run on the instrument. This includes β-FeOOH, a compound with little specific heat or other thermodynamic data available in the literature.

A final part of this work will relate to specific heat measurement of nuclear materials that were run on the current adiabatic and semi-adiabatic instruments. The first nuclear material is α-uranium run as a single crystal and also as a polycrystal. Aside from being a nuclear material, α-uranium is interesting in that the specific heat of the polycrystal is different from the specific heat of the single crystal due to structural anisotropies, which reflects differences in phase transitions, the Debye temperatures, and electronic and lattice energies. The second set of nuclear compounds are TiB_2 and ^6LiF, which have been investigated at low temperatures as part of a study for their potential use in neutron spectrometers.

References

[1] Gopal, E. S. R., *Specific Heats at Low Temperatures*, New York: Plenum Press, **1966**.

[2] Barron, T. H. K.; White, G. K., *Heat Capacity and Thermal Expansion at Low Temperatures*, New York: Kluwer Academic/Plenum Publishers, **1999**.

[3] Ott, J. B.; Boerio-Goates, J., *Chemical Thermodynamics: Principles and Applications*, London: Academic Press, **2000**.

[4] McNaught, A. D.; Wilkinson, A., *Compendium of Chemical Terminology: IUPAC Recomendations*, Malden, MA: Blackwell Science, 2nd edn., **1997**.

[5] Kittel, C., *Introduction to Solid State Physics*, New York: John Wiley and Sons, 7th edn., **1996**.

[6] Stokes, H. T., *Solid State Physics*, Provo, Utah: Brigham Young University, 3rd edn., **2000**.

[7] Woodfield, B. F.; Boerio-Goates, J.; Shapiro, J. L.; Putnam, R. L.; Navrotsky, A., *J. Chem. Thermo.* **1999**, *31*, 245–253.

[8] Bader, S. D.; Phillips, N. E.; Fisher, E. S., *Phys. Rev. B* **1975**, *12*, 4929–4940.

[9] Stevens, R.; Boerio-Goates, J., *J. Chem. Thermodyn.* **2004**, *36*, 857–863.

[10] Westrum, Jr., E. F.; Furukawa, G. T.; McCullough, J. P., in J. P. McCullough; D. W. Scott, eds., *Experimental Thermodynamics*, Plenum Press, vol. 1, 1968 pp. 133–214.

[11] Woodfield, B. F., *Specific Heat of High-Temperature Superconductors: Apparatus and Measurement*, Ph.D. thesis, University of California, Berkeley, **1995**.

[12] Boerio-Goates, J.; Callanan, J. E., in B. W. Rossiter; R. C. Baetzold, eds., *Physical Methods of Chemistry*, John Wiley and Sons, vol. 6, 2nd edn., 1992 pp. 621–717.

[13] Stimson, H. F.; Lovejoy, D. R.; Clement, J. R., in J. P. McCullough; D. W. Scott, eds., *Experimental Thermodynamics*, Plenum Press, vol. 1, 1968 pp. 15–57.

[14] Soulen Jr., R. J.; Fogle, W. E., *Physics Today* **1997**, pp. 36–42.

[15] Mangum, B. W.; Furukawa, G. T., Guidelines for realizing the international temperature scale of 1990 (ITS-90), Tech. Rep. 1265, National Institute for Standards and Technology, Gaithersburg, MD 20899, **1990**.

Chapter 2

Instrumentation: Apparatus and Electronics

Several instruments have been used to measure the specific heat of the different samples studied in this project. Thus, it is necessary to provide descriptions of each instrument. We will begin with a brief description of the adiabatic and semi-adiabatic apparatuses that have been in use for several years, and have been documented and well characterized. The remainder of the discussion will be a detailed and comprehensive description of the new microcalorimeter that has been constructed as part of this project. This chapter will focus chiefly on the physical configuration of the instrument, while the implementation of the data collection and temperature control will be discussed in the next chapter.

2.1 The Adiabatic Calorimeter

The current adiabatic apparatus is a variation of the apparatus designed by Westrum. It has a working range between 5 K and 400 K, and has been described in detail in several communications, and is illustrated in figure 2.1.[1, 2, 3, 4] The calorimeter vessel is constructed from copper and plated with gold, and has an inter-

nal volume of 10.5 cm^3. Temperature is measured using a Rosemont Aerospace 25.5 Ω secondary standard thermometer that has been calibrated on the ITS-90 temperature scale. Adiabatic conditions of the calorimeter are maintained in the cryostat by the use of four adiabatic shields. The main adiabatic shield, by which most of the radiative heat from the calorimeter is transferred, is a cylinder 16 cm high and 6 cm in diameter. On the top and bottom of the main shield are two circular shields 6 cm in diameter that are maintained at the same temperature as the main shield and serve to completely surround the calorimeter in an adiabatic environment. The fourth shield is a copper ring of 8 cm in diameter and 1 cm high around which the thermometer leads, heater leads, and thermocouple wiring are wound in order to bring the temperature of these wires to the temperature of the calorimeter and minimize heat loss. The four shields are maintained at the temperature of the calorimeter through the use of four Linear Research Model LR-131-488 temperature controllers that use analog PID control circuitry to adjust the heat output to the adiabatic shields. The sample and shields are cooled using two copper tanks positioned above the calorimeter that can be filled with either liquid nitrogen, to cool the sample down to 50 K (with pumping), or liquid helium, to cool the sample below 50 K.

The accuracy of the adiabatic apparatus is generally better than ± 0.1% above 20 K, with a resolution of better than ± 0.1% from 20 K to 400 K on measured samples of benzoic acid and sapphire.[1, 2, 3] Recent measurements on high purity copper (99.999%) have also confirmed the accuracy of measurements taken by this apparatus, and they fall within the parameters above.[4] From this point forward, this apparatus will generally be referred to as the large-scale adiabatic apparatus since this work discusses two different adiabatic instruments.

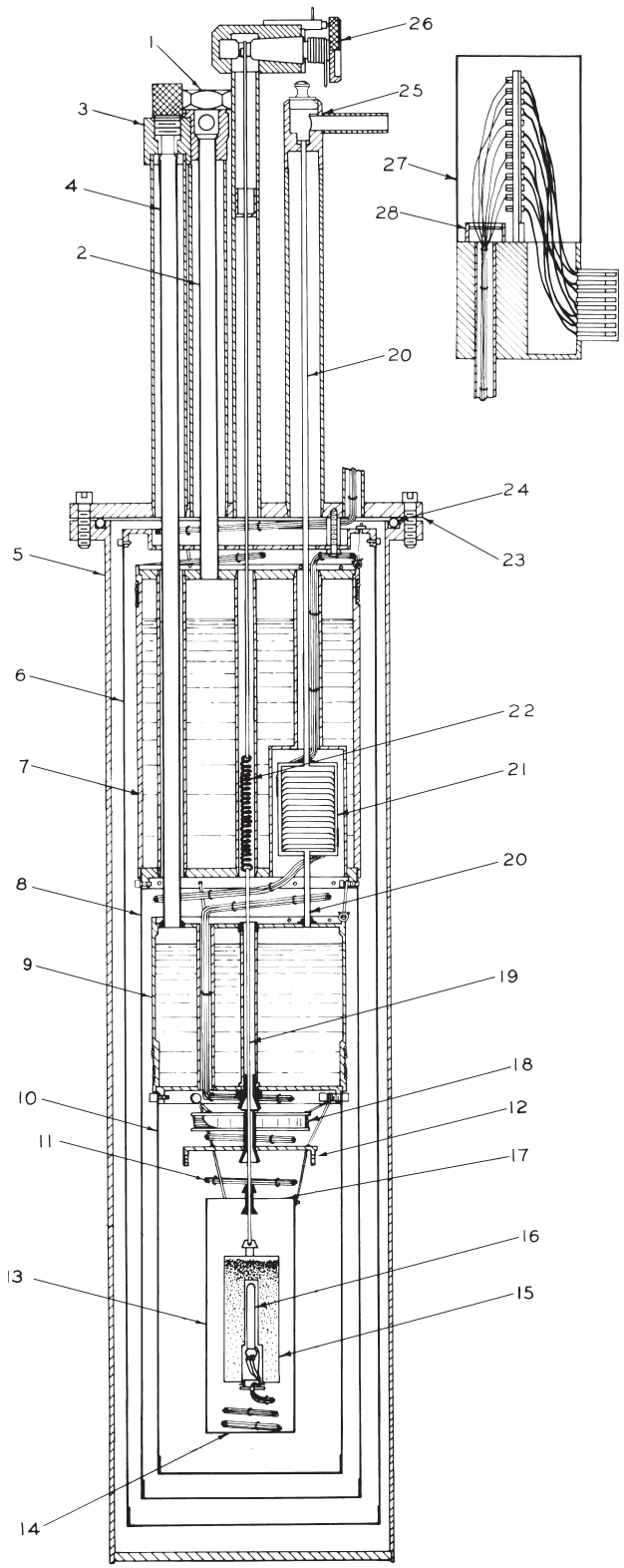

1. Liquid nitrogen inlet/outlet connector
2. Liquid nitrogen filling tube
3. Compression fitting to seal inlet to liquid helium tank
4. Liquid helium filling tube
5. Brass vacuum jacket
6. Outer "floating" radiation shield
7. Outer vacuum vessel
8. Nitrogen radiation shield
9. Liquid helium tank
10. Helium radiation shield
11. Bundle of lead wires
12. GASH adiabatic shield
13. MASH adiabatic shield
14. BASH adiabatic shield
15. Calorimeter vessel
16. Calorimeter heater/thermometer assembly
17. TASH adiabatic shield
18. Temperature controlled ring
19. Supporting braided silk line
20. Helium outlet tube
21. Economizer (effluent helium vapor heat exchanger)
22. Coil springs
23. cover plate
24. O-ring gasket
25. Helium outlet connector
26. Calorimeter windlass
27. Terminal block and shield
28. vacuum seal

Figure 2.1. The current large-scale adiabatic apparatus used for measuring specific heat.

2.2 The Semi-Adiabatic Calorimeter

The semi-adiabatic apparatus was designed and constructed previously and is built around a commercial ^{4}He and ^{3}He stage, which is immersed in a bath of liquid helium that allows the sample to be cooled to 0.3 K (A diagram can be seen in figure 2.2).[5] Attached to the ^{3}He stage is a constant temperature block that is constructed of gold-plated copper and around which is wound manganin wire that is used as a resistive heater. The constant temperature block also holds a platinum resistance thermometer and a germanium resistance thermometer, that serve as reference thermometers for the system, as well as additional thermometers used to control the block temperature. Below the constant temperature block is a cage structure that serves as a support for the sample platform and as a takeoff junction for the sample and heater leads, all of which is surrounded by a thermal shield that helps create a more uniform heat sink for the sample. The sample platform consists of a 0.5 in. gold-plated copper disk underneath which is a 15000 Ω thin film chip resistor that serves as a heater, a Lakeshore Cryotronics model PT-111 platinum resistance thermometer (for measurement above 12 K), and a Lakeshore Cryotronics Cernox thin film thermometer (for measurement below 40 K). The sample platform is held in place by nylon monofilament line that is attached to the top and bottom of the cage support structure. A gold wire extends from the top of the sample platform and serves as a means of rapid cooling via a mechanical heat switch.

With the combination of thermometers, this apparatus has a working temperature range from 0.4 K to 100 K with the use of both the semi-adiabatic pulse and the isothermal techniques. From measurements on high purity copper, the overall uncertainly in the measurements of this instrument below 30 K gives an accuracy of better than ± 0.25 % and a precision of better than 0.1 %.[6] Above 30 K, the

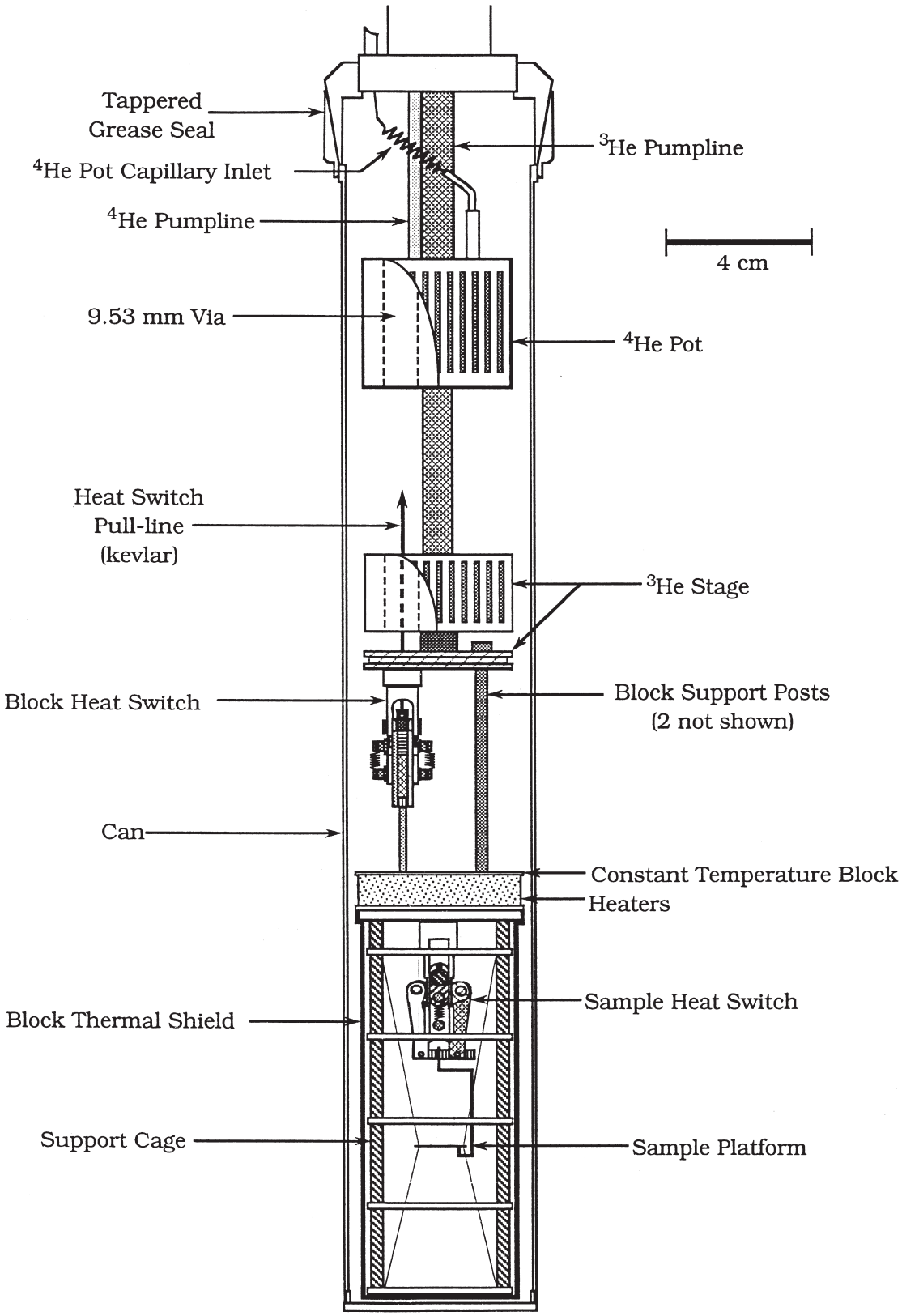

Figure 2.2. The semi-adiabatic apparatus used for measuring specific heat

accuracy drops to ± 0.5 % but maintains the same precision of 0.1 % on samples with high thermal conductivity.[6]

2.3 The Small-Scale Apparatus

As new and novel chemical compounds are being synthesized, there is a continual need to explore the thermodynamic properties of these materials. However, there is a conflict between the resources of the synthetic chemist and the needs of the thermodynamicist. Traditional methods of adiabatic calorimetry have required relatively large amounts of sample to perform the calorimetric measurements, much more than the synthetic chemists can easily provide for many samples. While the current large-scale calorimeter requires only 10 cm^3 of sample, this is still a relatively large amount of sample when one considers that for some synthetic methods, it may take months to synthesize a fraction of that amount.[4] Although the trend over the past several decades has been a steady decrease in the amount of sample required for adiabatic specific heat measurements, it has not kept pace with the production of new materials.[a] Thus, to accommodate emerging trends in synthetic chemistry, a new microcalorimeter and its associated cryostat have been constructed.

The current cryostat for the microcalorimeter was built by Dow Chemical in Midland, Michigan and modified for use with a calorimeter designed by Robert Putnam. The cryostat was shipped to BYU, but in the process, the cryostat received significant damage. Repairs included re-welding of several joints and a nearly complete re-wiring of the apparatus, and the original calorimeter for use in the cryostat at BYU was a modification of the design by Ogata and Matsuo.[8] However, the calorimeter had only

[a] As a point of reference, William Giauque used 2.5 kg of gold to measure its specific heat in the 1940's.[7] Measuring the same sample on the current large scale calorimeter would require only about 25 g of sample: 1% of the amount Giauque used.

a limited lifetime of use at BYU. This may have been partially due to the fact that the reported accuracy of benzoic acid run in this calorimeter was only 2.5 percent.[8] The following sections will detail the design and functions of the cryostat, calorimeter, and the electronics

2.3.1 The Cryostat

The cryostat for the microcalorimeter is also a variation of the design by Westrum, which can be seen in figure 2.3. The main function of the cryostat is to thermally isolate, cool, and control the temperature of the calorimeter, and this is achieved by a variety of means. The sample is cooled by means of two brass refrigerant tanks positioned above the calorimeter vessel. The lower tank (closest to the calorimeter) can hold either liquid helium for measurements below 50 K or liquid nitrogen for measurements above 50 K. It is called the helium tank. The upper tank is designed to hold nitrogen only, and it is referred to as the nitrogen tank. Both tanks are attached to two external 1/2 inch copper pipe manifolds that allow gaseous helium or nitrogen to be vented away from the cryostat, or allow liquid nitrogen to be pumped on via a vacuum system. Pumping on the nitrogen in the helium tank provides a means to cool down to 50 K using nitrogen. To achieve rapid cooling, the calorimeter is raised into contact with the helium tank by means of a dual windlass system.

The calorimeter is suspended by a size 2 braided surgical silk thread that runs from the region of the main adiabatic shield to top of the calorimeter ending at a windlass. This serves to adjust the position of the calorimeter in the cryostat and to help thermally isolate the calorimeter, since the braided silk is an extremely poor thermal conductor. The only other physical connections from the calorimeter to the surroundings are the thermometer/heater leads and two thermocouples. These

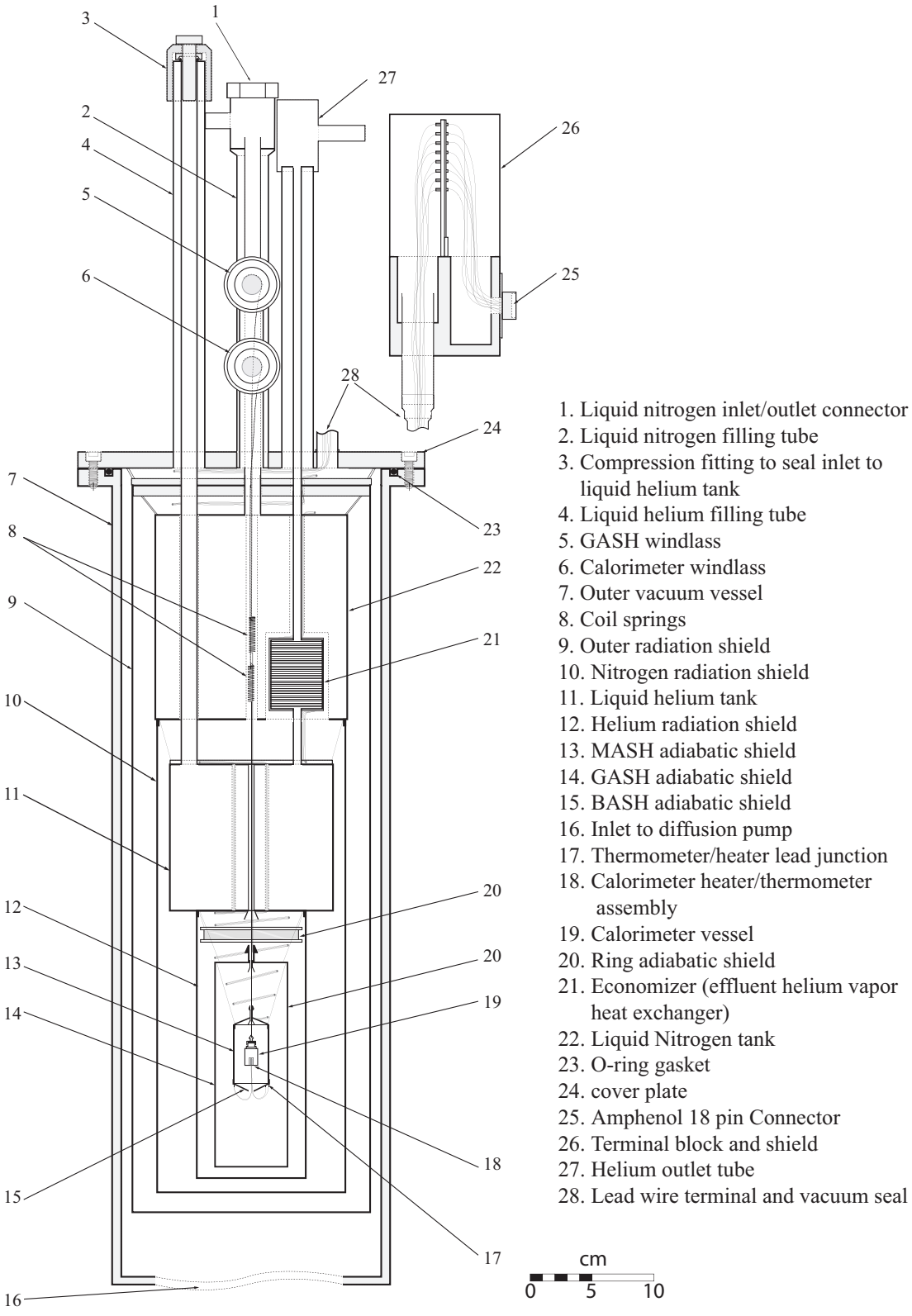

Figure 2.3. The microcalorimeter cryostat

thermocouples are used to control the shield temperature, and they extend from the main adiabatic shield to the thermocouple wells on the calorimeter. The thermal isolation of the calorimeter is furthered by maintaining the system under a dynamic vacuum that employs an oil diffusion pump to minimize conductive heat transfer from and by three chrome-plated radiation shields that surround the calorimeter and adiabatic shields to minimize the effects of thermal radiation.

Adiabatic Shields

The most critical components of the cryostat are the adiabatic shields that surround the calorimeter and maintain the adiabatic conditions during specific heat measurements. The detailed configuration of the adiabatic shields can be seen in figure 2.4. Like the shields for the large-scale apparatus, the shields for the microcalorimeter are constructed from copper and have been gold plated to facilitate rapid heat flow and thermal equilibrium. The main adiabatic shield (MASH) is a cylinder 2.75 cm high and 2.75 cm in diameter, and on the top and bottom of MASH are two conical shields 2.9 cm in diameter. These shields are referred to as TASH and BASH respectively (for top and bottom adiabatic shields). While these three shields are wired independently and have separate connections at the top of the calorimeter, the heaters for these shields have been connected in series at the heater power supply, so in effect, they operate as a single shield. The wiring was configured in this manner because in the initial test operations, the shield control was more stable in this configuration as opposed to controlling the three shields independently. (Much of this will be detailed further in a discussion about shield control in chapter 3.) Surrounding these shields is a guard adiabatic shield (GASH), a cylinder 16.5 cm by 5.85 cm in diameter, capped on both ends, that completely encases the main set of adiabatic shields. A final thermally controlled site, referred to as Ring, is a copper loop of 8 cm

in diameter and 1 cm high around which the thermometer leads, heater leads, and thermocouple wiring are wound in order to bring the temperature of these wires to the temperature of the calorimeter to minimize heat loss.

As mentioned previously, the calorimeter, which is suspended by the braided silk line, can be raised up into contact with the helium tank for rapid cooling, and this is accomplished by use of a dual windlass systems. The first windlass is connected to the silk thread which suspends the calorimeter and allows the calorimeter to be raised into contact with TASH. Then both TASH and the calorimeter can be raised into contact with GASH, and finally the calorimeter and all the adiabatic shields can be raised up into contact with the the helium tank. The second windlass is attached to a second silk thread that is secured to the top of GASH and allows GASH to be raised and lowered independently of the calorimeter. This was done so the thread holding the calorimeter does not have the strain of supporting the calorimeter, the central adiabatic shields, and GASH when the calorimeter is raised up to the helium tank.[8]

Cryostat Wiring

The wires from the calorimeter heater, calorimeter thermometer, and from the adiabatic shield thermocouples and heaters are attached to three 18 pin Amphenol® connectors at the top of the cryostat. These wires are soldered to a patch board to which are soldered additional wires that go to the Amphenol® connectors. As the lead wires descend to the area of the shields and calorimeter, they are kept as bundles and thermally attached to the nitrogen and helium tanks with GE 7031 varnish to pre-cool these leads, to avoid introducing heat into the calorimeter. From the Amphenol® connectors, 18 individually shielded twisted pair cables run from the cryostat to the instrument rack in three separate bundles. Table 2.1 gives a description of the wiring

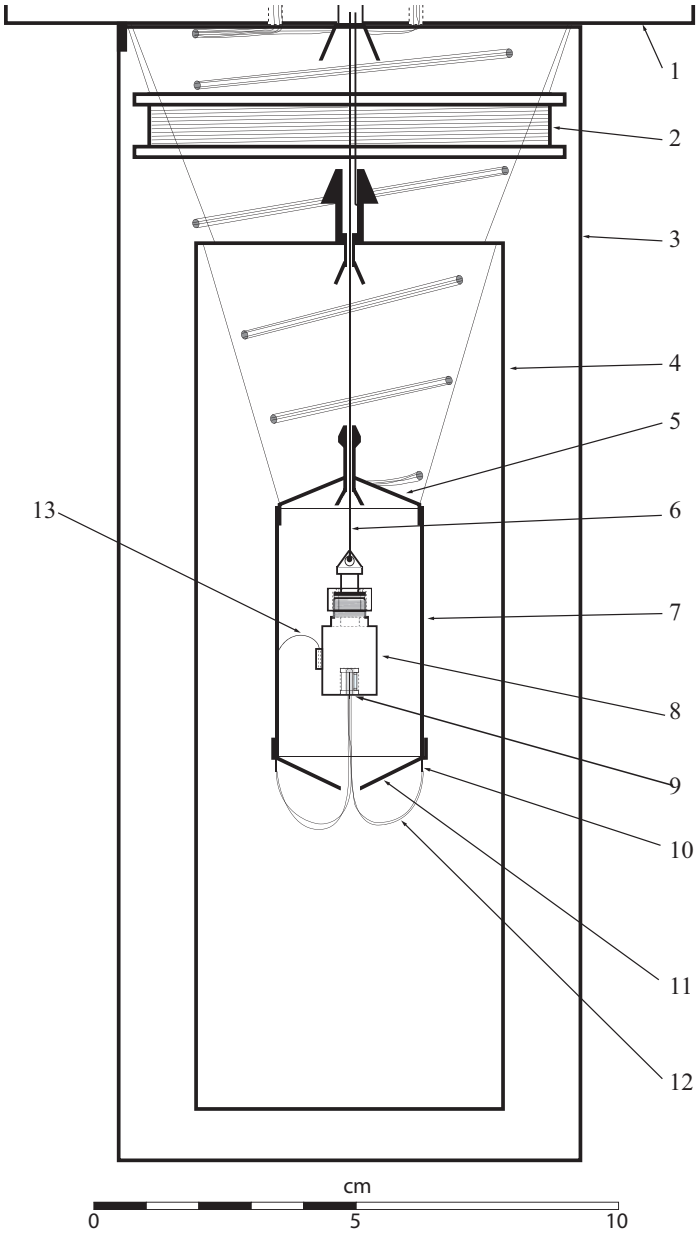

1. Bottom of liquid helium tank.
2. Ring adiabatic shield
3. Helium radiation shield
4. GASH adiabatic shield
5. TASH
6. Silk thread for suspending the calorimeter
7. MASH adiabatic shield
8. Calorimeter vessel
9. Calorimeter heater/thermometer assembly
10. Thermometer/heater lead junction
11. BASH adiabatic shield
12. Thermometer/heater leads
13. MASH thermocouple leads

Figure 2.4. Enlarged diagram of the cryostat showing the calorimeter and the adiabatic shields.

Table 2.1. Connector configuration for small-scale apparatus. The pin numbers correspond to the the respective pins on the 3 Amphenol® connectors, labelled A, B, and C.

Connector A

cable #	Pin 1 (black)	Pin 2 (red)	Ω	Description	Junction #	
1	A	L	91.4	MASH Thermocouple	9	1
2	B	N	41.3	BASH Thermocouple	10	2
3	M	K	38.8	TASH Thermocouple	11	3
4	C	P	127.3	Ring Thermocouple	12	4
5	T	J	96.6	GASH Thermocouple	13	5
	D	R		-	14	6
6	S	H	254.1	He(ℓ) tank top Thermocouple	15	7
7	F	G	129.4	N_2(ℓ) tank absolute Thermocouple	16	8
	-	+			-	+

Connector B

cable #	Pin 1 (black)	Pin 2 (red)	Ω	Description	Junction #	
8	A	L	24.5	Ring heater	1	9
9	B	N	31.1	TASH heater	2	10
10	M	K	32.1	BASH heater	3	11
11	C	P	22.2	MASH heater	4	12
	T	J		-	5	13
12	D	R		spare	6	14
	S	H		-	7	15
13	F	G	111.7	GASH heater	8	16
	-	+			-	+

Connector C

cable #	Pin 1 (black)	Pin 2 (red)	Ω	Description	Junction #	
14	A	L	143	Thermometer V	9	1
15	B	N	133	Thermometer I	10	2
16	M	K	15 kΩ	Calorimeter heater V	11	3
17	C	P	15 kΩ	Calorimeter heater I	12	4
	T	J	96.6		13	5
18	D	R	–	spare	14	6
	S	H			15	7
	F	G			16	8
	-	+			-	+

connections that are on the Amphenol® connectors as the wiring proceeds from the connector to the patch board and then down to the specified component.

2.3.2 Microcalorimeter

The purpose of this section is to discuss the specifics of the microcalorimeter design, and the differences between the current large-scale calorimeter (the 10 cm^3 and 50 cm^3 volume calorimeters) and the variations from the Westrum design. The principle difference between the current BYU large-scale calorimeter and the microcalorimeter, apart from the size, is the thermometer and the heater. The current microcalorimeter is essentially a scaled down version of the current large-scale calorimeter rather than a modification or redesign of the original calorimeter designed by Putnam.[8]

The calorimeter vessel is constructed primarily from copper that has been gold-plated and has an internal volume of 0.875 cm^3. The main body of the calorimeter is a gold-plated copper cylinder of 0.5 in. high and 0.4 in. in diameter. Figure 2.5 shows the calorimeter components and relative positions. The bottom of the calorimeter has a 0.21 in. deep cylindrical recess of 0.14 in. diameter into which the thermometer/heater assembly is inserted. On one side of the calorimeter body, there is a gold-plated copper block with two holes that serve as wells for thermocouples that are used for maintaining adiabatic conditions. On top of the main calorimeter body is a machined piece of Monel® alloy (Ni65/Cu33/Fe2) which serves to seal the calorimeter under a partial pressure of helium gas. The bottom of this piece has a hexagonal shape that helps prevent the calorimeter from rotating as it is being sealed, and the upper portion of this piece is threaded and the top has been machined to a knife edge. Additional parts of the calorimeter include a phosphor bronze nut which is threaded

to match the threads on the Monel® piece, a gold-plated copper fitting (referred to as the cone) which is used to suspend the calorimeter , and a 0.22 in. diameter, 0.02 in. thick gold disk which serves as a gasket. The calorimeter is assembled by placing a gold gasket on top of the knife edge followed by the cone and nut. Subsequently, the nut is screwed down and tightened to 15 inch-pounds of torque. This action drives the knife edge into the gold gasket creating a gas-tight seal. As part of the sealing process, the calorimeter is placed in a sealing chamber, which is then placed under vacuum to remove all of the air from the inside of the calorimeter, and the calorimeter is then backfilled with 15 to 20 torr of helium gas to facilitate heat exchange between the calorimeter and the sample.

The thermometer/heater sleeve, as seen in figure 2.6, fits up into the recess on the calorimeter and is constructed around a gold-plated copper cylinder with a well for the thermometer, a channel for the heater and the leads, and and outer recess designed to help guide the leads. The thermometer is a platinum resistance thermometer model PT-111 from LakeShore Cryotronics Inc.[b] that is 5.0 mm long by 1.75 mm in diameter, and is held in place by General Electric (GE) 7031 adhesive and insulating varnish. The heater for the calorimeter is a 15000 Ω thin film chip resistor manufactured by the Vishay Company.[c] The resistor is set in the channel that has been lined with lens paper and attached using the GE 7031 electrical varnish. Electrical leads for the thermometer and heater were made from red and green coated 0.005 inch phosphor bronze wire from the California Fine Wire company (5%, CDA 510-"A").[d] The wires were soldered to the heater and thermometer leads with standard 60-40 lead-tin electrical solder. The wires were guided into the channel and then wrapped around

[b]Corporate offices located at 575 McCorkle Blvd, Westerville, OH 43082, http//www.lakeshore.com

[c]Corporate offices located at 63 Lincoln Highway, Malvern, PA 19355, http//www.vishay.com

[d]Corporate offices located at 338 South Fourth Street, Grover Beach, CA 93433, http//www.calfinewire.com

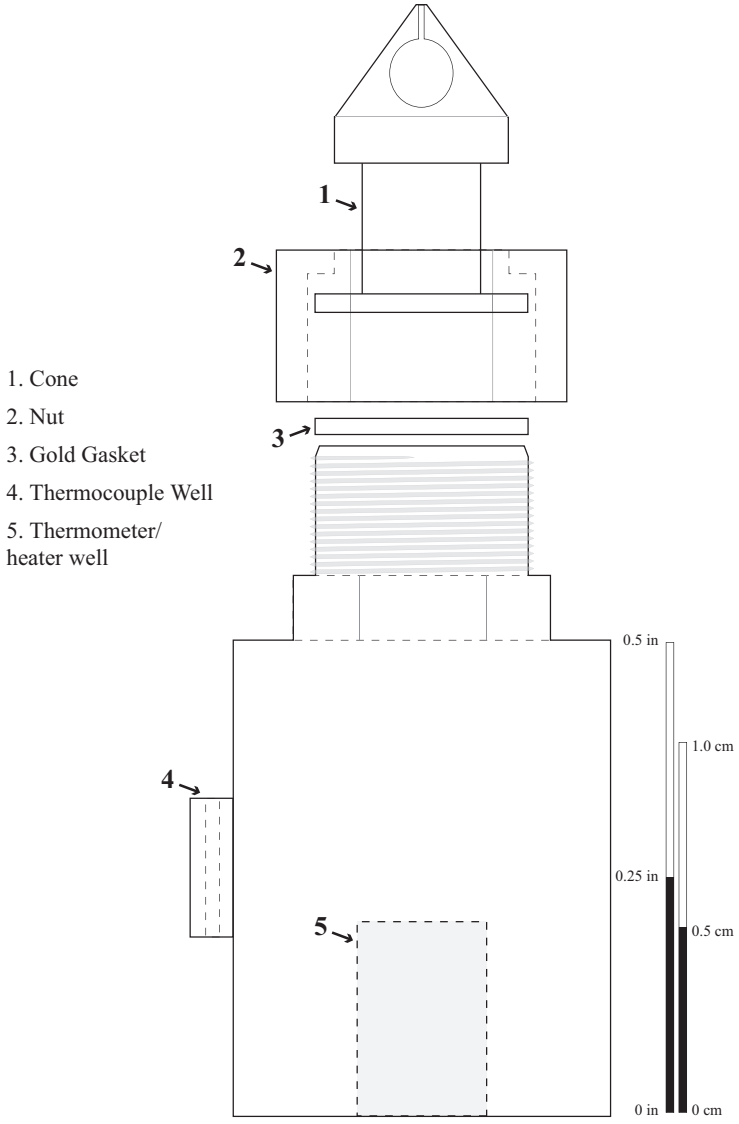

Figure 2.5. The microcalorimeter

1. Lakeshore PT-111 Platinum Resistance Thermometer

2. 15 kΩ Chip Resistor (calorimeter heater)

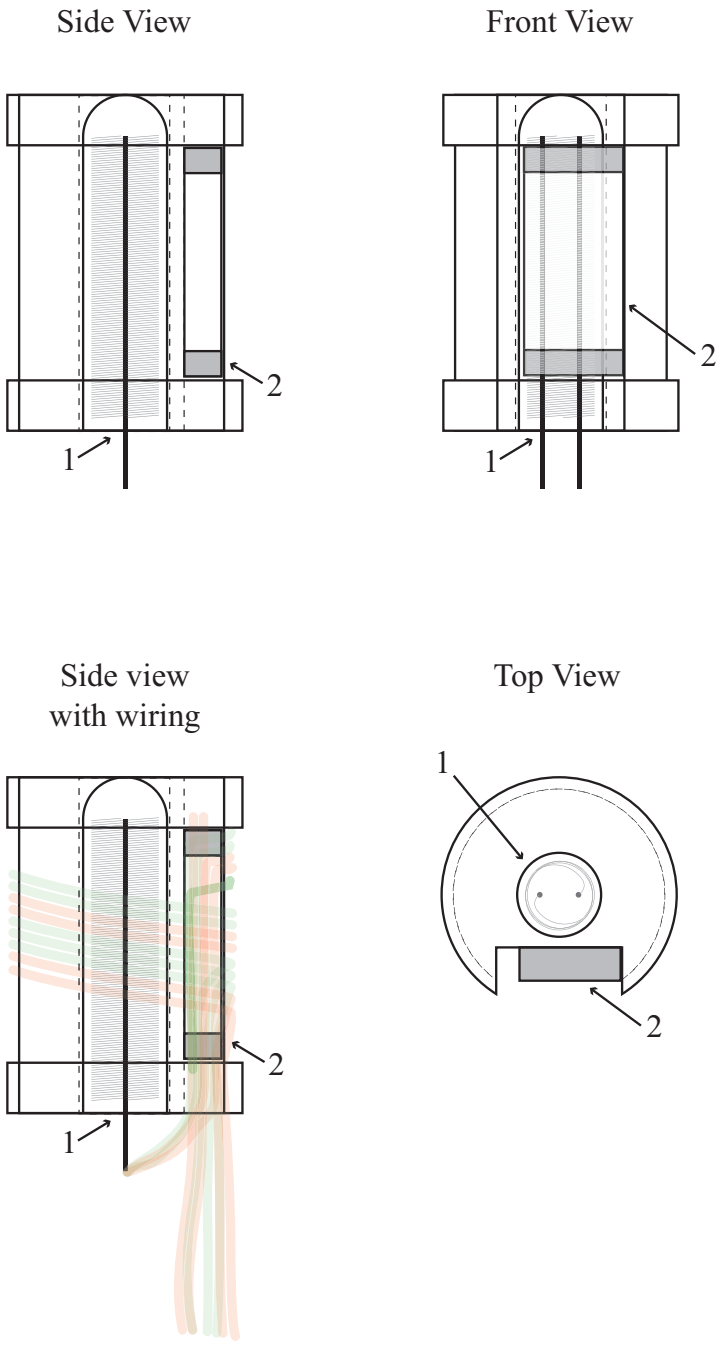

Figure 2.6. The thermometer/heater sleeve assembly for the microcalorimeter

Table 2.2. Thermometer and heater lead connections for the microcalorimeter. The number refers to the connection number on the bottom of the adiabatic shield, and the letter refers to the letter on the Amphenol® connector on the top of the cryostat.

number	Letter	Description	wire color	wrap color
1	L	Thermometer V+	red	white
2	L	Thermometer I+	red	blue
11-12	L	Heater V-/ I-	green	red
3	L	Heater V+	red	red/white
4	L	Heater I+	red	red
10	L	Thermometer I-	green	blue
9	L	Thermometer V-	green	white

the outer recess once before being guided back down the channel and secured with GE 7031 varnish. This was done to prevent any direct strains on the solder joints from movements in the wire leads. Phosphor bronze leads were used instead of copper, since phosphor bronze has a higher tensile strength and lower thermal conductivity than copper. The ends of the leads were soldered into pins for attachment to the Bottom Adiabatic Shield (BASH) (refer to figure 2.4). By standard convention, the wire leads were color coded such that red designates the positive leads and green the negative leads. The wires were then wrapped with colored silk thread to identify whether the lead was connected to the heater or the thermometer, and to designate the wires as either current or potential leads. The legend for the lead and wire colors can be found in table 2.2. The thermometer/heater assembly also has a loop of 28 gauge platinum wire, attached with the GE varnish, that is used to insert and remove the thermometer/heater assembly from the calorimeter. Once the thermomter/heater sleeve was completed and the wiring was found to be free of electrical shorts, a final layer of GE 7031 varnish was applied and then cured under an infrared lamp to harden the varnish and make it more inert to chemical treatment.

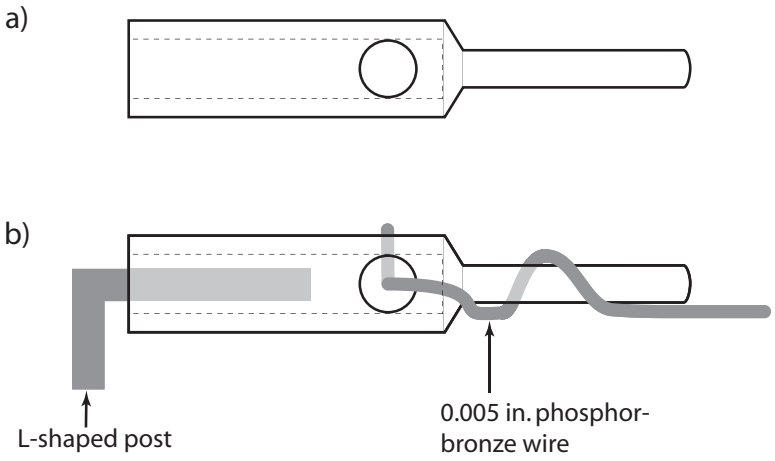

Figure 2.7. Diagram of the thermometer/heater lead connector pins showing a) the pin itself, and b) how the pin serves as an intermediated between the thermometer/heater leads and the L-shaped posts on BASH

A small amount of Apiezon T grease has been applied to the main body of the thermometer/heater assembly to help the thermometer/heater assembly stay in place upon insertion into the recess on the calorimeter. The grease also facilitates the transfer of heat between the calorimeter and the thermometer and heater.

After a sample is run on the calorimeter, the thermometer/heater sleeve is removed to prevent damage and to allow the calorimeter to be set upright (for weighing, removal of the sample, etc.). However, this means a certain amount of grease is left on the calorimeter, and is removed when the calorimeter is cleaned. To compensate for this mass loss, the amount of grease left on the calorimeter is calculated and the same amount is added back into the calorimeter recess on the subsequent loading of a sample, before the thermometer/heater assembly is inserted back into the calorimeter. In this way, the mass of the Apiezon T grease on the calorimeter remains constant and therefore does not have to be adjusted for in the specific heat calculations.

One difficulty in constructing the thermometer/heater sleeve was how to design the connections from the phosphor bronze leads to the terminals on the bottom of

BASH, which then go to the connectors on the top of the calorimeter and finally to the control electronics. The current large-scale calorimeter (as do many instruments of this type) uses male/female type terminal connections which are supported on a thermal equilibration block attached to the inside of its bottom adiabatic shield. However, because of the size and mass of BASH and the other adiabatic shields, this method was not feasible, so the original design by Robert Putnam used a series of seven L-shaped posts fastened to the outside of BASH to which the leads from the calorimeter were soldered.[8] A drawback with this design is the difficulty in soldering the bare wire to the post and the reproducibility of the solder joints. To remedy these problems, gold plated solder tail pins (used to mount microchips onto circuit boards) are used as an intermediate between the post connectors on BASH and the leads from the calorimeter. These pins are 7.5 mm long by 1.3 mm in diameter with a 0.8 mm cavity on one end that extends 4.5 mm down the length of the pin where the diameter of the pin decreases to 0.5 mm (see figure 2.7). The cavity in the pin is large enough that it can be filled with solder, and fitted over the posts on BASH to create a solder connection. This connection has been found to be very consistent and relatively easy to make and subsequently undo. To facilitate the connections to the calorimeter leads, a 0.030 inch diameter hole was drilled into each pin on the largest part of the shaft, perpendicular to the cavity, and 3.5 mm from the cavity end of the pin. The lead wires were fed through this hole, wrapped around the narrow portion of the pin, soldered into position, and further secured into place with shrink wrap tubing matching the color of the lead wire. In this way, the pins are permanently attached to the heater/thermometer assembly leads, and serve as an efficient means of connecting leads to the cryostat wiring.

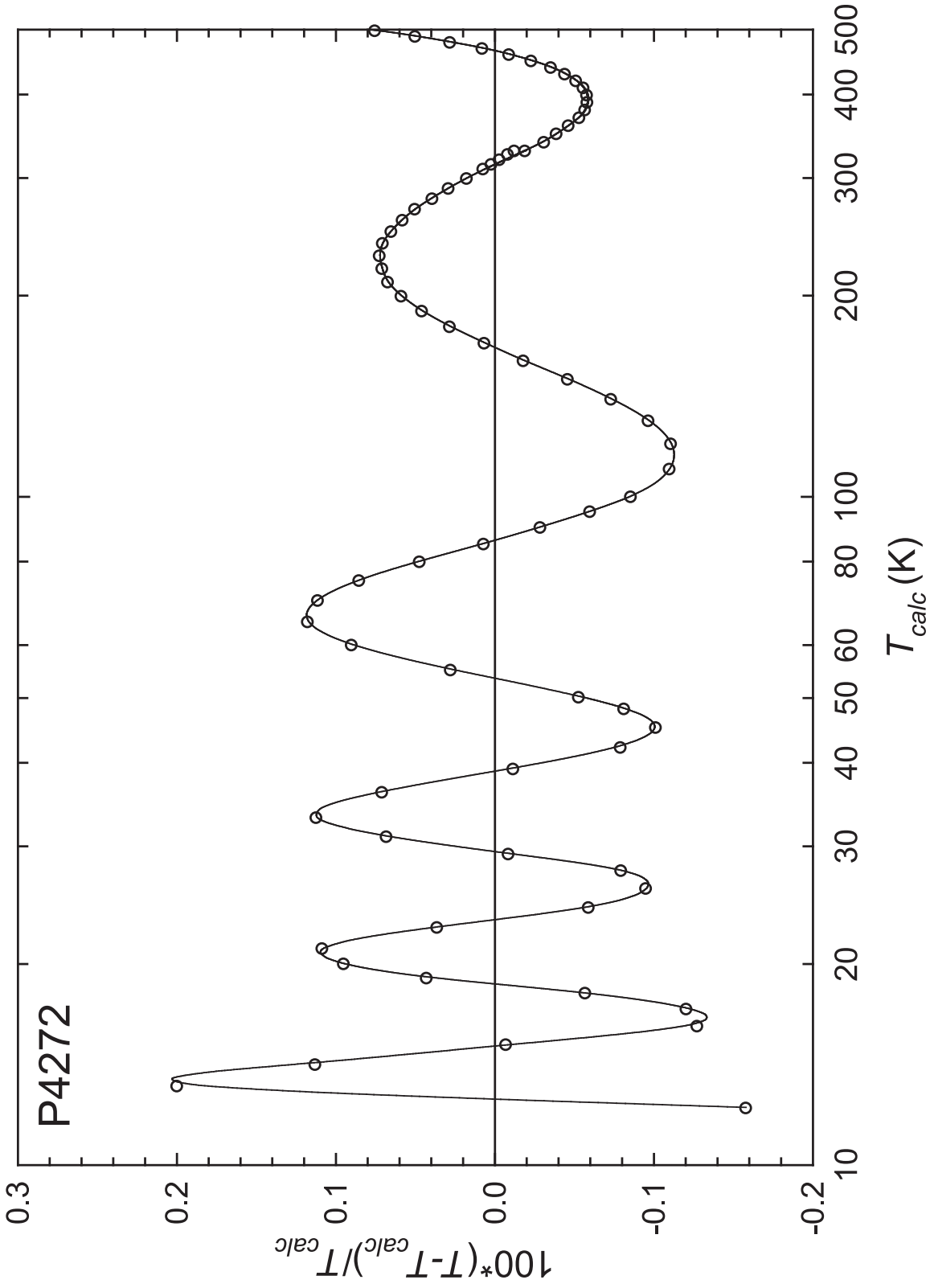

Figure 2.8. Deviation of the calibration points of the P4272 thermometer with respect to the polynomial fit function along with the cubic spline curve used to smooth the data.

Thermometer Calibration

As mentioned previously, the calorimeter thermometer is a LakeShore Cryotronics Inc. model PT-111 platinum resistance thermometer, serial number P4272. The thermometer was calibrated by LakeShore from 12.8 K to 500 K at various temperatures, and is traceable back to ITS-90. However, this particular model of thermometer does not meet the specifications for a standard platinum resistance thermometer, and thus cannot use the ITS-90 standard reference function for the $R-T$ data. Therefore, the data was fit to a polynomial function of the type $T = A_1R^{-6} + A_2R^{-5} + A_3R^{-4} + \cdots + A_{10}R^3$ using a least squares method. However, the R-T data is known with better accuracy and precision than can adequately be represented by the polynomial function. This is seen in figure 2.8, where there are systematic deviations between the fit and the calibration data, shown as a percent difference between the actual temperature and the temperature calculated from the fit of $100{\cdot}(T - T_{calc})/T_{calc}$. To make the fit a better representation of the data, the deviation was fit using a cubic spline function that was then combined with the original polynomial into a file that is accessible to the data collection and analysis programs to transform resistance data into temperature. The temperature scale file for this thermometer is labelled P4272H0.scl and is organized in a convention set forth in the Woodfield/Boerio-Goates laboratory to calculate temperatures for similar thermometers.

2.3.3 Electronic Controls

Central to the ability of the specific heat apparatus to conduct its measurements is the effective layout and design of the control instrumentation and electronic circuitry. The control electronics for the microcalorimeter are driven by the data collection computer via the IEEE-488 General Purpose Interface Bus (GPIB). The current computer

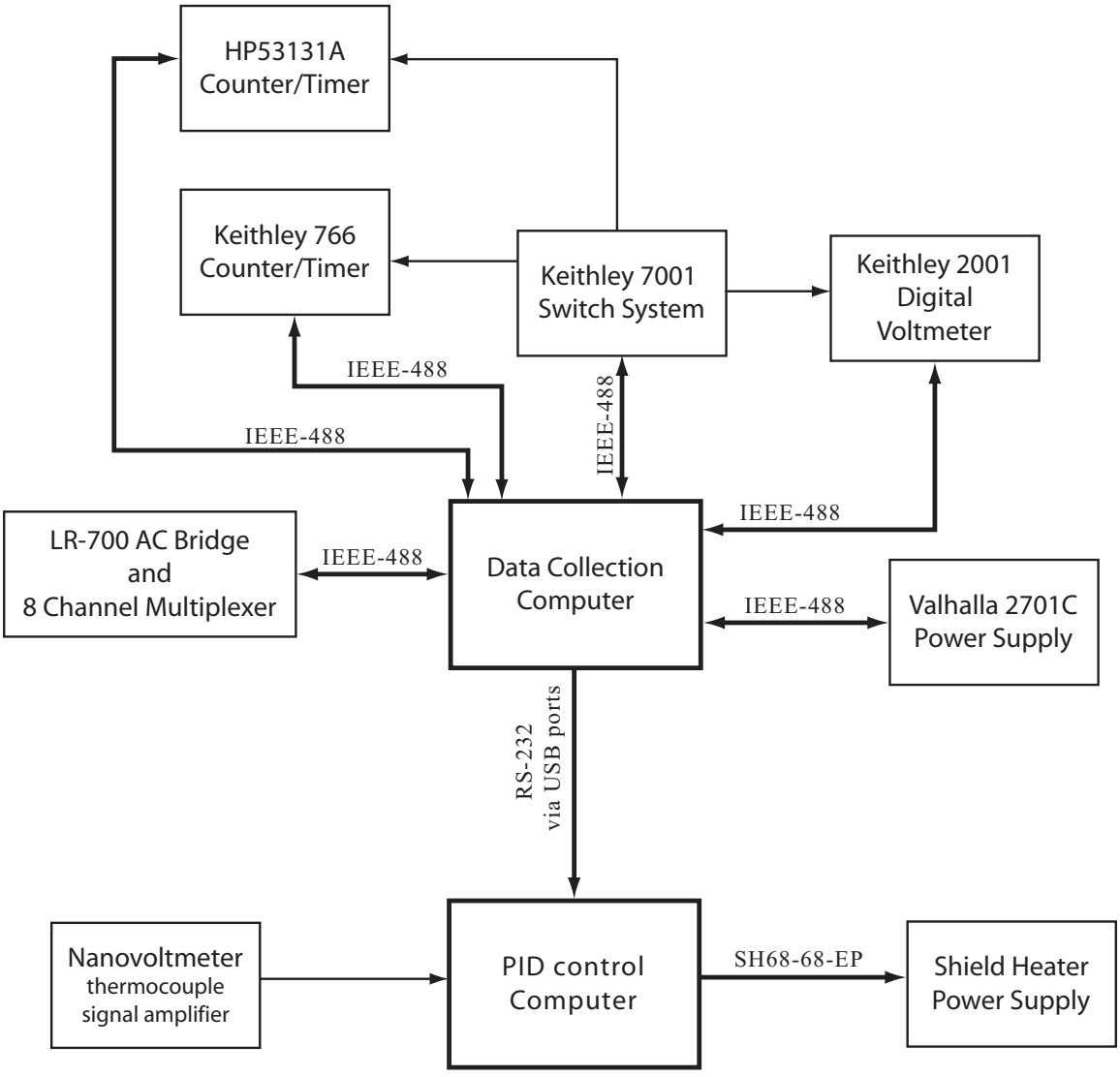

Figure 2.9. Computer interfacing schematic

is a PC with a Pentium® II 350 MHz processor running Windows® XP, with a National Instruments PCI-GPIB card used to control the IEEE-488 bus. Six instruments connected along the interface bus perform all of the necessary functions for collecting specific heat data, which is remotely operated by a Visual BASIC program that collects and stores all the data from the peripheral instruments (The autocalv1b program, which will be elaborated on in chapter 3 and appendix B). Figure 2.9 shows a schematic drawing of all the instruments interfaced with the data collection computer.

IEEE Bus Electronics

One of the main instruments on the data collection computer IEEE-488 bus is the Linear Research LR-700 AC Resistance Bridge that is used to measure the resistance of the calorimeter's platinum resistance thermometer. An eight channel multiplexer is connected directly to the resistance bridge, and the first three channels of this multiplexer are connected to a 10 Ω dummy resistor, the calorimeter thermometer, and a dead short, respectively. The remaining five channels are connected to set of 0.1, 1.0, 10, 100, and 1000 Ω standard resistors that are contained in an isolated box and are used to calibrate the resistance bridge and compensate for measurement drifts. The bridge is able to measure resistance in one of two methods: either determining the resistance directly, or determining the resistance change relative to a setpoint. The second method operates by selecting an offset value at the current resistance (RSet) and then measuring the resistance difference from the setpoint (ΔR) or the resistance difference multiplied by a factor of ten (10ΔR). The overall resistance determined by adding the resistance difference to the setpoint, and latter method allows for the most sensitive determination of resistance.

Other instruments connected to the data collection computer via the IEEE-488 interface are: a Hewlett-Packard HP53131A Counter/Timer and a Keithley 677

Counter/Timer, a Valhalla Scientific 2701C power supply, a Keithley 7001 switch system, and a Keithley 2001 digital multimeter. With the exception of the shield control circuits, these instruments make up the rest of the control circuity for the calorimeter, and comprise the heater and timer circuits. Both of these circuits have some portion of wiring routed through the Keithley 7001 switch system, which has a 7059 low emf scanner card and a 7066 relay card that serve as the main switches, and this allows for the simultaneous opening and closing of switches on both of the independent heater and timer circuits. This will be described in detail in subsequent sections.

An additional connection to the data collection computer is the shield control computer, where the interface allows the data collection computer to relay the temperature dependent settings for the PID control algorithm (The specifics of the instrument configurations on this computer will be detailed in chapter 3). In the past, the simplest and most reliable method for connecting two computers was to use a null modem cable over the RS-232 interface; however, an emerging trend in the computer industry has been to exclude an RS-232 connection on newer computers. Thus, to be prepared for any future changes in computer hardware, we have decided to interface the computers using a new standard for connecting peripheral devices: the Universal Serial Bus (USB). The interface uses two USB to RS-232 converter cables (one for each computer) that are installed into a free USB port, and then software is used to create a virtual RS-232 (serial) port. In essence, we are still communicating over an RS-232 cable, and taking advantage of the simplicity of this type of computer interface, but there is no longer as much concern with using interface hardware that may soon become obsolete.

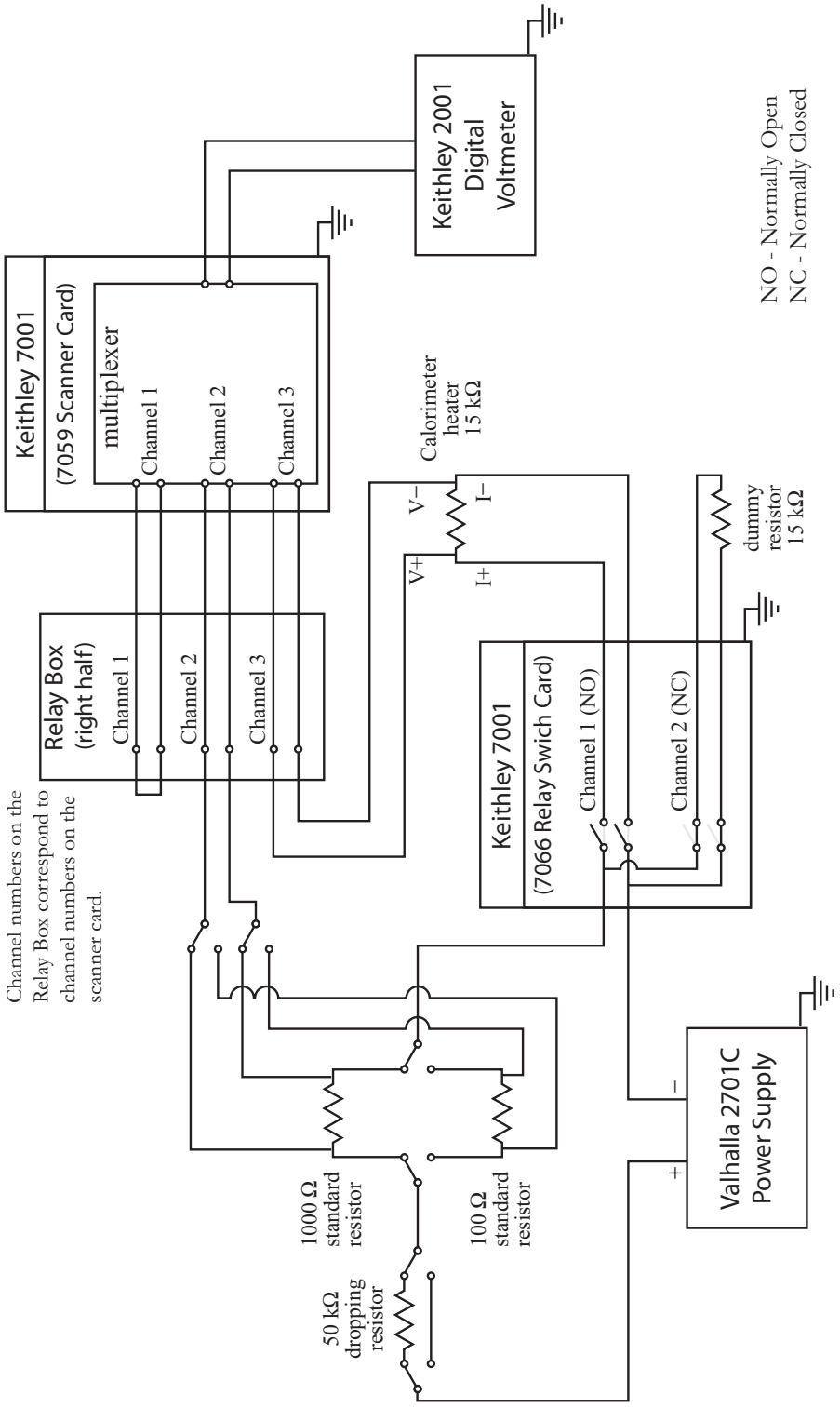

Figure 2.10. Schematic for the sample heater

Calorimeter Heater Circuit

The heater circuit is designed to provide a stable current across the calorimeter heater that allows for accurate measurements of the resistive power generated from the heater. It is configured in such a way that this instrument set could also be used to run the large-scale apparatus. Figure 2.10 shows the wiring, switches, and instrumentation for the sample heater. The power for the circuit is driven by the Valhalla Scientific 2701C that operates in a constant voltage mode where it maintains a fixed potential across the heater circuit, but to help reduce fluctuations and stabilize the current, a 50 kΩ dropping resistor has been placed in series with the circuit. A 1000 Ω standard resistor used for determining the current, is also in the circuit. Both the dropping resistor and standard resistor portions of the circuit can be reconfigured by sets of jumper plugs if the need arises to use the instrument set for the large-scale apparatus. In this mode of operation the Valhalla 2701C would likely operate in a constant current mode, so there is no need for a dropping resistor, and the 1000 Ω standard resistor should be changed to 100 Ω resistor to better match the resistance of the large-scale calorimeter heater.

During the drift portion of the measurement, the current is routed to a dummy resistor, and during the pulse the current is switched to the calorimeter heater to supply the power for the pulse. This is accomplished by using two double-pole double-throw switches on the 7066 card in the Keithley 7001 (channels 1 and 2), one in a normally closed position (the dummy resistor) and the other in the normally open position (the calorimeter heater); thus, when the measurement begins (the first drift), the power goes to the dummy resistor. At the beginning of a pulse, the positions of these two switches are reversed, and the power flows through the calorimeter heater. The dummy resistor is 15 kΩ resistor identical to the calorimeter heater that is used

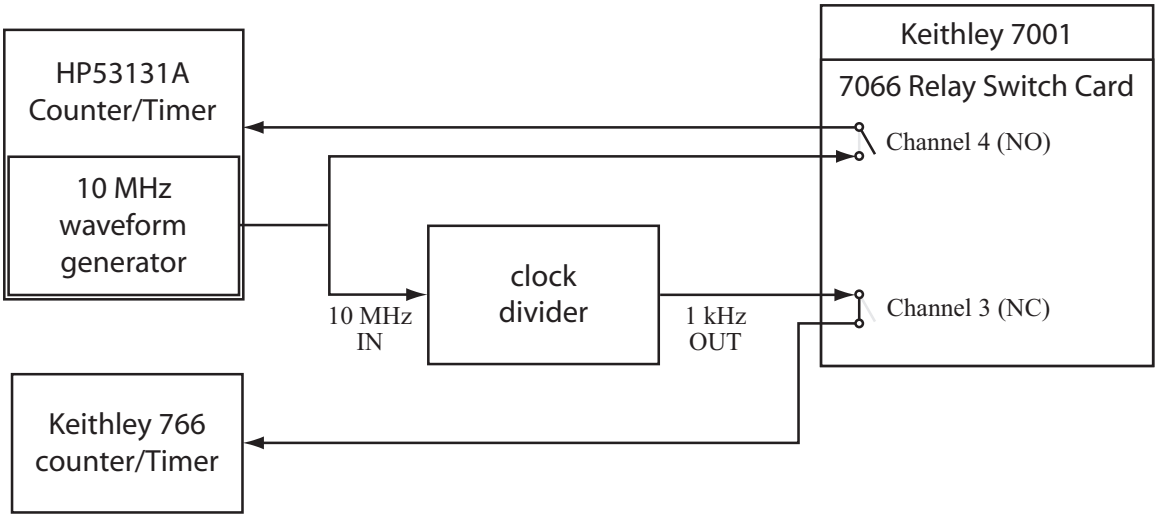

Figure 2.11. Schematic for the timing circuits

to ensure the power supply sees a constant load at all times. When the power is going through the heater, the Keithly 2001 Digital Voltmeter (DVM) is used to measure the potential across the heater and the standard resistor in order to determine the total heat input into the calorimeter. The input into the DVM is routed through the 7059 low emf scanner card on the Keithly 7001 unit, allowing for multiple (but not simultaneous) voltage signals to be measured via the various channels on the card. Input for each channel on the card is run to an external relay box on the instrument rack for easier access, and all inputs are labelled to correspond to the respective channels on the scanner. The first channel is simply a dead short, and it is also the default channel on the card, so the DVM is not required to measure an open circuit. During the pulse, the input to the DVM is switched to the second and third channels to measure the potentials across the standard resistor and the calorimeter heater, respectively, in order to determine the power across the calorimeter heater.

Timer Circuit

Another important factor in measuring the specific heat is knowing the time stamp for each point in the drift, and more importantly, the duration of the of the pulse, since the total heat output from the resistive heater is an integration of the heater power over time. While some of the time measurement can be obtained by using the internal clock on the computer microprocessor, more accurate measurements are possible using an external timing device. The time base for this circuit originates from the HP53131A counter/timer 10 MHz waveform generator output from a BNC connector on the back of the instrument. This signal is split with a BNC divider, and part of the waveform is input into a home built clock divider that is capable of transforming the incoming frequency down to 1 kHz and 10 kHz. The 1 kHz signal and the original 10 MHz signal are routed through the switches on the 7066 card in the Keithley 7001 (channels 3 and 4), and then continue out to the inputs of the Keithley 766 and HP53131A counter/timers, respectively. Figure 2.11 shows a diagram for this circuit. The counter/timers are set to the totalize mode, so the instruments count the total number of waveform peaks from the moment the switches on the Keithley 7001 are closed until they are opened again; thus, from the frequency of the waveform, the number of counts relates directly to a time in seconds. The signal to the Keithley 766 is used to measure the time during the drift, and the signal to the HP53131A is used to measure time during the pulse. Since the switches for the timing signal are on the same card as the switches for the heater circuit, the waveform signals can be started and stopped simultaneously with the beginning and end of a pulse; thus, we can obtain the most accurate total elapsed times for both the pulse and the drift.

2.3.4 Nominal Resistance of the Standard Resistors

An important part of the heater circuit and for the calibration of the AC resistance bridge is knowing the resistance of the standard resistors with a high degree of accuracy. To ensure a high level of reproducibility and long term stability, the resistors used are typically Leeds and Northrup oil-filled, wound-wire, standard resistors, many of which are over thirty years old. It is often advantageous to use standard resistors this old since their age has allowed the resistance to better stabilize and will generally have a better performance than newer resistors; however, the nominal resistance of the standard will drift from its original value over time. Thus it was necessary to check the resistance of the standard resistors so the present day value of the resistance was known for use in the calculation of the specific heat.

The 10 Ω standard resistor used for calibrating the AC resistance bridge was compared against the two 10 Ω resistors used on the current semi-adiabatic calorimeter to calibrate its AC resistance bridge. This pair of 10 Ω resistors has been calibrated at NIST, thus the nominal resistance of these standards is known a very high degree of accuracy. Several replicate measurements of the resistance were made on all of the standards using using the AC resistance bridge on the semi-adiabatic apparatus, and from the values of the two known resistances, the nominal resistance for the microcalorimeter standard resistor was determined as 9.99835 Ω with an overall accuracy within 4 ppm (a typical accuracy for this type of resistor). Since the thermometer standard resistor had been well defined, it was then used as a reference to determine the nominal resistances for the standards used in the heater circuit. The comparisons were made on the 100 Ω and 1000 Ω resistors using the small-scale apparatus AC resistance bridge, and the nominal resistances were found to be 100.00356 Ω and 1000.8224 Ω, respectively, with both of the accuracies within 5 ppm.

References

[1] Boerio-Goates, J.; Woodfield, B. F., *Can. J. Chem* **1988**, *66*, 645–650.

[2] Boerio-Goates, J., *J. Chem. Thermodyn.* **1991**, *32*, 403–409.

[3] Woodfield, B. F., *I. The Construction of a Low-Temperatre Calorimeter. II. Calorimetric Studies of the Phase Transitions in CHI_3, $K_2Mn_2(SO_4)_3$, and $K_2Mg_2(SO_4)_3$.*, Master's thesis, Brigham Young University, **1988**.

[4] Stevens, R.; Boerio-Goates, J., *J. Chem. Thermodyn.* **2004**, *36*, 857–863.

[5] Woodfield, B. F., *Specific Heat of High-Temperature Superconductors: Apparatus and Measurement*, Ph.D. thesis, University of California, Berkeley, **1995**.

[6] Lahley, J. C., *Mechanics of Metals with Phase Changes*, Ph.D. thesis, Brigham Young University, **2000**.

[7] Geballe, T. H.; Giauque, W. F., *J. Am. Chem. Soc.* **1952**, *74*, 2368–2369.

[8] Putnam, R. L., *Thermodynamic Study of Lyophilized Yeast Cells. Construction of an Automated Micro-Scale Adiabatic Calorimeter for Measurement of Heat Capacities of Solid Samples from 13 K to 325 K and Data Acquisition Software for Use with the Brigham Young University Cryogenic Adiabatic Calorimeters*, Master's thesis, Brigham Young University, **1995**.

Chapter 3

Instrumentation: Data Collection & Temperature Control

This chapter is a continued description of the new instrumentation for the small-scale apparatus discussed in chapter 2, but it will emphasize software control more than hardware design and instrumentation. This chapter includes a discussion of the principles of shield control using the PID algorithm, how this is implemented in the new apparatus, and the various computer control programs used in the process of gathering the specific heat data.

3.1 Fundamentals of PID Control

In science, engineering, and industrial settings, it is often desirable or necessary to automatically control a physical variable such as temperature, fluid flow, speed control, etc. In this context, we define automatic control as the ability to manipulate a particular physical variable by some mechanical or electronic system without human intervention. This is frequently accomplished by means of a feedback control system, where the control system tries to maintain the physical property (the value of this is called the control or process variable) at a specific value (the setpoint). This control

system operates by measuring the error (the difference between the control variable and the setpoint) which invokes the response of some type of compensator (controller) that produces a new value for the process variable.[1] The new value of the control variable (and thus the error) in turn drives a new response to the compensator. This process continues indefinitely, leading (hopefully) to a stabilized system, where the error is minimized, and there are no undue oscillations in the systems.[2]

A familiar application of feedback control is thermal regulation such as in ovens or home central heating systems. In the central heating system, the homeowner adjusts a thermostat (the controller) to the desired temperature (the setpoint) and then leaves and lets the system maintain that temperature. In this example, when the temperature measured at the thermostat falls below a certain threshold value, the thermostat will switch on the heater (the response). The temperature in the house will rise until the thermostat reaches an upper threshold limit, at which point the heater is turned off. In this way, the temperature of the house is maintained at a near constant value. This is an example of a simple ON/OFF type controller.

One of the most common types of feedback controls in industrial applications is the PID system, which is an abbreviation for Proportional, Integral, and Derivative control.[1] This is essentially an equation that the controller uses to evaluate the error, and then generates a response (often the equation is realized as an electronic circuit to perform the mathematical operations).[2] Basically, there are three constants in the equation (one for each of the proportional, integral and derivative operations) with the error as the independent variable and the response as the dependant variable. Also, in contrast to the ON/OFF controller, the PID controller will generate a graduated percentage response instead of just a 0% or 100% response. The following sections describe the functionality of the proportional, integral and derivative variables.

3.1.1 Proportional (Gain) control

The proportional gain (often referred to as simply the gain) controls how the system responds to large fluctuations in the feedback loop.[2, 3] The proportional control responds directly or proportionally to the magnitude of the error, e (the value of the setpoint minus the value of the control variable). Thus, when the error is large, the output gain, or response of the controller, is large. Conversely, when the error is small, the output gain is small. The signal for the proportional control can be described in terms of the output gain u by:

$$\begin{aligned} u &= u_{max}, \quad e > e_0, \\ &= u_0 + K_c e, \ \ -e_0 < e < e_0, \\ &= u_{min}, \quad e < -e_0 \end{aligned} \tag{3.1}$$

where u_0 is the level of the signal when the error is zero and K_c is the proportional gain of the controller.[3] The terms u_{max} and u_{min} refer to the maximum and minimum values of the output gain, and e_0 and $-e_0$ are the upper and lower threshold limits for the error.

To give further explanation of how the proportional control works, we shall return to the example of temperature control. In this situation, if the temperature is well below the value of the setpoint, the error will be large, and will be greater than the upper threshold limit for the error, e_0. Thus, the output gain will be at a maximum in order to heat the system up to the setpoint. As the error falls below the value of the upper threshold limit, the output gain will respond proportionally to the magnitude of the error. The system then begins to control, since the output gain can now compensate directly for the error in the system. However, the proportional gain

cannot correct for small errors in the system, and ultimately, this leads to periodic oscillations in the system.[2] This is where integral control becomes important in the feedback control system.

3.1.2 Integral Control

The purpose of the integral control is to eliminate problems with steady state error by correcting small errors in the system that persist over time.[2, 3] Essentially, the integral control adjusts the value of u_0 by integrating the error signal over time. Thus, u_0 can be expressed as:

$$u_0 = \frac{K_c}{T_i} \int e dt \tag{3.2}$$

where T_i is the integral time constant. The integral of the control error is proportional to the area under the curve of the error over time.

Returning to the temperature control example, without any integral control, the temperature would reach a steady state condition where it would oscillate around the setpoint. Addition of the integral control provides an additional degree of response to the error. For instance, in the oscillating system, at some point in time the system would start to get hotter than the setpoint, which results in a negative error signal. As this happens, the controller continually integrates the error, which is then added to the proportional response. Since the integral term is negative, the total output gain is less, so the system does not heat up as much as it would with only the proportional control. Likewise, as the system cools below the setpoint, the controller continues to integrate the error, which is added to the controller response. However, since the integrated error is now positive, the gain output is greater than the the proportional response alone, and the system does not cool as much. As the control

process continues, the system oscillations should decrease if the appropriate integral time constant is chosen.

In practice, the value of the integral time constant (often referred to as the temperature time constant, or *ttc*, in thermal applications) is often set as the value of the time of periodic oscillations when there is just proportional control. In this way, the integral is able to dampen the periodic oscillations caused by the proportional control. In many control systems, the proportional and integral controls are all that are necessary to maintain adequate stability in the system. However, the proportional and integral controls do not respond effectively to small errors in the system or rapidly changing conditions.

3.1.3 Derivative Control

The derivative control is used to predict how the system will behave and to compensate for rapidly changing errors in the system.[3] Effectively, the derivative control looks at the rate of change of the error and uses this to predict how the system will behave in order to avoid overshoot or undershoot from the proportional control. In short, this serves to dampen a system. The derivative response can be expressed as:

$$u_d = K_c \cdot T_d \frac{de}{dt} \tag{3.3}$$

where T_d is the derivative time constant of the controller.[3] This gain from the controller is used to predict the error at time $t + T_d$ based on the current rate of change in the error.

There is often deviation from equation 3.3 for practical reasons when PID controllers are constructed, where the time derivative of the control variable is used rather

than the derivative of the error. This is primarily done since the setpoint is generally constant and does not contribute to the derivative term. Also, if the setpoint is changed, the derivative of the error will change drastically; whereas, the derivative of the control variable will not.[3] Thus, the expression for the derivative response can be given in terms of the control variable, x, as:

$$u_d = K_c \cdot T_d \frac{dx}{dt} \tag{3.4}$$

Both equations 3.3 and 3.4 are acceptable for use in control algorithms since there is generally no noticeable difference in the derivative response between the equations.[3] For the current design of the shield control, derivative response in the form of equation 3.4 is used.

The derivative control becomes especially important in systems where the feedback loop is updated very quickly.[2] In these systems, the proportional response must be set high to effectively compensate for rapidly changing errors caused when the proportional gain forces the system to overshoot, but the addition of the derivative control dampens the overshoot, since it responds to the rate of change in the error.[2]

3.1.4 The PID Controller

When the proportional, integral and derivative gains are operating in parallel with each other, the total output gain of the control process can be expressed as:

$$u = K_c \left(e + \frac{1}{T_i} \int e dt + T_d \frac{dx}{dt} \right) \tag{3.5}$$

There are several other methods of applying the proportional, integral and derivative controls, such as a series type control, but for our purposes, we will limit the discussion

to parallel type control, since in this configuration, one can get very precise control of thermal systems.

In the past, the complexity of this system, with the three processes working simultaneously, may have contributed to its limited use; however, with the advent of modern computers, it is relatively simple to implement.

3.1.5 PID tuning

The main difficulty in using the PID control system is effectively tuning it to the optimal values for the proportional, integral and derivative gains. While a well tuned system may converge quickly to the setpoint and continue operations with very little noise, a poorly tuned system may have large oscillations, or worse, become increasingly divergent causing complete loss of control. Thus, finding the optimal values of the control parameters is a crucial part of the the control process.

Speed and stability are the two main factors with which one must contend when trying to achieve good control of the system, but what is the exact definition of "good" control? Does good control mean the system dampens without any overshoot, or does it mean that the system needs to come to equilibrium quickly and initial oscillations in the system are less important? For our application of the PID controller, we want a system that comes to equilibrium relatively quickly, but stability is the greatest concern.

The process of determining the optimal PID parameters can be time consuming, but in the long run, the benefits outweigh the time spent. Unfortunately, there is no one set way to determine the optimal parameters, although there are a variety of well established methods for controller tuning, each with its own set of determining factors. The most basic way to find the optimal control parameters is simply trial

Table 3.1. Effects of PID parameters on speed and stability from Kiong *et al.*[3]

	Speed	Stability
K_c increases	increases	decreases
T_i increases	decreases	increases
T_d increases	increases	increases

and error; however, this method can be extremely time consuming, inefficient, and it may not yield satisfactory results.

For the purposes of the small-scale apparatus, the method of choice is a variation of the Ziegler-Nichols frequency response method. First, the integral and derivative controls are disabled, and the proportional gain is slowly increased until the loop begins self-oscillation (where the value of the proportional constant is K_π).[3] Once there is a stable oscillation, the oscillation period, T_π, can be measured and used to calculate the controller parameters. Ideally, one could just input these parameters into a formula and obtain the controller parameters; however, depending on the needs and user definitions of good control, there are a variety of tuning formulas that can be used, and this list varies depending on the source consulted.[2, 3] Hence, application and experience aid the user in deciding which tuning formula to use.

For the purposes of the cryostat shield temperature control, the integral constant is set to the period of oscillation ($T_i = T_\pi$) and the derivative constant is set to be one third of the internal constant (Additional tuning formula can be found in references 2 and 3).

3.2 Small-Scale Apparatus PID Control System

For calorimetry, we use the PID control to maintain the temperature of the adiabatic shields. However, in this application, instead of controlling the temperature of the adiabatic shields at a single temperature, the aim is to keep the shields at the same temperature as the calorimeter. This is achieved by using a series of thermocouples wired between the calorimeter and the shields. In theory, when the calorimeter and the shield are at the same temperature, there will be no voltage across the thermocouple leads, and any net voltage means there is a temperature difference (this is the error signal). The voltage across the thermocouple leads is then amplified and input into the PID control algorithm, which then sends output to the shield heater, thus completing the feedback loop. In actuality, there is often a net voltage across the thermocouples even though the calorimeter and shields are at the same temperature; however, this net voltage is dependent on the absolute temperature of the shields and is compensated by an offset voltage on the amplifier. As described in chapter 2, there are are technically five shields (MASH, TASH, BASH, Ring and GASH), but the shields immediately surrounding the calorimeter (MASH, TASH and BASH) have had their heaters wired together in series, so they behave as a single shield that uses voltage from the MASH thermocouple to control this shield (for convenience the shields are collectively referred to as MASH). The shields have been configured in this manner for purposes of stability, since when attempting to control MASH, TASH and BASH independently, changes in one shield created perturbations in the adjacent shields that the PID algorithm had difficulty compensating for, the heat flow became inconsistent, and the system was generally unstable. The shield heaters have been wired together via the connector cables at the shield heater box on the instrument rack in order to make it easier to check the continuity of the heater wiring each time the calorimeter is loaded (it is standard operating procedure to check the continuity

of all the electronic circuits before each new sample is loaded) and to allow for the shields to be easily reconfigured to run separately at some point in the future.

3.2.1 PID control hardware

The specific design of the small-scale apparatus shield control is shown in figure 3.1 for the control of the three major shield systems. The control routine begins with the voltage generated across the shield thermocouples, which for MASH run between the shield and the calorimeter, and for Ring and GASH run between the respective shields and MASH. The thermocouples have been constructed with chromel-copper/iron wire junction and two chromel-constantan junctions in the circuit that results in a highly sensitivity thermopile.[4] The voltage potential across the thermocouple leads is measured by one of several nanovoltmeters (one for each shield) that serve to amplify the potential from a range of $\pm$ 3 microvolts to a $\pm$ 1 volt signal. The desired value (setpoint) is zero volts where there are assumed to be no temperature gradients. MASH and Ring use Tinsley model 6050 nanovoltmeters, and GASH uses a Keithley model 2182 nanovoltmeter to amplify the signals from the respective shields. During operation GASH and Ring are set permanently cold relative to MASH using offsets on the respective amplifiers so that GASH and Ring do not dump excess heat back into the calorimeter. This also prevents MASH from going hot relative to the calorimeter in case GASH and Ring heat up above the their respective setpoints.

The output from the nanovoltmeters is routed to a National Instruments model NI 4351 high precision data acquisition card using channels 1, 3, and 7 for the amplified voltages from the MASH, Ring, and GASH thermocouples, respectively. The NI 4351 card converts the analog voltage signals from the amplifiers to a 24 bit digital signal, which is then relayed to three separate PID algorithms running in Labview (one

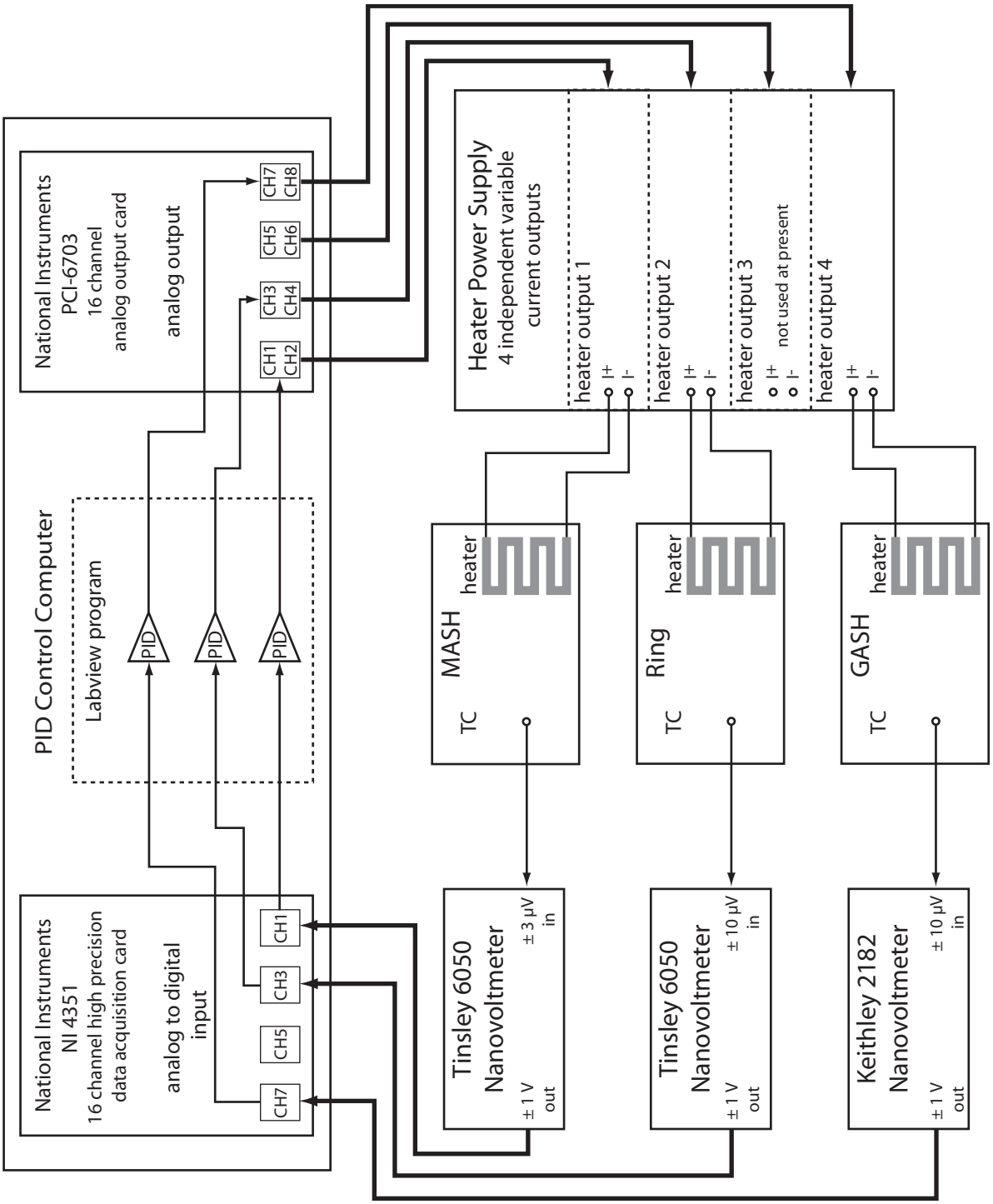

Figure 3.1. The PID loop schematic for the three adiabatic shields.

Table 3.2. Channel assignments for National Instruments PCI-6703 card.

Channel	Signal	Voltage
0	MASH range (MAX I)	0, 1, 2 ..., 10 V
1	MASH output gain	0 - 10 V
2	Ring range (MAX I)	0, 1, 2 ..., 10 V
3	Ring output gain	0 - 10 V
4	range (MAX I) (not used)	0, 1, 2 ..., 10 V
5	output gain (not used)	0 - 10 V
6	GASH range (MAX I)	0, 1, 2 ..., 10 V
7	GASH output gain	0 - 10 V

for each shield) that will be elaborated on in the subsequent section. The Labview program regulates two distinct aspects of the shield control, namely the maximum current output and the output gain for the PID control. The output gain drives the power output to the shield heater as a percentage of the maximum power (from 0 to 100 %), where the maximum power is a set of predetermined current values equivalent to current ranges on the heater power supply. Thus, for each shield, there are two sources of data output, one for the current range, and one for the percent of the current range (output gain). The data outputs from the Labview program are routed to a National Instruments PCI-6703 analog output card that converts the digital signal into an output of 0 to 10 volts. Table 3.2 identifies the outputs for each channel of the PCI-6703 card, which is then received by the heater power supply. This power supply regulates the current across the shield heaters, which effects the temperature of the shields, and in turn changes the potential across the shield thermocouples, thus completing the PID loop.

PID Heater Power Supply

The heater power supply for the PID system was designed and constructed by the Chemistry/Bio Ag instrument shop at BYU according to our specifications. An electronic schematic diagram of the power supply can be found as figure 3.4 at the end of this chapter. The power supply is a four channel DC current output device, where each channel operates independently, and each has a front panel interface that allows the user to view and modify the heater's current output (see figure 3.2). Each output channel has its own power switch and a toggle switch that allows the unit to run in a local or remote mode. In the remote mode, the power supply changes the heater current settings based on inputs from the PID control computer and the front panel does not respond to user intervention (with the exception of the power switch). In this mode, the maximum current is shown in an LED display, and the percent output is shown using an analog meter. When the power supply is in manual mode, the maximum current is selected by a knob on the front panel, but the value is not shown in the LED display. The percent current is adjusted by the % Full Scale knob, the value of which is reflected in the analog meter. This configuration allows for maximum flexibility in sending current through the adiabatic shield heaters.

The power supply has been designed to receive inputs, as voltages, from the National Instruments PCI-6703 card via a 64 lead cable, to control both the maximum current, and the percent output. As the Labview program and the PCI-6703 card output two data sources for each shield heater, the heater power supply accepts the data source and converts it to the appropriate current output. For each heater current, the maximum current is regulated by one input channel that translates a signal sent as 1 volt increments to set the current range, where each voltage input is assigned a specific maximum current value (see table 3.3). The second input channel controls

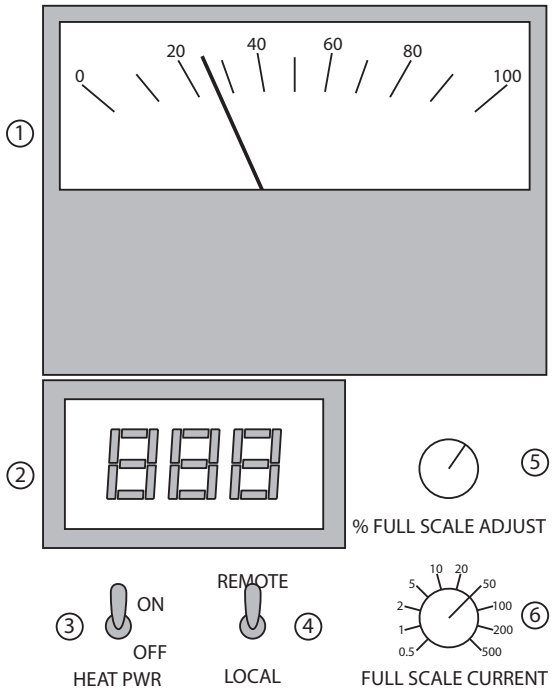

1. Current output indicator
2. Maximum current indicator
3. Heater current ON/OFF switch
4. Local/Remote toggle
5. Manual current percent output (range of max current)
6. Manual maximum current selector

Figure 3.2. Front panel interface for the PID heater power supply. This is duplicated four times, one for each output channel

the percent output of the maximum current, where the percentage of the maximum voltage (10 V) is interpreted directly as a percentage of the maximum current. For an example of how the input voltages are translated to the heater current, let us assume that the first input channel receives a signal of 9 V, then from table 3.3 the maximum output current is 200 mA. If there are 6.25 volts across the second input channel, then the percent output of maximum current is 62.5 %, that gives a total heater current of 125 mA (200·0.625). When the PID control program is in operation, the maximum current remains constant for a long period of time (the maximum current often changes at the pulse-drift transition), and the percent of the maximum current is adjusted to maintain the shield control.

Table 3.3. Maximum current ranges assigned to input voltages for the heater power supply

Voltage input	Maximum Current
0 V	0.0 mA
1 V	0.5 mA
2 V	1.0 mA
3 V	2.0 mA
4 V	5.0 mA
5 V	10.0 mA
6 V	20.0 mA
7 V	50.0 mA
8 V	100.0 mA
9 V	200.0 mA
10 V	500.0 mA

3.2.2 PID control software

The PID control program was written using Labview as an alternative to using an electronic controller as is used on the current large-scale apparatus. The program was designed to not only act as a stand alone digital replacement for an analog instrument, but it is also designed to take parameters from the data collection computer to change the PID settings as needed. Another advantage of using Labveiw is that it is relatively simple to make changes to the PID control program, and many complex algorithms can be condensed into a single module (denoted as a *sub vi* by Labview).

At the start of the program, the program initializes the PCI card and prepares it to receive signals, prepares the RS-232 interface and clears any data in the buffer, and gives variables initial values. The main part of the program runs as a continuous loop that repeats three times a second, to continually update the shield heater and maintain control (see figure 3.3). The loop operates by running all of the required operations and then idling until the processor clock indicates that 333 ms have passed since the beginning of the loop before continuing to the next loop cycle. At each

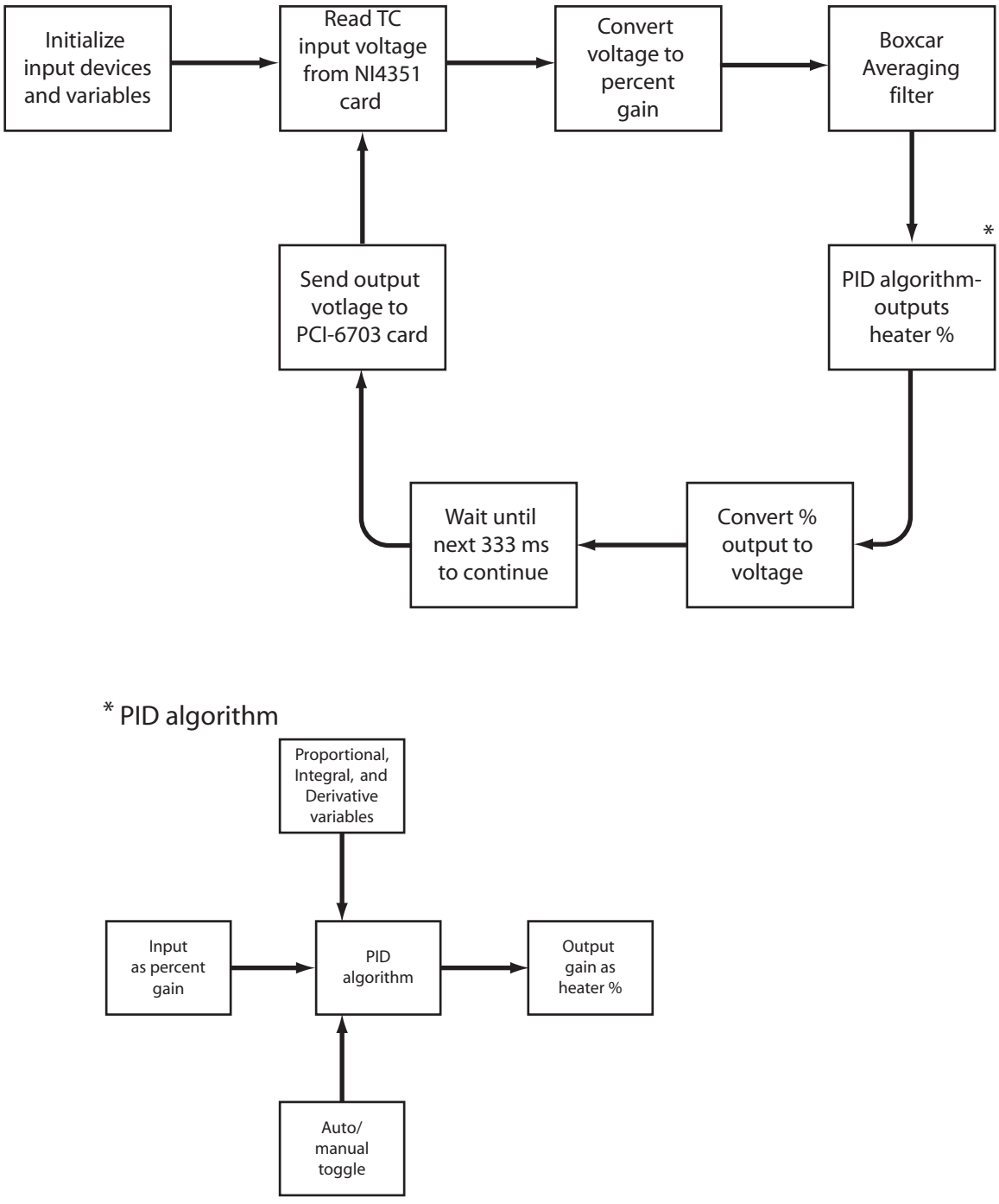

Figure 3.3. Flow diagram if the PID control program

iteration of the loop, the program first reads from the NI 4351 data acquisition card to extract the amplified thermocouple voltages. This process actually uses most of the time in the loop, and is the rate limiting step for the loop speed. The time for the data collection is a product of the resolution of the data (24 bit for this particular card) and the number of samples processed by the multiplexer (currently 3, one for each shield thermocouple voltage read). After the data is read, the voltage data for each shield is separated into individual data packets, then the voltage is converted into a percent input gain (relative control variable) where -1 volt is 0%, +1 volt is 100%, and 0 volts is 50%. The input gain is then processed using a moving boxcar that averages the signal with the previous data points. The size of the boxcar is determined by the filter setting on the front panel of the Labview program as a function of seconds. The filter time is divided by the loop time to give the number of points in the boxcar walking window; thus, a 3 second filter divided by a 333 ms loop results in a walking window of 10 points. The averaged percent input gain is sent to a PID algorithm (a canned *sub vi* written by National Instruments) where the input gain is compared against the setpoint (input gain of 50 % or zero volts) and delivers the appropriate output gain.

The PID *sub vi* receives several sources of input to calculate the appropriate output gain. Primarily, the PID algorithm uses input of the proportional, integral, and derivative time constants to calculate the output gain (refer back to equation 3.5), where these variables can be adjusted though the program's front panel interface. The PID *sub vi* is also able to toggle between automatic and manual modes of operation. In the automatic mode, the program uses the PID equation as the output gain, while in the manual mode, the user is able to set the output gain. In switching from manual to automatic mode, there is a bumpless transfer of the output gain, so that the initial value output gain in the automatic mode is the same as the value of the output gain

in the manual mode.

A discussed previously, the Labview program outputs two data sources that operate independently of each other and are responsible for the overall shield control. The first is the output gain % from the PID algorithm, where the percent value is transformed to a voltage (between 0 and 10 V) and output through one channel of the PCI-6703. The second output is for the maximum current, which is controlled by user input from the front panel interface of the Labview program. The maximum current values correspond to the current ranges on the heater power supply (refer to table 3.3) except that the Labveiw program has two additional current ranges, 300 mA and 400 mA, that were added to provide better shield control for currents above 200 mA. For these two settings, the Labview program instructs the heater power supply to select a range of 500 mA, but the output gain is scaled to limit the maximum output to 300 mA or 400 mA.

3.3 Data collection program

Operating in parallel to the shield control program, the data collection program is responsible for controlling the small-scale apparatus instrumentation and storing the relevant information used to calculate the specific heat. This program originated from the MS-DOS/BASIC autocal program written by Dr. Brian Woodfield and is designed to run the large-scale apparatus. This BASIC code was updated and rewritten in Visual BASIC 6.0 to be run on the Windows® operating system, and further modified to work with the current instrument set. This program has undergone several iterations, and the current version has been designated as Autocalv2b (often referred to as just autocal).

The following sections describe the organizational structure, primary algorithm

sequence, and the format of the output file for the program. Additional information on the user end operation of the program and all of its capabilities can be found in appendix B.

3.3.1 Organizational Structure

The Autocalv2b program is organized into 18 main components: 12 forms and 6 modules. The forms are the code and the elements related to the graphical interface. Specifically, for each window in the autocal program there is a form with all of the associated objects on that form. Along with this, there is code that references all of the objects (including the form itself) that tell the program how to respond to user initiated events. The modules, on the other hand, contain the bulk of the actual program algorithms and are responsible for the running of the program. While the forms are an integral part of the program, their function is generally obvious upon visual inspection (more can be found on the user end of the forms in appendix B), which is not true of the modules; thus, there will be a brief account of the utility of the modules but not of the forms.

Module 1 contains the main code of the program including the code for the measurement algorithm. In addition, the *main* subroutine located in *Module 1* is the first code run when the program starts. All of the other modules contain code that is peripheral to the main operations of the program. Two of the modules (*NiGlobal* and *VBIB32*) contain code from National Instruments Inc. that is responsible for sending instructions to the GPIB card (There is an additional module for Autocalv2 run on the large-scale calorimeter, *NiDAQ32R*, that controls code for a data acquisition card). This allows the program to send commands to the various instruments over the GPIB and to receive data back from the instruments. The *Cp_calc* module contains

the code for calculating the heat capacity on the fly. Associated with this module are the *Matrix_Operators* and *Cp_subtraction* modules. The *Matrix_Operators* module has algorithms that preform various linear algebra operations used in calculating fore and after drifts. The *Cp_subtraction* module contains the code for subtracting functions from the raw heat capacity data to give the molar heat capacities. These last two modules have been kept separate from the *Cp_calc* module primarily because the code in the respective modules is closely related, and these modules are used in other programs as well.

Additionally, there is another component which operates outside of the program itself. This is an ActiveX module that is setup through the *Setuppad.exe* program, and the program calls on this while running.

3.3.2 Algorithm Structure

A complete annotation of the algorithm structure of the program would take several chapters to fully elucidate. Therefore, this section will serve only to highlight the more important parts of the program, and discuss in general terms what the program does during different stages. For information on specific sections of the code, and to follow the complete algorithms, see the in-line comments within the program itself.

Startup and the Mainsub Subroutine

On initiation of Autocalv2b, the program immediately does two things. First, the program sends up a splash screen which informs the user the program has started. Secondly, the program sends out information over the GPIB to correctly set up the instrumentation so the program is ready to collect data. At this point, the program

also defines most of the variables that are used in the program, including variables read in from files such as the PID settings. This is all controlled through the *init* subroutine. Once this finishes, the program displays the mainscreen and enters the *mainsub* subroutine.

The *mainsub* subroutine is a set of nested do loops that sends commands to the AC resistance bridge to take a reading of the calorimeter temperature every 10 seconds, and checks for any user initiated events. Much of what can be done from this section of the program will be discussed in appendix B. However, when any of windows is opened, the window can be either modal or non-modal. When a window is modal, the background program (i.e. the *mainsub* routine) does not run, and only continues when the modal window is closed. For example, when the Schedule window is opened to allow the user to set the conditions of the measurement, the programs stops taking temperature meausements, and only resumes when the Schedule window is closed. If a window is non-modal the background program continues to run and takes priority. Such is the case of the *Tdot* and *T$* window, where opening this window shows the *Tdot* history, but the program continues to make temperature measurements.

When the user decides to move to the measure part of the program (from the *Measure* button or [**F1**]), the program does a quick check to make sure that it has a proper schedule file, and then it stops the *mainsub* subroutine, opens the measure window, and starts the *measure* subroutine.

Measure

When the program begins the measurement subroutine, it performs three main operations. First, the program opens the output file and downloads the header information (date, name of sample, thermometer, etc.). Second, the Keithley counter/timer is

cleared, and then the switch unit routes a 1 kHz waveform to the Keithley counter/timer, thus starting the time measurement for the drift. Third, the AC resistance bridge is set to 10ΔR mode, and takes a reading of Rset.

The program waits 30 seconds for the AC bridge reading to stabilize. Then a time measurement from the Keithley is recorded, a measurement of 10ΔR every ten seconds is made for the duration of the *time interval* (typically 50 seconds, but can vary depending on the drift time interval), and then a second time measurement is made. The time and 10ΔR values are averaged, and the resistance of the thermometer determined by adding 10ΔR to Rset, which in turn is used to calculate the temperature. This cycle is repeated for the total number of drift points.

On ending the drift, but before starting the pulse, the program must take care of several issues before it can proceed. First, the program calculates the next temperature, retrieves from memory or calculates the pulse voltage, and sends the voltage setting to the Valhalla power supply. Then the program determines the correct PID setting for the pulse and sends the new setting to the PID control computer. Finally, to start the pulse, the program sends a command to the switch unit to close four channels. This does four operations spontaneously: opens the heater circuit going across the dummy resistor; closes the circuit across the calorimeter heater, thus heating the calorimeter; sends a 10 MHz waveform to the HP counter/timer, starting the pulse time; and stops the 1 kHz signal to the Keithley counter/timer, stopping the drift timer (The drift timer still runs until the moment the pulse starts, after which time the final drift time is recorded).

The pulse continues by taking a time reading, followed by eight replicate heater voltage measurements, eight replicate heater current measurements, and then a final time measurement. The program then counts down the remaining time for the current one minute pulse time interval (each pulse is an integer multiple of minutes). Then

these two steps are repeated until the end of the pulse.

At the end of the pulse, the program sends a command to the switch unit to open the four channels it closed on the start of the pulse, and sends new shield settings to the PID control computer. The program is now back in the drift mode, and this cycle of drift - pulse - drift continues until the end of the measurement.

3.3.3 The Output File Format

As the Autocal program is running, it outputs all of the information to a file as defined in the pulse schedule window. The following is a summary of the format of the file:

Header Line Description and date

Thermometer Thermometer file name

Rheat, (Rheat) Heater circuit standard resistor

nrdngs, (nrdngs) Number of bridge readings per point

window, (window) Walking window size for calculating Tdot

*************** spacer line (*×70)

Bridge Info Denotes AC resistance bridge parameters at the start of a drift

Bridge Range

Bridge Current

Rset Records the Rset value for this drift.

Drift(alli) Denotes beginning of the drift time temperature measurements

time1$_n$ Time reading before resistance measurements for point n (n=1 to the number of points on drift)

10ΔR$_1$, 10ΔR$_2$, . . . , 10ΔR$_{nrdngs}$ Values of 10ΔR for the number of points as defined by *nrdngs*

time2$_n$ Time reading after the resistance measurements for point n

⋮

⋮ *The previous three values repeat for all of the points on the drift*

⋮

Done Indicates end of the Drift measurement

End Time Total elapsed time (in seconds) for the drift

Pulse Indicates the beginning of the pulse measurement

Pulse time Time of the pulse (in minutes)

Pulse EMF Indicates that the following values relate to the direct voltage potential across the calorimeter heater

time1_emf$_i$ Time reading before the emf measurements for pulse point i (i=1 to the # of points in the pulse)

emf$_1$**, emf**$_2$**, ..., emf**$_8$ Eight replicate values of the emf measurement for pulse point i

time2_emf$_i$ Time reading after the emf measurements for pulse point i

Pulse I Indicates that the following values relate to the heater current by way of the voltage potential across a standard resistor.

time1_I$_i$ Time reading before the current measurements for pulse point i (i=1 to the number of points in the pulse)

I$_1$**, I**$_1$**, ..., I**$_1$ Eight replicate values of the current for pulse point i

time2_I$_i$ Time reading after the current measurements for point i

⋮

⋮ *The previous values for the emf and I are repeated for all of the points*

⋮ *on the pulse*

End Time pulse Total elapsed time (in seconds) for the pulse

*************** spacer line (*×70)

⋮

⋮ *The Drift and Pulse continue for all successive points until the end*

⋮

Done End of last drift

End End of file

********** ending line (*×70)

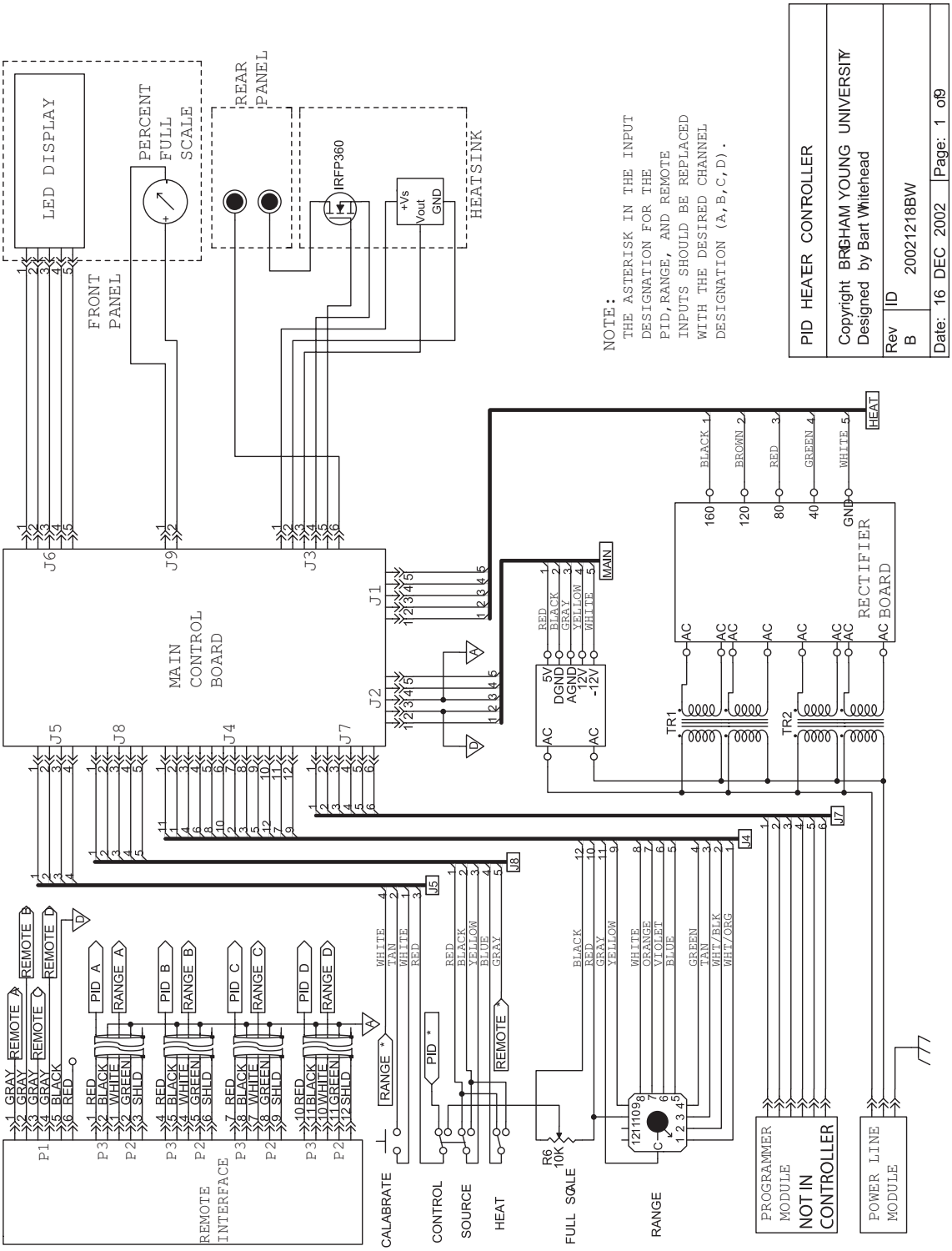

Figure 3.4. PID heater schematic

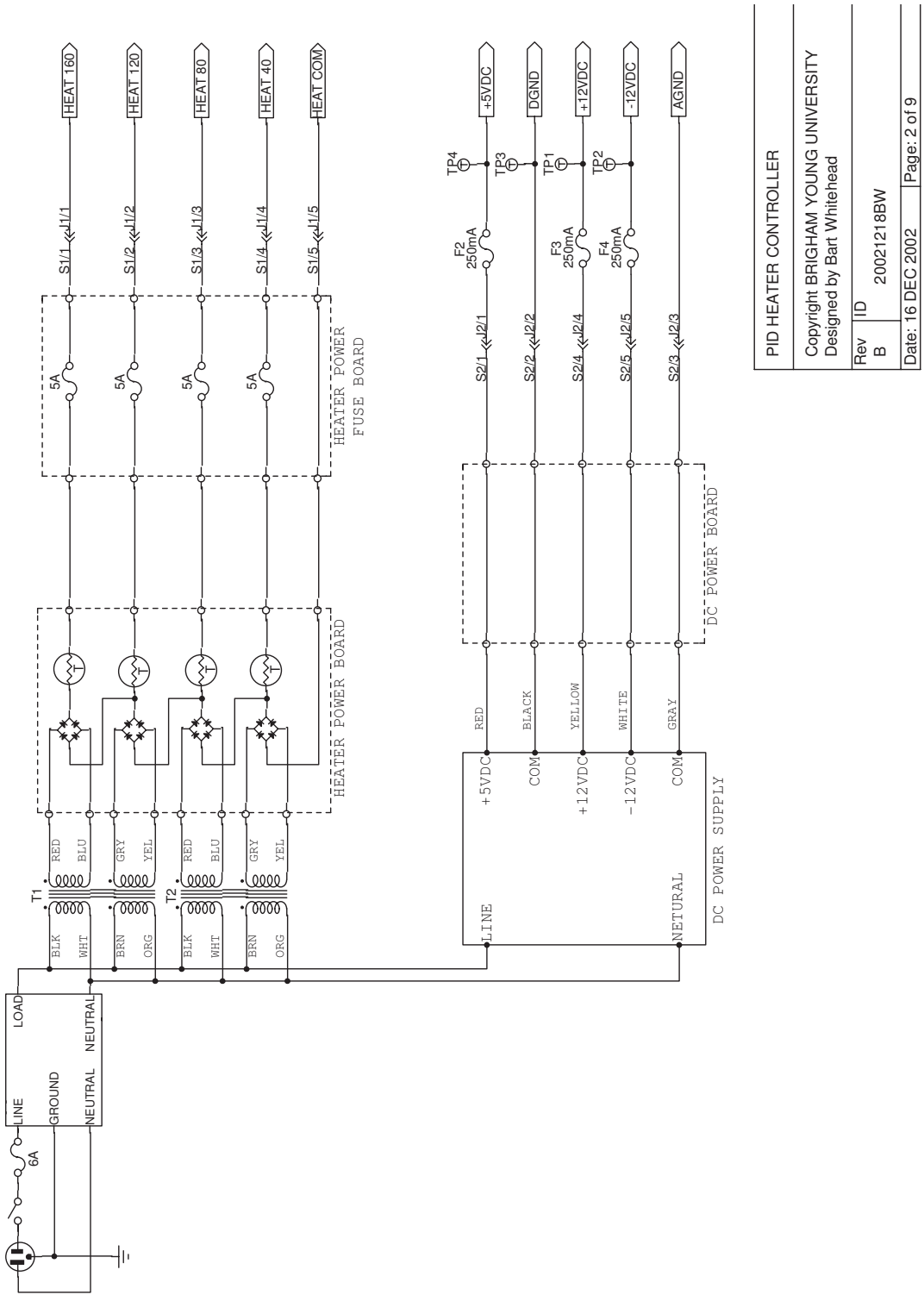

Figure 3.4. continued...

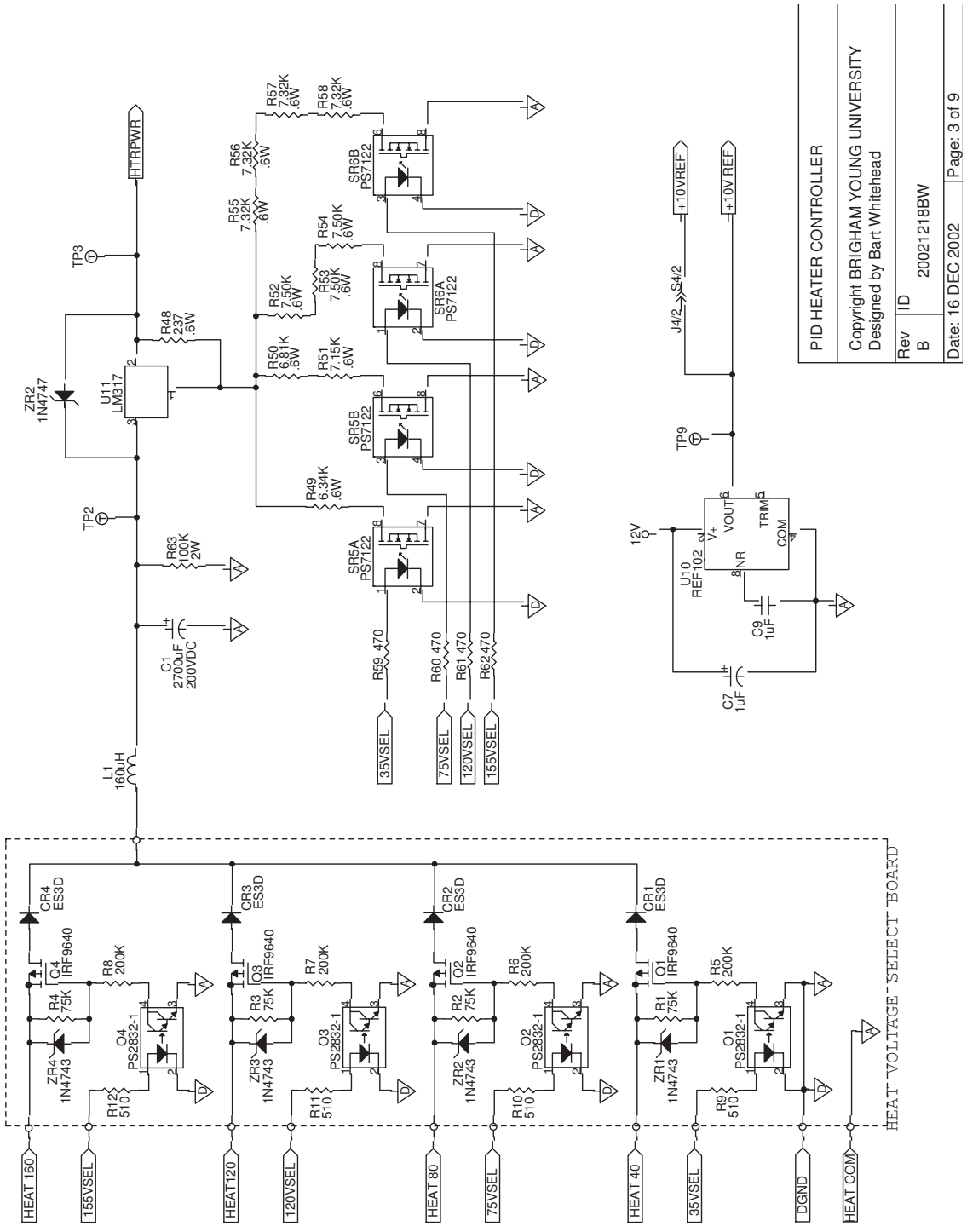

Figure 3.4. continued...

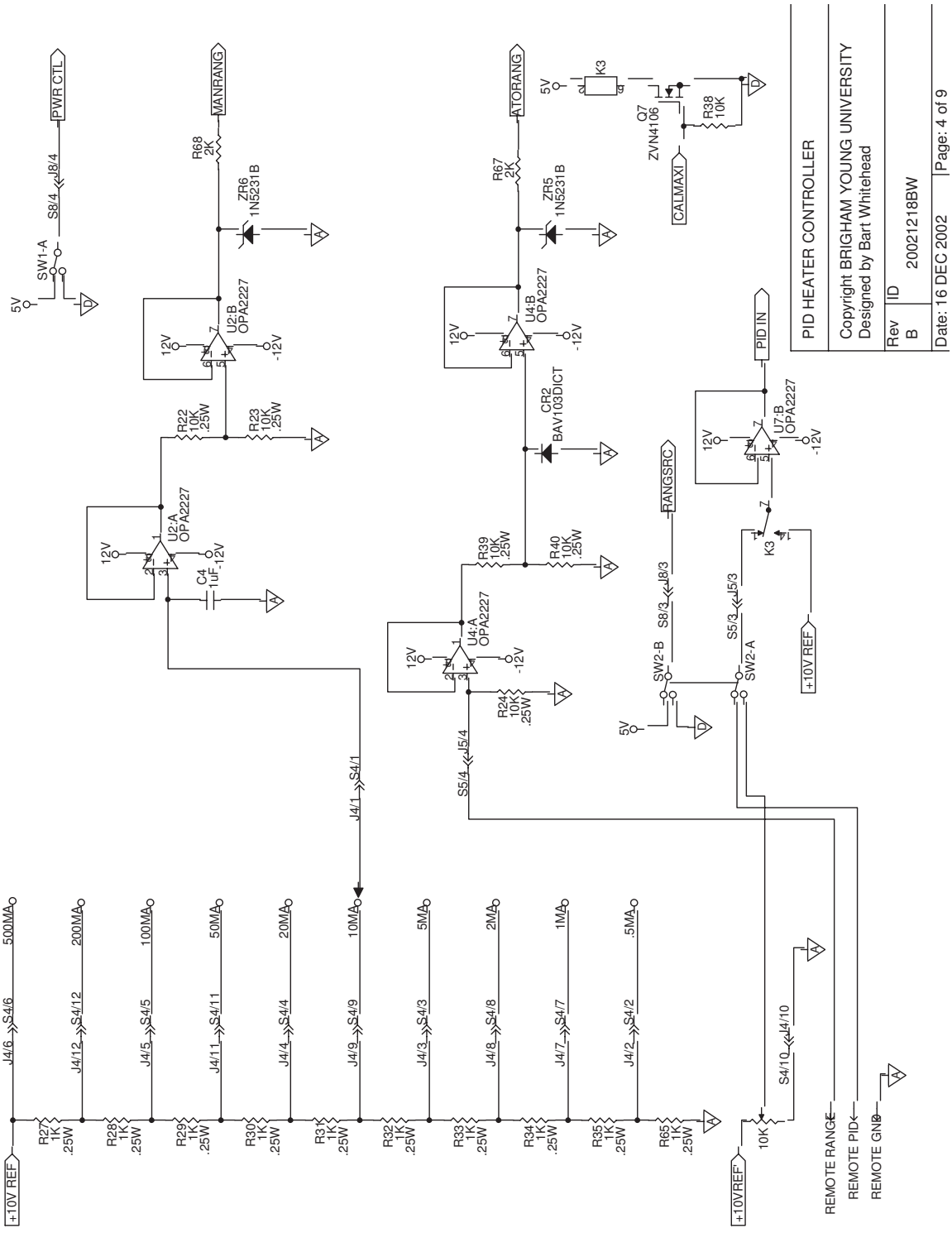

Figure 3.4. continued...

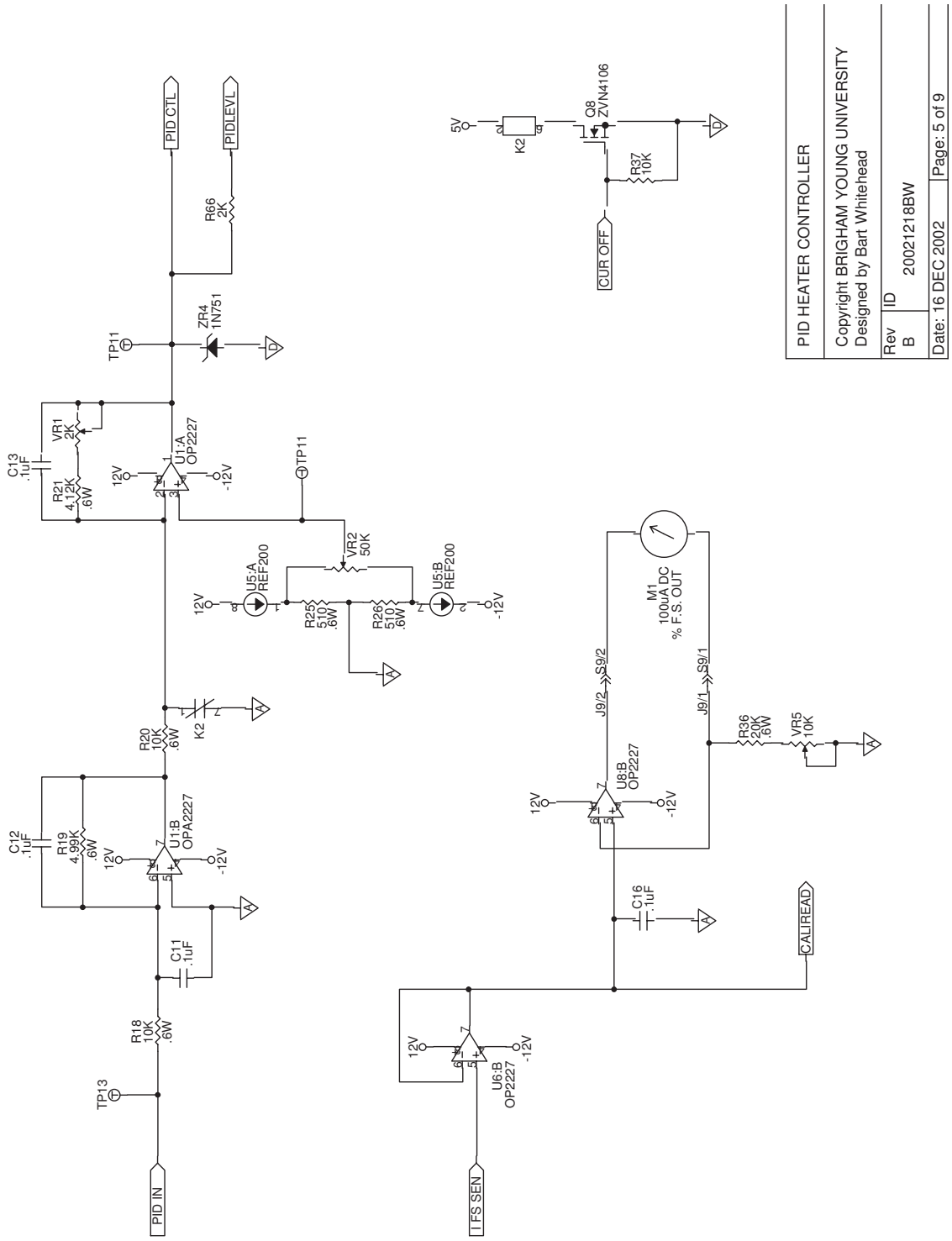

Figure 3.4. continued...

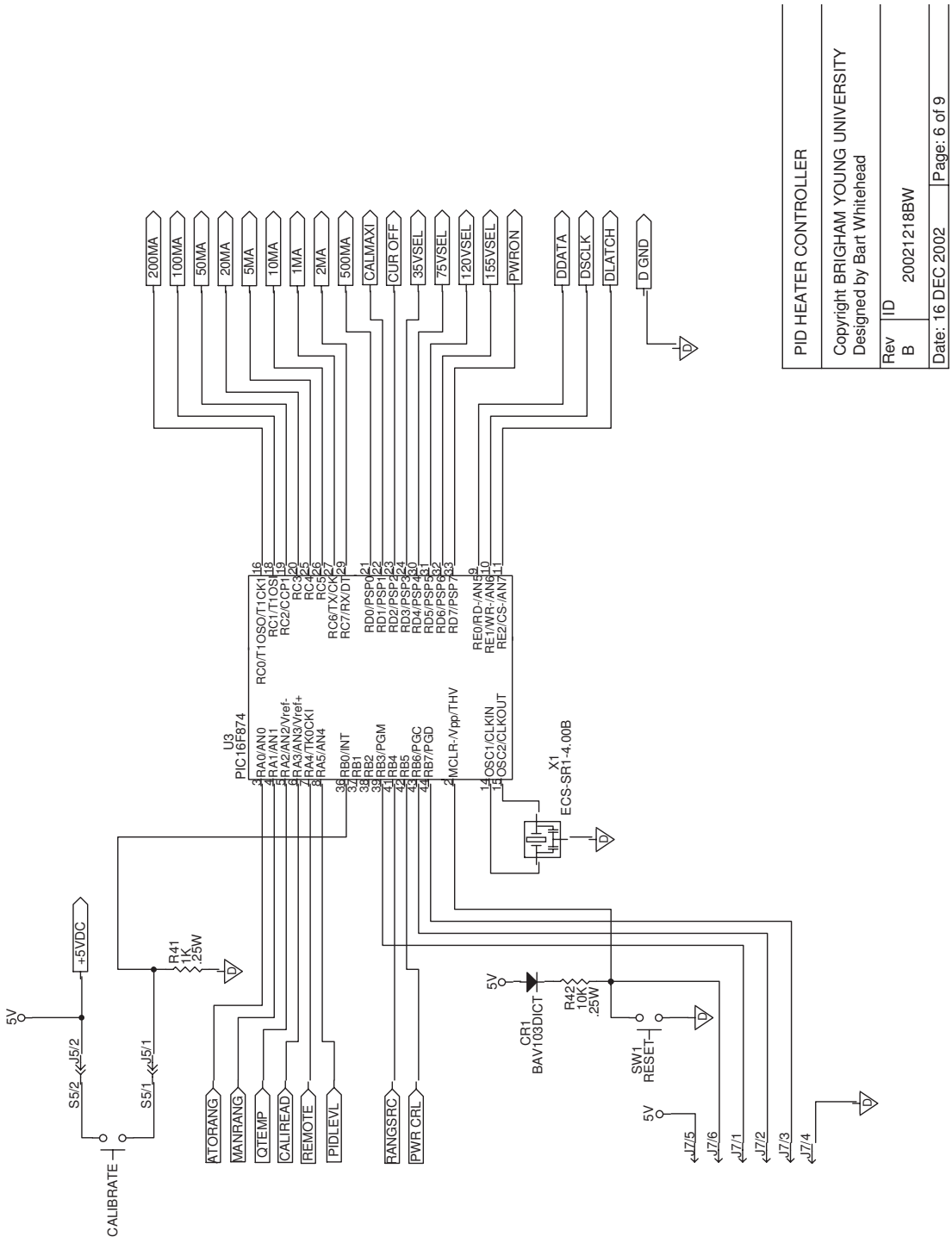

Figure 3.4. continued...

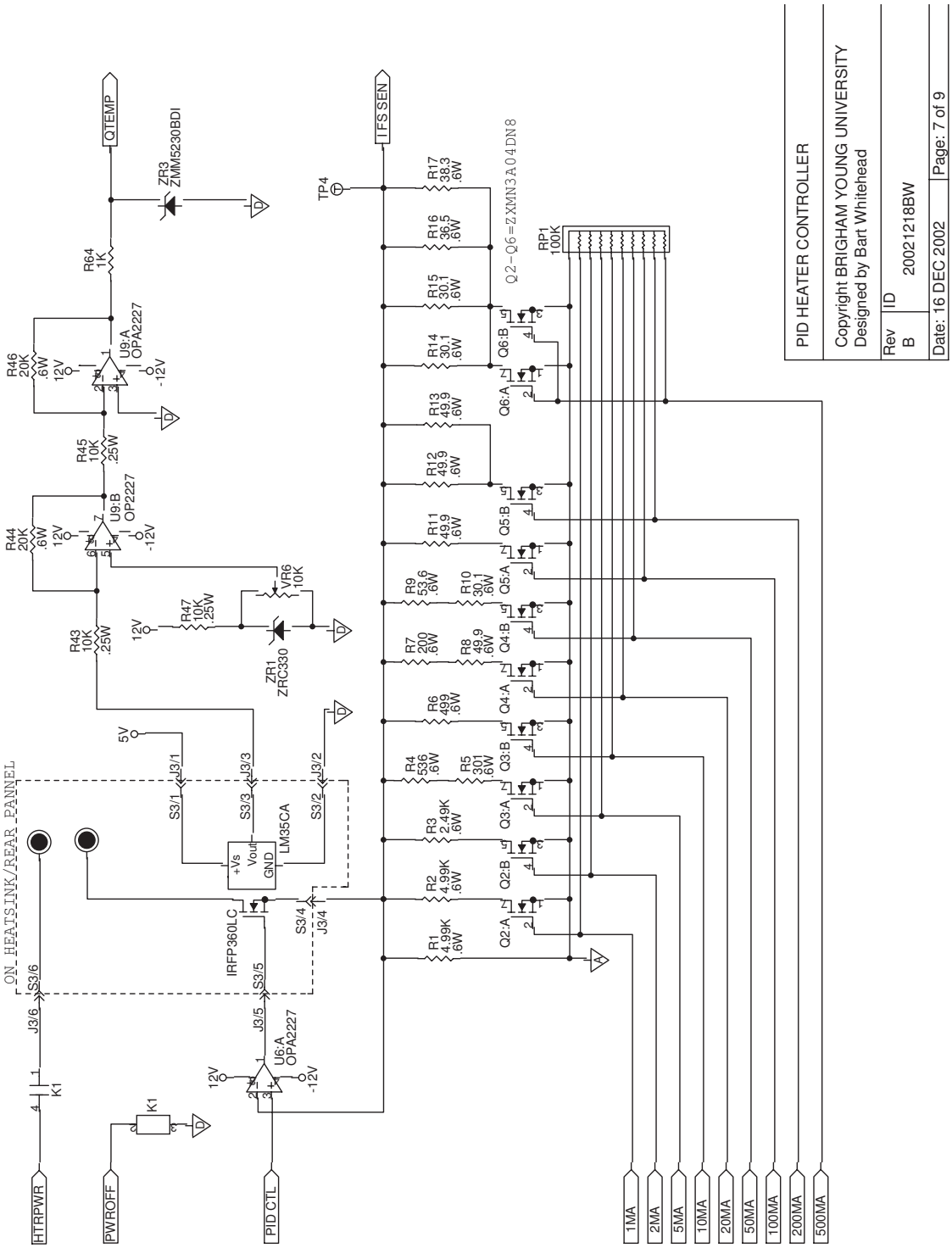

Figure 3.4. continued...

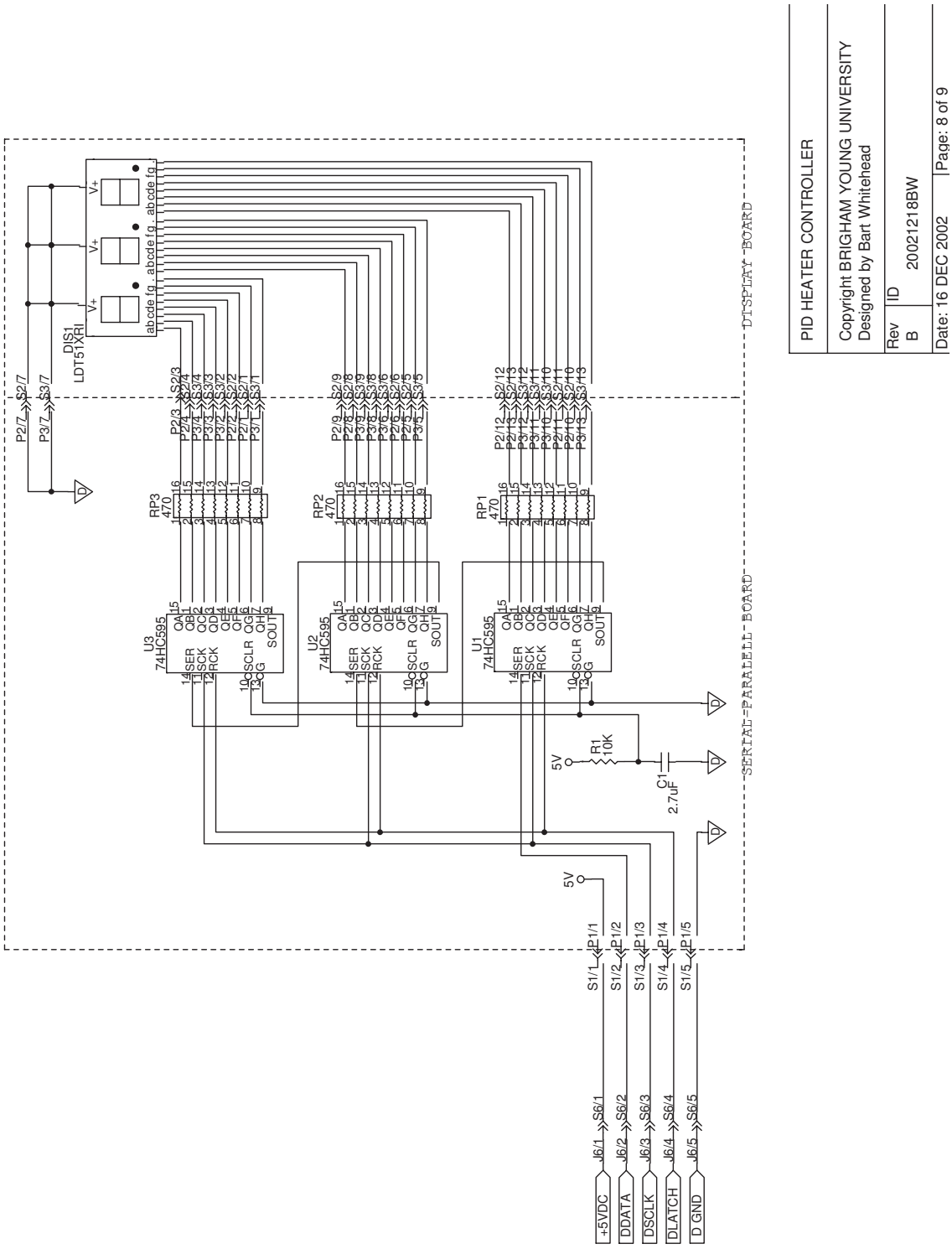

Figure 3.4. continued...

References

[1] Phillips, C. L.; Harbor, R. D., *Feedback Control Systems*, Upper Saddle River, New Jersey: Prentice Hall, 4th edn., **2000**.

[2] Stenerson, J., *Fundamentals of Programmable Logic Conrollers, Sensors, and Communications*, Upper Saddle River, New Jersey: Prentice Hall, 3rd edn., **2004**.

[3] Kiong, T. K.; Quing-Gou, W.; Chieh, H. C., *Advances in PID Control*, London: Springer-Verlag, **1999**.

[4] Putnam, R. L., *Thermodynamic Study of Lyophilized Yeast Cells. Construction of an Automated Micro-Scale Adiabatic Calorimeter for Measurement of Heat Capacities of Solid Samples from 13 K to 325 K and Data Acquisition Software for Use with the Brigham Young University Cryogenic Adiabatic Calorimeters*, Master's thesis, Brigham Young University, **1995**.

Chapter 4

Measurement of Copper, Sapphire, and Benzoic Acid Reference Materials

For any calorimetric apparatus, it is necessary to check the general operation of the instrument with the measurement of a reference material. This allows us to determine the overall uncertainty in the measurements and also allows us to examine factors for which corrections may need to be made (such as heat leaks) or to find experimental defects that would need to be fixed.[1]

Reference materials are those substances that are well characterized and whose specific heats are well known and highly reproducible. Many of these reference materials have been prepared and characterized in large batches for distribution as specific heat standards, which allows for more accurate comparison between different laboratories.[a] The standard reference materials of choice for low-temperature specific heat measurements are copper, aluminum oxide (sapphire), and benzoic acid. We have measured these materials on the new microcalorimeter in an effort to determine the

[a] In cooperation and advisement with the Calorimetry Conference, the National Institute for Standards and Technology (NIST) has prepared a variety of specific heat standards that are available for purchase.[2]

precision and accuracy of the specific heat measurements and to quantify heat leaks from the calorimeter to the adiabatic shields. We present this data along with the measurement of the empty calorimeter.

4.1 Empty Measurements

For any calorimeter, it is important to know the specific heat of the addenda, so that as samples are measured, the addenda specific heat may be subtracted to determine the specific heat of the sample. For the small-scale apparatus, the addenda is the empty microcalorimeter, evacuated, filled with a few torr of helium exchange gas, and sealed with a gold gasket, along with the thermometer/heater sleeve and Apiezon T grease in the thermometer and thermocouple wells. The mass of the calorimeter does not change between runs and the Apiezon T grease is kept constant by careful weighing, but the volume of helium and the mass of the gold gasket is not consistent, and compensation for the mass differences must be made with every sample. Generally, the empty is run before any other samples are run in the calorimeter, and new values for the empty specific heats are measured only when there are major changes to the cryostat or the calorimeter.

The first empty run with the small-scale apparatus (designated bmt1) used a 0.2505 g gold gasket with 20 torr of helium exchange gas. This empty was run controlling four of the adiabatic shields: MASH, TASH, Ring, and GASH, while applying no heat across the BASH heater, leaving the temperature of BASH to float freely. Also, GASH was controlled without an offset voltage, so that it ran at the same temperature as MASH. However, during the measurement of copper, this configuration proved too unstable to work with and gave inconsistent results. After experimenting with several different modes of operation, the best control and reproducibility was found by controlling MASH, TASH, and BASH as a single shield (collectively now

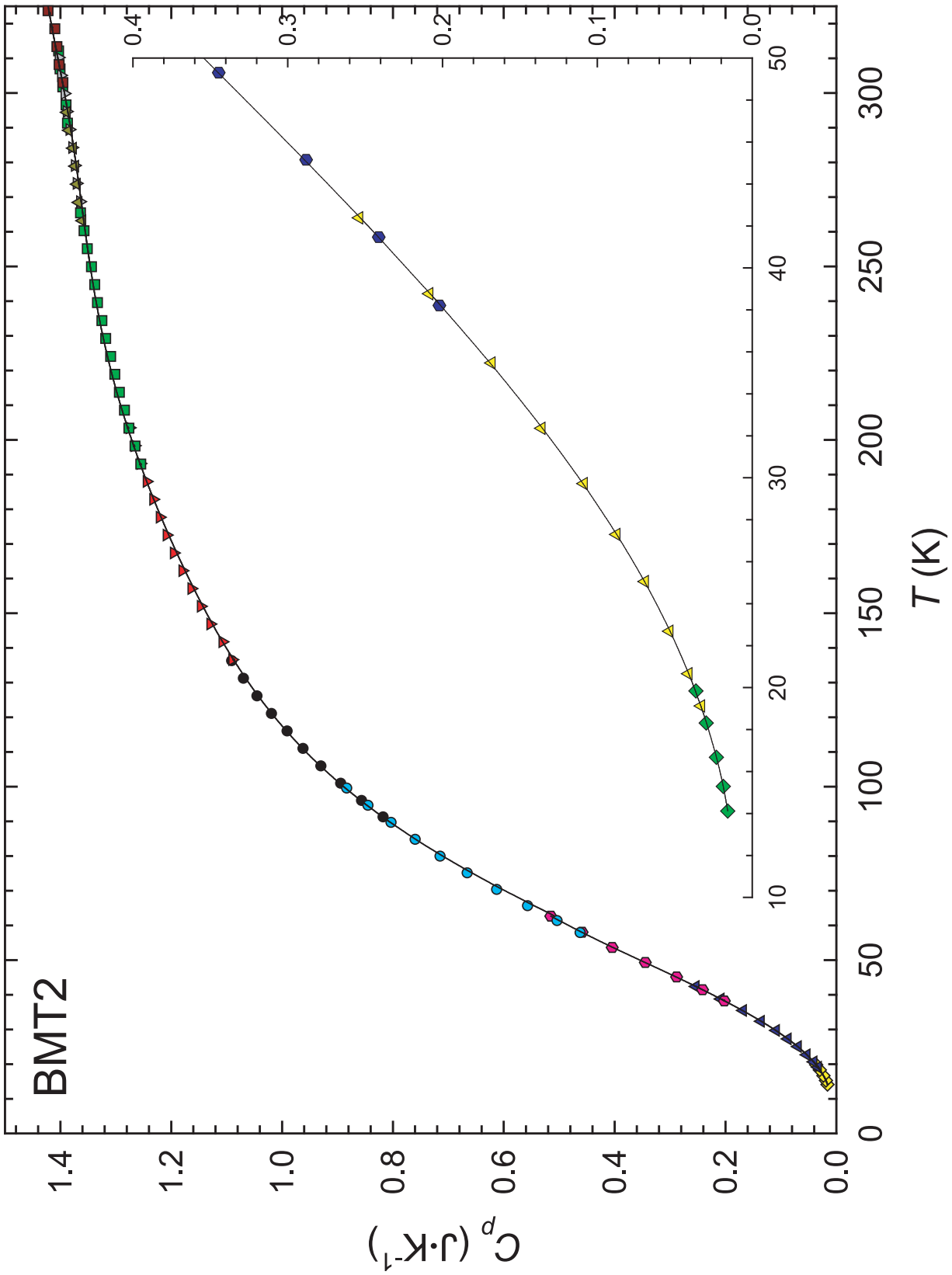

Figure 4.1. Specific heat and initial fit of the empty

called MASH), using the MASH thermocouple proper as the input into the PID algorithm for the main shield, and maintaining a -10 μV offset for the GASH thermocouple insuring that it is consistently colder than MASH. Since the shield modifications were performed while running the copper sample, a new empty needed to be run after the copper was unloaded. This second empty (bmt2) used a 0.2475 g gold gasket and 18 torr of helium exchange gas, and upon running, the measured specific heat of the second empty was much more consistent than that of the first empty. Therefore, it is this empty that is currently being used as the addenda subtraction for sample specific heat measurements.

The specific heat of empty 2 is shown in figure 4.1 along with an initial fit, and the data behaves in the typical manner of simple metals. The fit consists of two orthogonal polynomial functions of the type $C = A_0 + A_1T + A_2T^2 + \cdots + A_nT^n$ that have been joined to make a smooth representation of the data. The term orthogonal polynomial refers to the method used to fit the data to the equation, since it is fit using an orthogonal minimization routine as opposed to the least squares method that is most often employed in fitting algorithms. This method has an advantage over the least squares approach in that one can continue to add powers to the polynomial while only slightly increasing any rounding errors to the fit. Although the orthogonal minimization can represent a smooth curve with high precision, the method itself does not deal effectively with anomalies in a curve such as inflection points, or sharp changes in curvature such as magnetic phase transitions. Thus, when specific heat data is fit with orthogonal polynomials, it is typical that more than one equation is used to represent the data.

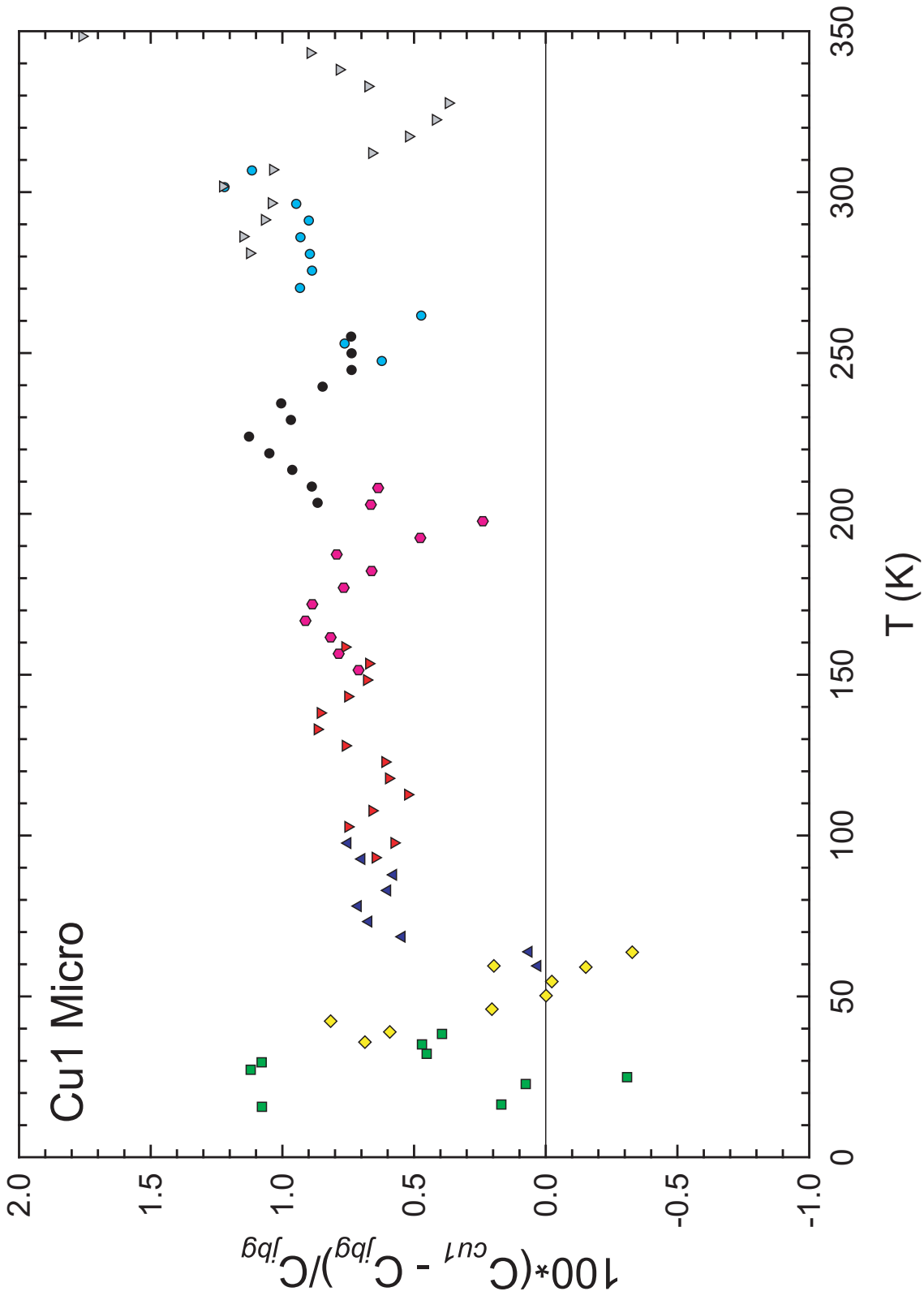

Figure 4.2. Deviation of the specific heat of copper run on the microcalorimeter (C_{cu1}) from copper run on the large-scale calorimeter (C_{jbg}). The various symbols represent the different series of data collected.

4.2 Copper

Copper was the first standard run on the small-scale apparatus (as mentioned in the discussion of the empty measurements) since it is the standard most often used for low-temperature measurements, it is readily available, relatively inexpensive, and can be manufactured with high purity.[1, 3] Also, copper is a utilitarian standard because it has a high thermal conductivity and a relatively high specific heat at low temperatures, and this makes it suitable as a standard over a large temperature range.[3] The copper sample of choice for a reference material is the 1965 Calorimetry Conference Copper Standard that was prepared at Argonne National Lab from 99.999+% pure copper and vacuum annealed. The specific heat of the Calorimetry Conference Standard has been well defined between 1 K and 400 K, primarily by Martin, and has two reference functions recommended by IUPAC[b]: one between 1 K to 30 K, and the other between 15 K to 300 K and there are additional reference functions for copper published by CODATA[c] as well.[1, 4]

Although the Calorimetry Conference Standard was not available to us, a suitable high-purity copper sample that was well characterized was at hand. Our copper sample was obtained from Los Alamos National Laboratory, and was assayed as being 99.999 % pure by inductively coupled plasma mass spectroscopy. The sample was prepared as copper shot and then etched in 8 M nitric acid, dried, annealed at 1173 K in a reducing atmosphere of H_2 gas for 20 days, and finally annealed at 1173 K in a high vacuum for 7 days.[3] The specific heat of this sample of copper had been measured previously on the current large-scale calorimeter, and was used to refine the specific heat of copper between 15 K and 400 K on the ITS-90 temperature

[b]Between 30 K and 300 K there has been some disagreement between the values recommended by IUPAC (Martin) and CODATA, but recent measurements on copper by Stevens and Boerio-Goates [3]concur with the values given by Martin.

[c]Committee on Data for Science and Technology

scale.[3] Along with the specific heat data, we also have functions that represent the heat capacity as a smooth curve, where the uncertainties of the curves are generally better than 1% below 25 K, 0.2% between 25 K and 60 K, and 0.05% above 60 K.[3] Thus, we have a copper reference sample with a well known specific heat, and a means to compare the results from the small-scale apparatus to the current large-scale apparatus.

The microcalorimeter was loaded with 4.1841 g of the copper sample after removing the sample from the dry argon atmosphere where it is stored when not in use. The calorimeter was evacuated for two and one-half hours, backfilled with 20 torr of He gas, and then sealed. As mentioned previously, the experimental conditions were changed during the course of the specific heat measurements, so the initial measurements of the specific heat before the shield reconfiguration will not be discussed. A secondary result of the shield modifications is that the specific heat of the empty calorimeter was measured after the standard was run, thus the results of the standard measurements could not be evaluated in a timely manner since the fit of the empty must be subtracted from the total specific heat of the sample to obtain the specific heat of copper.

The results of the specific heat measurements plotted as a percent deviation from the copper function file as measured on the current large-scale calorimetercan be seen in figure 4.2. On examination of the deviation plot, one can see that the specific heat data runs high compared to that of the reference. Below 50 K the data is 0.4% high with a standard deviation of $\pm 0.8\%$, and above 50 K the data on average is 0.7% high with a standard deviation of $\pm 0.3\%$. While these results do not reflect the desired accuracy and precision of the calorimeter, the fact that the data is consistently high indicates that there is a relatively constant and persistent source of error. The most likely cause of the high specific heat is a heat leak that has not been

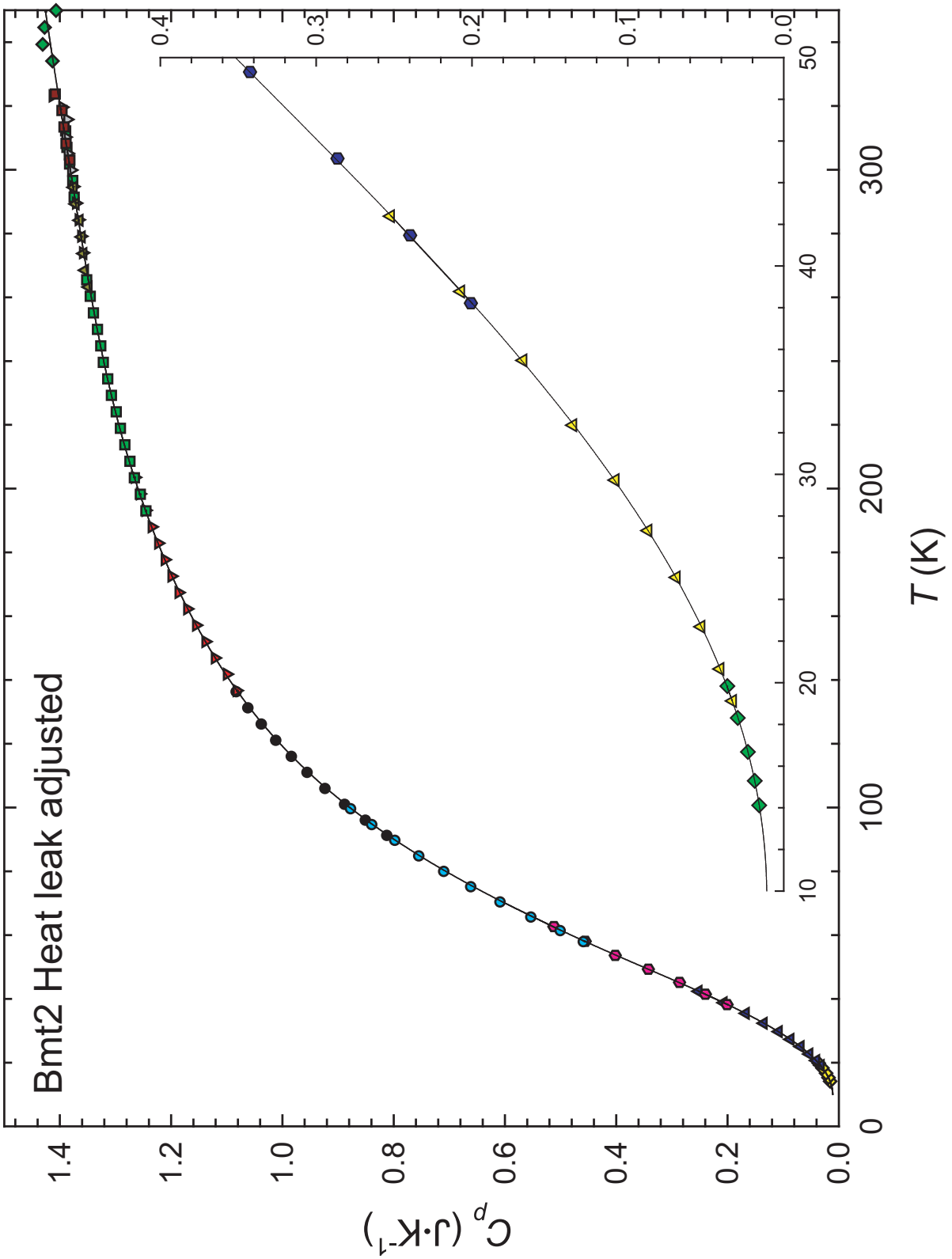

Figure 4.3. Adjusted specific heat for the empty with the various symbols representing the different runs. The smoothed line is a plot of the function used to represent the data.

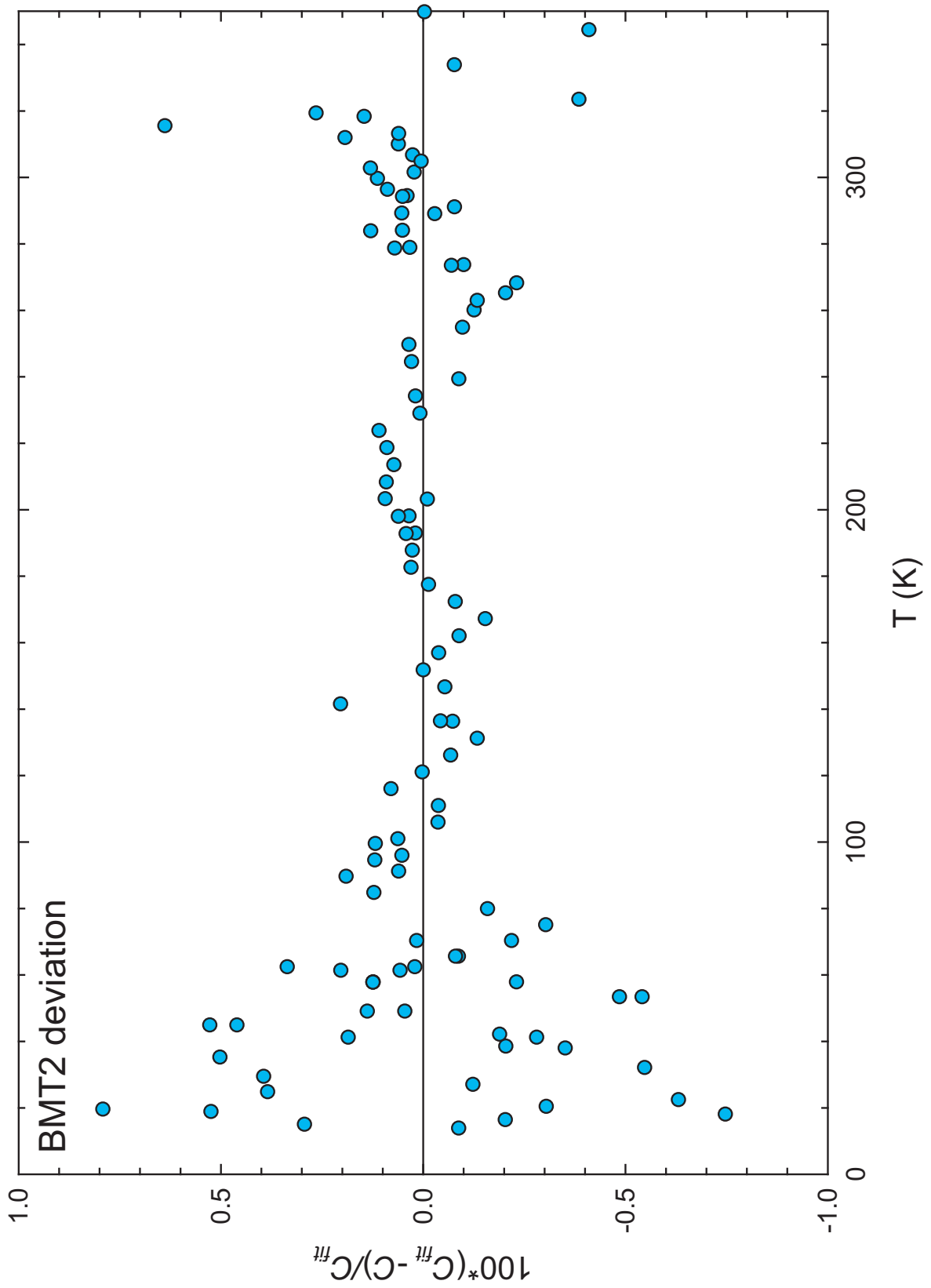

Figure 4.4. Deviation of the adjusted empty specific heat data from the polynomial fits (bmt2).

compensated for in the specific heat calculations. That is to say, during the pulse portion of the measurement, some amount of the heat input into the calorimeter does not enter the sample, but dissipates into the surroundings, most likely through the heater/thermometer leads. This explanation is supported by the fact that the quasi-adiabatic conditions could not be maintained without using the GASH heater. In other words the calorimeter could not maintain a constant temperature and always cooled without GASH. This means that there is some inherent heat flow out of the calorimeter into the adiabatic shields. Once the heat leak is known, it can be compensated for to give more accurate specific heat results.

The first approximation of the heat leak was found by determining the net heat change of the copper data needed to adjust the measured specific heat to be in agreement with that of the standard reference function. However, for consistency in all of the specific heat calculations, the same heat leak correction must be made to the empty as well. Thus, simultaneous adjustments to copper and the empty were made so that the measured specific heat of copper came into agreement with the standard. The resultant final heat leak correction is a percentage of the total heat input into the calorimeter that is represented by quadratic function with respect to temperature. A secondary consequence of the heat leak correction was the need to determine a new function for the empty, since the heat leak adjustments also apply to the empty. The adjusted data for the empty along with the fit, which like the original fit is two polynomial functions spliced together, is given in figure 4.3, and the percent deviation from the fit is shown in figure 4.4. The standard deviation from the fits is $\pm 0.15\%$ above 50 K, but the error increases to $\pm 0.4\%$ below 50 K.

From the heat leak adjustments, the new specific heat for copper falls into agreement with that of the reference function file generated from measurements on the large scale calorimeter, and this can be seen in figure 4.5. The resulting uncertainty

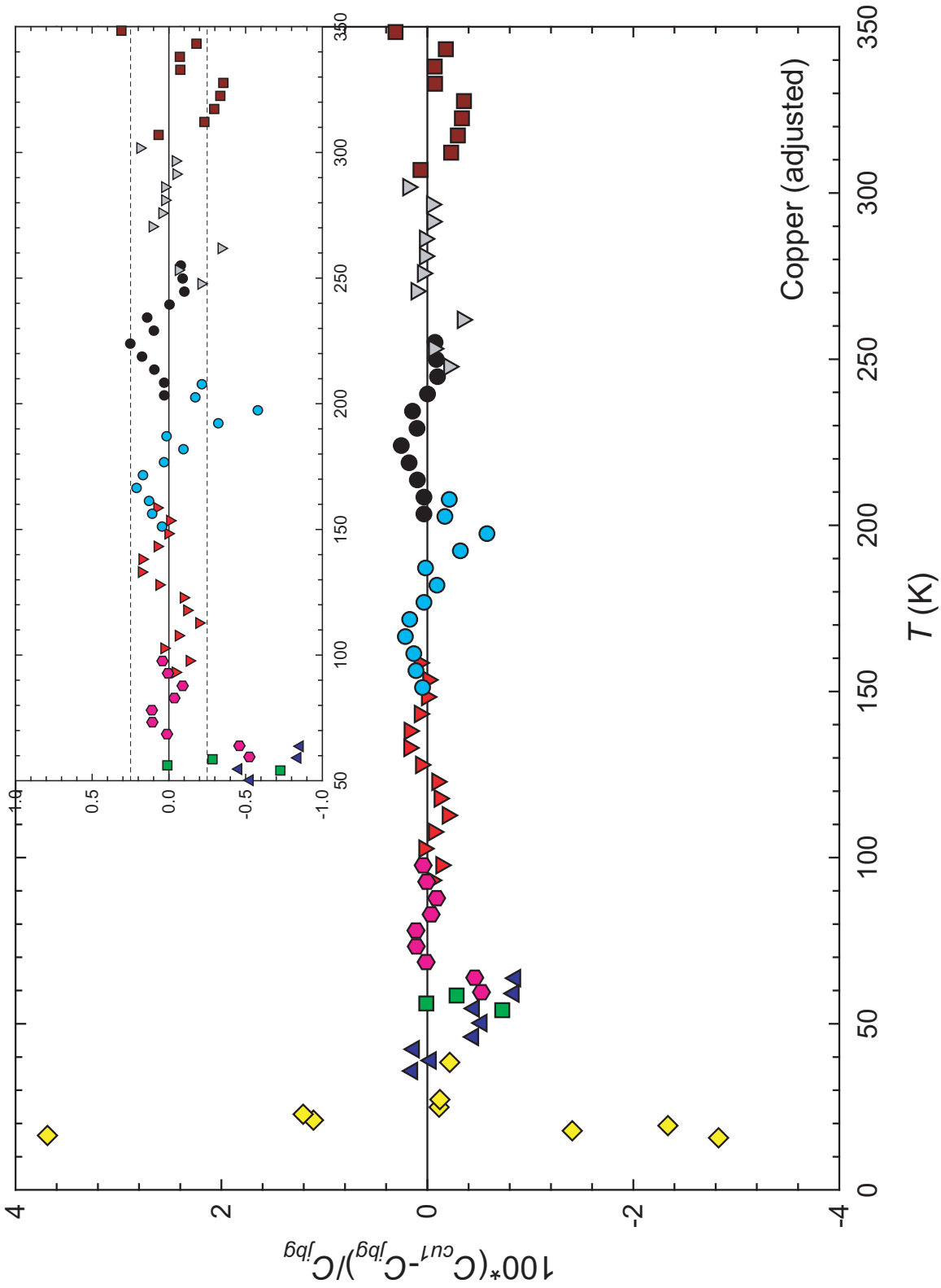

Figure 4.5. Deviation of the adjusted specific heat copper from the standard reference. The inset shows the 95% confidence levels of the deviation above 50 K. The various symbols represent the different series of data collected.

for copper is ±0.24% above 50 K and increases to ±0.4% below 50 K, which is close to the desired precision for this instrument. However, this copper data cannot be used to quantify the overall uncertainty for the calorimeter since the data was adjusted to fit the standard in order to determine the heat leak. Thus, to independently verify the overall experimental uncertainty, other standards were measured.

The heat leak correction determined from copper has been applied to all subsequent measurements on the small-scale apparatus. The correction has been incorporated into the data analysis program for the small scale apparatus (appendix B); thus, all specific heat measurements on this apparatus will include the heat leak correction.

4.3 Sapphire

The second reference material run in the calorimeter was a 1.7314 g sample of synthetic sapphire (α-Al_2O_3) purchased from NIST. NIST has measured the specific heat of the standard reference material sapphire (SRM 720) and has published data tables and thermodynamic functions for sapphire from 10 K to 2250 K, which have an accuracy of ±0.1% above 70 K.[5] The accuracy of the sapphire specific heat published by NIST begins to decrease sharply below 70 K, since the specific heat of sapphire diminishes at a much faster rate than that of typical calorimeter vessels (which are generally constructed from copper and other metals).[5] Thus the specific heat for the sapphire standard was only measured from 75 K to 325 K. This particular sample of sapphire has also been run on the large-scale calorimeter; thus, it is also useful for comparison of the two instruments.

The specific heat of sapphire was compared against the NIST reference function, and the deviation plot can be seen in figure 4.6. On the initial examination of the deviation from the reference function, the deviation appeared to be high with respect

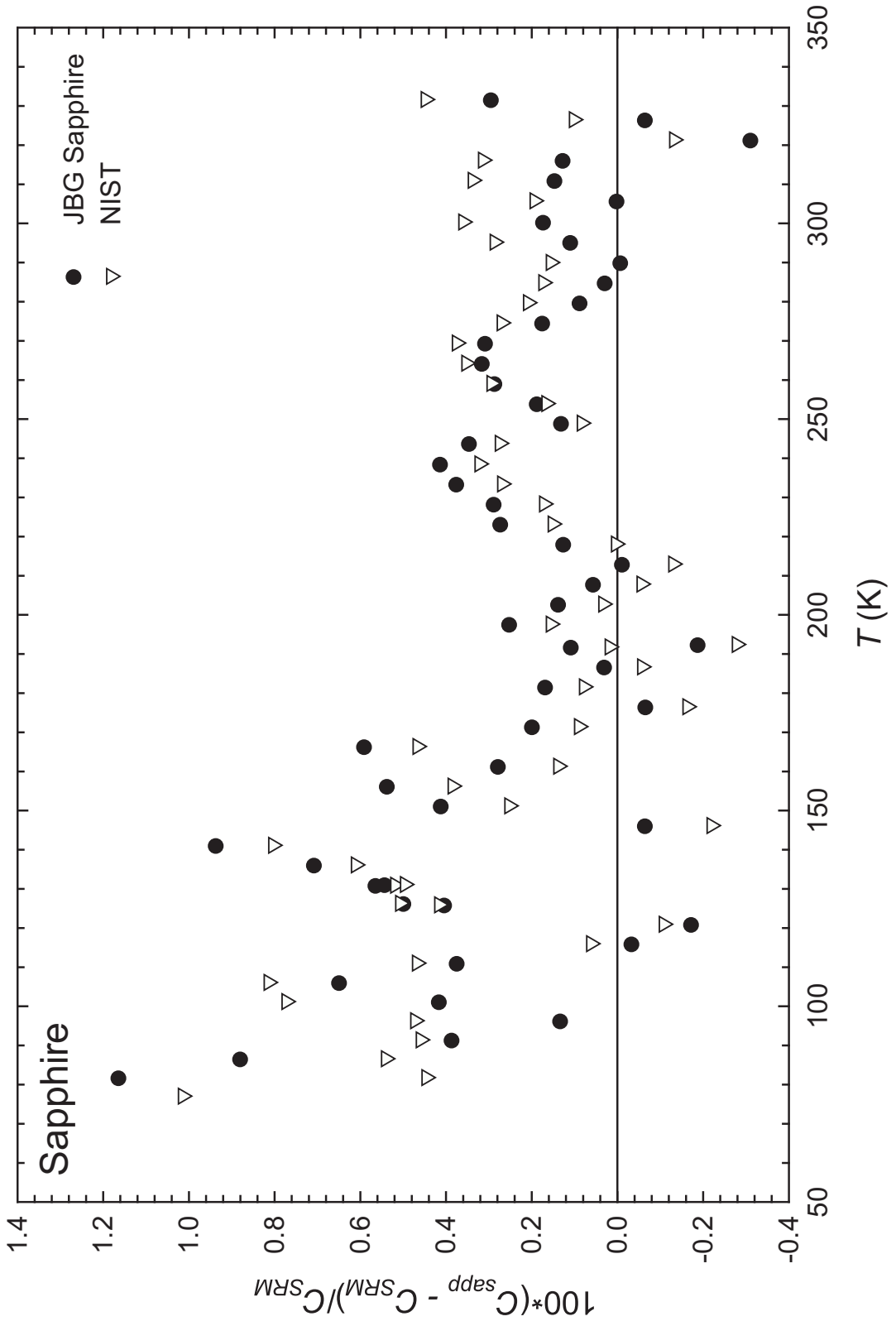

Figure 4.6. Deviation of the specific heat sapphire (SRM 720) compared to standard reference function defined by NIST and compared to the same sample run of the large-scale calorimeter (JBG).

to the reference and the scatter was larger than expected. This was partially thought to be attributed to the reference function being defined using ITS-68 rather than ITS-90, and there was also a question as to the absolute accuracy of the specific heat reference function, as in the case of copper.[3] Thus, the specific heat of sapphire run on the small-scale apparatus was also compared to the specific heat measurements of the same sample ran on the large-scale apparatus. The deviation of the current data to both the NIST reference function and the measurements from the large-scale apparatus have been plotted in figure 4.6. Unfortunately, the deviation with respect to the sample run on the large-scale apparatus did not change the overall error and scatter in the sapphire measurements. However, the average scatter of the data along with the standard deviation does give a truer sense of the overall uncertainty of the specific heat measurements. Below 100 K the average error is +0.6% with an uncertainty of ±0.5%, from 100 K to 175 K the average error is +0.4% with an uncertainty of ±0.3%, and above 175 K the average error drops to +0.15% with an uncertainty of ±0.2%. While these are reasonably good values for the uncertainty in the specific heat measurements, they were not as good as expected; thus, it was decided that an additional standard should be measured to verify these results.

4.4 Benzoic Acid

The final standard run in this series of calibration and validation of the calorimeter was benzoic acid. This sample was a standard for specific heat measurements created for the Calorimetry Conference in 1949 and obtained from the National Bureau of Standards (now NIST). The benzoic acid is kept in a vacuum desiccator when not in use to prevent degradation and water absorption onto the sample. On loading of the sample, 0.6286 g of the benzoic acid crystals, each between 2 and 3 mm in

size, were placed into the calorimeter and sealed with 18 torr of He exchange gas. Like the two previous samples, this sample had been run on the large-scale apparatus and smoothed function files of the specific heat data were at hand, making it a good system for study and comparison.

The specific heat of benzoic acid was measured from 15 K to 300 K, and the data was compared to the smoothed specific heat functions for this sample. The percent deviation from the reference is shown in figure 4.7, and there is fair agreement with the standard above 60 K, although the sample data appears to be slightly high with respect to the standard. Below 60 K it is difficult to visually ascertain the agreement with the standard since scatter of the data drastically increases. However, the average scatter of the data along with the standard deviation can quantify the agreement with the standard; thus, above 175 K there is an average specific heat difference of +0.15% ±0.2%, between 60 K and 175 K the average deviation is +0.22% ±0.4%, and below 60 K the average deviation from the standard is +0.2% ±2.0%. While the standard error for this sample is slightly higher than desired, especially below 60 K, the data is still in relatively good agreement with the standard, and will be useful in quantifying the overall uncertainty for this instrument.

4.5 Conclusions and Recommendations

The measurement of these standards has allowed for the calculation of the heat leak out of the calorimeter, and the ability to determine the relative error for samples run on this instrument. From the measurements of sapphire and benzoic acid, and taking the relative deviations from the measurements, we can determine that the relative uncertainty in the specific heat for samples is: +0.15% ±0.2% above 175 K, +0.2% ±0.3% between 100 K and 175 K, +0.4% ±0.4% between 50 K and 100

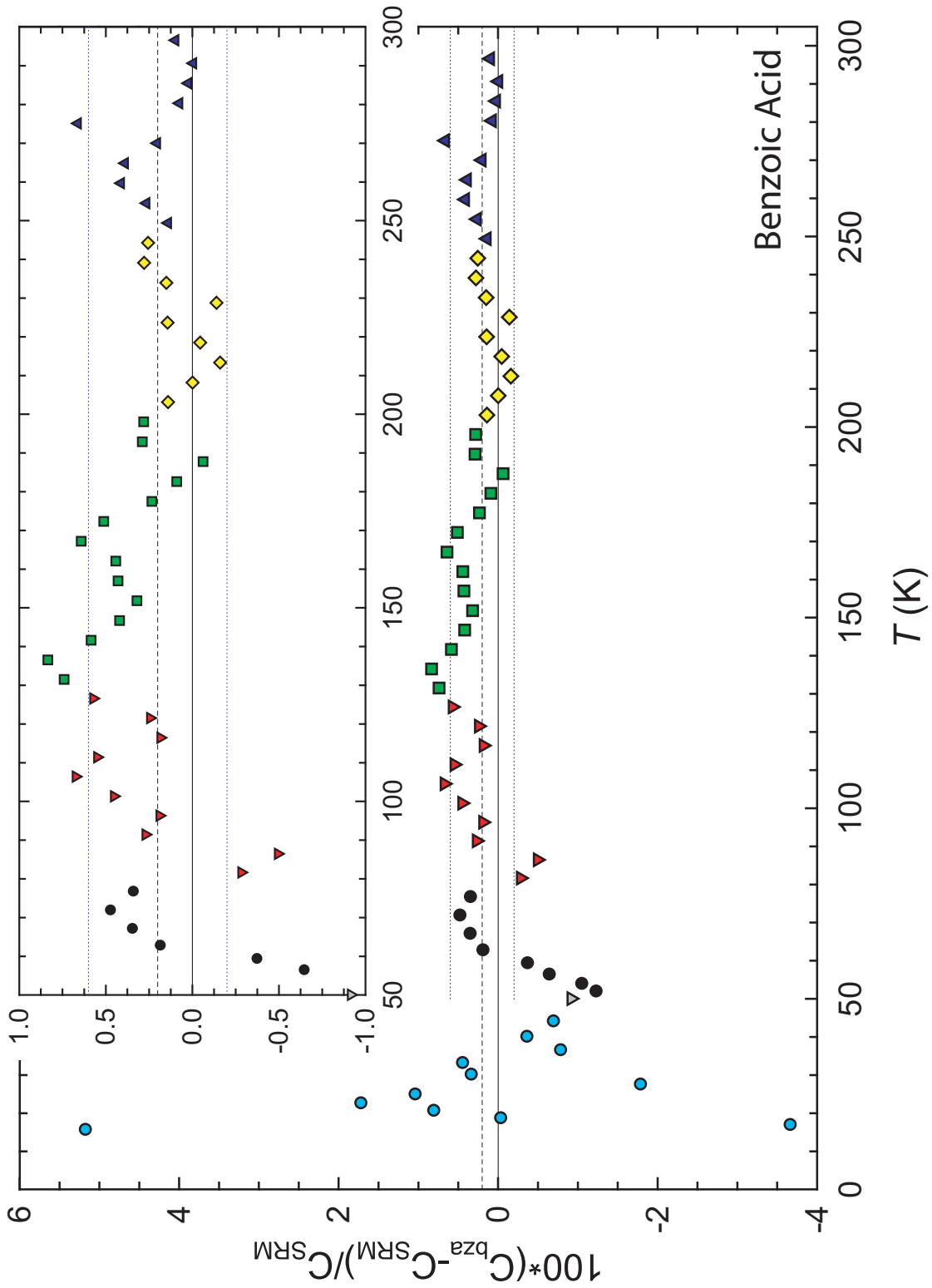

Figure 4.7. Deviation of the specific heat benzoic acid compared to standard reference function defined by the same sample run of the large-scale calorimeter. The plot also displays the average specific heat difference of +0.2% ----, along with the 95% confidence level above 50 K ·····.

K, and +0.4% ±1% below 50 K. While these results show that the accuracy and precision of the small-scale apparatus is not up to the standards of the large-scale apparatus, the overall uncertainty of the small-scale apparatus is still acceptable, especially considering the sample size, making this instrument the most accurate calorimeter for samples of this size. One troubling fact of these results is that the measurements consistently average a few tenths of a percent high, rather than the scatter data being centered around the reference function. This is indicative of one of two problems; (a) either there is still some consistent heat leak out of the calorimeter that has not been accounted for, or (b) there is a heat leak out of the system due to problems with shield control. While it is possible that there is a portion of the heat leak that has not been accounted for in the specific heat calculations, it is more likely that this is simply a shield control issue that can be resolved by tighter control of the shields, since the shields are the main source of limiting heat loss out of the calorimeter.

Subsequent measurements on additional samples run on the microcalorimeter have shown an increased reproducibility of the data that can be correlated with an increase in the precision of the shield control. Primarily, it has been the ability to limit the deviations in the temperature of GASH relative to MASH that have produced the most improvement in the reproducibility (precision) of specific heat measurements, making GASH as important as MASH in maintaining the adiabatic conditions and ensuring that the heat loss is consistent. The control of GASH after the standards were run was improved by increasing the sensitivity of the GASH thermocouple reading, which was accomplished by multiplying the input signal before it is processed by the PID algorithm (this is an adjustable factor that can be changed on the front panel of the Labview PID control program). Aside from increasing the reproducibility of the specific heat, the increase of the GASH temperature control can be seen in the

reduction of noise in the drift measurements, which is most evident in the helium region, where the drifts tend to reflect any periodic oscillations in the temperature of GASH.

Further increases to the accuracy and precision of the specific heat measurements on this apparatus may be made in the future by implementing changes to the experimental setup when time and funding permit. The first recommended change is to increase the loop time of the PID algorithm in Labview, which would allow the derivative action of the control loop to respond better to the rapid fluctuations in the thermocouple response. This would require obtaining a different data acquisition card than the one presently used, and would also result in a loss in resolution of the thermocouple signal, since we would most likely be changing from a 24-bit signal to a 16- or 18-bit signal. However, a loss in the resolution of the data input signal would most likely be compensated for by the increased response time of the PID algorithm. A second recommendation to improve the error is to move the thermometer/heater lead connections to the inside of BASH, instead of allowing the leads to hang outside of the main shield system (refer to figure 2.4). This would hopefully minimize the heat loss out of the calorimeter. Some provisions for this change have already been made with the construction of a connector that fits on the inside of BASH, but implementing this change would necessitate the measurement of a new empty and the determination of a new function for the heat leak correction. Also, since the leads run through a hole on the center of BASH, they help center the calorimeter inside the adiabatic shields; thus, if the lead connections were moved to the inside of BASH another means of centering the calorimeter would be needed. A final recommendation to improve the shield control would be to rewire the shield heater and thermocouple wires as twisted pairs to minimize any electromagnetic interference between the heaters and the thermocouples. This is mentioned because occasionally there seems to

be a minor problem with interference drastically changing the apparent thermocouple response. This last recommendation is drastic and should only be implemented if a complete rewiring of the cryostat is warranted.

References

[1] Barron, T. H. K.; White, G. K., *Heat Capacity and Thermal Expansion at Low Temperatures*, New York: Kluwer Academic/Plenum Publishers, **1999**.

[2] Westrum, Jr., E. F.; Furukawa, G. T.; McCullough, J. P., in J. P. McCullough; D. W. Scott, eds., *Experimental Thermodynamics*, Plenum Press, vol. 1, 1968 pp. 133–214.

[3] Stevens, R.; Boerio-Goates, J., *J. Chem. Thermodyn.* **2004**, *36*, 857–863.

[4] Martin, D. L., *Rev. Sci. Instrum.* **1958**, *1987*, 639–646.

[5] Certificate: Standard reference material 720, synthetic sapphire (α-Al_2O_3), Tech. rep., National Bureau of Standards, Washington, DC 20234, **1982**.

Chapter 5

Specific Heat Measurements of Akaganéite: β-FeOOH

5.1 Introduction

Iron oxides (and oxyhydroxides) have been in use by humans for centuries as pigments, catalysts, and the chief source of iron and steel, and because of this, the chemistry of the various iron oxides has been studied extensively.[1] There has been a renewed interest in the iron oxides with the recent exploration of Mars by the Mars Exploration Rovers Spirit and Opportunity, and the characterization of the iron containing minerals on the surface of that planet using onboard Mössbauer spectrometers. Particularly, the Spirit Rover has discovered hematite and other mineral deposits were found contain a number of iron-bearing phases that could include the minerals goethite, lepidocrocite, jarosite, schwertmannite, and akaganéite.[2] While most of the iron oxides and oxyhydroxides have been well studied and the thermodynamic properties have already been determined, there have been few calorimeteric measurements of akaganéite (β-FeOOH), and thus there is little thermodynamic data for this mineral.

Most of the iron oxides are made up of close packed layers of anions (oxygen) as either hexagonal closed packed (hcp) or cubic closed packed (ccp), with the iron atoms occupying about half of the interstitial octahedral (and in some cases the tetrahedral) sites. The different arrangement of the site occupancies gives rise to the different polymorphs. Akaganéite is unique in that its structure consists of two double chains of edge sharing iron octahedra running parallel to the crystallographic b-axis, each sharing corner oxygens with two other double chains, creating a three dimensional structure made up of 4.9Å diameter tunnels running parallel to the b-axis with walls made up of the double chains of octahedra (the structure of akaganéite is given in figure 5.1).[3] Akaganéite is always found with some Cl^- (and OH^-) ions occupying some of these tunnels, and there is evidence that the presence of chloride (and possibly other anions such as OH^-) is an integral part of the structure, helping to stabilize the tunnels in akaganéite, where complete removal of the chloride ions leads to the transformation of akaganéite to goethite or hematite (hematite being the most stable).[1, 4] Thus, stoichiometrically pure β-FeOOH is never found because some minimum amount of the anions (0.25-0.5 mmol Cl^- per mole of FeOOH) is needed to maintain structural integrity, and values of 2 to 7 mmol Cl^- per mol of FeOOH are typical for most samples of akaganéite (samples of over 100 mmol Cl^- per mol of FeOOH have been reported or approximately 2/3 occupancy of the chloride positions).[1] The presence of these tunnels make akaganéite the least dense of all the iron oxides, and the inclusion of the chloride ions causes the crystallographic lattice of the anions to lay in a body-centered cubic arrangement rather than the typical hcp or ccp arrangement of the other iron oxides.

Aside from the interspersed chloride ions, akaganéite is stoichiometrically related to several other polymorphs of FeOOH: goethite and lepidocrocite (α-FeOOH and γ-FeOOH, respectively, the α phase being the most stable). Like many of the iron

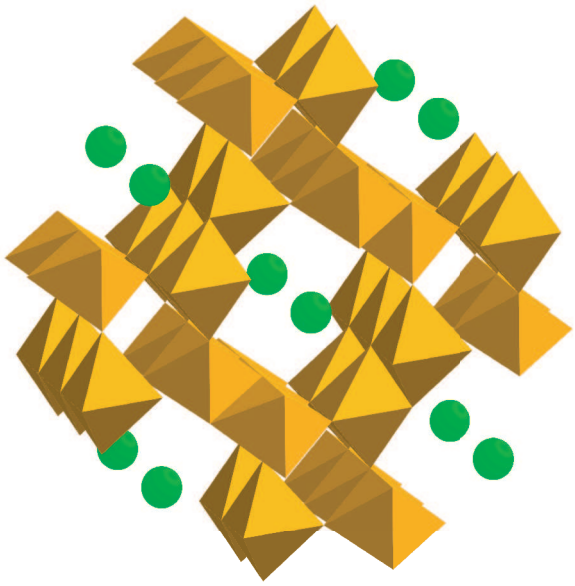

Figure 5.1. The structure of akaganéite showing the iron-oxygen octahedra, and the position of the interstitial chlorine ions. The Cl^- ions are shown at 50 percent occupancy of the possible positions. Structure data from Post and Buchwald.[5]

oxide and oxide hydroxides, akaganéite is formed via the hydrolysis of Fe^{3+} salt solutions, where the mineral will precipitate out of the solution over time (this process is regulated by the temperature and pressure). However, the formation of akaganéite requires a Cl^--rich environment to help direct the formation of the crystal structure, making its presence in nature rare.[1] During formation, the hydrolysis conditions also determine the amount of water present in the crystal, where the water occupies some of the positions in the tunnels (tunnel water).[6] Thus, to fully characterize a sample of β-FeOOH, one must know the stoichiometric ratios of chlorine and water, since these are both highly variable in the sample.

Like all of the iron oxides, akaganéite exhibits magnetic properties due to the alignment of spins of the unpaired electrons on the iron atoms. The spins in β-FeOOH change from paramagnetic to antiferromagnetic ordering below the Néel temperature, which is nominally given as 290 K.[1] However, in contrast to most of the other iron

oxides, T_N for akaganéite varies widely from sample to sample. Magnetic susceptibility measurements have shown a direct correlation of the Néel temperature to the amount of intra-tunnel water present in a sample, more so than the amount of chlorine ions in the tunnels, and this is directly related to the formation conditions since they determine the water content in the tunnels. From controlled studies of the water content, the Néel temperature was found to vary from 300 K at the lowest water contents to 250 K at the highest water contents.[6] Specific heat measurements will hopefully yield more information about the nature of the magnetic transition and the Néel temperature.

The calorimetric measurements on β-FeOOH will also yield the absolute entropy for akaganéite. A combination of the entropy with the enthalpy reported elsewhere leads to a quantitative determination of the Gibbs free energy of stability of this iron oxide. From solubility studies, the Gibbs free energy of formation, $\Delta_f G^\circ_m$, was found to be -751 kJ·mol^{-1}. The formation energies of goethite and hematite have been reported to be -488.6 kJ·mol^{-1} and -742.7 kJ·mol^{-1}, respectively. Calculation of reaction energetics of the decomposition of akaganéite into goethite or hematite based on the respective $\Delta_f G^\circ_m$ for each compound implies that akaganéite is the most stable of the three compounds ($\Delta_r G^\circ_m$ is +262 kJ·mol^{-1}and +261 kJ·mol^{-1}for the decomposition reactions to goethite and hematite, respectively).[7, 8] However, akaganéite is easily converted to goethite or hematite (depending on the reaction conditions), but the reverse reactions are not known to happen, implying that these other iron oxide phases are more stable.[1] Thus, there is some discrepancy in the current value of the Gibbs free energy of formation that the calculation of the entropy of akaganéite will help to resolve.

The values for the thermodynamic functions of the iron oxides, as well other compounds with bound or adsorbed water, have typically been reported as the dehydrated

species, where the water contribution has been subtracted or in some cases neglected completely.[a] Since this convention is widespread, we will report our thermodynamic values in this manner.

5.2 Experimental

The sample of akaganéite was synthesized by dissolving 40.1 g of $FeCl_3 \cdot 6H_2O$ in 1.5 L of water and hydrolyzed in a plastic flask for 8 days at 40-50°C. The resulting precipitate was decanted and dialyzed for two weeks, then dried at 40°C. The amount of water present in the sample was determined by measuring the mass loss of the sample after it is heated to 1100°C for 12 hours. Part of the mass loss is attributed to the decomposition of akaganéite to hematite:

$$\beta - \mathrm{FeOOH}_{(s)} \longrightarrow \tfrac{1}{2}\,\alpha - \mathrm{Fe_2O_{3\,(s)}} + \tfrac{1}{2}\,\mathrm{H_2O_{(g)}}\,. \tag{5.1}$$

From the reaction stoichiometry, water given off by this reaction should account for 10.14 % of the mass loss. Thus, any additional mass loss is from water in the tunnels or water adsorbed on the particle surfaces. Seven replicate measurements gave a total mass loss was 20.16 % ±0.08 %. That mass loss corresponds to 0.620 ±0.006 moles of water for every mole of β-FeOOH. Our estimates based on the synthesis conditions and vacuum desorption measurements suggest that between 0.25 and 0.5 moles of this water resides in the tunnels, and the remainder is adsorbed water.

In addition to the water analysis, it is important to know the amount of chloride residing in the tunnels, since Cl^- is always present in akaganéite, serving to stabilize the molecular framework. The Cl^- content was measured using liquid chromatography, and this akaganéite sample was found to contain 0.34 % chlorine by mass,

[a] Compounds that are understood to have water as part of the chemical formula (i.e. $Na_2CO_3 \cdot H_2O$)[8] are listed as such and the thermodynamic functions include this water.

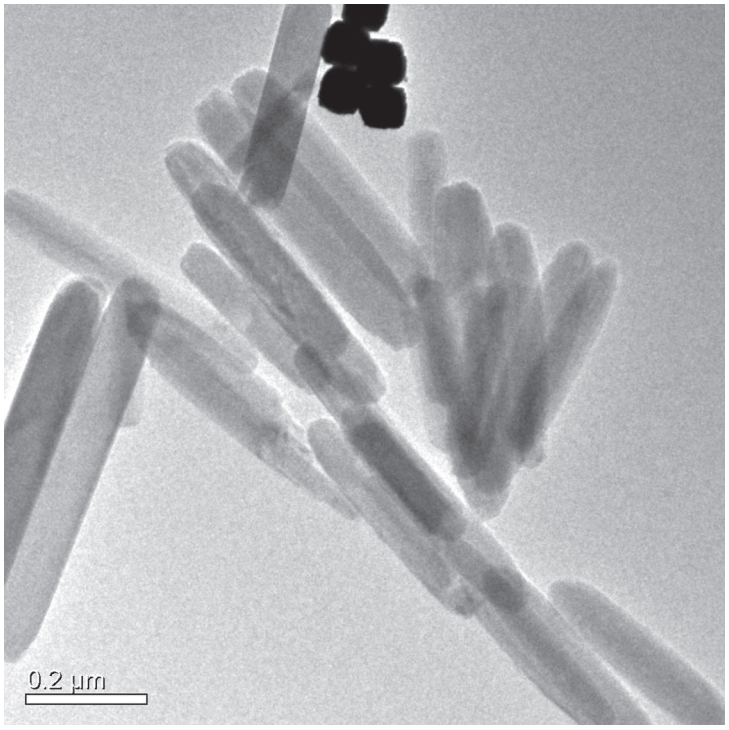

Figure 5.2. TEM image of a cluster of akaganéite (β-FeOOH) rods. Notice the rods in top center of the image that are on end.

or 0.0096 moles of Cl^- per mol of FeOOH. This translates to roughly 7.5 % of the possible chlorine ion sites being occupied. Thus, the resulting formula for this sample of akaganéite is β-FeOOH$\cdot$0.620$H_2O\cdot$0.0096Cl^-, where the charge is balanced by an equivalent number of protons in the lattice.

The sample was analyzed by powder X-ray diffraction (XRD) at room temperature on a Sintag Diffractometer (Cu-Kα radiation, λ=0.154176 nm) at a scanning rate of 0.50°/min at a power of 15 kW. The resulting powder pattern was consistent with that of akaganéite. No identifiable structural or chemical impurities were observed. From the peak widths at half the maximum height, the average size of the particles was estimated to be 34 nm. However, BET analysis indicated that this akaganéite sample had a surface area of 22.30 ± 0.28 m^2/g. This surface area is is consistent with particles of an average size of 100 nm (assuming the akaganéite particles are rods).

Thus, to determine the true nature of the akaganéite particle crystal sizes the sample was examined using a transmission electron microscope (TEM), revealing that the akaganéite particles are rods ranging between 25 and 80 nm in diameter and between 400 and 500 nm in length (see figure 5.2). The discrepancy in the average crystal size measurements from the XRD peaks indicate that the larger akaganéite crystals have multiple domains.[1]

The specific heat of the β-FeOOH sample was measured from 12 to 310 K using the new microcalorimeter described and characterized in chapters 2, 3, and 4. The sample was pressed into pellets under 1000 pounds of pressure. A pelletized sample with mass 0.9935 g was placed into the calorimeter. The calorimeter was evacuated of air under a dynamic vacuum for 1.5 hours, reaching a final pressure of 5×10^{-4} torr, backfilled with 20 torr of helium exchange gas at 296 K, and finally sealed. After the calorimeteric experiments were completed, the sample was found to have lost -0.0124 g. We postulate that this represents a loss of adsorbed water, presumably during the evacuation step. The sample began to gain mass over time with exposure to air, and this has been attributed to rehydration. The sample was allowed to completely rehydrate over the next several days (until the mass no longer increased) reaching a final mass of 0.9992 g. The calorimeter was resealed by purging with a dynamic flow of helium gas for 1.5 hours and then sealed under 632 torr of helium (the current barometric pressure at the time of sealing). Additionally, due to the mass changes, the stoichiometric ratio of the water content on the akaganéite is different than that reported above; thus, the new molecular formulas contain 0.551 and 0.652 moles of water per FeOOH unit for the partially dehydrated and rehydrated samples, respectively.

5.3 Results and Discussion

The measured specific heat results are given in tables 5.1 and 5.2 for the β-FeOOH·0.551H_2O and β-FeOOH·0.652H_2O samples respectively; they are displayed graphically in figure 5.3. As expected, the β-FeOOH·0.652H_2O species has a higher specific heat than the less hydrated sample owing to the additional water on the surface. It is important to note that below 20 K the specific heat of the β-FeOOH·0.652H_2O sample appears to drop rather sharply; however, this glass-like transition is not the actual behavior of the specific heat but rather an artifact of helium adsorption and desorption on the surface of the akaganéite particles. This behavior of the helium exchange gas has been observed in zeolites, where there is a large surface area for the helium adsorption.[9] Its presence in the β-FeOOH·0.652H_2O specific heat (rather than in both samples) is due to the greatly increased quantity of helium exchange gas (632 torr) used to seal the calorimeter.

We have fit the specific heat data for both species of akaganéite using several sets of polynomial equations to obtain smooth representations of the specific heat. At the low-temperature end of the specific heat, below 30, the smoothed function of the specific heat was determined using a Debye extrapolation (plotting C/T vs. T^2) resulting in a function in the form of $C = \gamma T + \beta_3 T^3$, where the $\beta_3 T^3$ term approximates the lattice and the low-temperature magnetic contribution. The γT term in this instance does not represent an electronic contribution, since β-FeOOH is an insulator, rather it reflects an amount of inherent disorder in the β-FeOOH system. This type of behavior has been reported before in systems with small particle sizes, large surface areas, and in glasses.[10, 11] The high-temperature (above 30 K) specific heat data was fit with orthogonal polynomial functions of the type $C = A_0 + A_1 T + A_2 T^2 + \cdots + A_n T^n$.

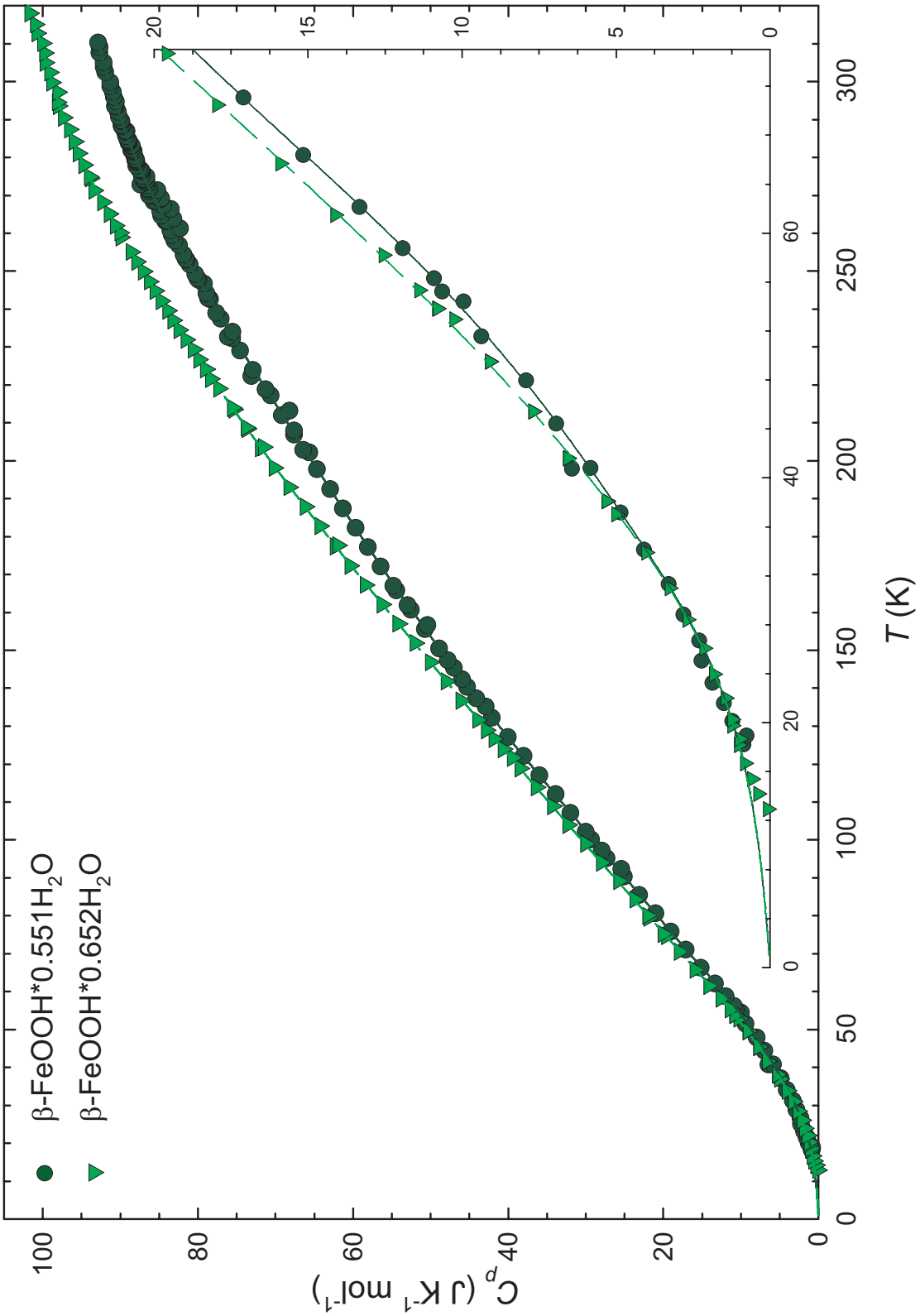

Figure 5.3. The specific heat experimental results of β-FeOOH from 12 to 320 K; the polynomial fits of the specific heat are shown as smoothed lines. The inset presents an expanded view of measurements of the two β-FeOOH samples below 50 K.

Additionally, we have calculated the configurational entropy for the chloride ions that reside in the tunnels according to procedures outlined by Ulbrich and Waldbaum[12] on the basis of crystallographic data obtained by Post and Buchwald.[5] The resulting expression for the conformational entropy, S_{CE}, of the chloride ions is:

$$S_{CE} = -R\frac{Y_i}{Z}\left[X_{oc}\ln X_{oc} + X_{vac}\ln X_{vac}\right] \tag{5.2}$$

where Z is the number of molecules per unit cell, Y_i is the multiplicity of the Cl^- site, X_{oc} is the mole fraction of the chloride ions occupying all the possible sites, and X_{vac} is the mole fraction of vacant sites.[12] From crystal structure data, there are 8 Fe^{3+} ions per unit cell and there is a two-fold multiplicity at the Cl^- site.[5, 13] The resulting conformational entropy is 0.3385 $J{\cdot}K^{-1}{\cdot}mol^{-1}$per mole of FeOOH. Interestingly, using statistical mechanics to model the chloride ions in the tunnels as a one dimensional gas, gives the same result as equation 5.2 above.

From the smoothed fits and the configurational entropy for the Cl^- ions, thermodynamic functions for the two akaganéite species were generated and are presented in tables 5.3 and 5.4. Our results yield values for $\Delta_0^{298.15}S_m^\circ$ of 80.28 $\pm$0.20 $J{\cdot}K^{-1}{\cdot}mol^{-1}$ and 85.67 $\pm$0.021 $J{\cdot}K^{-1}{\cdot}mol^{-1}$ for the β-FeOOH$\cdot$0.551H_2O and β-FeOOH$\cdot$0.652H_2O samples, respectively. The third law entropies at 298.15 K neglecting the configurational entropy of the chloride ions for the respective compounds are 79.94 $\pm$0.20 $J{\cdot}K^{-1}{\cdot}mol^{-1}$ and 85.33 $\pm$0.021 $J{\cdot}K^{-1}{\cdot}mol^{-1}$.

Table 5.1. Experimental molar specific heat, $C^{\circ}_{p,m}$, of β-FeOOH·0.551H_2O corrected for curvature. (M = 98.7757 g·mol^{-1}.)

T / K	$C^{\circ}_{p,m}$ / J·K^{-1}·mol^{-1}	ΔT / K	T / K	$C^{c}irc_{p,m}$ / J·K^{-1}·mol^{-1}	ΔT / K
18.221	0.8662	0.367	142.38	45.967	5.071
18.946	0.7646	1.036	145.46	47.009	5.080
20.138	1.2267	1.395	147.46	47.788	5.084
21.603	1.4970	1.588	150.54	48.905	5.085
23.257	1.8641	1.720	155.63	50.701	5.094
25.079	2.2261	1.875	160.73	52.537	5.098
26.713	2.2966	1.955	161.90	52.982	5.085
28.829	2.8103	2.377	165.83	54.420	5.103
31.324	3.2874	2.715	166.99	54.789	5.115
34.132	4.0930	2.914	172.10	56.461	5.119
37.187	4.8505	3.186	177.22	58.075	5.129
40.832	5.8251	3.740	182.35	59.671	5.128
44.444	6.9408	3.503	187.48	61.292	5.133
47.978	7.9174	3.615	192.61	62.954	5.131
51.581	9.3750	3.614	197.73	64.638	5.131
54.434	9.9454	1.810	202.87	66.392	5.139
55.239	10.652	3.711	206.93	67.603	5.142
56.315	10.908	1.984	208.01	67.619	5.148
58.766	11.925	2.922	212.06	69.149	5.148
62.130	13.331	3.805	217.20	70.638	5.153
66.383	15.156	4.695	218.90	71.291	4.908
71.093	17.096	4.710	223.92	72.946	5.135
75.839	19.034	4.766	229.06	74.528	5.145
80.637	21.014	4.805	232.36	75.584	5.108
85.464	23.086	4.841	234.02	75.538	4.759
90.339	25.084	4.884	237.49	77.053	5.150
95.236	27.316	4.899	237.80	76.994	5.148
97.264	27.927	4.903	238.96	77.623	5.132
100.17	29.313	4.941	242.64	78.451	5.153
102.19	29.996	4.951	242.95	78.680	5.145
107.16	31.946	4.979	244.11	78.870	5.151
112.14	33.904	5.001	247.79	79.911	5.152
117.15	35.942	5.013	248.10	80.072	5.145
122.17	37.980	5.030	249.26	80.321	5.153
127.21	40.057	5.041	251.73	81.024	5.155
132.25	42.112	5.049	252.95	81.449	5.151

Continued on next page

$\frac{T}{\mathrm{K}}$	$\frac{C^{\circ}_{p,m}}{\mathrm{J{\cdot}K^{-1}{\cdot}mol^{-1}}}$	$\frac{\Delta T}{\mathrm{K}}$	$\frac{T}{\mathrm{K}}$	$\frac{C^{c}irc_{p,m}}{\mathrm{J{\cdot}K^{-1}{\cdot}mol^{-1}}}$	$\frac{\Delta T}{\mathrm{K}}$
137.31	44.085	5.062	253.25	81.567	5.145
140.39	45.248	5.052	254.41	81.818	5.152
256.88	82.450	5.160	281.48	88.394	2.595
258.10	83.000	5.148	281.72	88.267	2.597
259.57	83.340	5.152	281.96	88.574	2.589
260.74	83.529	2.589	282.11	88.466	2.595
263.25	84.188	5.157	282.97	88.505	2.591
263.33	83.978	2.601	283.17	88.515	5.254
264.73	84.702	5.155	283.91	88.946	5.168
265.92	84.889	2.596	284.07	88.919	2.591
268.41	85.699	5.155	284.36	88.928	2.682
268.51	85.444	2.593	284.56	88.919	2.593
269.89	85.798	5.158	284.71	89.068	2.592
270.02	86.312	2.566	285.56	89.236	2.590
271.10	86.308	2.592	286.67	89.383	2.593
271.59	86.269	2.622	286.96	89.205	2.517
271.75	86.490	2.572	287.15	89.407	2.590
272.60	86.687	2.586	288.16	89.769	2.588
273.57	86.754	5.164	288.38	89.858	5.171
273.70	86.750	2.598	289.52	89.873	2.588
273.95	86.668	2.578	289.75	89.904	2.591
274.20	87.024	2.575	290.75	90.189	2.586
274.33	87.055	2.592	292.11	90.276	2.592
275.04	86.625	5.168	293.35	90.595	2.588
275.19	87.224	2.588	293.56	90.672	5.173
276.29	87.225	2.594	294.70	90.583	2.590
276.53	87.282	2.593	295.95	90.842	2.585
276.79	87.356	2.584	297.30	90.948	2.592
276.92	87.582	2.593	298.74	91.304	5.169
277.78	87.944	2.586	299.89	91.274	2.589
278.74	87.942	5.164	302.49	91.953	2.590
278.88	87.912	2.592	303.92	92.108	5.163
279.13	87.911	2.596	305.08	92.166	2.592
279.38	88.054	2.586	307.68	92.701	2.587
279.52	88.014	2.596	309.10	92.657	5.164
280.38	88.173	2.590	310.27	92.887	2.594

Table 5.2. Experimental molar specific heats, $C^{\circ}_{p,m}$, of β-FeOOH·0.652H_2O corrected for curvature. (M = 100.5981 g·mol^{-1}.)

T / K	$C^{\circ}_{p,m}$ / J·K^{-1}·mol^{-1}	ΔT / K	T / K	$C^{\circ}_{p,m}$ / J·K^{-1}·mol^{-1}	ΔT / K
12.943	0.08044	1.275	118.88	38.504	5.018
14.182	0.38540	1.178	121.68	39.445	4.898
15.377	0.59225	1.153	123.91	40.647	5.032
16.677	0.82699	1.390	126.64	41.865	5.036
18.186	1.0214	1.579	128.94	42.844	5.042
18.653	0.99247	1.719	131.68	43.946	5.060
19.753	1.2260	1.639	136.73	46.091	5.072
20.237	1.2251	1.705	141.80	48.029	5.086
22.000	1.4518	1.998	146.87	50.027	5.092
23.959	1.8242	1.974	151.96	52.033	5.098
26.073	2.1388	2.303	157.04	54.204	5.101
28.418	2.6957	2.378	162.14	56.286	5.107
30.988	3.2659	2.752	167.23	58.436	5.112
33.880	4.0250	3.028	172.34	60.401	5.121
37.004	4.9934	3.205	177.45	62.348	5.125
38.102	5.3061	3.427	177.72	62.011	5.031
41.609	6.5769	3.564	182.79	64.307	5.116
45.405	7.6957	3.997	187.91	66.211	5.126
49.521	9.1000	4.221	193.03	68.304	5.122
52.946	10.251	1.870	198.16	70.224	5.131
53.853	10.804	4.447	203.29	71.997	5.134
55.329	11.395	2.879	203.63	71.605	5.144
58.196	12.555	2.856	208.41	73.652	5.134
61.470	14.123	3.678	208.76	73.805	5.116
65.711	15.907	4.810	213.55	75.357	5.145
70.472	17.958	4.708	213.89	75.600	5.142
74.673	19.586	4.744	219.03	77.330	5.140
75.209	20.027	4.761	221.58	78.405	5.131
79.439	21.886	4.798	224.17	79.030	5.143
79.998	22.046	4.810	226.71	79.925	5.152
84.270	23.634	4.863	229.32	80.604	5.139
89.134	25.782	4.880	231.86	81.518	5.148
94.027	27.992	4.914	234.46	82.452	5.140
98.953	30.061	4.943	237.01	83.249	5.142
103.91	32.292	4.962	239.60	83.927	5.147
108.88	34.313	4.987	242.16	84.751	5.147

Continued on next page

$\frac{T}{\mathrm{K}}$	$\frac{C^{\circ}_{p,m}}{\mathrm{J{\cdot}K^{-1}{\cdot}mol^{-1}}}$	$\frac{\Delta T}{\mathrm{K}}$	$\frac{T}{\mathrm{K}}$	$\frac{C^{\circ}_{p,m}}{\mathrm{J{\cdot}K^{-1}{\cdot}mol^{-1}}}$	$\frac{\Delta T}{\mathrm{K}}$
113.87	36.389	5.003	244.75	85.543	5.149
247.31	86.257	5.150	287.33	96.612	3.100
249.90	87.056	5.150	290.44	97.376	3.106
252.47	87.938	5.143	293.56	97.998	3.105
255.06	88.602	5.148	294.57	98.143	2.572
258.91	89.946	3.080	297.16	98.086	2.598
260.21	90.096	5.150	299.76	98.867	2.591
262.01	90.698	3.105	302.36	99.122	2.588
265.11	91.435	3.108	304.94	99.722	2.591
268.21	92.291	3.110	307.54	99.818	2.602
271.32	93.412	3.107	310.13	100.05	2.585
274.44	93.888	3.111	312.73	100.76	2.600
274.88	94.029	3.117	315.09	100.95	2.081
277.99	94.713	3.115	317.99	101.69	3.705
281.10	95.459	3.109	321.15	102.17	2.583
284.22	95.959	3.110			

5.3.1 Magnetic properties

Noticeably absent from the specific heat data are any features associated with the antiferromagnetic transition, nominally reported at 290 K based on magnetic susceptibility measurements. However, this is not unusual since the small particle size of the akaganéite crystals tends to inhibit long range magnetic ordering, resulting in the magnetic transition occurring over a wide range of thermal energies. This is reflected in the specific heat, where the magnetic transition is spread out over a large temperature range, instead of being a sharp, well defined peak. On closer examination of the specific heat of the β-FeOOH·0.652H_2O sample, there is an inflection in the specific heat near 310 K that is most likely attributed to the onset of the magnetic ordering. Using the first derivatives of the fits to determine changes in the slope of the specific heat, the Néel temperature is estimated to be between 290 and 295 K. This correlates well with the work of Chambaere and De Grave who determined that for akaganéite samples with 0.25 to 0.5 moles of water per FeOOH, the Néel temperature should be between 295 K and 297 K.[6]

Because the transition is spread over a large temperature range, it is impossible to separate the magnetic specific heat from the lattice. However, statistical mechanics provides a way to estimate the theoretical entropy for the magnetic transition. For all of the iron oxides and oxyhydroxides, the crystal field splitting for Fe^{3+} ions in an octahedral co-ordination should split the d-orbitals into a high-spin configuration.[1] Thus, the total spin for the 5 Fe^{3+} electrons will be $\frac{5}{2}$. From this spin configuration, the entropy change for the magnetic transition should be $R\ln 6$ ($R\ln(2\cdot\frac{5}{2} + 1)$) or 14.897 $J\cdot K^{-1}\cdot mol^{-1}$, but this assumes complete ordering of all the Fe^{3+} electrons, which is clearly not the case. At present, the magnetic specific heat and entropy does not add much to the understanding of the akaganéite system. The effects of particle size wash

Table 5.3. Standard molar thermodynamic properties of β-FeOOH·0.551H_2O with the configurational entropy of Cl^-. $\Phi = \Delta_0^T S_m^o - \Delta_0^T H_m^o/T$(M = 98.7757 g·mol^{-1} and p^o=101.325 kPa.)

T / K	$C_{p,m}^o$ / J·K^{-1}·mol^{-1}	$\Delta_0^T S_m^o$ / J·K^{-1}·mol^{-1}	$\Delta_0^T H_m^o/T$ / J·K^{-1}·mol^{-1}	Φ_m^o / J·K^{-1}·mol^{-1}
0	0	0.3385	0	0.3385
5	0.1655	0.4985	0.0807	0.4178
10	0.3820	0.6752	0.1740	0.5013
15	0.7081	0.8870	0.2937	0.5933
20	1.212	1.155	0.4559	0.6988
25	1.962	1.501	0.6775	0.8231
30	2.998	1.945	0.9739	0.9715
35	4.270	2.501	1.352	1.149
40	5.628	3.159	1.801	1.358
45	7.073	3.904	2.305	1.599
50	8.659	4.730	2.860	1.870
60	12.39	6.627	4.127	2.500
70	16.65	8.855	5.609	3.245
80	20.81	11.35	7.250	4.100
90	24.93	14.04	8.986	5.053
100	29.05	16.88	10.79	6.092
110	33.16	19.84	12.63	7.207
120	37.22	22.90	14.51	8.386
130	41.19	26.04	16.41	9.623
140	45.03	29.23	18.32	10.91
150	48.73	32.46	20.23	12.24
160	52.28	35.72	22.12	13.60
170	55.69	39.00	23.99	15.00
180	58.99	42.27	25.85	16.43
190	62.20	45.55	27.68	17.87
200	65.36	48.82	29.48	19.34
210	68.49	52.08	31.26	20.82
220	71.60	55.34	33.03	22.31
230	74.69	58.59	34.77	23.82
240	77.72	61.84	36.50	25.34
250	80.64	65.07	38.21	26.86
260	83.39	68.28	39.89	28.39
270	85.90	71.48	41.55	29.93
273.15	86.63	72.48	42.07	30.42
280	88.11	74.64	43.17	31.47
290	89.97	77.77	44.76	33.01
298.15	91.24	80.28	46.01	34.27
300	91.50	80.85	46.29	34.56

Table 5.4. Standard molar thermodynamic properties of β-FeOOH·0.652H_2O with the configurational entropy of Cl^-. $\Phi = \Delta_0^T S_m^o - \Delta_0^T H_m^o/T$(M = 100.5981 g·mol^{-1} and p^o=101.325 kPa.)

T / K	$C_{p,m}^o$ / J · K^{-1} · mol^{-1}	$\Delta_0^T S_m^o$ / J · K^{-1} · mol^{-1}	$\Delta_0^T H_m^o/T$ / J · K^{-1} · mol^{-1}	Φ_m^o / J · K^{-1} · mol^{-1}
0	0	0.3385	0	0.3385
5	0.1653	0.4976	0.08033	0.4172
10	0.3866	0.6753	0.1746	0.5007
15	0.7197	0.8903	0.2969	0.5934
20	1.221	1.161	0.4612	0.7002
25	1.985	1.510	0.6846	0.8258
30	3.034	1.961	0.9848	0.9759
35	4.349	2.524	1.369	1.155
40	5.882	3.203	1.835	1.368
45	7.577	3.992	2.378	1.614
50	9.387	4.883	2.987	1.896
60	13.38	6.942	4.381	2.560
70	17.64	9.322	5.969	3.353
80	21.98	11.96	7.699	4.262
90	26.30	14.80	9.526	5.273
100	30.58	17.79	11.42	6.373
110	34.81	20.91	13.35	7.553
120	38.99	24.11	15.32	8.798
130	43.15	27.40	17.30	10.10
140	47.27	30.75	19.29	11.46
150	51.36	34.15	21.29	12.86
160	55.40	37.59	23.30	14.29
170	59.38	41.07	25.30	15.77
180	63.26	44.58	27.31	17.27
190	67.05	48.10	29.30	18.80
200	70.71	51.63	31.28	20.35
210	74.24	55.17	33.24	21.93
220	77.65	58.70	35.18	23.52
230	80.93	62.22	37.10	25.12
240	84.10	65.73	38.99	26.74
250	87.16	69.23	40.86	28.37
260	90.08	72.71	42.70	30.01
270	92.81	76.16	44.50	31.66
273.15	93.61	77.24	45.06	32.18
280	95.23	79.58	46.27	33.31
290	97.22	82.96	48.00	34.96
298.15	98.55	85.67	49.36	36.31
300	98.83	86.28	49.66	36.62

out the magnetic transitions and most probably leads to incomplete ordering. The molar entropy at 298.15 K of β-FeOOH would be significantly larger than reported here if full ordering had taken place.

5.3.2 Thermodynamic functions

To determine the thermodynamic properties of bare β-FeOOH, the role of hydration must be considered. The specific heat of the adsorbed (surface) water on β-FeOOH (per mole) can be found by taking the difference of the specific heats of the two hydrated species of β-FeOOH (giving C_p for 0.101 moles of water) and dividing by the molar difference of water between the two samples (0.101 moles). The specific heat curve of the adsorbed water is given in figure 5.4. At temperatures below 150 K, the specific heat of the adsorbed water behaves like bulk ice (there is a bit of a low temperature abberation to this trend most likely caused by propagation of errors between the fits of the two β-FeOOH hydration species). Above 150 K the specific heat begins to rise more steeply than bulk ice up to 273 K, where the specific heat of the adsorbed water is approximately equal to that of liquid water. This behavior is strikingly similar to the behavior of adsorbed water on nano-surfaces of anatase and rutile (polymorphs of TiO_2; see figure 5.4), which suggests that loosely bound water on the surfaces of nano-scale particles could have the same energetics regardless of the substrate material.[14] Water on the surfaces of these nano-particles (or on materials with large surface areas) has been referred to as "nano-water". The specific heat of the "nano-water" on anatase, rutile, and akaganéite could be used to model the adsorbed water on other surfaces.

From the β-FeOOH$\cdot$0.551H_2O sample, we can subtract the water specific heat contribution using different hydration models to calculate the entropy and other thermo-

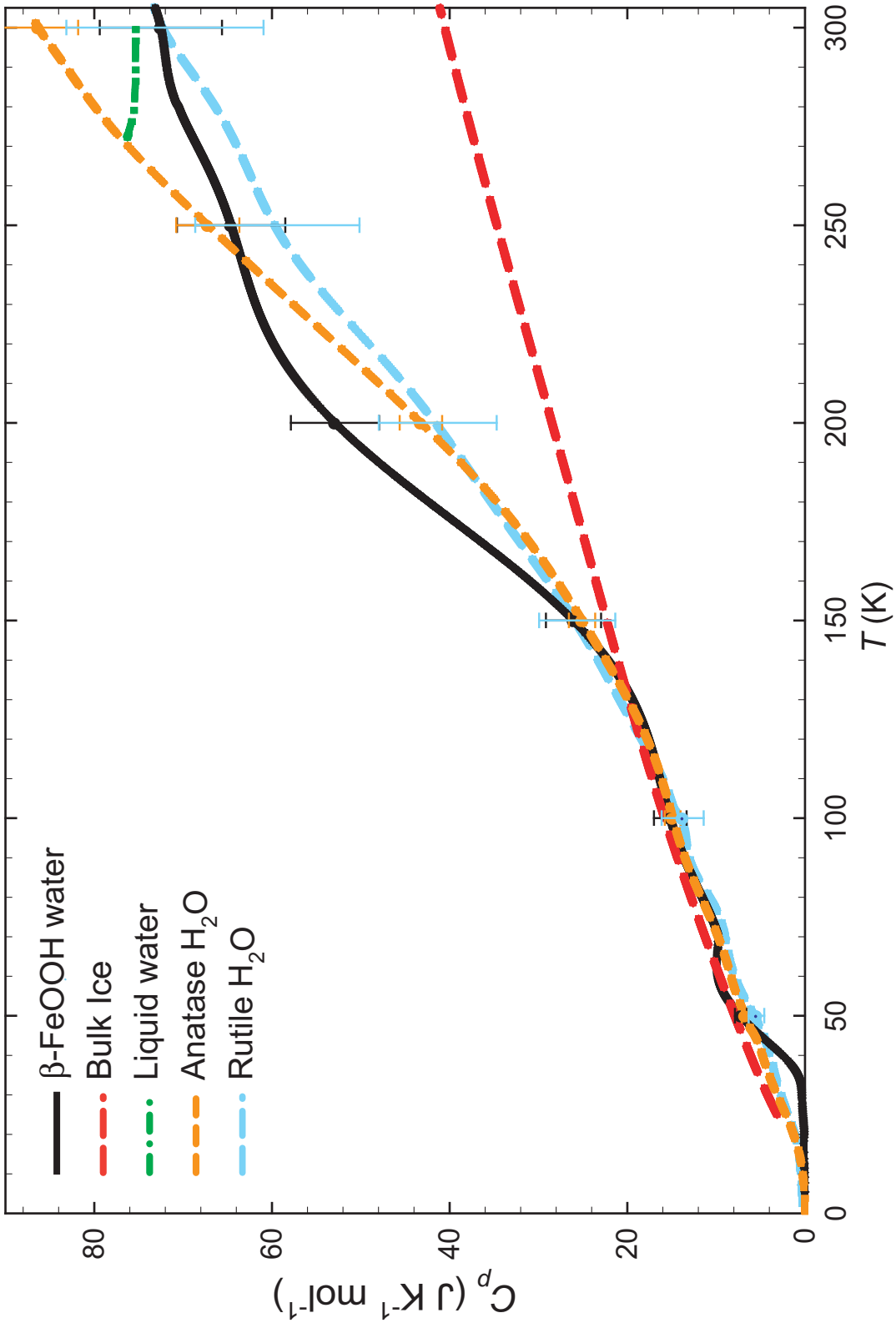

Figure 5.4. The molar specific heat of water adsorbed on β-FeOOH compared to the specific heats of water adsorbed on nanoparticles of anatase and rutile (TiO_2 polymorphs) along with bulk ice and water.

dynamic properties for bare β-FeOOH. However, it is not known how to best model the 0.551 moles of water bound to the β-FeOOH, since it is assumed that at least half of this water resides inside the channels of the akaganéite particles, rather than on the surface. This tunnel water could be viewed as bulk ice or could behave like the surface water as above. Most likely, the water can be viewed as intermediary between these two models, and thus applying both of these models will give upper and lower bounds to the thermodynamic functions. The specific heats of 0.551 moles of both bulk ice and "nano-water" were subtracted separately from the smoothed specific heat curve of β-FeOOH·0.551H_2O to determine the specific heat for bare β-FeOOH. In turn, these new values for the specific heat were used to generate thermodynamic functions for β-FeOOH and do not include the Cl^- conformational entropy. No additional corrections have been made for the chloride ions since it is not known how to model the chloride vibrational specific heat, and the mole fraction of the chloride ions is so small that the vibrational entropy contribution is much less than the overall uncertainty (including the water corrections).

The thermodynamic properties based on the subtractions of bulk ice and "nano-water" are listed in tables 5.5 and 5.6, respectively. At 298.15 K, the molar entropy for bare β-FeOOH is between 48.241 J·K^{-1}·mol^{-1} and 57.036 J·K^{-1}·mol^{-1}(for "nano-water" and bulk ice subtracted β-FeOOH, respectively; or the averaged value gives $\Delta_0^{298.15}S_m^\circ$ as 52.6 ±4.4 J·K^{-1}·mol^{-1}). Using this value for the entropy, and the enthalpy of formation, $\Delta_f^{298.15}H_m^\circ$, of –554.7 kJ·mol^{-1} obtained from Mazeina *et al.* for bare β-FeOOH, the Gibbs free energy of formation, $\Delta_f^{298.15}G_m^\circ$ for β-FeOOH is –481.7±1.3 kJ·mol^{-1} (an averaged Gibbs free energy from $\Delta_f^{298.15}G_m^\circ$ = –480.4 kJ·mol^{-1} based on the "nano-water" entropy, and $\Delta_f^{298.15}G_m^\circ$ = –483.0 kJ·mol^{-1} based on the bulk ice entropy).[8, 15]

Armed with this new value for the free energy of formation, we can re-examine

Table 5.5. Standard molar thermodynamic properties of bare β-FeOOH based on the corrections from β-FeOOH·0.551H_2O using bulk ice to model the water. $\Phi = \Delta_0^T S_m^o - \Delta_0^T H_m^o/T$(M = 88.8535 g·mol^{-1} and p^o=101.325 kPa.)

T	$C_{p,m}^o$	$\Delta_0^T S_m^o$	$\Delta_0^T H_m^o/T$	Φ_m^o
K	J · K^{-1} · mol^{-1}	J · K^{-1} · mol^{-1}	J · K^{-1} · mol^{-1}	J · K^{-1} · mol^{-1}
5	0.15247	0.14008	0.07749	0.06411
10	0.23017	0.27722	0.13989	0.13790
15	0.17650	0.36393	0.16382	0.20031
20	0.10940	0.40349	0.15676	0.24680
25	0.23414	0.43633	0.15531	0.28111
30	0.67452	0.51299	0.20069	0.31249
35	1.3982	0.66890	0.31793	0.35126
40	2.2439	0.90971	0.50486	0.40521
45	3.1988	1.2279	0.75000	0.47828
50	4.3071	1.6207	1.0489	0.57228
60	7.1045	2.6415	1.8143	0.82763
70	10.459	3.9852	2.8067	1.1791
80	13.738	5.5964	3.9687	1.6282
90	17.019	7.4035	5.2361	2.1680
100	20.340	9.3682	6.5801	2.7886
110	23.683	11.464	7.9829	3.4811
120	27.008	13.667	9.4301	4.2374
130	30.266	15.958	10.908	5.0504
140	33.416	18.317	12.404	5.9134
150	36.432	20.726	13.906	6.8204
160	39.303	23.170	15.405	7.7657
170	42.039	25.635	16.891	8.7443
180	44.658	28.113	18.362	9.7515
190	47.192	30.596	19.813	10.783
200	49.669	33.079	21.244	11.836
210	52.114	35.562	22.656	12.907
220	54.538	38.042	24.050	13.993
230	56.936	40.520	25.428	15.092
240	59.281	42.993	26.790	16.203
250	61.527	45.459	28.135	17.324
260	63.610	47.913	29.460	18.454
270	65.462	50.349	30.760	19.590
273.15	65.986	51.112	31.163	19.949
280	67.018	52.759	32.028	20.732
290	68.244	55.133	33.256	21.877
298.15	69.010	57.036	34.224	22.812
300	69.159	57.463	34.439	23.024
310	69.876	59.743	35.570	24.172

Table 5.6. Standard molar thermodynamic properties of bare β-FeOOH based on the corrections from β-FeOOH·0.551H_2O using surface "nano-water" to model the water. $\Phi = \Delta_0^T S_m^o - \Delta_0^T H_m^o/T$(M = 88.8535 g·mol^{-1} and p^o=101.325 kPa.)

T / K	$C_{p,m}^o$ / J · K^{-1} · mol^{-1}	$\Delta_0^T S_m^o$ / J · K^{-1} · mol^{-1}	$\Delta_0^T H_m^o/T$ / J · K^{-1} · mol^{-1}	Φ_m^o / J · K^{-1} · mol^{-1}
5	0.15247	0.14008	0.07749	0.06411
10	0.23017	0.27722	0.13989	0.13790
15	0.17650	0.36393	0.16382	0.20031
20	0.10940	0.40349	0.15676	0.24680
25	0.23414	0.43633	0.15531	0.28111
30	0.67452	0.51299	0.20069	0.31249
35	1.3982	0.66890	0.31793	0.35126
40	2.2439	0.90971	0.50486	0.40521
45	3.1988	1.2279	0.75000	0.47828
50	4.3071	1.6207	1.0489	0.57228
60	7.1045	2.6415	1.8143	0.82763
70	10.459	3.9852	2.8067	1.1791
80	13.738	5.5964	3.9687	1.6282
90	17.019	7.4035	5.2361	2.1680
100	20.340	9.3682	6.5801	2.7886
110	23.683	11.464	7.9829	3.4811
120	27.008	13.667	9.4301	4.2374
130	30.266	15.958	10.908	5.0504
140	32.808	18.304	12.391	5.9132
150	34.374	20.625	13.808	6.8169
160	35.235	22.874	15.124	7.7507
170	35.572	25.023	16.319	8.7040
180	35.652	27.059	17.391	9.6677
190	35.775	28.989	18.355	10.634
200	36.212	30.833	19.235	11.598
210	37.149	32.620	20.063	12.557
220	38.649	34.381	20.872	13.509
230	40.626	36.141	21.687	14.455
240	42.861	37.917	22.522	15.395
250	45.047	39.712	23.380	16.332
260	46.883	41.516	24.250	17.266
270	48.218	43.312	25.114	18.197
273.15	48.549	43.873	25.383	18.490
280	49.256	45.084	25.958	19.126
290	50.391	46.830	26.779	20.051
298.15	51.382	48.241	27.439	20.803
300	51.556	48.560	27.587	20.973
310	51.976	50.259	28.369	21.890

the thermodynamic favorability of the akaganéite decomposition reactions:

$$\beta\text{–FeOOH}_{(s)} \longrightarrow \alpha\text{–FeOOH}_{(s)} \tag{5.3}$$

and

$$\beta\text{–FeOOH}_{(s)} \longrightarrow \tfrac{1}{2}\,\alpha\text{–Fe}_2\text{O}_{3\,(s)} + \tfrac{1}{2}\text{H}_2\text{O}_{(l)}\,. \tag{5.4}$$

Published data for the free energy of formation of the product species in the above reactions yields the free energy of reactions 5.3 and 5.4 at 298 K as –6.7 kJ·mol^{-1}and –9.1 kJ·mol^{-1}, respectively (based on the average free energy of formation of akaganéite).[8, 16] These results confirm the observation that akaganéite is thermodynamically less stable with respect to hematite and goethite. Additionally, we have used the thermodynamic functions for α-FeOOH [16], α-Fe_2O_3 [17], and water [8, 18, 19] to establish the free energy of these reactions at selected temperatures (using both the bulk ice and "nano-water" models). These are given in tables 5.7a and 5.7b for reactions 5.3 and 5.4, respectively. As demonstrated in the tables, these reactions are favorable over all temperatures listed (regardless of the model used in the bare β-FeOOH calculations), and these reactions are both favorable with respect to changes in enthalpy and entropy. It should be noted that the free energy for the decomposition of akaganéite to hematite is greater than the decomposition to goethite, which agrees with the observation that hematite is the most stable of these compounds. The data in table 5.7 shows that these reactions become more favorable at higher temperatures, and this is what is observed by experiment.[1][20] Additionally, with increasing temperature, the entropy change for the reactions become larger, implying that these reactions are entropically driven. However, these reactions are not observed at lower temperatures, where they are thermodynamically favorable, which suggests that kinetics is a strong driving factor in the decomposition of akaganéite.

A final reaction to examine is the decomposition of akaganéite with bound water,

Table 5.7. Thermodynamic values for the decomposition reaction of β-FeOOH to a) α-FeOOH and b) α-Fe_2O_3 at selected temperatures from thermodynamic functions of bare β-FeOOH calculated from subtractions of both bulk ice and "nano-water".

a) β-$FeOOH_{(s)} \longrightarrow \alpha FeOOH_{(s)}$

	Bulk ice			"Nano-water"		
T / K	$\Delta_R^T S_m^\circ$ / $JK^{-1}mol^{-1}$	$\Delta_R^T H_m^\circ$ / $kJmol^{-1}$	$\Delta_R^T G_m^\circ$ / $kJmol^{-1}$	$\Delta_R^T S_m^\circ$ / $JK^{-1}mol^{-1}$	$\Delta_R^T H_m^\circ$ / $kJmol^{-1}$	$\Delta_R^T G_m^\circ$ / $kJmol^{-1}$
100	0.212	−5.117	−5.138	0.212	−7.140	−7.161
200	1.301	−4.945	−5.205	3.547	−6.566	−7.275
273.15	2.288	−4.708	−5.333	9.527	−5.152	−7.755
298.15	2.654	−4.600	−5.391	11.45	−4.600	−8.013
300	2.687	−4.472	−5.278	11.59	−4.565	−8.042

b) β-$FeOOH_{(s)} \longrightarrow \frac{1}{2}\alpha$-$Fe_2O_{3\,(s)} + \frac{1}{2}H_2O_{(l)}$

	Bulk ice			"Nano-water"		
T / K	$\Delta_R^T S_m^\circ$ / $JK^{-1}mol^{-1}$	$\Delta_R^T H_m^\circ$ / $kJmol^{-1}$	$\Delta_R^T G_m^\circ$ / $kJmol^{-1}$	$\Delta_R^T S_m^\circ$ / $JK^{-1}mol^{-1}$	$\Delta_R^T H_m^\circ$ / $kJmol^{-1}$	$\Delta_R^T G_m^\circ$ / $kJmol^{-1}$
100[a]	4.431	−5.340	−5.783	4.431	−7.362	−7.805
200[a]	6.521	−5.041	−6.345	8.768	−6.662	−8.416
273.15	19.84	−1.831	−7.251	27.08	−2.275	−9.672
298.15	21.64	−1.315	−7.767	30.43	−1.315	−10.39
300	21.77	−1.277	−7.807	30.67	−1.244	−10.45

[a]At this temperature, water is solid and the values listed are for this state.

since it is the hydrated species that one observes in nature and in the lab. From above, we have the molar entropy for β-FeOOH·0.551H_2O, and what is needed is the enthalpy of formation for this particular species, which can be found from Mazeina *et al.* as $\Delta_f^{298.15}H^\circ_{m,n} = -554.7 - 271 \cdot n$ kJ·mol^{-1}, where n is the moles of tightly bound (tunnel) water per mol of FeOOH.[15] However, for this particular sample, only 0.25 to 0.5 moles of water are thought to be tightly bound, and the remaining water is loosely adsorbed on the particles; therefore, this water must be accounted for separately. The enthalpy of hydration ($\Delta_{ads}^{298}H^\circ_m$ for weakly bound water) for akaganéite has been determined by Mazeina *et al.* as –15 kJ·mol^{-1}; thus, with this information, the overall enthalpy of formation for any akaganéite hydration species may be described in terms of the following reactions:

$$\mathrm{Fe_{(s)}} + (1+\tfrac{n}{2})\mathrm{O_{2(g)}} + (\tfrac{1}{2}+n)\mathrm{H_{2(g)}} \longrightarrow \beta\text{–FeOOH}\cdot n\mathrm{H_2O_{(s)}} \qquad \Delta_f^{298}H^\circ_{m,n} \quad (5.5)$$

$$\beta\text{–FeOOH}\cdot n\mathrm{H_2O_{(s)}} + x\mathrm{H_2O_{(}}_{l)} \longrightarrow \beta\text{–FeOOH}\cdot (n+x)\mathrm{H_2O_{(s)}} \quad \Delta_{ads}^{298}H^\circ_{m,x} \quad (5.6)$$

$$\mathrm{H_{2(g)}} + \tfrac{1}{2}\mathrm{O_{2(g)}} \longrightarrow \mathrm{H_2O_{(}}_{l)} \qquad \Delta_f^{298}H^\circ_{\mathrm{H_2O}} \quad (5.7)$$

where x is the moles of loosely bound water and the total enthalpy of formation can be found as:

$$\Delta_f^{298}H^\circ_{m,\beta\mathrm{FeOOH}\cdot(n+x)\mathrm{H_2O}} = \Delta_f^{298}H^\circ_{m,n} + x\left[\Delta_{ads}^{298}H_{m,x} + \Delta_f^{298}H^\circ_{\mathrm{H_2O}}\right] . \qquad (5.8)$$

Thus, the resultant enthalpy of formation for β-FeOOH·0.551H_2O is between –713.0 kJ·mol^{-1} and –705.5 kJ·mol^{-1}from equation 5.8 assuming 0.25 and 0.50 moles of tunnel water, respectively; and, the Gibbs free energy of formation of this species is between –609.8 kJ·mol^{-1} and –602.3 kJ·mol^{-1}. From these thermodynamic quantities, it is easy to calculate the Gibbs free energy at the standard reference temperature for the decomposition of β-FeOOH·0.551H_2O. Thus, for the decomposition to goethite:

$$\beta\text{–FeOOH}\cdot 0.551\mathrm{H_20_{(s)}} \longrightarrow \alpha\text{–FeOOH}_{(s)} + 0.551\mathrm{H_2O_{(}}_{l)} , \qquad (5.9)$$

Table 5.8. Thermodynamic values for the decomposition of hydrated akaganéite (β-FeOOH·0.551H_2O) at 298.15 K. The reported values for $\Delta_R^{298.15}H_m^\circ$ and $\Delta_R^{298.15}G_m^\circ$ give the upper and lower bounds assuming 0.25 and 0.25 moles of tunnel water per mol of FeOOH.

Product	$\frac{\Delta_R^T S_m^\circ}{\mathrm{JK^{-1}mol^{-1}}}$	$\frac{\Delta_R^T H_m^\circ}{\mathrm{kJmol^{-1}}}$	$\frac{\Delta_R^T G_m^\circ}{\mathrm{kJmol^{-1}}}$
Goethite	19.13	-3.8 to -11.3	-9.5 to -16.9
Hematite	37.33	-0.4 to -7.8	-11.6 to -19.1

the free energy of reaction, $\Delta_R^{298.15}G_m^\circ$, is between -9.5 kJ·mol^{-1} and -16.9 kJ·mol^{-1}. Likewise, for the decomposition to hematite:

$$\beta\text{–FeOOH} \cdot 0.551H_20_{(s)} \longrightarrow \tfrac{1}{2}\,\alpha\text{–}Fe_2O_{3\,(s)} + \left(\tfrac{1}{2} + 0.551\right) H_2O_{(l)}\,, \tag{5.10}$$

the free energy of reaction, $\Delta_R^{298.15}G_m^\circ$, is between –11.6 kJ·mol^{-1} and –19.1 kJ·mol^{-1}. All of the thermodynamic values for these reactions are listed in table 5.8. Again, the decomposition to hematite has a larger Gibbs free energy of reaction, consistent with hematite being the most stable of the three iron oxide species. For both of these reactions, the decomposition of the hydrated species is more favorable than for bare β-FeOOH, implying that water decreases the stability with respect to the theoretical dry compound, and it appears that entropy drives these reactions since there is a marked increase in Δ_RS for the decomposition of hydrated akaganéite over the dry species.

.

5.4 Conclusions

We have determined the molar entropy of bare β-FeOOH, $\Delta_0^{298.15} S_m^\circ = 53.8 \pm 3.3$ $\mathrm{J{\cdot}K^{-1}{\cdot}mol^{-1}}$, based on subtractions of the estimated contribution of water from the hydrated species. The entropy and Gibb's free energy of reactions have been reported for bare β-FeOOH in keeping with the convention for publishing this data; however, it may be more appropriate to report all of the thermodynamic functions with regard to the water residing in the tunnels. Not only does the water itself contribute to the specific heat and the entropy, but the hydration level effects the magnetic transition temperature, and the reported values of the thermodynamic functions at 298.15 K may be greatly effected with respect to the Néel temperature of an individual sample. Thus it would be useful to study the specific heat of akaganéite over a wide range of hydrated species (tunnel water). From this, we may also be able to establish the thermodynamic functions for a theoretical bulk crystal of akaganéite, since this mineral has not been found or synthesized as crystals much larger than the ones we have presently measured.

We have also shown that the previous value for the free energy of formation is inaccurate by several hundred kilo-Joules. In an attempt to resolve the source of the error in this value, we have calculated the entropy difference needed to bring the values for the new and old Gibbs free energies into agreement. Assuming the enthalpy of formation from Mazeina *et al.*is correct, the entropy difference for the Gibbs free energy of formation for both the bare and hydrates species are approximately 100R

References

[1] Cornell, R. M.; Schwertmann, U., *The Iron Oxides: Structure, Properties, Reactions, Occurrence and Uses*, New York: VCH publishers, **1996**.

[2] Morris, R. V.; Klingelhöfer, G.; Bernhardt, B.; Schröder, C.; Rodionov, D. S.; de Souza, P. A. J.; Yen, A.; Gellert, R.; Evlanov, E. N.; Foh, J.; Kankeleit, E.; Gütlich, P.; Ming, D. W.; Renz, F.; Wdowiak, T.; Squyres, S. W.; Arvidson, R. E., *Science* **2004**, *305*, 833–836.

[3] González-Calbet, J. M.; Alario-Franco, M. A.; Gayoso-Andrade, M., *J. Inorg. Nucl. Chem.* **1981**, *43*, 257–264.

[4] García, K. E.; Morales, A. L.; Barrero, C. A.; Arroyave, C. E.; Greneche, J. M., *Physica B* **2004**, *354*, 187–190.

[5] Post, J. E.; Buchwald, V. F., *Am. Mineral* **1991**, *76*, 272–277.

[6] Chambaere, D.; De Grave, E., *J. Magn. Magn. Mater.* **1984**, *42*, 263–268.

[7] Murray, J. W., in R. G. Burns, ed., *Reviews in Mineralogy: Marine Minerals*, Mineralogical Society of America, vol. 6, 1979 pp. 47–98.

[8] Robie, R. A.; Hemingway, B. S., Thermodynamic properties of minerals and related substances at 298.15 k and 1 bar (10^5 pascals) pressure and at higher temperatures, U.S. Geological Survey Bulletin 2131, **1995**.

[9] Boerio-Goates, J.; Stevens, R.; Hom, B. K.; Woodfield, B. F.; Piccione, P. M.; Davis, M. E.; Navrotsky, A., *J. Chem. Thermodyn.* **2002**, *34*, 205–227.

[10] Boerio-Goates, J.; Stevens, R.; Lang, B. E.; Woodfield, B. F., *J. Thermal. Anal.* **2002**, *69*, 773–783.

[11] Phillips, W. A., *Rep. Prog. Phys.* **1987**, *50*, 1657–1708.

[12] Ulbrich, H. H.; Waldbaum, D. R., *Geochim. Cosmochim. Acta* **1976**, *40*, 1–24.

[13] Hahn, T., ed.

[14] Boerio-Goates, J.; Stevens, R.; Lang, B. E.; Woodfield, B. F., Specific heat mesurments of various polymorphs of TiO_2, in preparation for Nano Letters.

[15] Mazeina, L.; Deore, S.; Navrotsky, A., *J. Phys. Chem.* **submitted**.

[16] Majzlan, J.; Lang, B. E.; Stevens, R.; Navrotsky, A.; Woodfeild, B. F.; Boerio-Goates, J., *Am. Mineral.* **2003**, *88*, 846–854.

[17] Grønvold, F.; Westrum, E. F., *J. Amer. Chem. Soc.* **1958**, *81*, 1780–1783.

[18] Osborne, N. S.; Stimson, H. F.; Ginnings, D. C., *J. Res. Nat. Bur. Stand.* **1938**, *23*, 197–260.

[19] Garvin, D.; Parker, V. B.; White, H. J. J., *CODATA Thermodynamic Tables: Selections for Some Compounds of Calcium and Related Mixtures*, New York: Hemisphere Publishing Co, **1987**.

[20] Chambaere, D. G.; De Grave, E., *Phys Chem Minerals* **1985**, *12*, 176–184.

Chapter 6

α-Uranium

6.1 Introduction

The material properties of α-uranium have been studied quite extensively since the time of the Manhattan Project because of its potential use in weapons and as fuel in nuclear reactors.[1] However, one of the difficulties in using uranium as a fuel source was that the samples exhibited anisotropic thermal expansion. Initially, it was thought that the anisotropy was merely a product of sample purity, but when the anisotropy was determined to be an intrinsic property of α-uranium, and because of other difficulties during irradiation, research into the metal's use in reactors was quickly abandoned.[1] Yet, it is this anisotropic thermal expansion and its subsequent contribution on the specific heat that is of interest in this paper.

The results of most previous specific heat studies of α-uranium have been inconsistent from study to study, which may be at least partially attributed to the system's inherent anisotropy. For instance, although α-uranium has a known superconducting transition below 0.6 K,[2] many early investigations into the origin of superconductiv-

ity found a wide variation in the transition and onset temperatures which could not be readily correlated with sample purity alone.[1] A second physical property exhibiting inconsistencies is the presence of several phase transitions at low temperatures. The first of these is at 43 K where there is a change in the lattice parameters and the unit cell volume has a distinct minimum.[3] Further investigations of elastic moduli and magnetic susceptibility yielded two additional phase transitions at 37 K and 20 K.[4, 5] These transitions, which have been designated as the α_1, α_2 and α_3 transitions respectively, are well understood and are attributed to a succession of charge density waves(CDW).[1, 6, 7] Interestingly, these transitions were not observed in the early specific heat measurements of α-uranium until samples were prepared that had large grain sizes or were 'pseudo' single crystals (polycrystals with grains oriented in roughly one general direction).[1, 8, 9, 10, 11] (The only phase transition known before this time was the α-β transition at 941 K, where space group of the crystal changes from the orthorhombic α phase to the tetragonal β phase.)

Finally, calculation of the Debye temperature (a measure of the stiffness of the lattice) by several investigators have given inconsistent results. The zero Kelvin Debye temperature extrapolated from elastic moduli on a single crystal is 250 $\pm$ 2 K. Yet, Debye temperatures extracted from specific heat measurements made on polycrystals varied greatly from sample to sample and were around 210 K.[1, 11, 12, 13, 14] It was only recently that specific heat measurements on a true single crystal of α-uranium at low temperatures gave a Debye temperature of 265 K that was in agreement with elastic moduli results.[7]

The variabilities in specific heat measurements are attributed in part to the suppression of the CDW in the polycrystalline samples, and the internal elastic strains at the grain boundaries cause by anisotropic expansion.[15] In such materials, changes in temperature will generate differing degrees of expansion along each side of a grain

boundary owing to the random orientation of the crystal grains in a sample. In turn, this will create elastic strains at the grain boundaries that will give rise to an excess energy for the system.[15, 16] This microstrain energy, $E_{\mu str}$, can be related to an excess specific heat, $C_{p,\mu str}$, by the relation $C_{p,\mu str} \propto \partial E_{\mu str}/\partial T$.[15] Thus the specific heat of the polycrystal, $C_{p,poly}$, can be expressed as $C_{p,poly} = C_{p,single} C_{p,\mu str}$, or rather the sum of the specific heats of the single crystal and the associated microstrain.

For most elements and metallic alloys, there are no observed differences in the specific heats from single and polycrystal samples. This is due in large part to the high structural symmetry of these materials that leads to isotropic thermal expansion and thus no microstrain effects.[15, 16] Any differences in the specific heats of polycrystal and single crystal samples would be attributed only to phonon scattering at the grain boundaries and would be regarded as a negligible contribution, well within experimental error. Thus in most cases it is generally accepted that there is no difference in specific heats between single and polycrystalline samples. However, it has been demonstrated that for a polycrystalline sample of an anisotropic material, thermal expansion anisotropies will generate internal elastic strains at the grain boundaries, thus causing an increase in the internal energy of the system.[15, 16] This energy change results in a microstructural (or microstrain) contribution to the specific heat. Thus, owing to its orthorhombic structure and highly anisotropic thermal expansion, α-uranium is expected to have a significant microstructural specific heat.

This has been measured using power compensated differential scanning calorimetry (DSC); however, there is some question as to the magnitude and form of the microstructural specific heat since DSC is not an equilibrium measurement and the apparent heat flow into the sample may not reflect the true thermodynamics of the system.[16, 17] In addition, DSC measurements are typically accurate to only a few percent and have a precision of about the same order as well.

Recently, we have obtained high-purity single crystals of α-uranium that are strain free and of a higher quality than earlier samples. In addition, crystals from the same batch as the single crystal were remelted to form a polycrystalline sample. In this work we will show the differences between the specific heats of single and polycrystalline samples of α-uranium using two high-accuracy, high-precision calorimeters. From this we will be able to show the microstructural specific heat over an extended temperature range and develop a thermodynamic model for the microstrain contribution cause by thermal expansion. Furthermore, we will be able to calculate the thermodynamic functions of polycrystalline α-uranium at the standard state and use the microstrain model to predict the values for the single crystal.

6.2 Experimental

The uranium single crystals were formed from electro-transport in a molten LiCl-KCl eutectic electrolyte containing UCl_3 at approximately 3 wt. percent.[18, 19] Single crystal uranium was deposited on a stainless steel cathode; the crystals had the shape of parallelogram shaped platelets. Since the uranium was deposited below the α-β transition temperature, the crystals are strain free. Thin cylindrical samples were prepared by spark-erosion cutting, cleaning in concentrated HNO_3 and electropolishing in H_3PO_4. The purity of the crystals is quite high since none of the UCl_3 impurities interferes with the electrotransport of uranium in the LiCl-KCl system.[18] Analysis of the crystal using Proton Induced X-ray Emission Spectroscopy (PIXE) found that the sample had fewer than a dozen metallic impurities, all of which were on the order of a few parts per million.

The polycrystal sample of uranium was cast from an induction melting of the uranium single crystal dendrites, as described above, in a BeO crucible under an

inert atmosphere. The sample was only melted once to minimize the possibility of contamination from the crucible or the carrier gas.[16] Then it was cut into cubes of approximately 4 mm on a side. Within a cube, the individual crystals were found to have a grain size ranging from 20 to 30 microns. All samples were stored under a dry argon environment and exposure to the atmosphere was kept at a minimum to avoid the formation of UO_2 on the surface.

The low-temperature specific heats of the single and polycrystal α-uranium were measured using a semi-adiabatic pulse technique from 0.5 K up to 100 K with several experiments performed using an isothermal technique from 10 K to 100 K. The apparatus is described in section 2.2 and additional details of the current and similar apparatuses can be found elsewhere.[19, 20] The accuracy of this apparatus over its working temperature range, when checked with high purity single-crystal copper, was found to be generally 0.25 % with a precision generally better than 0.1 %.

For the single-crystal measurements, two single crystals of uranium with a total mass of 0.3945 g were thermally attached to the sample platform using Apiezon N grease. Similarly, for the polycrystalline sample, two cubes of the polycrystal uranium, with a combined mass of 1.438 g, were mounted on the sample platform with Apiezon N grease. After the measurements, the specific heats of the empty platform and the Apiezon N grease were subtracted and the molar specific heats were calculated for the respective samples.

High-temperature specific heats of the polycrystalline sample, from 50 K to 400 K, were measured in an adiabatic calorimeter, the details of which can be found in section 1 and elsewhere.[21] The accuracy of the adiabatic apparatus is generally better than $\pm 0.1\%$ above 20 K, with a resolution of better than $\pm 0.1\%$ from 20 K to 400 K. A sample of 25.224 g of the polycrystals were loaded into the calorimeter, and sealed under a small amount of He gas to facilitate thermal exchange in the system.

As with the semi-adiabatic apparatus, the molar specific heat of the polycrystal was found by correcting for the calorimeter, the He exchange gas, and Apiezon T grease.

The agreement of the measurements made between 50 K and 110 K with the two calorimeters is within experimental uncertainty, however there was a consistent offset between the two measurements. Although small, the offset is attributed to temperature scale error and the difference in the measurement methods. To correct for this discrepancy, it was first assumed that the data from the adiabatic apparatus was the more correct since its accuracy is the higher of the two instruments. It was then assumed that all differences between the two instruments would be of the same magnitude for any high thermally conductive material. From this, the polycrystal data from the semi-adiabatic instrument was scaled multiplicatively to match that of the adiabatic instrument. The same scaling treatment was then applied to the single-crystal data for continuity. As a check to the validity of the analysis, an identical treatment was made for the specific heats of single and polycrystalline samples of copper run on the same apparatus. There was good agreement between these two measurements, which will be shown below.

6.3 Results

The measured specific heat for single crystal and polycrystalline α-uranium is given in tables 6.4 and 6.2 respectively, and also displayed in figure 6.1. In the transition regions, several repeat series were measured in order to obtain the best representation of the specific heat. (It should be noted that in one series of the single crystal data, the sample was cooled too quickly through the α_3 transition region and the transition was suppressed on heating.) Examination of the specific heat results shows two observations of note. The first is that the specific heat of the polycrystal

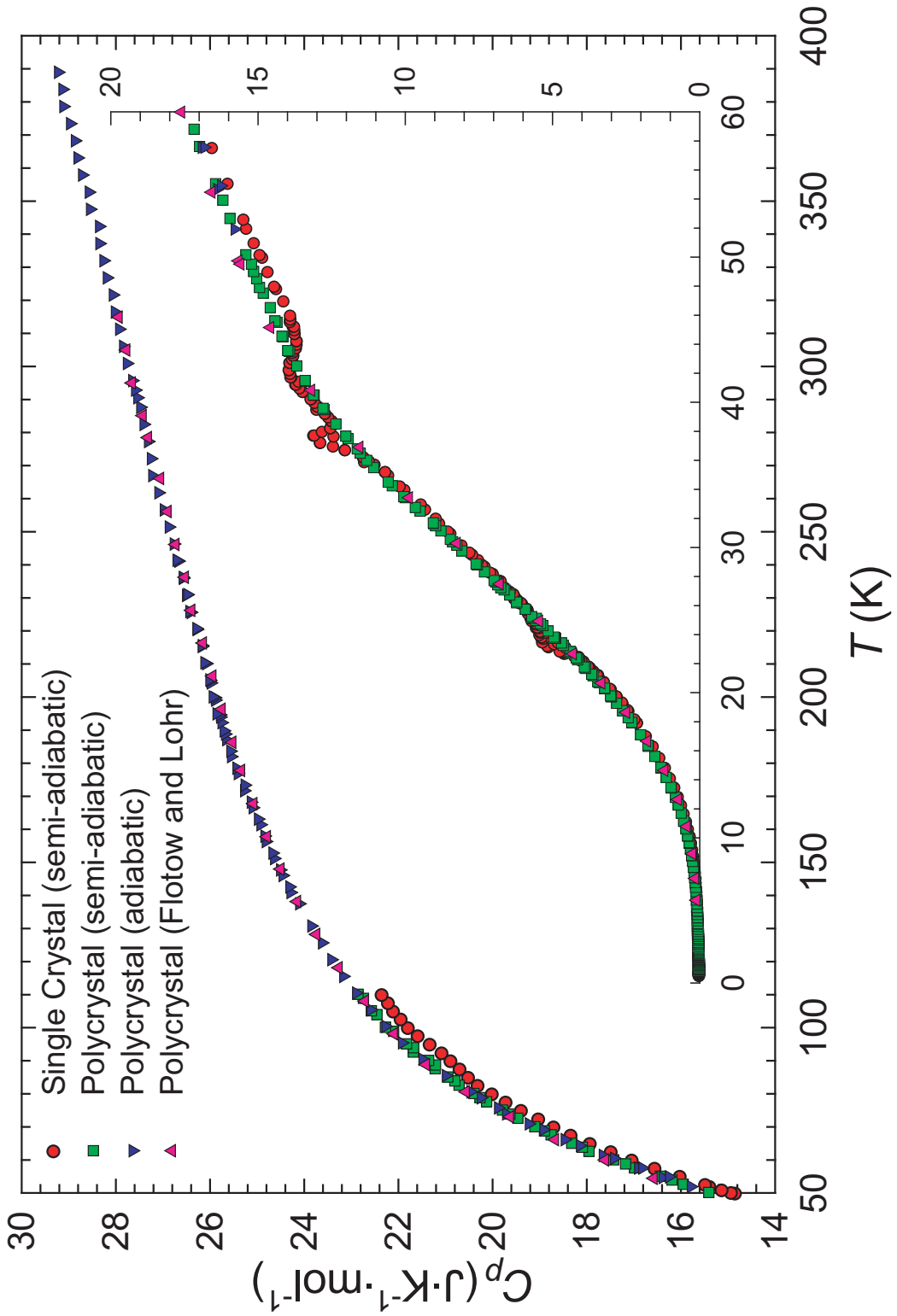

Figure 6.1. The experimental specific heat of α-uranium to 400 K showing the single crystal and polycrystalline data as run on the adiabatic and semi-adiabatic instruments from this work along with the published data of Flotow and Lohr.[9] Inset: Specific heat of α-uranium below 50 K.

is generally higher than that of the single crystal, and secondly, that the three transitions present in the single crystal are either absent or significantly broadened in the polycrystal. Indeed, the transition at 20 K is completely absent in the polycrystal while the transitions at 37 and 43 K have been dispersed into a very broad excess specific heat. The latter phenomenon is well documented and is attributed to the suppression of charge density waves in the polycrystal.[1, 7, 10, 11] However, the systematic variance in the specific heats between the polycrystal and the single crystal is a relatively recent observation that has been attributed to the microstrain.[16] It should be noted that the results of the polycrystalline sample reported here compare well with previous measurements of the specific heat of polycrystalline samples made by Jones, Gordon and Long[8] and Flotow and Lohr.[9] The overall agreement of the current data for the polycrystalline α-uranium and literature values is shown in figure 6.2 and demonstrates that the specific heat of the current study is a good average of the published values.

6.4 Discussion

An analysis of the specific heat results of both the single and polycrystal provides a unique opportunity to better understand the effects of microstrain on the electronic and lattice properties of α-uranium. We will do this by first comparing the specific heat data of the single and polycrystalline samples in the low-temperature limit, and second, exploring these differences at higher temperatures above the CDW transitions. Then we will explore the electronic contribution to the specific heat above 50 K by calculating the lattice contribution using phonon density of states data. Lastly, we will discuss the fitting of the specific heat data and subsequent calculation of thermodynamic data.

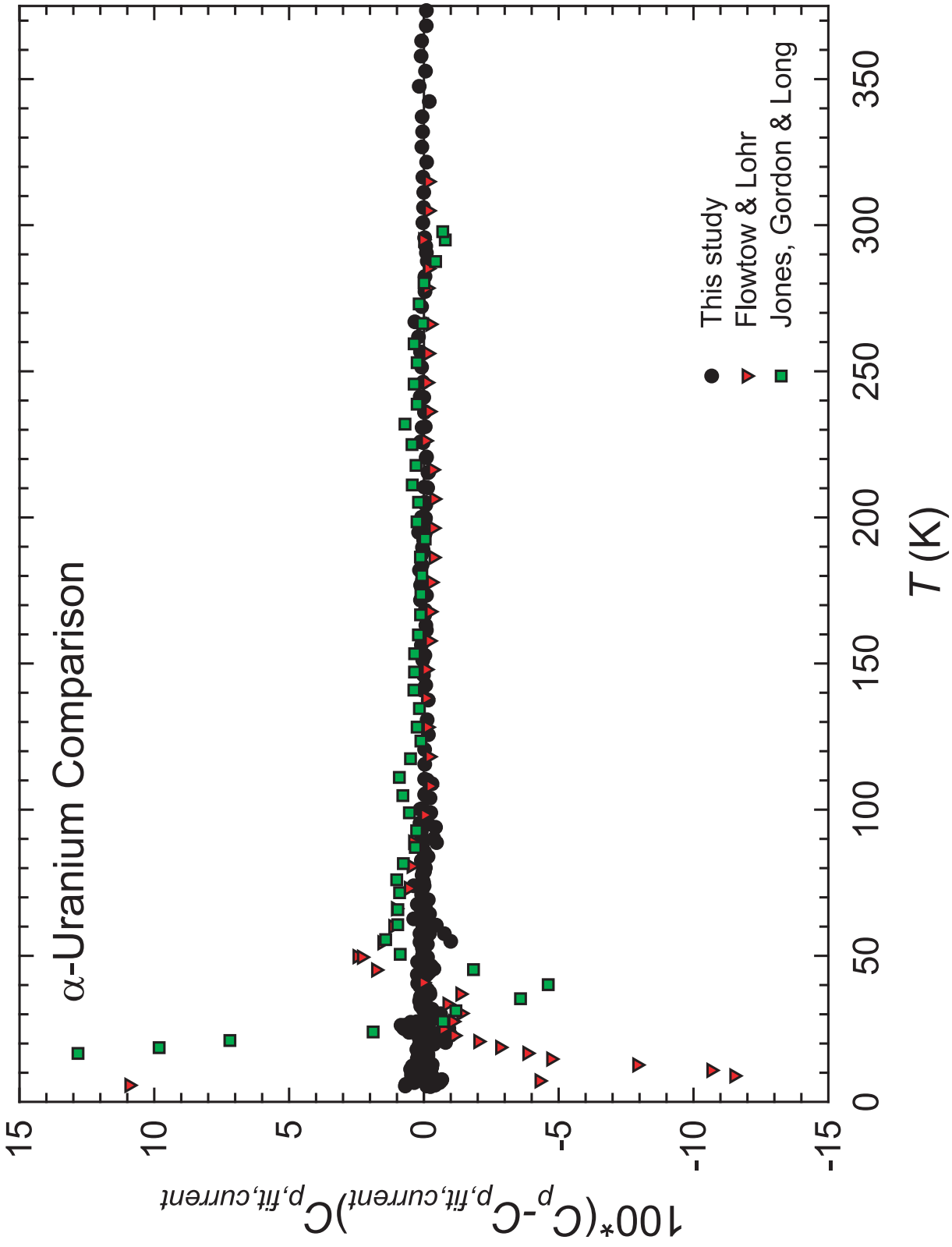

Figure 6.2. The specific heat of polycrystalline α-uranium from this study, Flowtow and Lohr[9], and Jones, Gordon, and Long[8] as compared to the fit of α-uranium from the current study.

Table 6.1. Experimental molar specific heat, $C^0_{p,m}$, of single crystal α-uranium corrected for curvature. The ^{235}U hyperfine contribution has been subtracted from points below 2 K. (M = 238.029 g·mol^{-1}.)

$\frac{T}{\mathrm{K}}$	$\frac{C_{p,m}}{\mathrm{J{\cdot}K^{-1}{\cdot}mol^{-1}}}$	$\frac{T}{\mathrm{K}}$	$\frac{C_{p,m}}{\mathrm{J{\cdot}K^{-1}{\cdot}mol^{-1}}}$	$\frac{T}{\mathrm{K}}$	$\frac{C_{p,m}}{\mathrm{J{\cdot}K^{-1}{\cdot}mol^{-1}}}$
Series 1		8.3796	0.18075	0.54011	0.0054816
1.7307	0.016275	9.2149	0.23917	0.57382	0.0054753
1.9025	0.018177	10.133	0.32267	0.63125	0.0059535
2.0924	0.020175			0.69509	0.0065112
2.3024	0.022475	Series 3		0.76373	0.0071530
2.5334	0.025030	0.72644	0.0067512		
2.7888	0.027985	0.79868	0.0074670	Series 6	
3.0714	0.031358	0.88075	0.0082010	8.7157	0.20522
3.3794	0.035268	0.96918	0.0090073	9.6771	0.28050
3.7155	0.039870	1.0651	0.0099483	10.636	0.38115
4.0892	0.045314	1.1701	0.010966	11.697	0.52513
4.5012	0.051642	1.286	0.012016	12.859	0.72320
4.9523	0.059779	1.414	0.013187	14.136	0.99113
5.4477	0.069729	1.5534	0.014590	15.546	1.3529
5.9929	0.082670	1.7081	0.016168	17.036	1.8070
6.5937	0.099661	1.8802	0.017970	18.805	2.4423
7.2544	0.12380	2.069	0.019965	20.725	3.2308
7.9781	0.15776			22.714	4.5791
8.7765	0.20660	Series 4		24.976	5.6842
9.6718	0.27762	0.69554	0.0064225	27.455	6.6976
		0.76419	0.0071233	30.179	8.0659
Series 2		0.84039	0.0079006		
1.8172	0.017250	0.92445	0.0086209	Series 7	
1.9980	0.019188	1.0162	0.0094561	9.2132	0.23951
2.1981	0.021299	1.1164	0.010439	10.151	0.32479
2.4188	0.023727	1.2274	0.011468	11.163	0.44508
2.6614	0.026515	1.3492	0.012616	12.281	0.61630
2.9288	0.029585	1.4836	0.013877	13.499	0.84515
3.2250	0.033283	1.6319	0.015407	14.86	1.1632
3.5496	0.037550	1.7956	0.017109	16.33	1.5753
3.9031	0.042578	1.9756	0.018992	17.954	2.1133
4.2958	0.048453			19.738	2.7993
4.7244	0.055535	Series 5		21.699	3.7208
5.1971	0.064538	0.54384	0.0049426	23.855	5.3476
5.7200	0.075960	0.60075	0.0056794	26.227	6.1190
6.2936	0.090788	0.66081	0.0061510	28.838	7.3727
6.9234	0.11108	0.72684	0.0068051	31.699	8.8269
7.6148	0.13969	0.79986	0.0074951		

Continued on next page

T / K	$C_{p,m}$ / J·K^{-1}·mol^{-1}	T / K	$C_{p,m}$ / J·K^{-1}·mol^{-1}	T / K	$C_{p,m}$ / J·K^{-1}·mol^{-1}
Series 8		22.180	3.9210	24.533	5.4887
17.959	2.1104	22.511	4.0885	26.992	6.4245
18.850	2.4331	22.842	4.3200	29.686	7.7994
19.790	2.8137	23.173	4.5382	32.657	9.3077
20.773	3.2319	23.504	4.7997	35.922	11.372
21.807	3.7394	23.836	5.0392	39.526	12.994
22.883	4.7300	24.167	5.2142	43.449	13.806
24.023	5.4203	24.498	5.4273	47.840	14.318
25.228	5.7213	24.832	5.5470	52.623	15.473
26.453	6.1802	25.165	5.6810	57.556	16.547
27.793	6.8388	25.495	5.7864	62.540	17.476
29.171	7.5068	25.825	5.8624	67.536	18.330
		26.155	6.0135	72.462	19.014
Series 9		26.487	6.2374	77.571	19.711
18.201	2.1965	26.818	6.3077	82.633	20.302
18.774	2.4018	27.151	6.5390	87.565	20.685
19.274	2.6006			92.452	21.069
19.771	2.8042	Series 11		97.605	21.575
20.271	2.9953	21.188	3.4306	102.67	21.936
20.77	3.2351	21.517	3.5977	107.58	22.207
21.254	3.4305	21.848	3.7826		
21.764	3.7097	22.179	3.9551	Series 13	
22.27	3.9996	22.512	4.2284	19.372	2.6209
22.754	4.5087	22.842	4.6584	21.267	3.4540
23.251	5.1530	23.171	5.1126	23.387	4.9253
23.752	5.2915	23.506	5.3237	25.730	5.8762
24.251	5.3849	23.838	5.3670	28.307	7.0934
24.746	5.5222	24.167	5.3895	31.135	8.5280
25.248	5.6815	24.502	5.5346	34.251	10.162
25.745	5.8225	24.834	5.5806	37.682	12.410
26.24	6.0533	25.164	5.7199	41.460	13.595
26.735	6.2790	25.495	5.8070	45.569	13.876
27.233	6.5818	25.825	5.8894	50.179	14.922
27.73	6.7386	26.157	6.0337	55.093	16.011
28.225	7.0090	26.486	6.2705	60.040	17.031
28.721	7.2855	26.817	6.3080	65.042	17.922
		27.150	6.5687	70.051	18.693
Series 10				75.059	19.383
21.188	3.4325	Series 12		80.058	20.001
21.517	3.5921	20.317	3.0309	85.063	20.505
21.849	3.7687	22.302	4.0749	90.071	20.878

Continued on next page

$\frac{T}{\mathrm{K}}$	$\frac{C_{p,m}}{\mathrm{J{\cdot}K^{-1}{\cdot}mol^{-1}}}$	$\frac{T}{\mathrm{K}}$	$\frac{C_{p,m}}{\mathrm{J{\cdot}K^{-1}{\cdot}mol^{-1}}}$	$\frac{T}{\mathrm{K}}$	$\frac{C_{p,m}}{\mathrm{J{\cdot}K^{-1}{\cdot}mol^{-1}}}$
95.075	21.320	Series 15		Series 16	
100.08	21.785	35.234	10.658	35.233	10.662
105.08	22.098	35.740	11.021	35.737	11.039
110.09	22.341	36.248	11.400	36.247	11.409
		36.750	12.022	36.749	12.030
Series 14		37.247	12.861	37.245	12.874
29.538	7.7051	37.751	13.068	37.750	13.096
30.992	8.4465	38.255	12.519	38.254	12.519
32.024	8.9447	38.755	12.477	38.752	12.500
33.005	9.4526	39.256	12.708	39.253	12.705
34.003	10.006	39.756	12.967	39.754	12.946
35.003	10.558	40.252	13.176	40.255	13.188
36.002	11.215	40.754	13.456	40.759	13.464
36.999	12.428	41.253	13.710	41.260	13.686
38.004	12.806	41.755	13.847	41.759	13.871
39.007	12.596	42.256	13.928	42.261	13.926
40.003	13.057	42.757	13.907	42.763	13.898
41.003	13.569	43.264	13.783	43.261	13.780
42.003	13.889	43.760	13.693	43.759	13.688
43.004	13.818	44.253	13.658	44.259	13.666
44.004	13.664	44.750	13.726	44.756	13.727
45.003	13.731	45.246	13.780	45.251	13.738
46.003	13.868	45.743	13.860	45.747	13.866
46.994	14.084				
48.002	14.432				
49.010	14.653				
50.002	14.837				
51.002	15.122				
52.000	15.380				

[a] Series 10 lists the data for the suppressed α_3 transition.

Table 6.2. Experimental molar specific heat results, $C^{\circ}_{p,m}$, of polycrystalline α-uranium corrected for curvature and variance between the apparatuses. The ^{235}U hyperfine contribution has been subtracted from points below 2 K. (M = 238.029 g·mol^{-1}.)

T / K	$C_{p,m}$ / J·K^{-1}·mol^{-1}	T / K	$C_{p,m}$ / J·K^{-1}·mol^{-1}	T / K	$C_{p,m}$ / J·K^{-1}·mol^{-1}
Series 1		7.6175	0.18832	19.732	2.9989
1.7283	0.018892	8.3754	0.24026	21.691	3.8825
1.9016	0.021161	9.2143	0.31068	23.788	4.9242
2.0939	0.023620	10.135	0.40915	26.212	6.2214
2.3046	0.026497			28.859	7.5922
2.5293	0.029782	Series 3		31.690	9.0452
2.7810	0.033536	0.87541	0.0089146		
3.0577	0.037901	0.96704	0.0099409	Series 6	
3.3655	0.043226	1.0612	0.010901	8.7853	0.27441
3.7013	0.049855	1.168	0.012131	9.6728	0.35669
4.0642	0.057685	1.286	0.013446	10.643	0.47214
4.4894	0.067488	1.4139	0.015051	11.701	0.62792
4.9546	0.079194	1.5546	0.016752	12.780	0.82402
5.4503	0.093512	1.7091	0.018664	14.164	1.1363
5.9914	0.11174	1.8812	0.020858	15.612	1.5257
6.5867	0.13529	2.0728	0.023603	17.098	2.0062
7.2420	0.16706			18.734	2.6053
7.9647	0.21084	Series 4		20.676	3.4155
8.7579	0.27052	0.8444	0.0085305	22.771	4.3981
9.6417	0.35339	0.9257	0.0095014	24.971	5.5571
10.612	0.46772	1.0113	0.010405	27.432	6.8558
		1.1133	0.011450	30.162	8.2447
Series 2		1.2300	0.012856		
1.8148	0.020139	1.3494	0.014301	Series 7	
1.9916	0.022551	1.4833	0.015904	21.174	3.6239
2.1908	0.025149	1.6306	0.017612	23.420	4.6961
2.4195	0.028336	1.7978	0.019892	25.741	5.9321
2.6663	0.032085	1.9756	0.022224	28.316	7.3114
2.9352	0.036516			31.135	8.7864
3.2251	0.041606	Series 5		34.244	10.440
3.5481	0.047432	9.224	0.31207	37.668	12.019
3.9021	0.054172	10.146	0.41074	41.447	13.404
4.2961	0.062847	11.161	0.54546	45.6	14.428
4.7261	0.073156	12.277	0.72961	50.166	15.408
5.1988	0.085812	13.431	0.96329	55.052	16.438
5.7275	0.10223	14.855	1.3154	60.05	17.430
6.2979	0.12375	16.370	1.7587	65.047	18.318

Continued on next page

T / K	$C_{p,m}$ / J·K^{-1}·mol^{-1}	T / K	$C_{p,m}$ / J·K^{-1}·mol^{-1}	T / K	$C_{p,m}$ / J·K^{-1}·mol^{-1}
6.9220	0.15121	17.945	2.3045	70.058	19.102
75.070	19.791	4.5001	0.067932	18.768	2.6172
80.081	20.397	4.9512	0.079601	19.270	2.8246
85.073	20.949	5.4456	0.094113	19.769	3.0272
90.090	21.359	5.9901	0.11271	20.268	3.2265
95.085	21.828	6.5922	0.13680	20.766	3.4608
100.10	22.275	7.2523	0.16946	21.264	3.6687
105.10	22.574	7.9770	0.21333	21.762	3.9179
110.12	22.856	8.7743	0.27350	22.260	4.1454
		9.6531	0.35554	22.757	4.3864
Series 8		10.618	0.46974	23.254	4.6337
20.312	3.2316			23.750	4.8939
22.384	4.1857	Series 10		24.248	5.1473
24.620	5.3270	0.88271	0.0089748	24.746	5.4060
27.072	6.6453	0.96814	0.0098627	25.243	5.7042
29.766	8.0810	1.0646	0.010919	25.749	5.9216
32.751	9.6580	1.1707	0.012100	26.235	6.2218
35.998	11.313	1.2874	0.013489	26.721	6.4526
39.579	12.792	1.4224	0.014919	27.227	6.7590
43.551	13.988	1.5615	0.016793	27.725	6.9807
47.901	14.946	1.7111	0.018701		
52.648	15.953	1.8826	0.020933	Series 13	
57.611	16.984	2.0717	0.023510	30.559	8.4686
62.600	17.950			31.491	8.9659
67.592	18.758	Series 11		32.497	9.4971
72.585	19.464	9.2064	0.31227	33.497	10.048
77.604	20.125	10.136	0.41035	34.496	10.58
82.603	20.712	11.144	0.54549	35.495	11.073
87.586	21.216	12.259	0.72983	36.494	11.531
92.621	21.680	13.480	0.97615	37.497	11.941
		14.825	1.3092	38.498	12.356
Series 9		16.304	1.7438	39.495	12.757
1.7361	0.018919	17.929	2.3048	40.499	13.115
1.9185	0.021278	19.713	3.0057	41.497	13.401
2.1107	0.023857	21.671	3.8777	42.497	13.685
2.3173	0.027146	23.825	4.9517	43.502	13.927
2.5344	0.030468	26.189	6.2184	44.506	14.154
2.7868	0.034838	28.799	7.5498	45.512	14.357
3.0663	0.038814	31.640	9.0359	46.519	14.586
3.3769	0.044257			47.519	14.821
3.7101	0.050684	Series 12		48.521	15.048

Continued on next page

T / K	$C_{p,m}$ / J·K^{-1}·mol^{-1}	T / K	$C_{p,m}$ / J·K^{-1}·mol^{-1}	T / K	$C_{p,m}$ / J·K^{-1}·mol^{-1}
4.0885	0.058584	18.272	2.4304	49.516	15.221
Series 14		70.905	19.229	Series 18	
20.701	3.4141	75.730	19.882	137.48	24.106
22.833	4.3841	80.600	20.468	142.59	24.317
25.118	5.5440	85.507	20.991	147.70	24.513
27.628	6.9259	90.447	21.488	152.82	24.673
30.394	8.3911	95.417	21.922	157.94	24.843
33.432	10.004	100.41	22.277	163.07	24.981
36.783	11.631	105.43	22.590	168.21	25.135
40.479	13.091	110.46	22.899	173.35	25.265
44.546	14.188	115.51	23.172	178.49	25.437
49.004	15.146	120.57	23.424	183.63	25.570
53.921	16.193	125.65	23.623	188.78	25.681
58.804	17.174	130.74	23.850	193.93	25.785
63.842	18.090	140.90	24.290	199.09	25.888
68.814	18.898	146.04	24.459	204.24	25.986
73.890	19.630	151.16	24.639		
78.836	20.267	156.28	24.816	Series 19	
83.905	20.800	161.41	24.928	194.62	25.791
88.727	21.212	166.54	25.095	199.79	25.898
93.956	21.678	171.68	25.277	204.95	26.003
98.930	22.102	176.82	25.412	210.11	26.083
103.95	22.455	181.97	25.553	215.26	26.175
108.86	22.742	187.12	25.658	220.43	26.286
		192.27	25.755	225.59	26.408
Series 15				230.75	26.508
54.909	16.255	Series 17		235.92	26.576
57.557	16.820	189.75	25.709	241.09	26.673
60.474	17.421	194.90	25.861	246.26	26.771
64.341	18.145	200.05	25.942	251.43	26.877
69.138	18.920	205.21	26.013	256.60	26.981
73.938	19.712	210.36	26.120	261.77	27.095
78.792	20.252	215.53	26.173	266.94	27.227
83.694	20.580	220.69	26.288	272.11	27.254
		225.85	26.439	277.29	27.316
Series 16		231.02	26.483	282.47	27.412
51.913	15.791	236.18	26.576	287.65	27.483
54.658	16.39	241.34	26.712	292.82	27.592
57.54	16.911				
61.373	17.659				
66.136	18.468				

Continued on next page

$\frac{T}{\mathrm{K}}$	$\frac{C_{p,m}}{\mathrm{J{\cdot}K^{-1}{\cdot}mol^{-1}}}$	$\frac{T}{\mathrm{K}}$	$\frac{C_{p,m}}{\mathrm{J{\cdot}K^{-1}{\cdot}mol^{-1}}}$	$\frac{T}{\mathrm{K}}$	$\frac{C_{p,m}}{\mathrm{J{\cdot}K^{-1}{\cdot}mol^{-1}}}$
Series 20		321.59	28.063	357.87	28.718
290.52	27.545	326.77	28.192	363.05	28.814
295.68	27.654	331.94	28.263	368.23	28.869
300.86	27.764	337.12	28.350	373.41	28.971
306.04	27.846	342.31	28.357	378.60	29.116
311.22	27.929	347.50	28.550	383.78	29.134
316.40	28.020	352.69	28.574	388.97	29.228

6.4.1 Low Temperature

When examining data from specific heat measurements, it is useful to look at a Debye low-temperature extrapolation by plotting C/T vs. T^2. Figure 6.3 presents the data in this form for both samples, using data from $0.6 < T/\mathrm{K} < 4$ K. For conductive materials, the low-temperature limit of the specific heat should fit the form of $C/T = \gamma_{el} + \beta T^2$, where $\gamma_{el}T$ is the electronic contribution to the specific heat and βT^3 is the contribution from the lattice. The low-temperature limit of the Debye temperature, θ_D, can be calculated from β using:

$$\theta_D = \sqrt[3]{\frac{\pi r R}{5\beta}} \tag{6.1}$$

where r is the number of atoms in the formula unit and R is the gas constant.[22] From Fig. 6.3, the low-temperature extrapolations of the specific heats of the polycrystal and single crystal samples show that the electronic contribution for the polycrystal is larger than that of the single crystal. Also, the contribution of β to the specific heat is markedly higher for the polycrystal than for the single crystal, which results in θ_D for the polycrystal being smaller than that of the single crystal. This discrepancy between the Debye temperatures for the polycrystal and single crystal has been noted previously.[7] Until recently, the low temperature θ_D values were always considerably lower than values calculated from single crystal elastic constant data.[12, 7] The Debye temperature of 256 K from the single crystal closely matches that of the value of θ_D = 250 K, as calculated from the elastic constant data.[12] Equally important, the value of θ_D = 180 K for the polycrystal is representative of the values from earlier measurements. [11, 7, 14] Since the two samples are from the same batch and were run on the same instrument, the differences in the values of γ and θ_D must be due to inherent differences between the single crystal and polycrystalline state. Thus, the polycrystal has different values for γ and θ_D due to the specific heat contributions

from the microstrain and from the suppression of CDWs that are responsible for the α_1, α_2 and α_3 transitions.

6.4.2 Microstrain

Above the temperature region of CDW's polycrystalline and single crystal α-uranium exhibit significant differences in their specific heats, as can be seen in figure 6.4. This difference is assumed to arise from the microstrain. The residual specific heat, calculated as the difference between the polycrystal and single crystal, has been plotted in figure 6.4. As a check for the validity of this data and analysis, we have calculated the specific heat difference for single crystal and polycrystalline copper (as mentioned previously). This has been plotted along with the residual specific heat of α-uranium. As expected for an isotropic material, copper displays no specific heat difference from the polycrystal to the single crystal, which further suggests that the specific heat difference between polycrystal and single crystal α-uranium arises from the microstrain. We now develop a thermodynamic model that accounts for the microstrain contribution.

Let us consider an anisotropic polycrystalline system composed of n crystal grains with complete random orientation throughout the system. If one visualizes a system where all of the domains are independent (not a real case), that is, there are no atomic level interactions at the domain boundaries, then as this sample undergoes anisotropic thermal contractions as it cools there will appear volume gaps between the domains. The real volume of the crystals then, is just the sum of all of the volumes of the individual domains. However the outside measurable volume will be greater than that of the real volume, which would be proportional to the average thermal expansion. At some temperature, T_0, these two volumes are equal, which should be

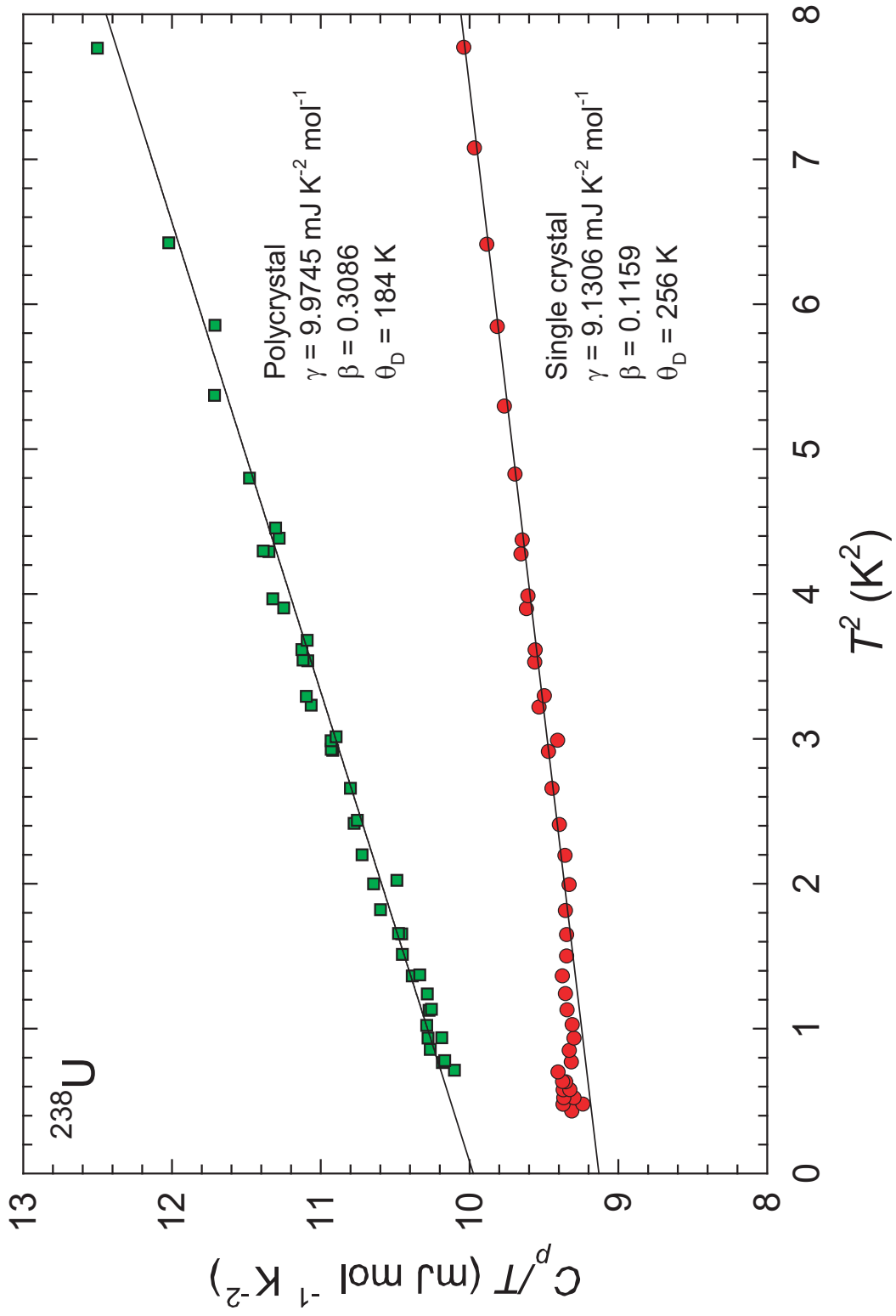

Figure 6.3. Debye low-temperature extrapolation of the specific heats of the polycrystal and single crystal samples of α-uranium from which γ_{el} and θ_D were determined.

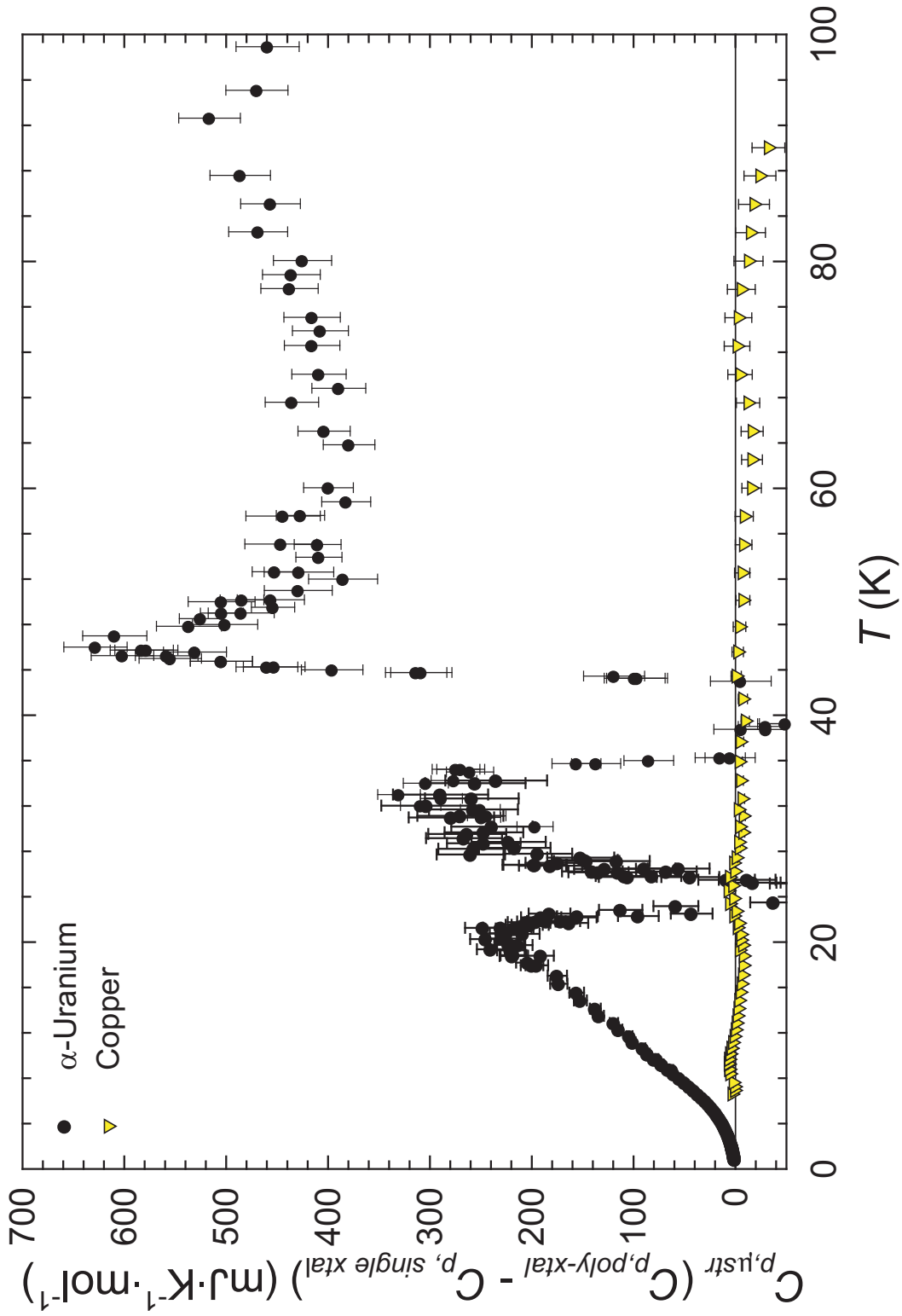

Figure 6.4. Residual (microstrain) specific heat for α-uranium from the difference between polycrystal and the single crystal specific heats, along with the residual specific heats for single and polycrystalline Copper.

at or near the temperature of formation. The difference between theses two volumes is the residual volume.

Applying this idea to the α-uranium system in which there *are* interactions between the domains, we will not have the presence of the gaps throughout the system. Thus to account for differences between these two systems, we say that the domains in α-uranium are stretched outwards to fill what would be the gaps. The stretching exerts a force per unit area (strain), which is equivalent to pressure, only acting outward from the crystal effectively expanding the lattice. Mathematically it would be considered negative hydrostatic pressure or negative strain, which has been shown to effect the specific heat in other systems such as $PbTiO_3$ and $Ce_{1-x}La_xRu_2Si_2$.[23, 24] The volume of what would be the gaps, or the residual volume, is the difference between the external volume of the crystalline system, which can be approximated by the average thermal expansion volume, and the volume of all of the individual single crystals, and can be denoted by ΔV. If we assume that an anisotropic change in volume will cause a change in pressure on each of the grains, then the resultant difference in the specific heat can be calculated from the thermodynamic relation (see appendix 7 for a derivation of this relationship):

$$\left(\frac{\partial C_p}{\partial p}\right)_T = -T\left(\frac{\partial^2 V}{\partial T^2}\right)_p . \tag{6.2}$$

This relationship is derived directly from fundamental thermodynamic equations and is always a valid representation of the change in specific heat due to the change in pressure over all conditions independent of the conceptualization. By integrating this relationship with respect to p (at any given temperature T and assuming the derivative is independent of pressure) gives:

$$\Delta C_p = -Tp\left(\frac{\partial^2 V}{\partial T^2}\right)_p \tag{6.3}$$

where p is the pressure applied to the crystal and which can be calculated using the

bulk modulus, B, using[25]:

$$-p = B\frac{\Delta V}{V}\,. \tag{6.4}$$

Thus the difference in the specific heat due to a change in pressure can be described in terms of a volume change as:

$$\Delta C_p = TB\frac{\Delta V}{V}\left(\frac{\partial^2 V}{\partial T^2}\right)_p \tag{6.5}$$

The volume, V, of the single crystal can easily be determined as a function of T through published values of the thermal expansion data for the three lattice parameters, and the value of ΔV is the residual volume as denoted previously.

A second source of the microstrain specific heat is due to a difference in volume between the single crystal and polycrystal. It can be shown from fundamental thermodynamic equations that the change in volume can change the specific heat through the relation:

$$\left(\frac{\partial C_p}{\partial V}\right)_T = \left(\frac{\partial}{\partial V}\left(\frac{\partial U}{\partial T}\right)\right)_T + \left(\frac{\partial p}{\partial V}\right)_T\left(\frac{\partial V}{\partial T}\right)_p \tag{6.6}$$

which can be simplified using the Maxwell relations to:

$$\left(\frac{\partial C_p}{\partial V}\right)_T = \left(\frac{\partial p}{\partial T}\right)_V + \left(\frac{\partial p}{\partial V}\right)_T\left(\frac{\partial V}{\partial T}\right)_p\,. \tag{6.7}$$

Using the definition of pressure as stated in equation 6.4 and then integrating, the change in the specific heat from the change in volume is thus;

$$\Delta C_p = B\Delta V\int_V^{V_0}\frac{1}{V^2}\left(\frac{\partial V}{\partial T}\right)_p dV\,. \tag{6.8}$$

However we know that V is a function of T, therefore the integral can be expressed as:

$$\Delta C_p = B\Delta V\int_V^{V_0}\frac{1}{V(T)^2}\left(\frac{\partial V(T)}{\partial T}\right)_p dV(T) \tag{6.9}$$

which can be transformed to an integral of T and is thus:

$$\Delta C_p = B\Delta V\int_T^{T_0}\frac{1}{V(T)^2}\left(\frac{dV(T)}{dT}\right)^2 dT\,. \tag{6.10}$$

This integral can then be evaluated numerically to give the change in specific heat due to the change in volume.

A third source of microstrain specific heat is expected to arise from the pressure-volume changes of the electronic structure. The electronic specific heat can be expressed as a function of molar volume, V_m, by:

$$C_{p,ele} = \frac{3\alpha V_m T}{\pi R\kappa\left(1+\lambda\right) N\left(E_F\right)} \tag{6.11}$$

where α is the thermal expansion coefficient, κ is the isothermal compressibility, R is the gas constant, λ is the electron-phonon interaction parameter and $N(E_F)$ is the band structure density of states.[26] By simple integration, the change in specific heat from the pressure-volume change is thus:

$$\Delta C_{p,ele} = \frac{3\alpha \Delta V_m T}{\pi R\kappa\left(1+\lambda\right) N\left(E_F\right)}\,. \tag{6.12}$$

assuming that all parameters are constant with respect to V. Changes in the electronic specific heat from pressure-volume changes have been reported in α-gallium (another metal with orthorhombic symmetry) near its superconducting transition.[26] The change in the electronic specific heat is thought to originate from changes in the Fermi surface of the metal due to anisotropic strains.[26] Thus it is reasonable to argue that similar changes in the electronic specific heat in α-uranium will arise due to microstrain energy. Therefore, the total change in the specific heat as a result of the microstrain will be the sum of the pressure-volume changes to the lattice and to the electronic structure. The molar volume of the single crystal and of the polycrystals was determined as a function of temperature using published data for the linear thermal expansion of single crystal α-uranium along the a, b, and c axis and the average value of volume expansion for the polycrystal.[27] The change in volume as a function of temperature, $\Delta V(T)$, was calculated as: $\Delta V(T) = V_{poly}(T) - V_{single}(T)$.

From equations 6.5 and 6.10, the lattice specific heat due to the pressure-volume change of the microstructure was calculated. (Note: the value of B was kept constant since it does not change appreciably nor did it effect the calculated values of the theoretical residual specific heat from 70 K to 300 K by more than 0.1%).[28] The calculated values for the lattice microstrain contribution were derived only from the literature values of the dependent variables in equations 6.5 and 6.10 with no additional adjustment parameters. Thus, this is purely a thermodynamic adjustment to the specific heat caused by pressure and volume changes. The negative pressures involved in the microstrain were calculated to be between -4 GPa and -11 GPa. This is in good agreement with negative pressures ranging from -7 GPa and -0.3 GPa reported by Tinte [23] and by Flouquet [24], respectively.

For the electronic microstrain contribution, the specific heat quantities were computed using the total electronic specific heat of the polycrystal. This was accomplished by first calculating the lattice specific heat above 50 K for the polycrystal from temperature dependent phonon density of states data obtained from Manley et al. (see below in section 6.4.3).[29] Figure 6.5 shows the lattice, electronic and overall microstrain contributions to the specific heat of α-uranium. From the figure, it can be seen there is good agreement between the measured microstrain specific heat and the theoretical model. Furthermore, since the microstrain specific heat model incorporates parameters derived only from thermodynamics, the agreement of the calculated and measured microstrain specific heats supports the validity of the current model.

6.4.3 Lattice and Electronic Specific Heat

For electrically conductive systems, using the Debye low-temperature extrapolation, the low-temperature electronic and lattice contributions to the specific heat, $\gamma_{el}T$

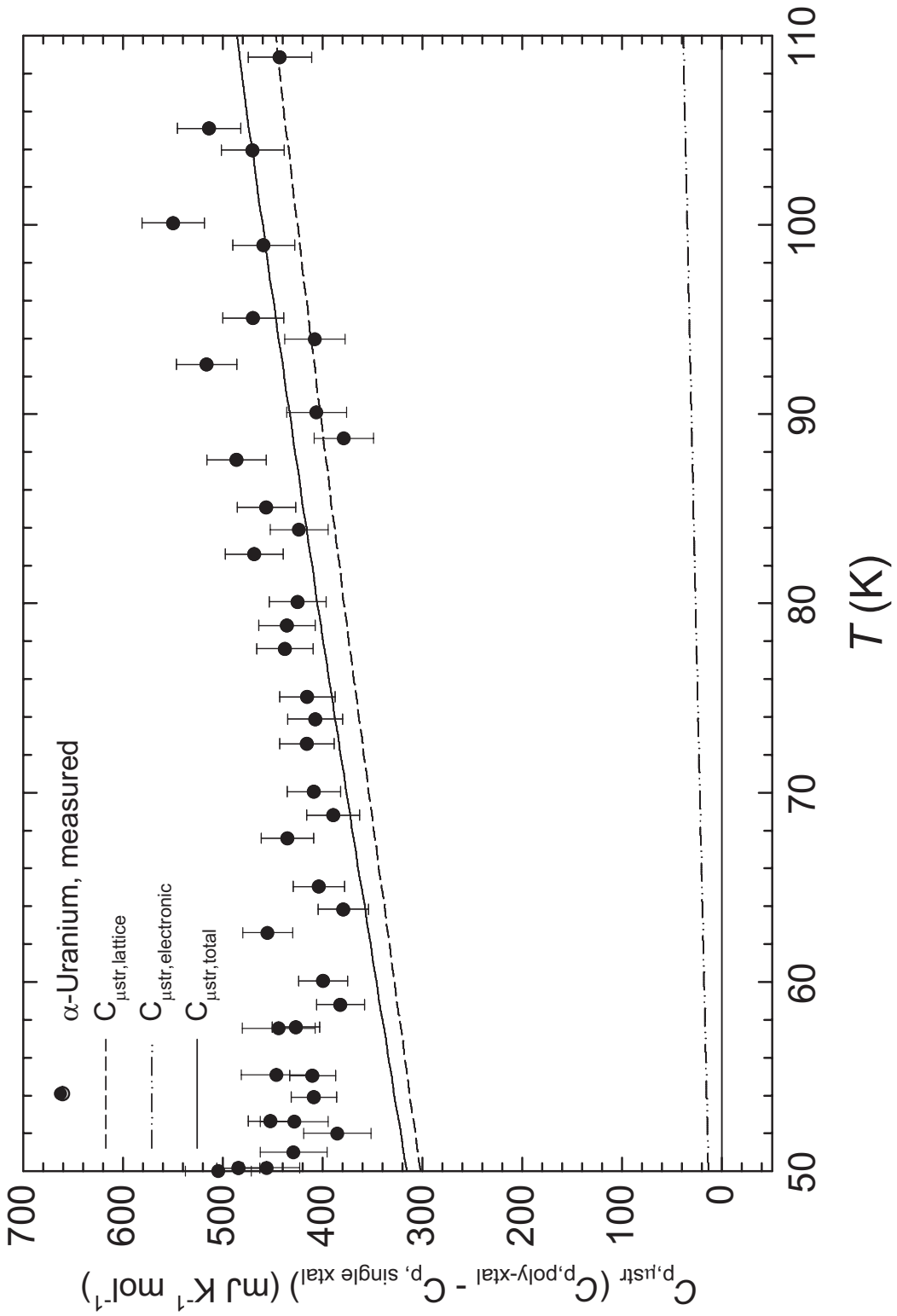

Figure 6.5. Microstrain specific heat of α-uranium along with the thermodynamic models for the microstrain specific heat from 0 to 110K. The lattice contribution to the specific heat as generated from equations 6.5 and 6.10, and the electronic contribution as determined using equation 6.12.

and βT^3 respectively can be obtained. In the vast majority of cases, the electronic specific heat, C_{el}, is assumed to be a linear function of T such that $C_{el} = \gamma_{el}T$. However, in the α-uranium system the α_1 and α_2 transitions are coupled to the electronic states and thus it is not obvious that C_{el} is a linear function at all temperatures, especially above the transitions. Therefore, to find the electronic contribution to the specific heat it is first necessary to find the specific heat which arises solely from the lattice and then subtract that from the total specific heat.

To obtain the energy of the lattice for the α-uranium polycrystal, we used the temperature dependant phonon density of states (DOS) of Manley *et al.* obtained by inelastic neutron scattering from 50 K to 1113 K on a polycrystalline sample.[29] The specific heat at constant volume of the lattice, ($C_{V,latt}$) can be calculated from the phonon density of states using equation 1.24. However, in this situation the phonon density of states was not sufficient to give a complete measurement of the lattice specific heat since there are two known changes in the α-uranium lattice below 50 K.[7] The specific heat calculation from equation 1.24 relies on the phonon DOS at zero Kelvin. Therefore, it was necessary to obtain a zero Kelvin DOS derived from the phonon DOS values at 50 K, 250 K and 300 K. This was then used to calculate the lattice specific heat, $C_{V,latt}$ from 50 K to 300 K.

Because the values of the lattice specific heat were calculated from an extrapolated density of states, it was important to know how the calculated specific heat changed due to uncertainties in the phonon DOS. Thus, values of $C_{V,latt}$ from 50 K to 300 K were obtained from the density of states at 50 K, 250 K and 300 K . Comparison of the $C_{V,latt}$ values generated from the four sets of data showed there were relative standard deviations of less than 0.2% between all the calculated values of $C_{V,latt}$ over the entire temperature range. Since there was relatively little difference between the calculated $C_{V,latt}$ values, and there was little difference between the extrapolated phonon DOS

and the phonon DOS measured at 50 K, the phonon DOS at 50 K was used in the final calculation to determine the specific heat of the lattice, with the standard error being the standard deviation at a given temperature between the four sets of data.

To obtain the lattice specific heat at constant pressure ($C_{p,latt}$) from these calculations, we use the relationship from classical thermodynamics:

$$C_p = C_V + BV_m\alpha^2 T \tag{6.13}$$

where B is the bulk modulus, V_m is the molar volume, and α is the coefficient of thermal expansion (equation 1.25). The values of V and α from 50 to 300 K were calculated from the known molar volumes of polycrystalline α-uranium at 298 K and the temperature dependent change in the molar volume.[27] The value of the bulk modulus was obtained from Fisher and McSkimin,[4] and, although B is known to vary with temperature, it was assumed that it would stay fairly constant in this region and that changes in B would be less than other sources of error. The calculated values of $C_{p,latt}$ from the phonon DOS can be seen in figure 6.6 along with the measured specific heat data.

As expected, the lattice specific heat is lower than the experimental C_p due to the electronic contribution. Taking the difference between the experimental and calculated lattice gives the electronic contribution for a polycrystalline α-uranium, which is displayed in figure 6.7a. The electronic contribution does not quite vary linearly with T but has a slight upward curvature. Calculating γ_{el} at each point ($\gamma_{el} = C_{p,el}/\mathrm{T}$) reveals that γ_{el} increases with temperature almost linearly, except in the lower-temperature region near the transition at 43 K (figure 6.7b). A linear regression of γ_{el} from above the transition, factoring in the experimental uncertainty, gives γ_{el} at 0 K for the polycrystal as 9.02 ± 0.14 mJ K^{-2} mol^{-1}. This is lower than the calculated γ_{el} at 0 K from the Debye low-temperature extrapolation of the polycrystal

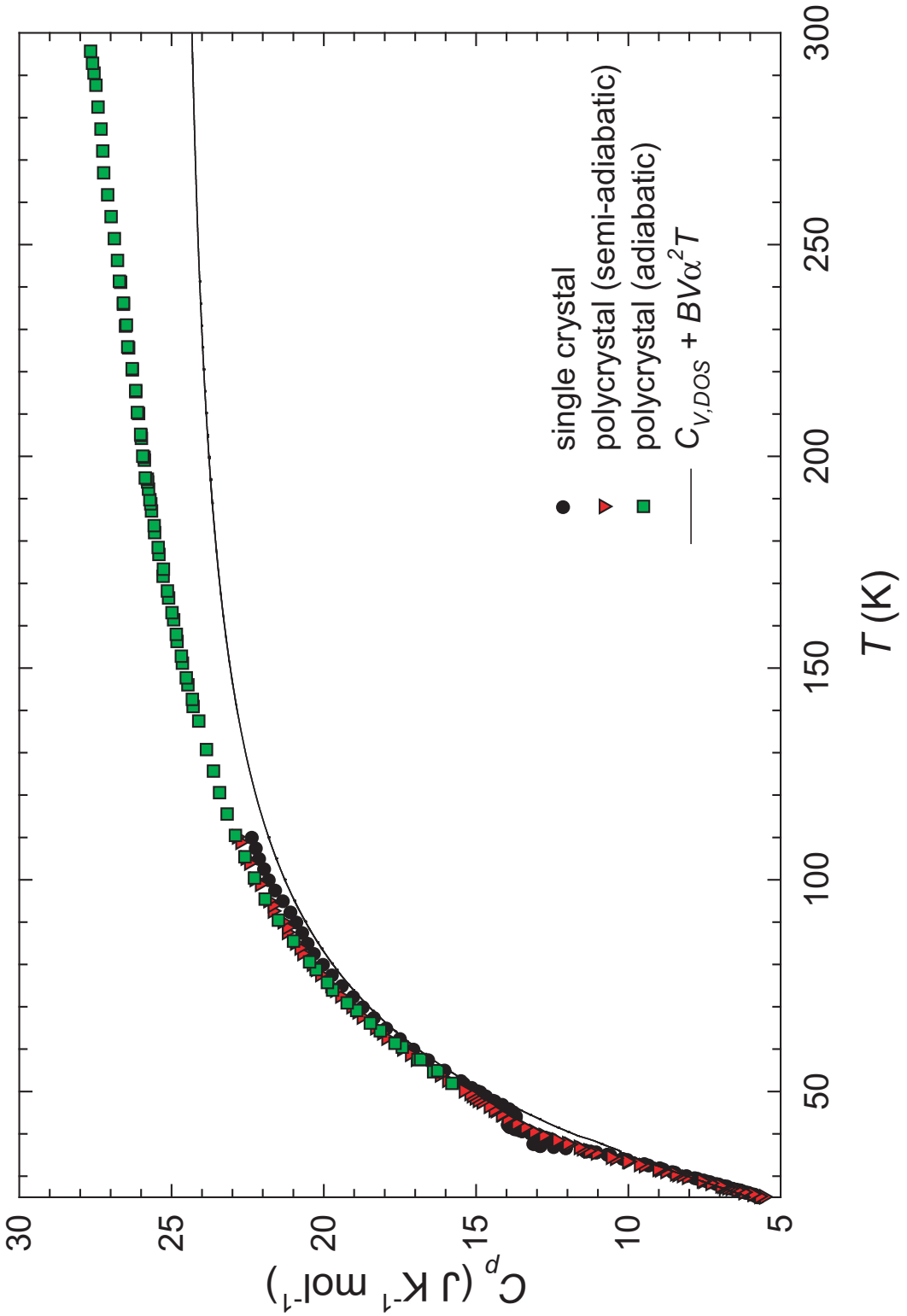

Figure 6.6. Specific heat for the lattice above 50 K as calculated from the phonon density of states of polycrystalline α-uranium with the measured specific heats.

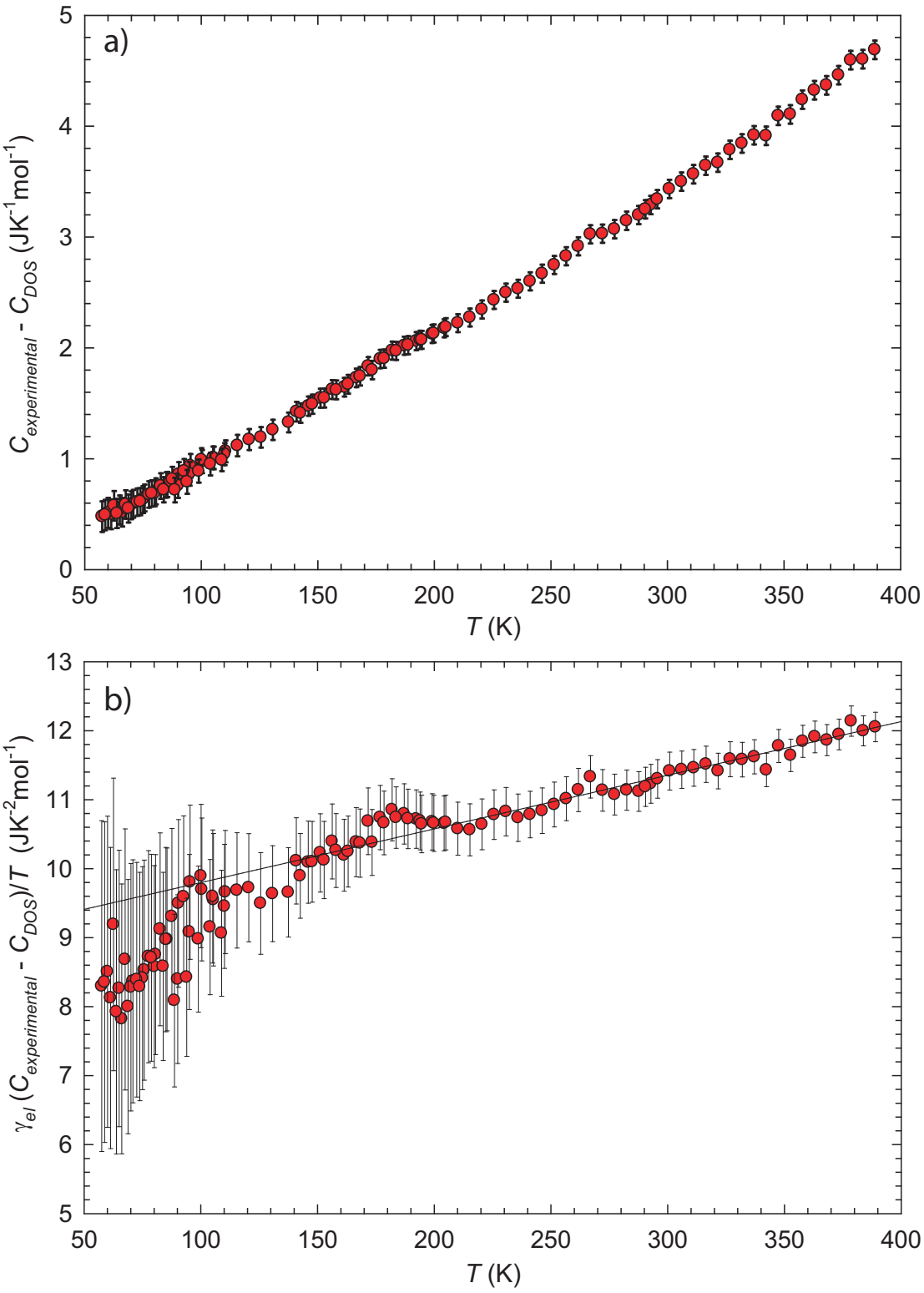

Figure 6.7. Electronic specific heat for polycrystalline α-uranium (part a), with the calculated γ_{el} (part b).

and single crystal where $\gamma_{el} = 9.9745$ mJ K^{-2} and $\gamma_{el} = 9.1306$ mJ K^{-2} respectively. However, γ_{el} for the single crystal is within the experimental uncertainty of the extrapolated value of γ_{el} from the polycrystal, and this data does not account for the structural and electronic transitions at 23 K, 37 K and 43 K, where the electronic contribution to the specific heat is unknown; thus, the value from the high temperature γ_{el} is in reasonable agreement.

6.4.4 Thermodynamic Calculations

We have fit the specific heat data for the polycrystal sample of α-uranium using four different fitting procedures for various temperature regions. For $T \leq 8$ K, an equation of the form $C^o_{p,m} = A_{-2}T^{-2} + \gamma T + B_3T^3 + B_5T^5 + B_7T^7 + B_9T^9$ was used where the $A_{-2}T^{-2}$ term fits the U-235 hyperfine contribution, γT fits the electronic contribution, and the remaining terms represents the contribution from the lattice. The root-mean-square deviation of the fit was 0.24 percent. Although there are more lattice terms for α-uranium than is common for most systems in this temperature region, it was necessary to use these terms to accurately represent the data. It is thought that the large number of lattice terms is due to the complex vibrational structure of α-uranium. The Debye temperature, θ_D, derived from B_3, is 184 K. This value is in good agreement with previously published data for the Debye temperature for polycrystalline samples.[1, 7] The hyperfine contribution is negligible above 2 K and it has been excluded from the calculations of the entropy and enthalpy increments since the hyperfine is a nuclear phenomenon. In the temperature range 8 K $\leq T \leq$ 32 K the data was fit to an equation of the form $C^o_{p,m} = a_0 + a_1T + a_2T^2 + \cdots + a_9T^9$. Likewise, for 32 K $\leq T \leq$ 55 K, a polynomial equation of order T^5 was used to fit the data and for 55 K $\leq T \leq$ 375 K, a polynomial equation of order T^9 was used. All of the fitting equations used above 8 K had a root-mean-square deviation of

Table 6.3. Summary of fitting data for α-uranium for the various temperature ranges.

Polycrystal

T range	fitting type	% RMS
0.5 K – 8 K	$C^o_{p,m} = AT^{-2} + \gamma T + B_3T^3 + B_5T^5 + B_7T^7 + B_9T^9$	0.24
8 K – 32 K	$C^o_{p,m} = a_0 + a_1T + a_2T2 + \cdots + a_9T^9$	0.1
32 K – 55 K	$C^o_{p,m} = a_0 + a_1T + a_2T2 + \cdots + a_5T^5$	0.1
55 K – 375 K	$C^o_{p,m} = a_0 + a_1T + a_2T2 + \cdots + a_9T^9$	0.1

Single crystal

T range	fitting type	% RMS
0.5 K – 10 K	$C^o_{p,m} = AT^{-2} + \gamma T + B_3T^3 + B_5T^5 + B_7T^7 + B_9T^9$	0.25
10 K – 20 K	$C^o_{p,m} = a_0 + a_1T + a_2T2 + \cdots + a_9T^9$	0.15
20 K – 26 K	spline	N/A
26 K – 33 K	$C^o_{p,m} = a_0 + a_1T + a_2T2 + a_3T^3$	0.1
33 K – 46 K	spline	N/A
46 K – 110 K	$C^o_{p,m} = a_0 + a_1T + a_2T2 + \cdots + a_9T^7$	0.1

better than 0.1 percent. Smoothed specific heat and thermodynamic functions for the polycrystalline sample were generated from the fitted data in the three temperature regions. A summary of the fitting procedures is given in table 6.3 and the values of the smoothed thermodynamic functions are given in table 6.4. Our results yield a value for $\Delta_0^{298.15} S^\circ_m$ of 50.21 $\pm$0.1 J·K^{-1}·mol^{-1}, which is in agreement with the currently accepted value reported by Flotow and Lohr, but the current measurements have yielded a smaller standard error than the $\pm$0.2 J·K^{-1}·mol^{-1}error from Flowtow and Lohr.[9]

While the calculation of the smoothed specific heat and thermodynamic values for the polycrystal sample were relatively simple and straightforward, the task of repeating this for the single crystal was much more difficult since the α_1, α_2, and α_3 transition regions could not be fit with simple polynomial expressions. Below 20 K, the data was fit from 0 K to 10 K and from 10 K to 20 K using equations of the forms $C^\circ_{p,m} = A_{-2}T^{-2} + \gamma T + B_3T^3 + B_5T^5 + B_7T^7 + B_9T^9$ and $C^\circ_{p,m} =$

$a_0 + a_1T + a_2T^2 + \cdots + a_9T^9$ respectively. Again, the $A_{-2}T^{-2}$ term corresponds to the U-235 hyperfine splitting. Above 20 K the fitting functions are a combination of two different fitting methods. The first method relies on orthogonal polynomial equations of various powers to represent the lattice specific heat of α-uranium and to account for various changes in curvature of the lattice contribution. Secondly, cubic spline functions, which were generated from hand drawn plots on large graph paper, were used to represent the transition regions. This includes an increase of the lattice specific heat at 23 K due to the apparently first order α_3 transition. A summary of the fitting methods and deviation from the fits is given in table 6.3. The transition entropies in the single crystals were obtained by subtracting an estimate of the lattice specific heats from those of the transitions and appropriate integration of the excess specific heat. These values have been published previously and have been reported as $\Delta S^{\circ}_{\alpha 1} = 0.12 \pm 0.01$ J·K^{-1}·mol^{-1}and $\Delta S^{\circ}_{\alpha 2} = 0.11 \pm 0.01$ J·K^{-1}·mol^{-1}for the α_1 and α_2 transitions respectively and $\Delta S^{\circ}_{\alpha 3} = 0.05 \pm 0.01$ J·K^{-1}·mol^{-1}for the α_3 transition.[7] Smoothed specific heat and thermodynamic functions for single crystal α-uranium were generated from the fitted data in the various temperature regions, with the U-235 hyperfine contribution subtracted. The data below 50 K is tabulated in table 6.4 along with the extrapolated high-temperature specific heat for the single crystal that will be discussed subsequently.

At temperatures greater than 50 K we use the for the microstrain, as discussed above, to predict the behavior of the single crystal by subtracting the microstrain specific heat from the smoothed fit of the polycrystalline data. From these results the thermodynamic functions for the single crystal were calculated. These values are listed in table 6.5 along with the smoothed thermodynamic functions generated from measured values below 100 K. The smoothed thermodynamic functions along with the raw data can be seen in figure 6.8.

The resultant data from these calculations give a value for $\Delta_0^{298.15} S_m^\circ$ as 49.19 ± 0.2 $\mathrm{J{\cdot}K^{-1}{\cdot}mol^{-1}}$. This value for the entropy of the single crystal is 1.02 $\mathrm{J{\cdot}K^{-1}{\cdot}mol^{-1}}$less than the value of $\Delta_0^{298.15} S_m^\circ = 50.21 \pm 0.1$ $\mathrm{J{\cdot}K^{-1}{\cdot}mol^{-1}}$for the polycrystal. It should be noted that only half of this entropy difference can be attributed to temperatures above 100 K, where the extrapolation of the specific heat data from the microstrain was used. The difference in entropy, as well as the difference in the other thermodynamic functions, between the single crystal and polycrystal, is about two percent (compare the values in tables 6.4 and 6.5). This demonstrates that the effect of the microstrain on the α-uranium system makes a significant contribution to the overall thermodynamics of the system. Thus, while the effects of grain boundaries are often regarded as a negligible effect, it cannot be ignored in systems in which there is anisotropic thermal expansion.

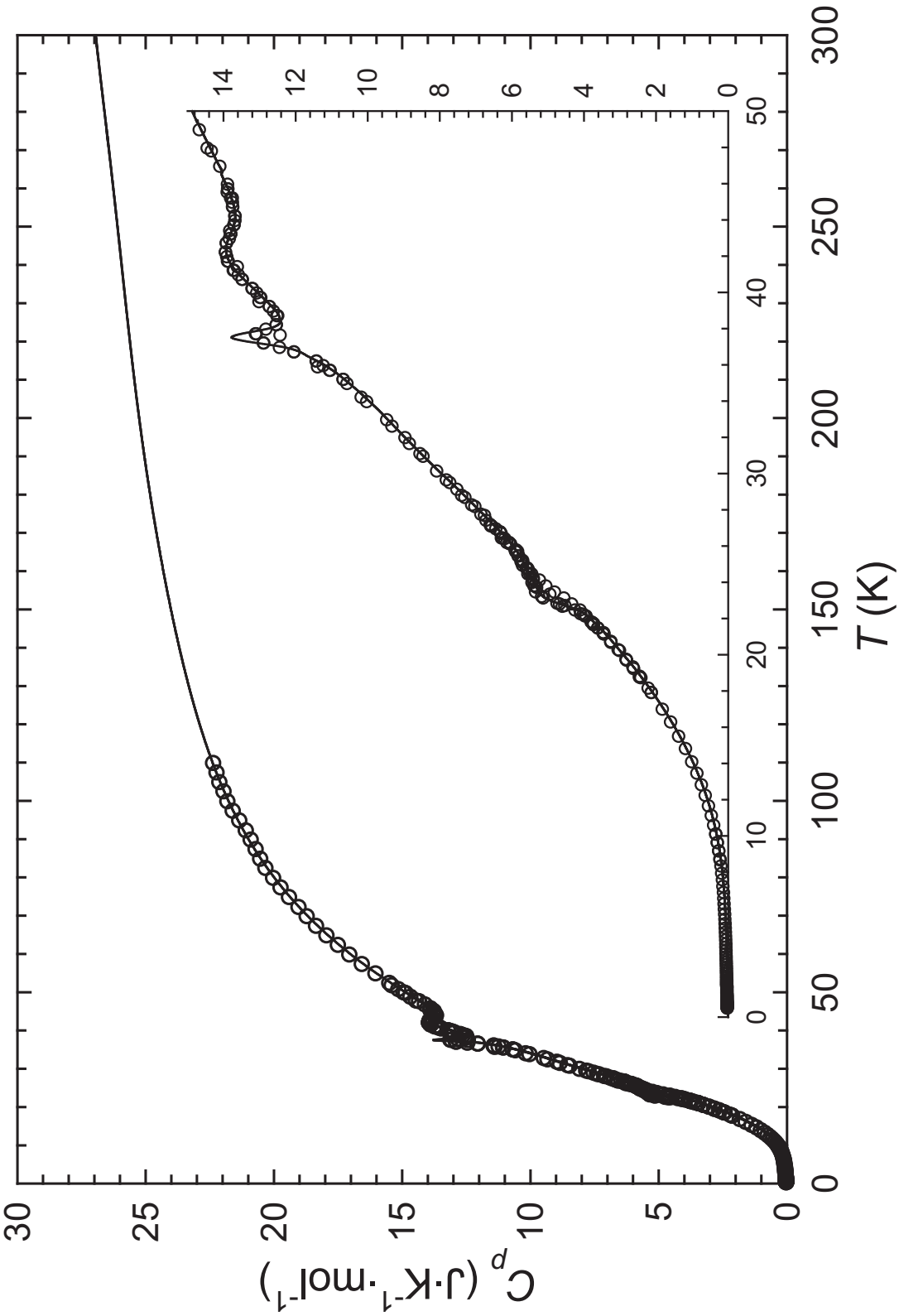

Figure 6.8. Specific heat of single crystal α-uranium from 0.5 K to 100 K with smoothed specific heat functions from 0 K to 300 K, using the theoretical microstrain specific heat to model the data above 110 K.

Table 6.4. Standard molar thermodynamic properties of polycrystalline α-uranium. $\Phi = \Delta_0^T S_m^\circ - \Delta_0^T H_m^\circ/T$(M = 238.029 g·mol^{-1} and p^o=101.325 kPa.)

T / K	$C_{p,m}^\circ$ / J · K^{-1} · mol^{-1}	$\Delta_0^T S_m^\circ$ / J · K^{-1} · mol^{-1}	$\Delta_0^T H_m^\circ/T$ / J · K^{-1} · mol^{-1}	Φ_m° / J · K^{-1} · mol^{-1}
5	0.080397	0.060925	0.033075	0.02785
10	0.39339	0.18833	0.11689	0.071445
15	1.3536	0.50216	0.34656	0.15561
20	3.1237	1.1158	0.80374	0.31205
25	5.5335	2.0624	1.5004	0.56201
30	8.2115	3.3081	2.3959	0.91223
35	10.817	4.7697	3.4129	1.3568
40	12.92	6.3602	4.4781	1.8821
45	14.298	7.9672	5.498	2.4692
50	15.341	9.5284	6.4309	3.0975
60	17.414	12.514	8.0935	4.4203
70	19.081	15.328	9.5485	5.7797
80	20.4	17.966	10.826	7.1399
90	21.43	20.43	11.949	8.4813
100	22.237	22.732	12.939	9.7926
110	22.879	24.882	13.815	11.068
120	23.404	26.896	14.593	12.304
130	23.85	28.788	15.288	13.5
140	24.24	30.57	15.914	14.656
150	24.59	32.254	16.481	15.774
160	24.909	33.852	16.998	16.854
170	25.199	35.371	17.472	17.899
180	25.463	36.818	17.908	18.91
190	25.702	38.202	18.312	19.889
200	25.919	39.526	18.687	20.838
210	26.117	40.795	19.037	21.759
220	26.302	42.014	19.363	22.652
230	26.479	43.187	19.668	23.519
240	26.653	44.318	19.956	24.362
250	26.829	45.41	20.227	25.183
260	27.009	46.465	20.484	25.981
270	27.192	47.488	20.729	26.759
273.15	27.251	47.804	20.804	27
280	27.378	48.48	20.964	27.517
290	27.561	49.444	21.188	28.256
298.15	27.707	50.21	21.364	28.846
300	27.739	50.382	21.403	28.978
310	27.908	51.294	21.61	29.684

Table 6.5. Standard molar thermodynamic properties of single crystal α-uranium. $\Phi = \Delta_0^T S_m^\circ - \Delta_0^T H_m^\circ/T$(M = 238.029 g·mol^{-1} and p°=101.325 kPa.)

T / K	$C_{p,m}^\circ$ / J · K^{-1} · mol^{-1}	$\Delta_0^T S_m^\circ$ / J · K^{-1} · mol^{-1}	$\Delta_0^T H_m^\circ/T$ / J · K^{-1} · mol^{-1}	Φ_m° / J · K^{-1} · mol^{-1}
5	0.060585	0.050517	0.026474	0.024044
10	0.31047	0.1464	0.089015	0.057388
15	1.2031	0.41382	0.28908	0.12474
20	2.9057	0.97304	0.71287	0.26018
25	5.648	1.9284	1.4385	0.48989
30	7.9554	3.1435	2.3155	0.82798
35	10.526	4.5592	3.3013	1.2579
40	13.06	6.1853	4.4142	1.7711
45	13.746	7.7972	5.4447	2.3524
50	14.874	9.3002	6.3279	2.9724
60	17.022	12.21	7.9385	4.2714
70	18.696	14.965	9.3608	5.6042
80	19.991	17.55	10.612	6.9377
90	20.993	19.965	11.712	8.2525
100	21.773	22.219	12.681	9.5377
110	22.392	24.324	13.537	10.787
120	22.896	26.295	14.296	11.998
130	23.32	28.145	14.975	13.17
140	23.687	29.886	15.584	14.302
150	24.014	31.532	16.135	15.397
160	24.309	33.091	16.637	16.454
170	24.578	34.573	17.096	17.477
180	24.824	35.985	17.519	18.466
190	25.049	37.334	17.909	19.424
200	25.253	38.624	18.272	20.352
210	25.44	39.86	18.609	21.252
220	25.613	41.048	18.923	22.125
230	25.777	42.19	19.218	22.972
240	25.937	43.29	19.494	23.796
250	26.097	44.352	19.755	24.597
260	26.261	45.379	20.002	25.377
270	26.43	46.373	20.237	26.136
273.15	26.485	46.68	20.309	26.372
280	26.604	47.338	20.461	26.876
290	26.779	48.274	20.676	27.598
298.15	26.919	49.019	20.845	28.174
300	26.949	49.185	20.882	28.303
310	27.108	50.071	21.081	28.991

References

[1] Lander, G. H.; Fisher, E. S.; Bader, S. D., *Adv. Phys.* **1994**, *43*, 1–111.

[2] Mott, N., *Nature* **1946**, *158*, 861.

[3] Barrett, C. S.; Mueller, M. H.; Hitterman, R. L. .

[4] Fisher, E. S.; McSkimin, H. J., *J. Appl. Phys.* **1958**, *29*, 1473.

[5] Steinitz, M. O.; Burleson, C. E.; A., M. J., *J. Appl. Phys.* **1970**, *41*, 5057–9.

[6] Smith, H. G.; Wakacayashi, N.; Crummett, W. P.; Nicklow, R. M.; H., L. G.; Fisher, E. S., *Phys. Rev. Lett.* **1980**, *44*, 1612.

[7] Lashley, J. C.; Lang, B. E.; Boerio-Goates, J.; Woodfeild, B. F.; Schmiedeshoff, G.; Gay, C. E.; McPheeters, C.; Thoma, D. J.; Hults, W. L.; Cooley, J.; Hanrahan, Jr., R. J.; L., S. J., *Phys. Rev. B* **2001**, *63*, 224510.

[8] Jones, W. M.; Gordon, J.; Long, E. A., *J. Chem. Phys.* **1952**, *20*, 695.

[9] Flowtow, H. E.; Lohr, H. R., *J. Phys. Chem.* **1960**, *64*, 904.

[10] Lee, J. A.; Sutcliffe, P. W.; Mendelssohn, K., *Phys. Letters* **1969**, *30A*, 106.

[11] Crangle, J.; Temporal, J., *J. Phys. F* **1973**, *3*, 1097.

[12] Fisher, E. S.; Dever, D., *Phys. Rev.* **1968**, *179*, 607.

[13] Flowtow, H. E.; Osborn, D. W., *Phys. Rev.* **1966**, *151*, 564–70.

[14] Dempesy, C. W.; Gordon, J. E.; R.H., R., *Phys. Rev. Lett.* **1963**, *11*, 547.

[15] Nagel, L. J.; Fultz, B.; Robertson, J. L.; Spooner, S., *Phys. Rev. B* **1997**, *55*, 2903.

[16] Manley, M.; Fultz, B.; Brown, D.; Clausen, B.; Lawson, A.; Cooley, J.; Hults, W.; Hanrahan, Jr., R. J.; Smith, J. L.; J., T. D., *Phys. Rev. B* **2002**, *66*, 024117.

[17] Boerio-Goates, J.; Callanan, J. E., in B. W. Rossiter; R. C. Baetzold, eds., *Physical Methods of Chemistry*, John Wiley and Sons, vol. 6, 2nd edn., 1992 pp. 621–717.

[18] McPheeters, C.; Gay, E.; Karell, E.; J.P., A., *Journal of Metals* **1997**, *49*, 22.

[19] Lashley, J. C.; Lang, B. E.; Boerio-Goates, J.; Woodfeild, B. F.; Darling, T. W.; Chu, F.; Migliori, A.; Thoma, D., *J. Chem. Thermo.* **2002**, *34*, 251–261.

[20] Woodfield, B. F., *Specific Heat of High-Temperature Superconductors: Apparatus and Measurement*, Ph.D. thesis, University of California, Berkeley, **1995**.

[21] Stevens, R.; Boerio-Goates, J., *J. Chem. Thermodyn.* **2004**, *36*, 857–863.

[22] Gopal, E. S. R., *Specific Heats at Low Temperatures*, New York: Plenum Press, **1966**.

[23] Tinte, S.; Rabe, K. M.; Vanderbilt, D., *Los Alomos National Laboratory, Preprint Archive: Condensed Matter* **2003**, p. 0306205, http://xxx.lanl.gov/pfd/cond-mat/0306205.

[24] Flouquet, J.; Barla, A. B.; Boursier, R.; Derr, J.; Knebel, G., *Los Alomos National Laboratory, Preprint Archive: Condensed Matter* **2004**, p. 0407437, http://xxx.lanl.gov/pfd/cond-mat/0407437.

[25] Kittel, C., *Introduction to Solid State Physics*, New York: John Wiley and Sons, 7th edn., **1996**.

[26] Griessen, R.; Krugmann, H.; Ott, H. R., *Phys. Rev. B.* **1974**, *10*, 1160–1172.

[27] Touloukian, Y. S., ed., *Thermophysical properties of matter:*, vol. 12 Thermal Expansion: Metalic Elements and Alloys, IFI/Plenum, **1979**, Purdue University. Thermophysical Properties Research Center.

[28] Mcskimin, H. J.; Fisher, E. S., *J. Appl. Phys.* **1960**, *31*.

[29] Manley, M.; Fultz, B.; McQueeney, R.; Brown, D.; Hults, W.; Smith, J. L.; J., T. D.; Osborn, R.; Robertson, J. L., *Phys. Rev. Lett.* **2001**, *86*, 3076.

Chapter 7

TiB_2 and LiF

7.1 Introduction

The genesis of this research is for the identification and development of materials suitable for use as absorbers in high-resolution cryogenic neutron spectrometers. It is well known that neutrons are difficult to detect since they are uncharged, thus their interaction with detectors is only via nuclear interactions. In addition, many of the older methods of neutron detection (such as the BF_3 detectors) were notorious for giving false signals from external heat sources if great care was not taken in the experimental design.[1] (This was the case for several researchers in the cold fusion debacle from 1989 and 1990.[1]) However, the aim of this project is to not only find a novel method to detect neutrons but to determine the energies of the incident neutrons as well.

The instrument design is a variation of a cryogenic gamma-ray spectrometer developed by Chow *et al.*[2] The instrument is essentially a microcalorimeter comprised of a neutron absorber, a thermometer, and weak thermal link to a cold bath to

detect heat pulses associated with (n, α) reactions. Details of which can be found elsewhere.[2, 3] The thermometer in the current design is a superconducting transition edge sensor (TES) – a multi-layer structure composed of alternating superconducting and non-superconducting films. The TES becomes superconducting at a temperature determined by the composition and thickness of the layers. The TES is held in equilibrium near the low-temperature limit of the narrow transition between the superconducting (S) and normal (N) states, so that a small increase in temperature resulting from a single (n, α) reaction causes a large change in resistance from which the incident neutron energy is deduced.

The energy resolution of a detector of this type is determined by thermal fluctuations and Johnson noise and is given by:

$$\Delta E = 2.35\xi\sqrt{k_b T_{op}^2 C}, \tag{7.1}$$

where k_b is Boltzmann's constant, T_{op} is the operating temperature (Kelvin), C is the total heat capacity of the microcalorimeter, and ξ is a parameter dependent on the sensitivity of the thermometer and operating conditions.[2, 4] Small values for ΔE (or higher energy resolution) can be obtained using small values of T_{op} and C. Chow *et al.* typically worked near 100 mK using a microcalorimeter with a total heat capacity of approximately 12.8×10^{-12} J·K^{-1} (80 keV·mK^{-1}) and a superconducting Sn absorber. The resulting resolution of the detector was 230 eV for 60 keV gamma rays.[2]

In general, high resolution neutron spectroscopy requires that the energy of an incident neutron be completely transformed to heat within the absorber so the signal will be proportional only to the sum of the kinetic energy of the neutron and the Q-value of the reaction. Practically, this means the neutron must take part in a nuclear

reaction in the absorber in which few gamma rays and no neutrons are emitted, and the reaction products have short ranges. The constraint on gamma rays reflects the inability of a small detector volume to capture energy diverted to (n, γ) reactions. In addition, the absence of gamma-rays simplifies the response function. Neutron scattering reactions produce recoil ions with energies dependent on the incident neutron's energy, the angle through which it is scattered, the mass of the target atom, and the Q-value of the reaction. Since the scattered neutron may neither be captured nor sensed, its information can be lost, and this prevents accurate recovery of the incident energy.

Taking all of this into consideration, the ideal reactions for this type of neutron spectroscopy are those resulting in charged particles (protons, alpha particles, etc.). It is also desirable that the reaction products have sufficiently simple structures so their production in excited states is either forbidden by conservation of energy or occurs with only a few Q-values. While fission reactions with actinides are seemingly excellent candidates, they must be rejected for this type of application since a significant amount of energy is lost to neutrons and gamma rays, and the fission products are complex enough to yield a wide range of Q-values. Instead, simple reactions involving ^{3}He, ^{10}B, and ^{6}Li are the most promising:

$$ {}^{3}_{2}He + {}^{1}_{0}\,n \rightarrow {}^{3}_{1}\,H + {}^{1}_{1}\,p + \Delta \tag{7.2} $$

$$ {}^{10}_{5}B + {}^{1}_{0}\,n \rightarrow {}^{7}_{3}\,Li + {}^{4}_{2}\,\alpha + \Delta \tag{7.3} $$

$$ {}^{6}_{3}Li + {}^{1}_{0}\,n \rightarrow {}^{3}_{1}\,H + {}^{4}_{2}\,\alpha + \Delta \tag{7.4} $$

where Δ represents the sum of the Q-value of the reaction (shared by the products) and the energy of the incident neutron, E_n. In most solids, the reaction products have ranges of a few microns if the incident neutrons have energies below 10 MeV.

Of these candidate nuclei, helium must be discarded immediately since it forms

no known compounds and the Q-value for the (n, p) reaction[a] is only 764 keV. With a Q-value this low, and a mass of only 3 amu, a ^{3}He nucleus recoiling from an (n, n) interaction with $E_n = 1$ MeV has roughly the same energy as the products resulting from a thermal neutron capture, which leads to a significant overlap of the capture and scattering signals and results in an indecipherable spectrum. On the other hand, the masses of lithium and boron, and the Q-values of the few acessable capture reactions, do allow the separation of capture events from scattering events based on pulse height. The ^{6}Li(n, α)t reaction produces an alpha particle and a triton, t (tritium nucleus), sharing $\Delta = 4.78$ MeV $+ E_n$. The ^{10}B(n, α)^{7}Li reaction has two branches, with 94% of the reactions (at least at thermal energies) leaving ^{7}Li in its first excited state (0.478 MeV), and 6% leaving ^{7}Li in its ground state. The Q-values for these reactions are 2.310 MeV and 2.792 MeV respectively. Therefore, the initial search for the candidate material for the detector began with compounds of ^{6}Li and ^{10}B.

For the current design of the neutron spectrometer, Ti$^{10}B_2$ (30 % ^{10}B, natural abundance) and ^{6}LiF (96 % ^{6}Li) appear to fulfill all of the requirements. The neutron spectrometer is designed to operate at 0.1 K, and it is necessary to know the specific heat of the detector crystal at the operating temperature. However, previous measurements of the low-temperature specific heats of these samples have been inconsistent (especially with regards to TiB_2), so it is essential that the specific heat of materials be known quite accurately at the detector operating temperatures. To this end, we have measured the specific heats of TiB_2 and ^{6}LiF down to 0.45 K and use this data to extrapolate the specific heats to 0.1 K.

[a]The notation written here is a shorthand for nuclear reactions. The form of this notation is ¡target nucleus¿ (captured particle, emitted particle(s)) ¡product nucleus¿. Thus, we could write the reaction $^{10}_5B + ^1_0 n \rightarrow ^7_3 Li + ^4_2 \alpha$ as ^{1}0B(n, α)^{7}Li. Often the particles in parenthesis are written by themselves to describe a particular class of nuclear interactions. In the case (n, p), the notation indicates a reaction where a neutron is captured and an proton is released

7.2 Experimental

The TiB_2 sample was provided by Y-12 National Security Complex which had been originally obtained from Semi-Elements, Inc. of Saxonburg, PA (now defunct). From secondary ionization mass spectrometry (SIMS) and X-ray photoelectron sepctroscopy (XPS), the sample was found to be 92 % $TiB_{2\pm0.1}$ with 4 % C and 4 % O impurities. The sample measured was a single cylindrical specimen approximately 8 mm high and 5 mm in diameter with an apparent metallic sheen. The sample weighed 0.5382 g, and was loaded on to the calorimeter by attaching it to the measurement platform using a small amount of Apiezon N grease. The total specific heat was measured from 0.47 K to 100 K, then the specific heat of the TiB_2 was determined by subtracting the known specific heats of the empty calorimeter and Apiezon N grease from the total specific heat of the system.

The ^{6}LiF sample was formed from ^{6}LiF powder purchased from the Saint-Gobain Crystals and Detectors Company. The sample was assayed at 96 % isotopic purity with a melting point of 848°C. The powder was placed in a graphite liner and inserted into a fused silica ampoule. The sample was heated to 150 °C under dynamic vacuum of 4.4 $\times 10^{-7}$ torr for 90 minutes to eliminate water present in the powder and the ampule was subsequently sealed. The sealed ampule with the ^{6}LiF powder was then placed in a Bridgeman furnace and lowered slowly from the hot zone (temperature just above the melting point) to the cold zone (temperature just below the melting point) to form a large single crystal. The crystal was cut to a square prism measuring 7 mm x 7 mm x 3.5 mm and was a clear, colorless single crystal with no visible internal defects. The sample weighed 0.4385 g and was also loaded onto the calorimeter platform with a small amount of Apiezon N grease. The specific heat of the calorimeter, Apiezon N grease, and the ^{6}LiF sample was then measured from 0.45 K to 40 K. By subtracting

the known specific heats of the calorimeter and Apiezon N grease from the total specific heat of the system, the specific heat of ^{6}LiF was determined.

The specific heats of both the TiB_2 and the ^{6}LiF were measured on an semi-adiabatic calorimeter built on a ^{3}He pumped cryogen stage that is immersed in liquid He. The working range of this instrument is typically from 0.45 K up to a maximum of 40 K to 100 K, depending on the overall thermal conductivity of the sample. A description of a similar apparatus as well as additional details of the current apparatus can be found elsewhere (see section 2.2).[5, 6] The specific heat values obtained from this instrument typically have an accuracy better than 0.25 % with a precision better than 0.1 % based on measurements of a high purity copper sample. The TiB_2 and ^{6}LiF samples had a significantly smaller specific heat than copper, thus the results have an increased uncertainty. The approximate contributions to the total heat capacity for copper, TiB_2 and ^{6}LiF over various temperatures are given in table 7.1 with an estimation of the overall uncertainty for the measured compounds.

The uncertainty calculations for our specific heat measurements is handled in a unique manner since the equilibrium adiabatic techniques that we use preclude us from performing repeat measurements at each temperature. Consequently, the use of standard statistical methods involving replicate measurements cannot be applied. Historically, estimates of the accuracy and precision (uncertainties) in specific heat data have been achieved by performing measurements on standard references materials such as copper or benzoic acid and comparing these results, including the precision of empirical and theoretical fits, to the results of other laboratories over a period of many decades. The uncertainty estimate for both TiB_2 and ^{6}LiF have been determined by the percent deviation from copper, as measured on this apparatus, and the ratio of the percent contribution of the respective sample heat capacity to the percent contribution of copper. The percent contribution is the fraction of the heat capacity

Table 7.1. Average percent contributions to the total specific heat and estimated uncertainty for copper, TiB_2, and LiF

	Percent contribution			uncertainty (in percent)		
T (K)	copper	TiB_2	^{6}LiF	copper	TiB_2	^{6}LiF
0.5	73	49	4.6	0.2	0.3	3.5
1	73	47	7.9	0.22	0.32	2.0
5	57	15	7.4	0.22	0.72	1.5
10	55	6.9	9.3	0.22	0.84	1.1
20	65	4.1	14	0.21	1.3	0.89
30	70	4.3	19	0.21	1.5	0.67

attributed to the sample out of the total heat capacity (the heat capacity of the sample, the addenda, and Apiezon N grease). The error bars shown in all the figures are from this estimation of uncertainty which is summarized in table 7.1; where there are no error bars, the uncertainty is less than the symbol size.

7.3 Results and Discussion

The total molar specific heats of TiB_2 and ^{6}LiF are shown in figures 7.1 and 7.2, respectively. The measured specific heat of TiB_2 agrees fairly well with the previously published values of Westrum and Castaing, although the specific heat reported here is slightly lower.[7, 8] This is likely due to the better crystallinity of the current sample and the higher stoichiometric ratio of boron in this sample than in earlier samples. (For example the Westrum sample was characterized as $TiB_{1.96}$ and was a powdered sample rather than a single crystal).[7] The ^{6}LiF sample also has a lower measured specific heat when compared to previous measurements, but there is not as much difference here as was seen in the TiB_2 measurements. This is attributed to the enrichment of the ^{6}Li isotope, since lighter isotopes tend to give a lower specific heat. In this case, the previous measurements of both Clusius and Martin report the

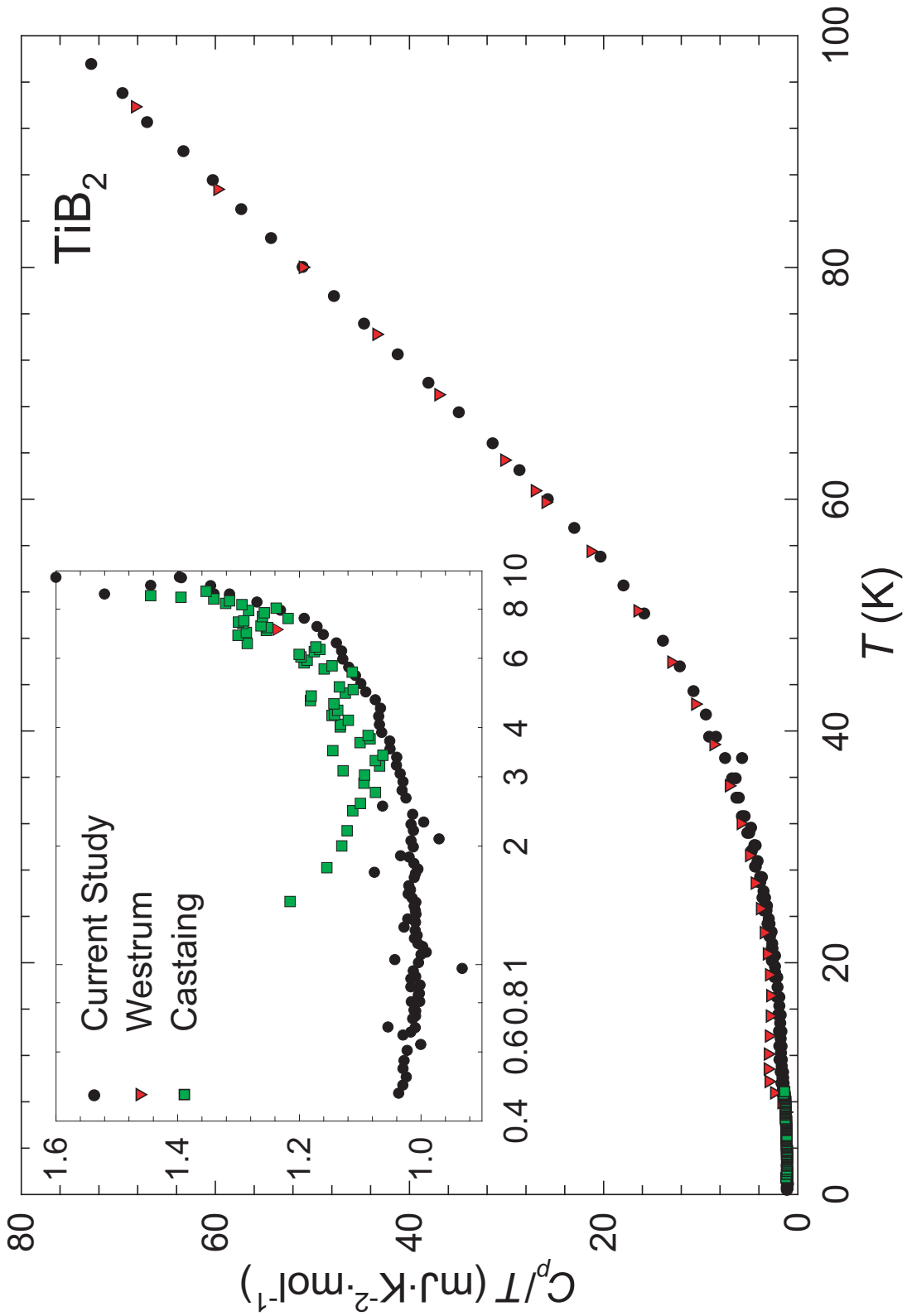

Figure 7.1. Specific heat of TiB_2 from this study, along with the data from Westrum and Castaing from $T = 0.5$ to 100 K.[7, 8]

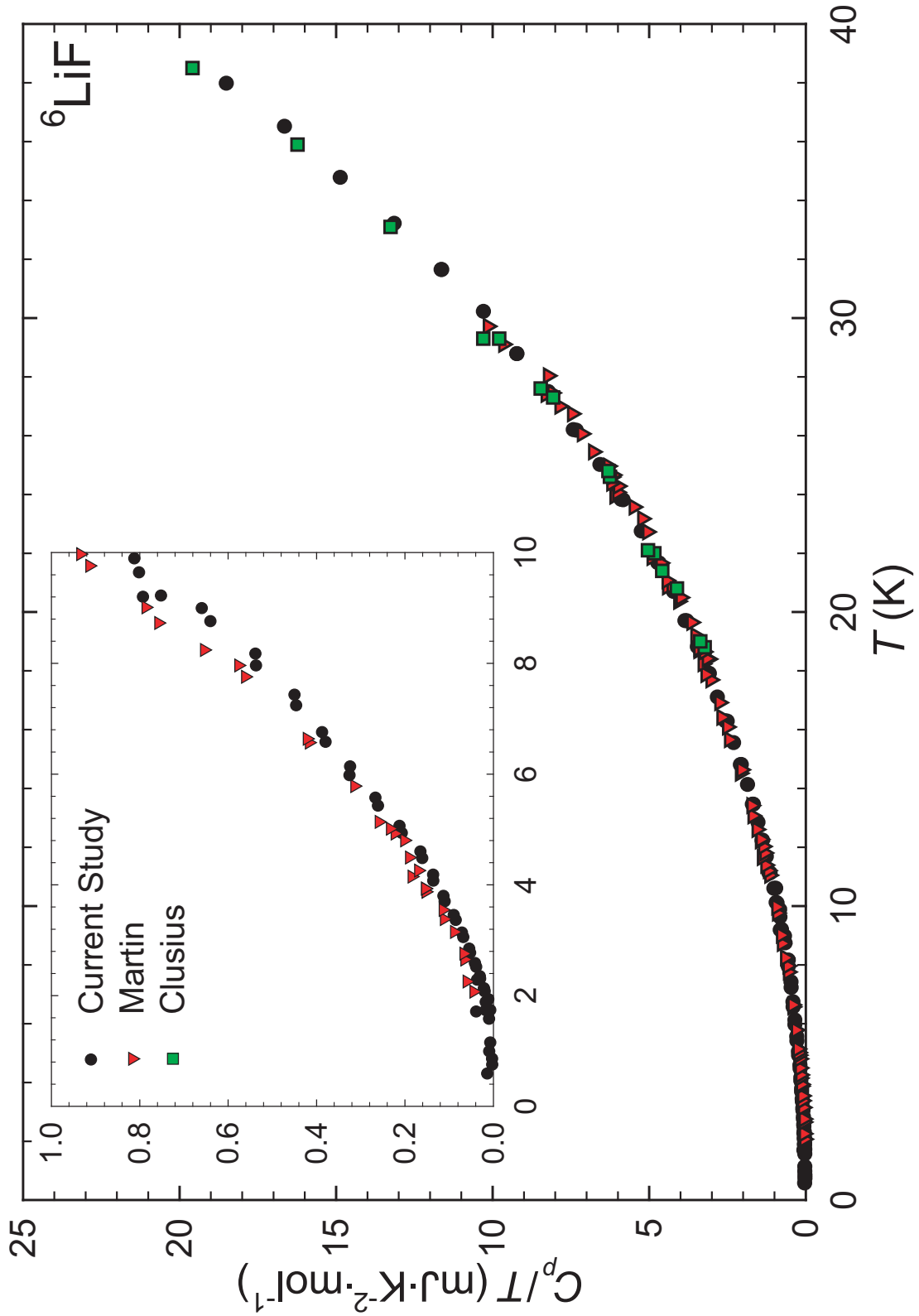

Figure 7.2. Specific heat of LiF from this study, along with the data from Clusius and Martin from $T = 0.5$ to 40 K. [9, 10]

specific heats of LiF with natural isotopic abundance (7.52% ^{6}Li and 92.48% ^{7}Li), whereas in this sample, the lighter ^{6}Li isotope has been increased from the natural abundance to 96%.[9, 10]. A simple isotopic correction can be applied to the specific heat using the square root of the ratio of the molecular weights, which results in good agrement with the current data and the literature values, except below 5 K, where there is greater deviation from Martin's data, but Martin's data does fall within our experimental uncertainty. (It should be noted that the isotopic correction mentioned above only works well in the low-temperature limit, where the density of states can be modelled with an harmonic approximation.)

7.3.1 TiB_2

To extrapolate the specific heat of TiB_2 to 0.1 K, we must obtain a model of the lattice and electronic specific heats. Typically, at temperatures below 10 K, the lattice and electronic specific heat are determined using the Debye extrapolation, which when the data is plotted as C/T vs. T^2 (see figure 7.3) should be a linear fit of the equation $C/T = \gamma + \beta T^2$. For TiB_2, the trend is linear as expected, except below 2 K where the value of C/T begins a steep upturn. This upturn is attributed to the hyperfine splitting of nuclear moments of both Ti and B by local magnetic fields. Titanium has two naturally occurring isotopes with a nuclear spin and nuclear moment, ^{47}Ti and ^{49}Ti, but the combination of these are only 13.8 percent of the natural abundance and the nuclear moments of the isotopes are relatively small. Likewise, the isotopes of boron, ^{10}B and ^{11}B, also have nuclear spin and nuclear moments, but these isotopes constitute 100 percent of the natural abundance of boron. Furthermore, the nuclear moments of these isotopes are significantly larger than those of the titanium isotopes. Thus, the contribution to the specific heat below 2 K is due almost entirely to the ordering of the nuclear spins of the boron isotopes.

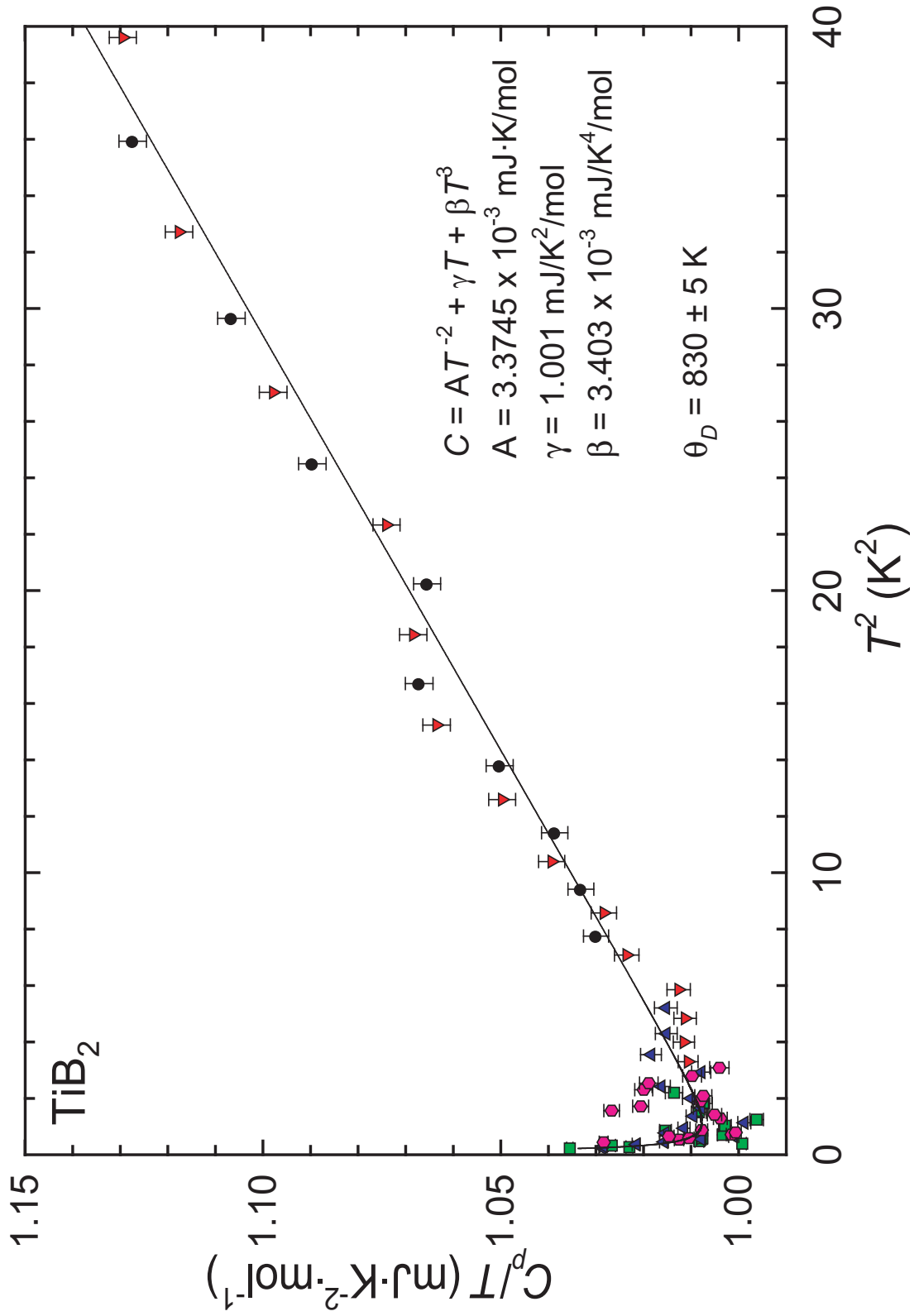

Figure 7.3. Low-temperature Debye extrapolation of TiB_2 with the hyperfine contribution. The various symbols represent the different series of data collected.

In order to model the electronic and lattice specific heat at low temperatures, the specific heat was fit to an equation of the form:

$$C = AT^{-2} + \gamma T + \beta T^3 \tag{7.5}$$

where AT^{-2} models the hyperfine contribution, γT is the electronic contribution, and βT^3 is the lattice specific heat. The resulting fit of this equation is shown in figure 7.3, and is plotted as C/T versus T^2 to show that the specific heat has a linear component in the Debye extrapolation until the onset of the hyperfine contribution. Values of γ and β obtained from the fit are 1.001 $\pm$ 0.019 mJ·K^{-2}·mol^{-1} and 3.403$\times$10^{-3} $\pm$ 0.070$\times$10^{-3} mJ·K^{-4}·mol^{-1} respectively and are slightly lower than previously published results, which again is consistent with the nature of this sample.[7, 8](The uncertainty here is caluclated from the standard deviation of the slope and intercept) Furthermore, the calculated Debye temperature, θ_D, for this sample is 830 $\pm$ 5 K compared to the values of 820 K and 807 from Castaing and Tyan, respectively, which is also consistent with using a sample that is higher in quality.[8, 11]

Although equation 7.5 adequately represents the experimental data to within experimental error, the AT^{-2} term is only an approximation of the high-temperature side of the hyperfine specific heat and cannot be used to predict the nuclear specific heat at low temperatures. To correctly extrapolate the specific heat to 0.1 K, a more exact model of the hyperfine contribution must be applied. Nuclear moments can generally be considered as two-level systems where the energies of the nuclear spin system populate one of the two levels. Specific heats of two-level systems are calculated from Schottky functions that have the form:

$$C_{\text{Schottky}} = nR\left(\frac{\theta_S}{T}\right)^2 \frac{g_0}{g_1} \frac{\exp\left(\theta_S/T\right)}{\left(1 + \left(g_0/g_1\right)\exp\left(\theta_S/T\right)\right)^2} \tag{7.6}$$

where θ_S is the Schottky temperature, n is the number of level systems(moles) in the sample and g_0/g_1 is the ratio of the degeneracies of the two levels, which for the nuclear splitting is set to 1.[12] The low-temperature specific heat can then be fit to the equation:

$$C_{tot} = C_{\text{Schottky}} + \gamma T + \beta T^3 \tag{7.7}$$

Since we are only working with the high-temperature side of the Schottky function, two different models were used to predict the behavior of the spin system below our measurements. The first model assumes that there is a weak, local magnetic field present at every B atom throughout the sample. This implies that the hyperfine contribution arises from the splitting of the nuclear levels in each B atom and thus n in equation 7.6 must be set to 2, since there are 2 moles of boron per mole of TiB_2 assuming that boron gives the only contribution to the hyperfine splitting. The second model assumes that the magnetic moments are not uniform throughout the system, and would be consistent with the hyperfine contribution arising from bonding inhomogeneities in the system. This could result from interstitial vacancies in the Ti-B lattice or from impurities in the sample, changing the bonding characteristics in some fraction of the sample. This would imply that n in Equation 7.6 represents the number of moles of the bonding inhomogeneities in the sample and should be allowed to float or vary in the fit and come to a "best" value. In both models, the splitting of the two nuclear levels is represented by θ_S and is allowed to vary in the fit.

A summary of the fitting results for both hyperfine models is given in table 7.2 and shown in figure 7.4. While both models yield similar results, the values of n and θ_S from the respective fits and what is known about the sample itself can give insight to the validity of the models. First, of the Schottky temperatures calculated

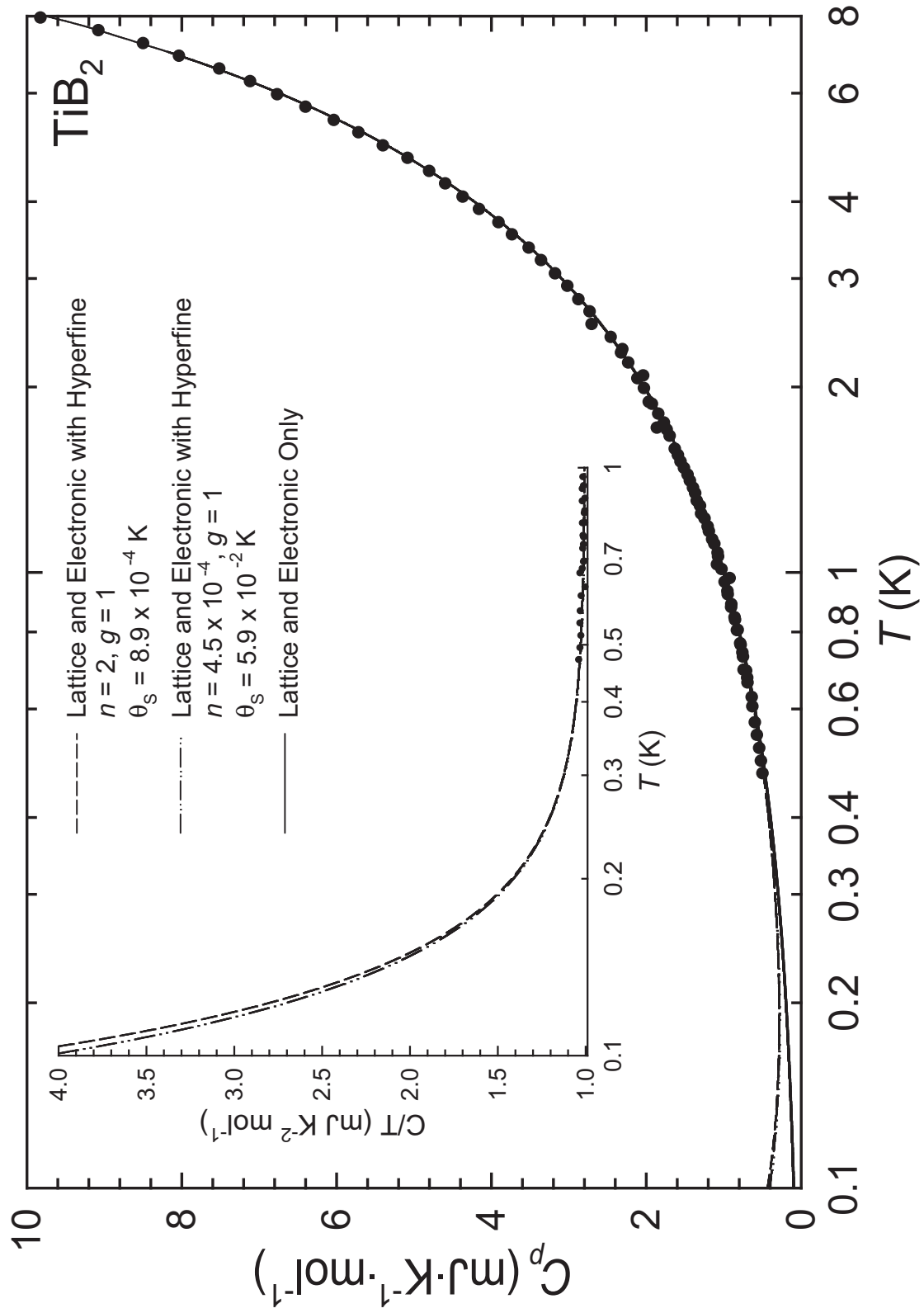

Figure 7.4. Low-temperature fits of the lattice and electronic specific heats of TiB_2 along with the additional hyperfine models for the specific heats and the extrapolation of the specific heat to 0.1 K.

from both models, the value of $\theta_S = 0.059$ K from the second model seems to be a more reasonable value based on comparisons to Schottky temperatures of similar boron compounds such as CaB_6.[13] Although this is not a quantitative measure of the validity of the second model, it is a useful comparison since we expect there to be similar bonding in the two systems. Secondly, from the high degree of covalent bonding in the Ti-B system, it is not expected to have unpaired electrons that would contribute to the local magnetic field at each B atom. Also, previous measurements on poorer samples of TiB_2 show a larger upturn and a higher onset temperature, suggesting that this feature is sample dependent.[8] The first model assumes that the magnetic moment in the sample is homogeneous, and it implies that all Ti-B bonds are the same, and must, therefore, all have some ionic character. The second model attributes the magnetic moments of the sample to bonding inhomogeneities. The value of n from the second model, 4.5×10^{-4} moles, is more consistent with the defects and bonding inhomogeneities that would be expected from a crystalline sample.

Of the two calculated models and from what is known about the sample, the second model seems to be more plausible, although the first model cannot be completely ruled out. The second model gives a specific heat at 0.1 K of 0.408 ± 0.027 $mJ{\cdot}K^{-1}{\cdot}mol^{-1}$using the value at 0.1 K from the first model to estimate the uncertainty. The uncertainty in the extrapolated specific heat was estimated in this manner since (a) there are no statistical methods available for calculating the uncertainties in Schottky functions and (b) the first model is an upper bound for the number of spin states in the system and the difference in specific heat between the two models would seem to provide a reasonable upper bound for the uncertainty. Presently, for a sample of this quality this would be the best calculation of the specific heat for TiB_2 at 0.1 K. It should be noted, however, that if the second model is correct, the size of

Table 7.2. Summary of Schottky fits for TiB_2

	n	Θ_S (K)	C_p ($T = 0.1$ K) ($mJ{\cdot}K^{-1}{\cdot}mol^{-1}$)
Debye Extrapolation	-	-	0.100 ± 0.001
Model 1	2	8.9×10^{-4}	0.435 [a]
Model 2	4.5×10^{-4}	5.9×10^{-2}	0.408 [a]

[a] Absolute uncertainties for the Schottky functions are unknown, but the maximum value for the uncertainties are estimated to be ± 0.027 mJ /K /mol.

the nuclear contribution ($C_{Schottky}$), and therefore the value of the specific heat at 0.1 K, will be sample dependent since the concentration of bonding inhomogeneities will vary from sample to sample. Also implied with the second model is that the ideal or intrinsic specific heat will be one without the hyperfine splitting, and consequently, the extrapolation should only use the electronic and lattice terms in equation 7.5. Thus, the best case of intrinsic specific heat at 0.1 K would be 1.0 $\times10^{-4}$ ± 0.01 $\times10^{-4}$ $J{\cdot}K^{-1}{\cdot}mol^{-1}$, although each sample of TiB_2 would have to be measured to obtain an accurate value for the specific heat.

7.3.2 LiF

As in the case of TiB_2, the Debye extrapolation was used for $T \leq 10$ to model the lattice and electronic specific heat of ^{6}LiF. Figure 7.5 shows the plot of C/T vs. T^2; however, unlike TiB_2 there is no low-temperature upturn and the y-intercept is zero. The absence of the upturn in ^{6}LiF indicates there are no nuclear hyperfine interactions, and the zero-intercept indicates the absence of an electronic contribution to the specific heat. In most respects, this makes the estimation of the low-temperature heat capacity easier since there is only the lattice contribution, but from figure 7.5 (and table 7.1) it can be seen that there is a greater uncertainty primarily due to the sample size and the significantly smaller heat capacity contribution.

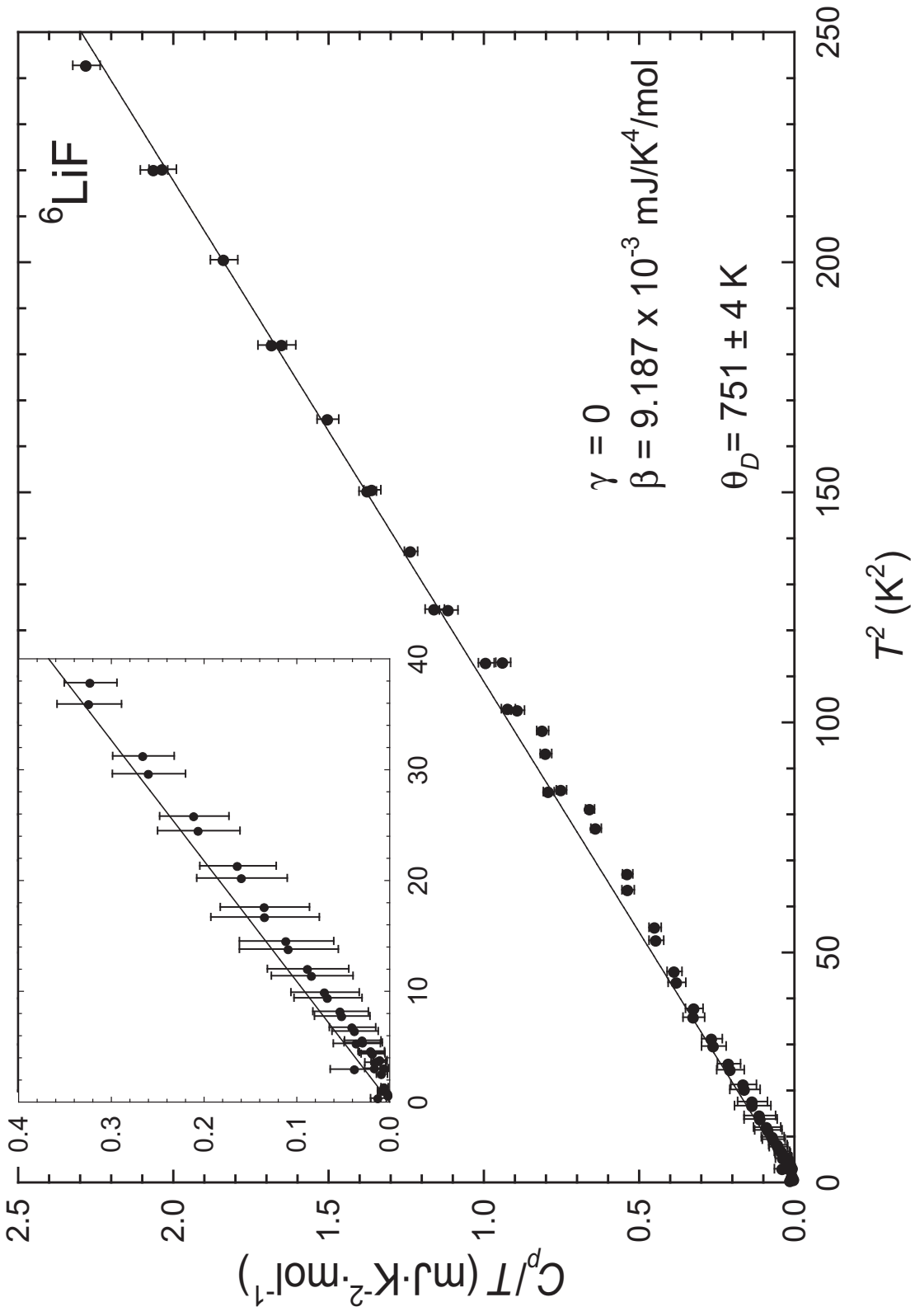

Figure 7.5. Low-temperature Debye extrapolation of ^{6}LiF

Although ^{6}LiF has an increased uncertainty in the specific heat below 10 K, it was relatively easy to fit the data to an equation of the form $C = \beta T^3$ where the value of β was found to be 9.187 $\times 10^{-6}$ J·K^{-4}·mol^{-1} for $T^2 < 250$ K. This gives a Debye temperature of 751 $\pm$ 4 K, which is slightly higher than Martin's reported value of 737 $\pm$ 9 K.[10] This discrepancy can be attributed to the isotopic differences between the two samples. When an isotopic correction is applied, making an adjustment to the natural abundance of Li isotopes, the Debye temperature is 746 $\pm$ 4 K. Although this value is still slightly higher than that reported by Martin, it is within the error limits reported by Martin, thus this is an acceptable value for the Debye temperature.

The aim of these measurements was to calculate the heat capacity of ^{6}LiF at 0.1 K. Unlike the TiB_2 sample, the absence of any electronic and nuclear contribution makes the extrapolation down to 0.1 K relatively straightforward. It is only the uncertainly of the heat capacity values that causes complications in the calculations. However, extrapolating the lattice heat capacity of the ^{6}LiF to 0.1 K gives C = 9.19 $\times 10^{-9}$ $\pm$ 0.15 $\times 10^{-9}$ J·K^{-1}·mol^{-1}, where the uncertainty is obtained from the standard deviation of β. The resulting extrapolation of the specific heat to 0.1 K can be seen in figure 7.6.

7.4 Conclusion

This study has given us the best available values for the specific heats of TiB_2 and ^{6}LiF at 0.1 K. However, using the specific heat data of TiB_2 (especially extrapolated values) for thermodynamic purposes is not recommended since the specific heat appears to be highly sample dependent, which is further complicated by the complex nature of the Ti-B system. Indeed, if one examines the phase diagram for Ti-B there is a significant range of stoichiometric ratios that are considered TiB_2.[14] From this

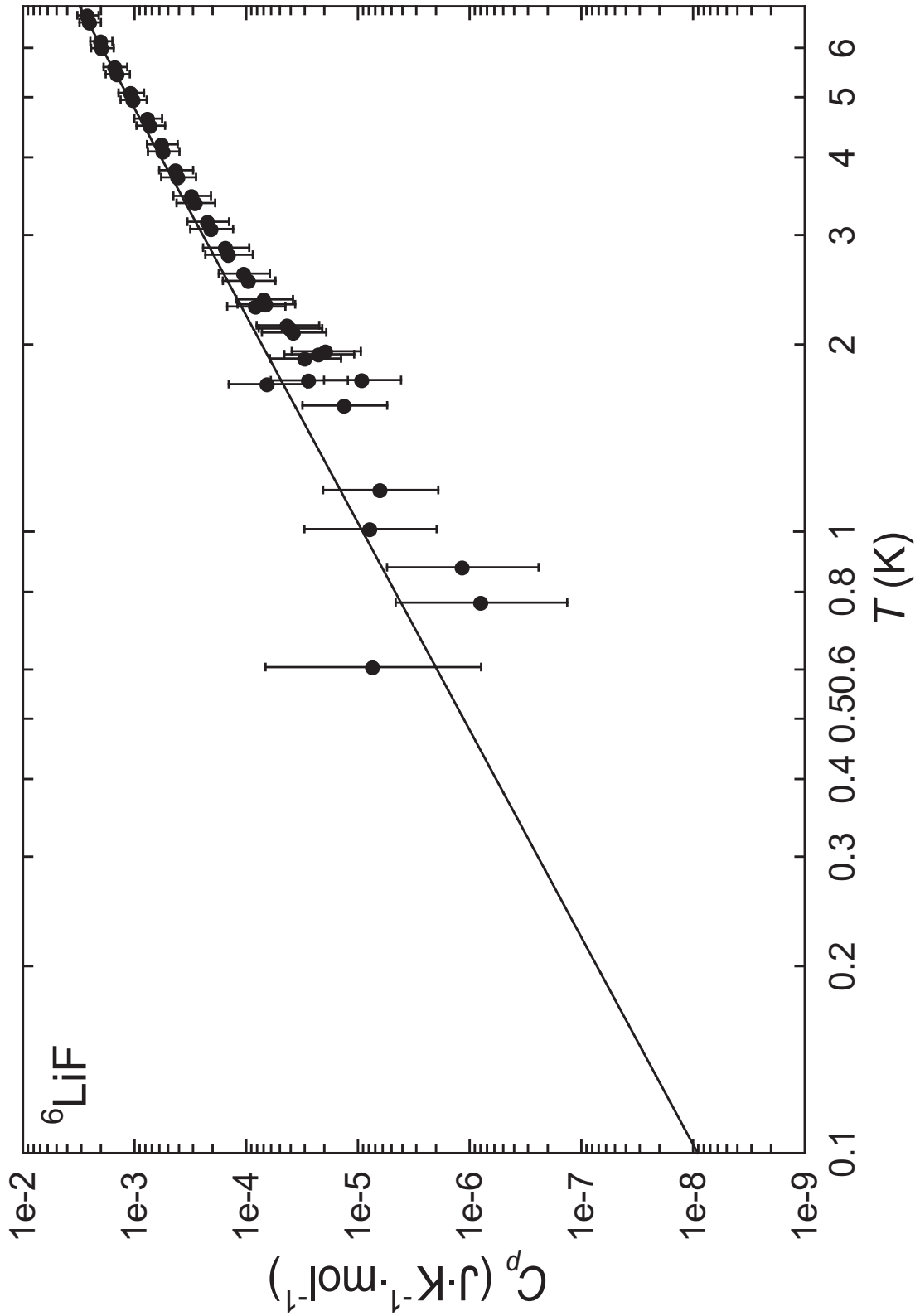

Figure 7.6. Low-temperature fits of the lattice specific heat of ^{6}LiF along with the of the specific heat down to 0.1 K.

and the variation in the specific heat between the current study and literature, it is likely that one must measure the low-temperature specific heat for each sample of TiB_2 in order to obtain the most accurate value. ^6LiF, on the other hand, has a more consistent stoichiometric ratio, which should lead to more reproducible specific heat results. However, the specific heat is effected a great deal at low temperatures by the isotopic ratio of Li. Specifically, in this sample the enrichment of the ^6Li isotope from natural abundance to 96 % gives a total molecular weight change of -3.4 %; nonetheless, the isotopic specific heat difference can be easily accounted for in the low temperature limit.

Reprinted from *the Journal of Nuclear Materials*, in press, accepted 16 August 2005, Brian E. Lang, Marcus H. Donaldson, Brian F. Woodfield, Arnold Burger, Utupal N. Roy, Vincent Lamberti, Zane W. Bell, *Specific heat measurements of TiB_2 and ^6LiF from 0.5 to 30 K*, 9 Pages.,

References

[1] Taubes, G., *Bad Science: The short life and weird times of cold fusion*, New York: Random House, **1993**.

[2] Chow, D. T.; Lindeman, M.; Cunningham, M.; Frank, M.; Barbee, T. W. J.; Labov, S. E., *Nucl. Instr. and Meth. A* **2000**, *444*, 196–200.

[3] Niedermayr, T.; Hau, I. D.; Miyazaki, T.; Terracol, S.; Burger, A.; Lamberti, V. A.; Bell, Z. W.; Vujic, J. L.; Labov, S. E.; Friedrich, S., *Nucl. Inst. and Meth. A* **2004**, *520*, 70–72.

[4] Moseley, S. H.; Mather, J. C.; McCammon, D., *J. Appl. Phys.* **1984**, *56*, 1257–1262.

[5] Lashley, J. C.; Lang, B. E.; Boerio-Goates, J.; Woodfeild, B. F.; Darling, T. W.; Chu, F.; Migliori, A.; Thoma, D., *J. Chem. Thermo.* **2002**, *34*, 251–261.

[6] Woodfield, B. F., *Specific Heat of High-Temperature Superconductors: Apparatus and Measurement*, Ph.D. thesis, University of California, Berkeley, **1995**.

[7] Westrum, E. F. J.; Clay, G. A., *J. Chem. Thermo.* **1978**, *10*, 629–636.

[8] Castaing, J.; Caudron, R.; Toupance, G.; Costa, P., *Solid State comm.* **1969**, *7*, 1453–1456.

[9] Clusius, K.; Goldman, J.; Perlick, A. Z., *Zaturforschg.* **1949**, *4a*, 424–453.

[10] Martin, D. L., *Phil. Mag.* **1955**, *46*, 751–758.

[11] Tyan, Y. S.; Toth, L. E.; Chang, Y. A., *J. Phys. Chem. Solids* **1969**, *30*, 785–792.

[12] Gopal, E. S. R., *Specific Heats at Low Temperatures*, New York: Plenum Press, **1966**.

[13] Vonlanthen, P.; Felder, E.; Degiorgi, L.; Ott, H.; Young, D.; Bianchi, A.; Fisk, Z., *Phys. Rev. B* **2000**, *62*, 10076.

[14] Ma, X.; Li, C.; Du, Z.; Zhang, W., *Journal of Alloys and Compounds.* **2004**, *370*, 149–158.

Appendix A

Derivations of Various Thermodynamic Relationships

A.1 Derivation of equation 6.9

Starting from the thermodynamic definition of specific heat at constant pressure

$$C_p = T\left(\frac{\partial S}{\partial T}\right)_p \tag{A.1}$$

$$\left(\frac{\partial C_p}{\partial p}\right)_T = \frac{\partial}{\partial p}\left(T\left(\frac{\partial S}{\partial T}\right)_p\right)_T \tag{A.2}$$

$$\left(\frac{\partial C_p}{\partial p}\right)_T = \left(\frac{\partial T}{\partial p}\right)_T\left(\frac{\partial S}{\partial T}\right)_p + T\left(\frac{\partial}{\partial p}\left(\frac{\partial S}{\partial T}\right)_p\right)_T \tag{A.3}$$

$$\left(\frac{\partial C_p}{\partial p}\right)_T = T\left(\frac{\partial}{\partial p}\left(\frac{\partial S}{\partial T}\right)_p\right)_T \tag{A.4}$$

$$\left(\frac{\partial C_p}{\partial p}\right)_T = T\left(\frac{\partial}{\partial T}\left(\frac{\partial S}{\partial p}\right)_T\right)_p . \tag{A.5}$$

From the Maxwell relations it is known that:

$$\left(\frac{\partial S}{\partial p}\right)_T = -\left(\frac{\partial V}{\partial T}\right)_p . \tag{A.6}$$

Therefore, equation (A.5) can be expressed as:

$$\left(\frac{\partial C_p}{\partial p}\right)_T = T\left(\frac{\partial}{\partial T}\left(-\frac{\partial V}{\partial T}\right)_p\right)_p \tag{A.7}$$

$$\left(\frac{\partial C_p}{\partial p}\right)_T = -T\left(\frac{\partial^2 V}{\partial T^2}\right)_p . \tag{A.8}$$

A.2 Derivation of lattice microstrain specific heat from the change in volume from basic thermodynamic relationships.

Starting with the Maxwell relation

$$dU = TdS - pdV \tag{A.9}$$

$$\left(\frac{\partial U}{\partial T}\right)_p = T\left(\frac{\partial S}{\partial T}\right)_p - p\left(\frac{\partial V}{\partial T}\right)_p \tag{A.10}$$

$$\left(\frac{\partial U}{\partial T}\right)_p = C_p - p\left(\frac{\partial V}{\partial T}\right)_p \tag{A.11}$$

$$C_p = \left(\frac{\partial U}{\partial T}\right)_p + p\left(\frac{\partial V}{\partial T}\right)_p \tag{A.12}$$

$$\left(\frac{\partial C_p}{\partial V}\right)_T = \left(\frac{\partial}{\partial V}\left(\frac{\partial U}{\partial T}\right)_p\right)_T + \left(\frac{\partial p}{\partial V}\right)_T\left(\frac{\partial V}{\partial T}\right)_p + p\left(\frac{\partial}{\partial V}\left(\frac{\partial V}{\partial T}\right)_p\right)_T \tag{A.13}$$

$$\left(\frac{\partial C_p}{\partial V}\right)_T = \left(\frac{\partial}{\partial V}\left(\frac{\partial U}{\partial T}\right)_p\right)_T + \left(\frac{\partial p}{\partial V}\right)_T\left(\frac{\partial V}{\partial T}\right)_p . \tag{A.14}$$

The derivative of U with respect to T and V (equation A.14) can then be evaluated as follows:

$$dU = TdS - pdV \tag{A.15}$$

$$\left(\frac{\partial U}{\partial V}\right)_T = T\left(\frac{\partial S}{\partial V}\right)_T - p\left(\frac{\partial V}{\partial V}\right)_T \tag{A.16}$$

$$\left(\frac{\partial U}{\partial V}\right)_T = T\left(\frac{\partial S}{\partial V}\right)_T - p \tag{A.17}$$

$$\left(\frac{\partial}{\partial T}\left(\frac{\partial U}{\partial V}\right)_T\right)_p = \left(\frac{\partial T}{\partial T}\right)_p\left(\frac{\partial S}{\partial V}\right)_T + T\left(\frac{\partial}{\partial T}\left(\frac{\partial S}{\partial V}\right)_T\right)_p - \left(\frac{\partial p}{\partial T}\right)_p \tag{A.18}$$

$$\left(\frac{\partial}{\partial V}\left(\frac{\partial U}{\partial T}\right)_p\right)_T = \left(\frac{\partial S}{\partial V}\right)_T + T\left(\frac{\partial}{\partial T}\left(\frac{\partial S}{\partial V}\right)_T\right)_p \cdot \tag{A.19}$$

From the Maxwell relations it is known that:

$$\left(\frac{\partial S}{\partial V}\right)_T = \left(\frac{\partial p}{\partial T}\right)_V \cdot \tag{A.20}$$

Thus substitution of equation (A.20) into equation (A.19) yields:

$$\left(\frac{\partial}{\partial V}\left(\frac{\partial U}{\partial T}\right)_p\right)_T = \left(\frac{\partial p}{\partial T}\right)_V + T\left(\frac{\partial}{\partial T}\left(\frac{\partial p}{\partial T}\right)_V\right)_p \tag{A.21}$$

$$\left(\frac{\partial}{\partial V}\left(\frac{\partial U}{\partial T}\right)_p\right)_T = \left(\frac{\partial p}{\partial T}\right)_V + T\left(\frac{\partial}{\partial T}\left(\frac{\partial p}{\partial T}\right)_p\right)_V \tag{A.22}$$

$$\left(\frac{\partial}{\partial V}\left(\frac{\partial U}{\partial T}\right)_p\right)_T = \left(\frac{\partial p}{\partial T}\right)_V \cdot \tag{A.23}$$

Combining equations A.14 and A.23 will give

$$\left(\frac{\partial C_p}{\partial V}\right)_T = \left(\frac{\partial p}{\partial T}\right)_V + \left(\frac{\partial p}{\partial V}\right)_T\left(\frac{\partial V}{\partial T}\right)_p \tag{A.24}$$

where p is the applied pressure due to the microstrain, and can be calculated in terms of the Bulk Modulus, B, by:

$$-p = B\frac{\Delta V}{V} \cdot \tag{A.25}$$

Thus equation A.24 will yield:

$$\left(\frac{\partial C_p}{\partial V}\right)_T = \left(\frac{\partial}{\partial T}\left(\frac{-B\Delta V}{V}\right)\right)_V + \left(\frac{\partial}{\partial V}\left(\frac{-B\Delta V}{V}\right)\right)_T \left(\frac{\partial V}{\partial T}\right)_p \tag{A.26}$$

$$\left(\frac{\partial C_p}{\partial V}\right)_T = -B\Delta V \left(\frac{\partial}{\partial V}\left(\frac{1}{V}\right)\right)_T \left(\frac{\partial V}{\partial T}\right)_p \tag{A.27}$$

$$\left(\frac{\partial C_p}{\partial V}\right)_T = B\Delta V \left(\frac{1}{V^2}\right) \left(\frac{\partial V}{\partial T}\right)_p \tag{A.28}$$

$$dC_p = \frac{B\Delta V}{V^2} \left(\frac{\partial V}{\partial T}\right)_p dV \tag{A.29}$$

$$\int dC_p = \int_V^{V_0} \frac{B\Delta V}{V^2} \left(\frac{\partial V}{\partial T}\right)_p dV \tag{A.30}$$

$$\Delta C_p = B\Delta V \int_V^{V_0} \frac{1}{V^2} \left(\frac{\partial V}{\partial T}\right)_p dV \cdot \tag{A.31}$$

However, it is known that volume, V, is a function of T ($V(T)$), therefore the integral can be expressed as:

$$\Delta C_p = B\Delta V \int_V^{V_0} \frac{1}{V(T)^2} \left(\frac{\partial V(T)}{\partial T}\right)_p dV(T) \cdot \tag{A.32}$$

This can be simplified from the relation:

$$dV(T) = \frac{dV(T)}{dT} dT \tag{A.33}$$

which gives

$$\Delta C_p = B\Delta V \int_T^{T_0} \frac{1}{V(T)^2} \left(\frac{\partial V(T)}{\partial T}\right)_p \left(\frac{dV(T)}{dT}\right) dT \tag{A.34}$$

$$\Delta C_p = B\Delta V \int_T^{T_0} \frac{1}{V(T)^2} \left(\frac{dV(T)}{dT}\right)^2 dT \cdot \tag{A.35}$$

Appendix B

Additional Information on Data Collection and Analysis Programs

This section describes the new data collection, data analysis, and PID control programs for the new small-scale apparatus. It is intended as a user guide and as a source of reference for control code algorithms.

B.1 The Autocal Program

This program originated from the MS-DOS/BASIC autocal program written by Dr. Brian Woodfield and designed to run the Boerio-Goates large-scale calorimeter. This BASIC code was updated and re-written in Visual BASIC 6.0 to be run on the Windows® operating system. This was done for two primary reasons. First, continual updates of the Windows® operating system were severely limiting the support of MS-DOS programs thus making them increasingly obsolete. Second, updating the software to run in the Windows® environment makes the computer interface more user friendly which decreases the learning curve of the software; thus, new users spend more time collecting data and learning the scientific principles of the machinery and less time merely learning the program.

Once this program (designated autocalv2) was successfully re-written and generally de-bugged, its code was taken and modified to interface with the instrumentation for the microcalorimeter over the General Purpose Interface Bus (GPIB). This program has been designated Autocalv2b. While the two programs are distinct, designed to run solely on their respective instrument sets and output the raw data in entirely different formats, the user interfaces of the two programs are essentially the same. The main differences in the user interface revolve around commands related to the AC resistance bridge which is used to measure the thermometer resistance in the microcalorimeter; whereas, the large-scale calorimeter uses a DC technique to measure the thermometer resistance.

B.1.1 The Main Window

On opening the Autocal Program, a splash screen appears as the program initializes all of the instrumentation via the GPIB. Once the initialization is complete, the main window comes up (figure B.1), and the program begins to make a reading of the calorimeter temperature every ten seconds. From this window, the user can enter the measurement window or other set-up related windows. Once the heat capacity measurement is complete, the program automatically returns to the main window and proceeds to make temperature readings every ten seconds. The following is a list of menu/button options available in this window (Items available by function key are listed in brackets []):

Measure Brings up the measurement screen and begins the data collection as outlined in the schedule. [**F1**]

Parameters Brings up a menu of settings for the program. Detailed in Section B.1.2. [**F2**] or *file>parameters*

Heater OFF(ON) Toggle switch that manually turns the calorimeter heater on or off to allow the calorimeter to be heated up to the desired temperature. [**F5**]

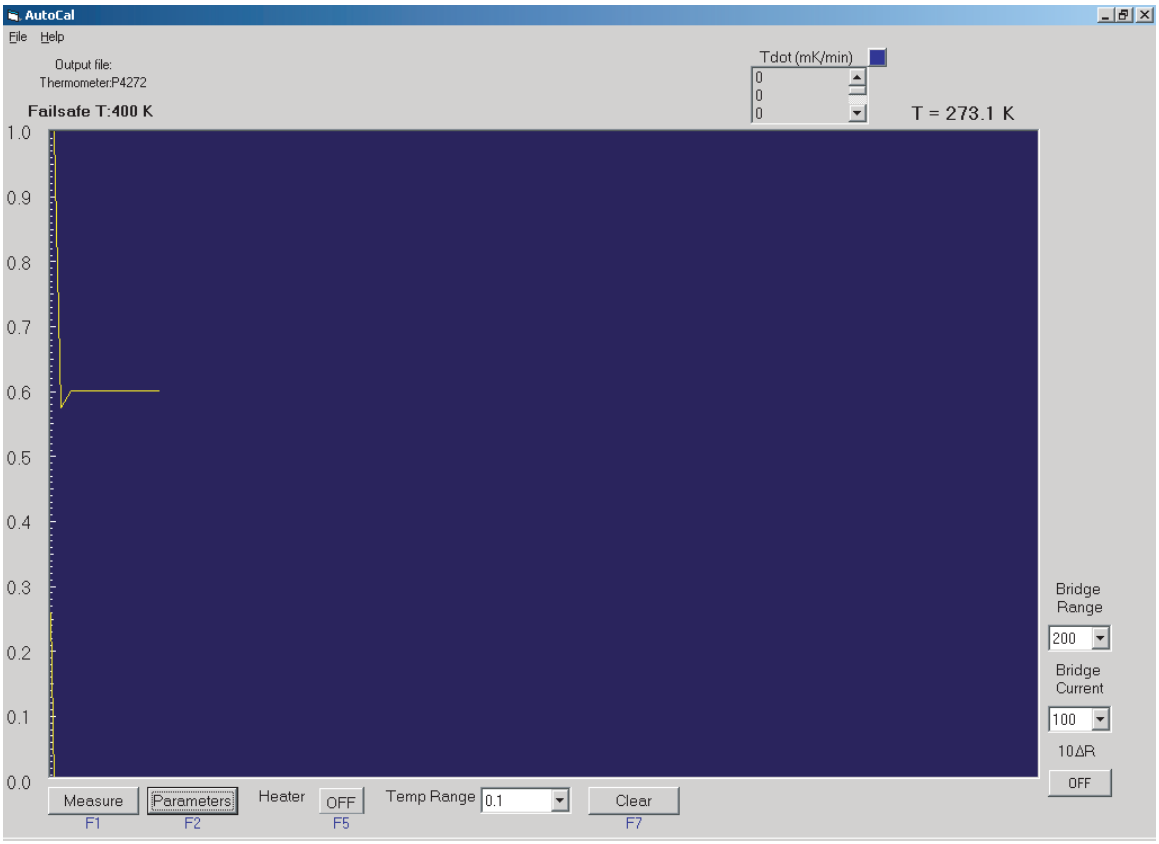

Figure B.1. The main screen for the autocalv2b program.

Clear Clears the screen of old temperature data plots. [**F7**]

Temp Range List box that allows user to change the sensitivity of the temperature display. Value in the box is the range of the vertical temperature scale. Default value is 0.1 K.

Bridge Range List box that allows the user to set the maximum resistance range on the AC Bridge. The user sets the range to be as close to the measured resistance as possible without setting the max range below the thermometer resistance. Otherwise a reading error occurs. The bridge range in this screen carries over to the measurement mode. Default value is 200 Ωs.

Bridge Current List box that sets the current going through the thermometer from the AC resistance bridge. Carries over to the measurement mode. Default value is 100 mA.

10ΔR OFF(ON) Toggle switch that turns on/off the AC resistance bridge's 10ΔR mode. This mode increases the sensitivity of the resistance reading by increasing

the number of significant figures (Does not effect the bridge reading in the measurement mode.)

Tdot Displays dT/dt averaged over the last n number of points, where n is determined by the window size in the parameters menu window (see section B.1.2). Displayed in milliKelvin per minute. Clicking the blue button to the right brings up a separate window that displays Tdot.

file>cp calculation Drop down menu item that opens an input screen to adjust the heat capacity subtraction. (see section B.1.3)

file>schedule Drop down menu item that brings up the schedule menu window for the data collection routine. (see section B.1.4)

file>load Allows user to load an existing schedule file into the schedule menu window.

file>exit Exits the Autocal program. [**F12**] or window close button.

help>debug Opens a debugging window.

B.1.2 Parameters Menu

The parameters menu screen allows the user to change several of the operating conditions of the program. Most of these effect the variables in the measurement mode of the program; however, a few do not. All of the changes to the parameters are updated as soon as the user tabs (or clicks) to the next menu item. It should be noted that there is some redundancy in the parameters window with controls in the main screen, but as these variables are updated in the parameters window, they are changed in the main screen as well and vice versa. The following is an explanation of the functionality of the parameters menu items.

Thermometer Allows the user to select the thermometer function (.scl) file to use via a list box, if a different thermometer from the default (P4272) is used in the measurement. For instance, the microcalorimeter instrument set can be used with the current large-scale adiabatic calorimeter, which would require the autocal program to use a different thermometer function file to convert the measured thermometer resistance to temperature. The thermometers currently available

for use are hard coded into the autocal program and any additions/changes must be made in the Visual BASIC code.

Heater R Allows the user to select the resistance of the standard resistor in the heater circuit via a list box. The default value for the microcalorimeter heater circuit is 1000 Ωs. The value displayed in the list box is only an approximation of the resistance. However, the true resistance is linked to the approximate value displayed in the list box, and these values are hard coded into the autocal program.

Heater Voltage Constant voltage applied across the calorimeter heater circuit in μV. This is changed by typing numeric text into the text box. The default value is 1μV. This value does not effect the measurement mode of the program. Note: Changing the heater voltage does not turn the calorimeter heater on or off.

Failsafe temperature Sets the maximum temperature (in K) to which the calorimeter can be heated. The default value is 400 K. In the main screen, this will automatically turn off the calorimeter heater once the temperature reaches the failsafe temperature. In the measurement mode, the program will adjust the pulse voltage so that the calorimeter will not exceed the failsafe temperature.

Thermometer Current List box that sets the current going through the thermometer from the AC resistance bridge. Carries over to the measurement mode. Default value is 100 mA.

Thermometer Range List box that allows the user to set the maximum resistance range on the AC Bridge. The user sets the range to be as close to the measured resistance as possible without setting the max range below the thermometer resistance. Otherwise, a reading error occurs. The bridge range in this screen caries over to the measurement mode. Default value is 200 Ωs.

Temperature Range List box that allows user to change sensitivity of the temperature display. Value in the box is the range of the vertical temperature scale. Default value is 0.1 K.

Window Size List Box that allows user to select the number of points in a walking window used to calculate Tdot in the main screen. Default is 5 points.

Time Interval Time in seconds between each measured point in the main screen window. Default is 10 seconds.

B.1.3 Cp Subtraction Window

This window allows the user to set the function files and molar/mass contributions of all the components of the calorimeter, so the molar specific heat of the current compound can be calculated as the program is running. This option works in conjunction with the new functionality of this program, which allows the operator to see an estimate of the heat capacity as the measurements are being made, rather than having to wait until the program has fully completed to view any results. On opening this window, the user is prompted to enter the number of functions to be subtracted and to list them in a series of text boxes. For functions which are split up over several function files (to accommodate different temperature regions), the files can be listed in the same text box separated by a comma (with no spaces). The operator is then forwarded to a second menu screen where the gram/molar contributions of the function files and the total molar contribution of the sample can be entered.

The data input from this window is not only stored in the resident memory, but it is also written to the file *C:\labware2000\autocal1b\cp_sub.ini*. Once this file is written, each time the program opens, the parameters are read from this file, and the program uses them for the C_p calculation. Thus, the operator does not need to update these values for every run, only when the parameters change, such as when a new compound is loaded into the calorimeter.

B.1.4 Pulse Schedule

This window allows the user to create or change an existing schedule for collecting the specific heat data. This window must be opened in the course of running the program in order to run in the measurement mode. If it is not done before the user attempts to collect the data, the user will automatically be directed to the

Pulse Schedule Window. If the user attempts to continue the program at any time without updating the essential information in the Pulse Schedule window, the user will be prompted to give this information. In this way, the user will always provide the program all of the information needed to run the measurement/data collection routine correctly.

In this window, the user is prompted to create two new files – an output file and a schedule file. The output file records all of the time and resistance data for the pulses and drifts from the measurement mode. The format and evaluation of these files will be discussed subsequently. Unlike previous versions of this program, the schedule file that is created serves more as a record of the parameters used in the course of data collection, and not to direct the measurement itself. Rather, when the user selects the *Accept Schedule* Button, all of the variables for the data collection mode are stored in resident memory. Also, the date of the run is automatically time stamped onto both the output file and the schedule file.

The directories of these two output files are set by the program. For the schedule file, the directory is hard coded in the program and is set to *C:\workdata\schedule*. For the output file, the directory is set by the file *C:\labware200\autocal1b\autocal.ini*. The directory will stay the same until a new directory is selected in the pulse schedule window (selecting *Accept Schedule*); thus updating the *autocal.ini* file. Also, if the *autocal.ini* file is deleted the default directory becomes *C:\workdata* until a new directory is selected, at which time a new *autocal.ini* file is created.

Below is a description of the function of each of the components in the pulse schedule window:

Description This text box allows the user to enter a description about the sample being run. This text and the date become the header line for the schedule and output files.

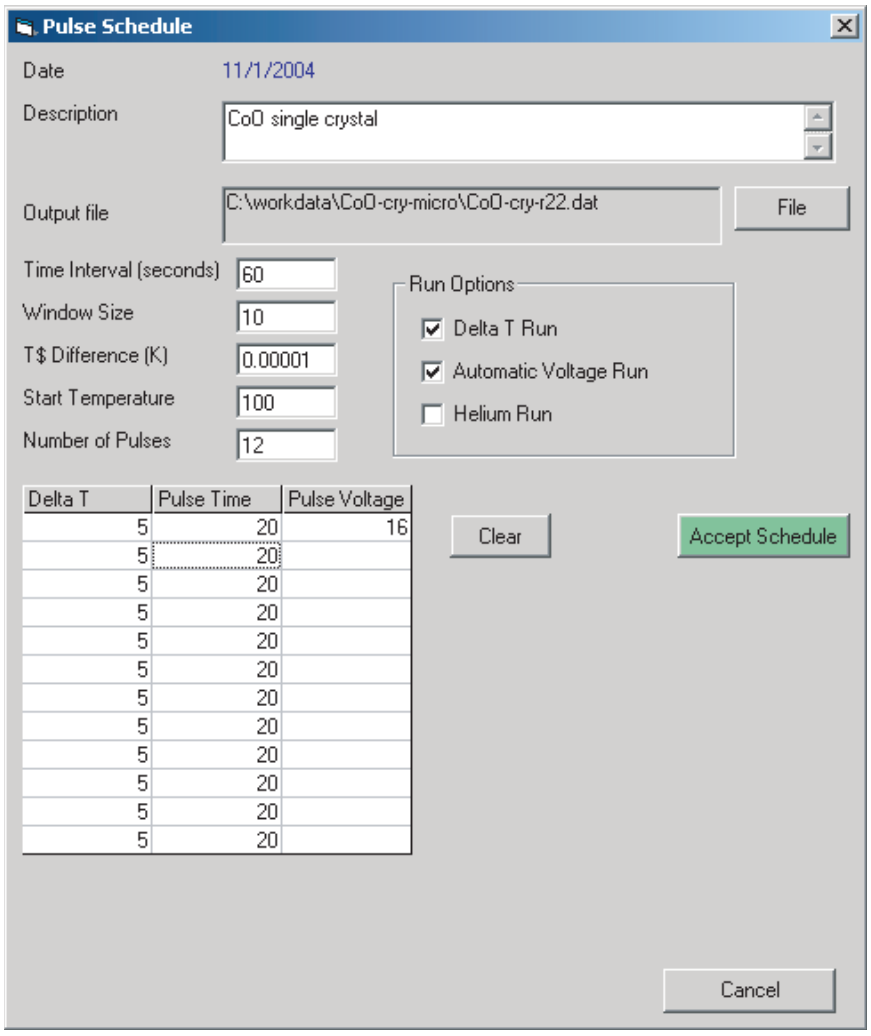

Figure B.2. The pulse schedule window for the autocalv2b program.

Output File Clicking the file button brings up a windows save dialog box allowing the user to name the file. Existing files can only be overwritten after the user is prompted to confirm the overwriting operation.

Time interval Time in seconds between each measured point in a drift. The default value is 60 seconds. Normally, this is only changed during runs in the helium region, where the time interval is set to 45 seconds.

Window size Number of points in the walking window that is used to calculate Tdot (dT/dt) and T$ (extrapolated temperature at t=0 for the drift) for the drift at each temperature. Default value is 10.

T$ Difference This is the threshold limit used to determine if the program will begin a pulse before the requisite number of points for a drift. If the difference

in calculated T$ for three consecutive points in a drift is less than or equal to this threshold value, the program will automatically enter the pulse mode without finishing the remaining points for the drift. The default value is 0.00001 K (0.01 mK) to keep the program from pulsing prematurely under most circumstances. This parameter can also be changed in the measurement window.

Start Temperature Temperature at which the run is to be started.

Run Options These are check boxes that allow the user to change the temperature/current setting for the run. Following are descriptions of the functionality of these choices:

Delta T Run Checking this option tells the program to make any adjustments to the pulse voltage based on temperature differences between points rather than on absolute temperature values. This option is almost always used, so by default this setting is selected.

Automatic Voltage Run When this option is selected, the first pulse voltage is obtained from the first row in the schedule data grid. Subsequent pulse voltages are calculated by the program base on the previous pulse voltage, the expected ΔT, and actual ΔT. Deselecting this option requires the user to enter a voltage value for every pulse. This option is selected by default.

Helium Run Selecting this option changes all of the ΔTs in the schedule grid to increments of $T/10$ beginning with the Start Temperature (If *Delta T Run* is not selected, the absolute temperatures have values of T + $T/10$. Deselecting this option, restores the data in the schedule grid to the original values).

Number of Pulses Sets the number of pulses to be measured. This value also controls the number of rows in the Temprature/Time/Pulse Voltage grid, which represents the measurement schedule. The following is a description of the functionality of the various item associated with the control grid:

Delta T This field is the expected difference in temperature between each drift when the *delta T Run* box is checked. Otherwise the field is the expected temperature (in K) for each drift in the measurement.

Pulse time Time, in minutes, for each pulse.

Pulse Voltage Voltage for the pulse. The value in the top row must always be filled in. If the run option *Automatic Voltage Run* is selected no other values need to be entered. (See entry for *Automatic Voltage Run*)

SHIFT Selecting a cell in the schedule grid and then holding the SHIFT key allows the user to copy the contents of the selected cell down the column.

Clear Empties the selected cell(s) of data. Holding SHIFT while performing this operation Deletes the selected row(s) and adjusts the Number of Pulses accordingly.

Accept Schedule Allows the user to save the schedule file and return to the main screen.

Cancel Returns program to the main screen with out saving any of the schedule parameters.

B.1.5 The Measure Environment

Once the operator presses the *Measure* button [**F1**], the program brings up a new screen and enters its measurement mode. In this mode, the program begins its first drift by re-initializing the AC resistance bridge, and then waiting 30 seconds for the bridge to stabilize. At this point, the program records the temperature of the calorimeter over the *time interval* as defined in the *pulse schedule* window; this is one data point for the drift. This cycle repeats until either the number of data points is equal to the max points or the *T$* difference condition has been satisfied. The program then starts the pulse by turning on the calorimeter heater and simultaneously sending a signal to start the counter timer (see section 2.3.3 on electronic configuration). Once a minute, for the duration of the pulse, the program collects the heater voltage and the heater current. During the pulse, most of the user operations in the drift mode are unavailable. Once the pulse has ended, the control commands are returned to normal and the program again enters the drift mode.

Following are a list of options available during the drift mode for the measurement environment:

Mark Places a control command in the output file that is useful for keeping track of points in a given drift by highlighting the points from the first marked point onward. Once the mark option has been triggered, the program displays the total of marked points.[**F1**]

Max Points Sets the maximum number of points for the drift via the arrow buttons or by the up/down ($\uparrow$ / $\downarrow$) keys. Holding down shift while clicking the button increases or decreases the number of points by 5. The default value sets max points at 25.

Pulse Manually initiates the pulse cycle after the next point. [**F3**]

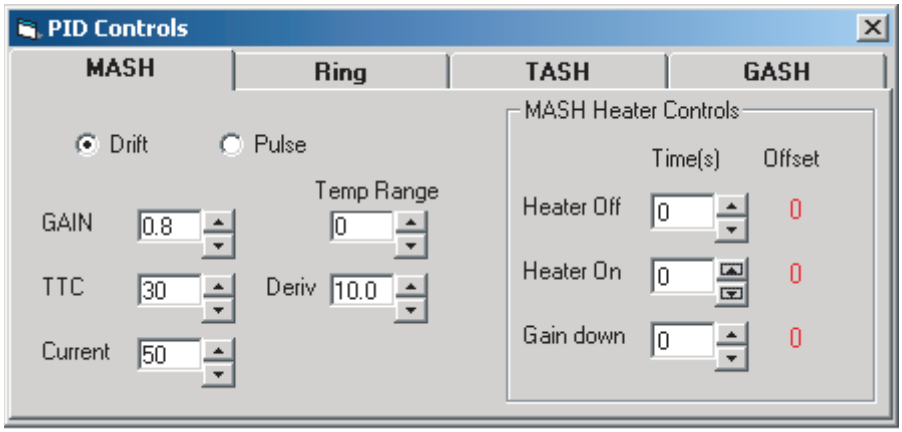

Figure B.3. PID control window

Clear Clears the screen of old temperature data plots. [**F7**]

Temp Range List box that allows user to change the sensitivity of the temperature display. Value in the box is the range of the vertical temperature scale.

Heater V Brings up a window that displays the next pulse voltage (either the calculated voltage in or taken directly from the schedule parameters), and allows the user to input a new pulse voltage.[**F8**]

Cp Calc Brings up a new window that shows the estimated heat capacity of the sample.[**F9**]

PID settings Displays the PID settings window (see section B.1.6).[**F10**]

**Tdot / T$** Displays dT/dt(Tdot) and T$ (extrapolated temperature at t=0 for the drift) for the last n number of points, where n is determined by the window size in the parameters menu window (see section B.1.2). Clicking the blue button to the right brings up a separate window that displays Tdot and T$.

file*>*exit Exits the measure environment, and the program returns to the main screen. [**F12**] or window close button.

help*>*debug Opens a debugging window.

B.1.6 PID Settings

In the measurement environment, the program is set up to send commands to the PID control program to adjust the parameters for optimal shield control at a

given temperature. The code for these commands is in one file for each shield that is read into the program when it is started (i.e. the data for MASH is in the file *C:\labware2000\mash.tbl*). The main purpose for this is that PID settings not only change as a function of temperature, but also when the program switches from drift to pulse mode, and it is generally more effective for the program to change the parameters than for the operator to do so at every pulse/drift change. However, due to variations in the system, it is sometimes desirable for the operator to be able to override the normal settings, which is the purpose of this window. This section will deal with only the operations of this window and not how the various settings effect the PID control, since this was discussed in section 3.1.

The PID control window (see figure B.3) has four tabs with the names of the shields (MASH, Ring, TASH, and GASH), which allow the user to change the parameters for the shield that is selected. Although at present there are only three shields in use on the microcalorimeter (TASH is not used), the system was originally set up for use with four shields, and this same window is currently employed in the program for the large-scale calorimeter (the code is the same between both programs). Opening this window calls up the most current setting for the PID controls. When the parameters are changed, the new values are the ones that are recalled when this window is opened.

The Following is a summary of the commands available in this window:

Drift/Pulse These radio buttons allow the user to switch between the drift and pulse settings.

Temp Range Displays the lower value of the temperature range over which the PID parameters are valid. Changing the value in this box allows the user to view and update the settings over all of the working temperature ranges.

Gain Allows the user to adjust the gain (proportional) setting.

TTC Allows the user to adjust the integral or thermal time constant (TTC).

Deriv Allows the user to adjust the derivative control.

Current Allows the user to change the maximum current value for the present temperature range.

MASH Heater Controls The MASH heater controls work independently of the PID controls, but these parameters are useful for maintaining good shield control. These controls originated with measurements on the large-scale calorimeter. For certain temperature ranges, just after the the end of a pulse, MASH would have the tendency to heat up too much and not come into control, thus placing the system into a non-adiabatic state. To compensate for this, the MASH heater was turned off a few seconds before the pulse was to end, causing the system to heat less and allowing the shield to come to equilibrium more quickly. The heater would be turned back on after making sure that the PID controller would not dump too much heat to the shield. Initially, the gain setting was increased to help the system return to equilibrium quickly, then once the shield was controlling, the gain was dropped back down to the normal operating level. The amount of time required for each of these operations is temperature dependent and is defined by a set of functions written into the code. The function of this window is to allow the user to input variations to the time required for each of these operations, and the difference from the calculated value is displayed as the offset. The value of the offset remains constant until it is changed by the user. Essentially, this is just a constant that is added to the temperature dependent functions of the mash heater controls. At present, these controls have been disabled for the microcalorimeter since they are not needed. However, they *are* used for the large-scale calorimeter, so a description has been included.

Heater Off Displays time (in seconds) before the end of the pulse that the MASH heater will be turned off at the current temperature.

Heater ON Displays time (in seconds) after the beginning of the drift when the MASH heater will be turned back on.

Gain Down Displays time (in seconds) after the beginning of the drift when the PID gain control for MASH will be returned to its nominal value. This value takes into account the time required for the controller to return the shield to a state of equilibrium with the calorimeter.

B.2 Autocalc Program

The purpose of the autocalc program is to take the output file from autocal and process it to give the specific heat data for the temperatures measured. This program is a modification of the old DOS autocal program that had been in use for analyzing

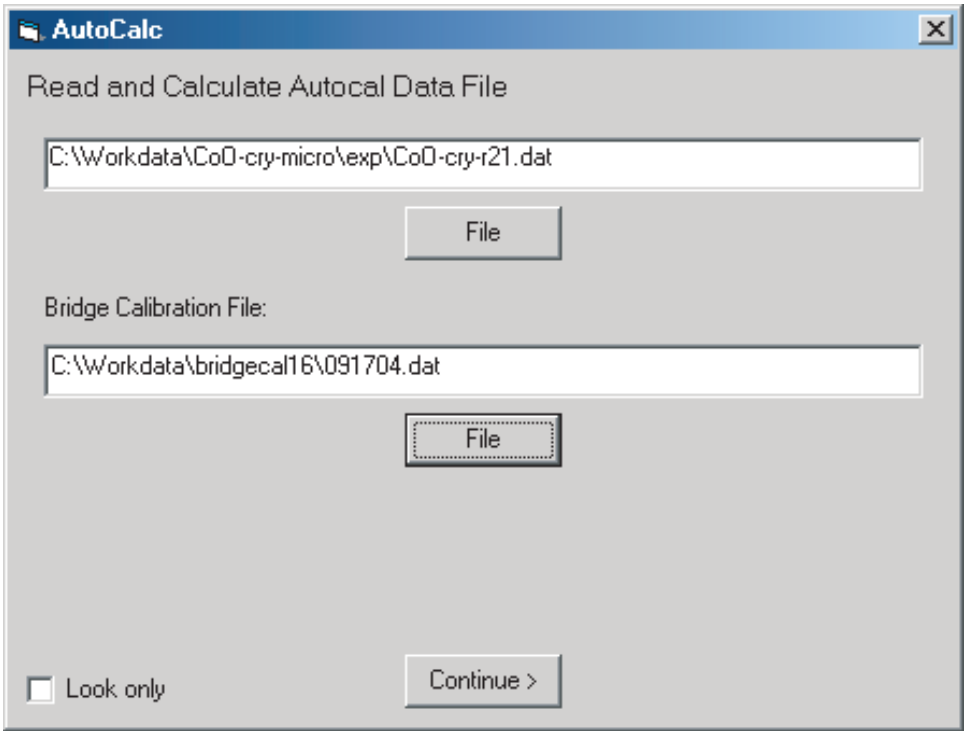

Figure B.4. Input window for the Autocalc program

the specific heat data for the large scale calorimeter with three major differences. The first difference is that the code had to be altered to read in the new output format for the autocalc v2b program and to use the bridgecal data file (see section B.4.1) to correct the resistance measurements. The second difference is that the hierarchy of the code structure itself had to be completely restructured in order to work with Visual BASIC's event-driven programming environment. To check that this program would work as it should, the autocalc program was first modified to work with the output files from the current large-scale calorimeter, and the resulting program generated data equivalent to the old autocalc program, thus indicating that the new program operated correctly. The final difference in this program is that it automatically allows the user to apply a curvature correction to the data and select the output file names. Previously, this operation required the user run two additional programs after completing the DOS autocalc program.

On opening the program (Autocalc v2b for analyzing the autocal data from the microcalorimeter), the user is prompted to enter the Autocal data file and the bridge calibration file. The user can either type in the file path or select the respective *file* buttons under each text box to open the file through a standard *file open* window. At this point, the user can select *continue* to allow the program to open the files and begin the process of calculating the data. The user can also select the *Look Only* box which will allow the user to see the behavior of the drifts but will not calculate specific heat values.

Continuing through the program, the points of each drift are displayed, and the user is allowed to select the points which best represent the equilibrium or steady state condition of the drift. It is these point, in conjunction with the pulse data, that are used to calculate the specific heat. The following is a list of options available for the user to select and adjust the data points in the drift screen:

←, → The left/right arrow keys allow the user to select or deselect points to be included in the drift calculation.

ALT + ←, ALT + → Using **ALT** with the arrow Keys allows the user to select a point for deletion (shown in red), and subsequently remove the selected point by using the **DELETE** key. Alternatively, one or more points may be selected by selecting an area on the screen via the mouse by clicking and holding the left mouse button. Also, the left most point can be deleted by using the **F4** key.

FIT Fits the selected points of the drift and displays the calculated T$. This can be repeated as many times as necessary after selecting or deselecting points. Once the user is done with this drift and continues to the next drift, the most recent equation is used in calculating the midpoint temperatures for the foredrift and afterdrift. [**F1**]

SAVE Saves the drift file data in the temp directory. This is generally useful for working out problems that may arise. [**F2**]

Number of fits, [F3] Allows the user to fit the drift in one or two equations (splitting the foredrift and afterdrift to 2 different equations). [**F3**] toggles between the two options.

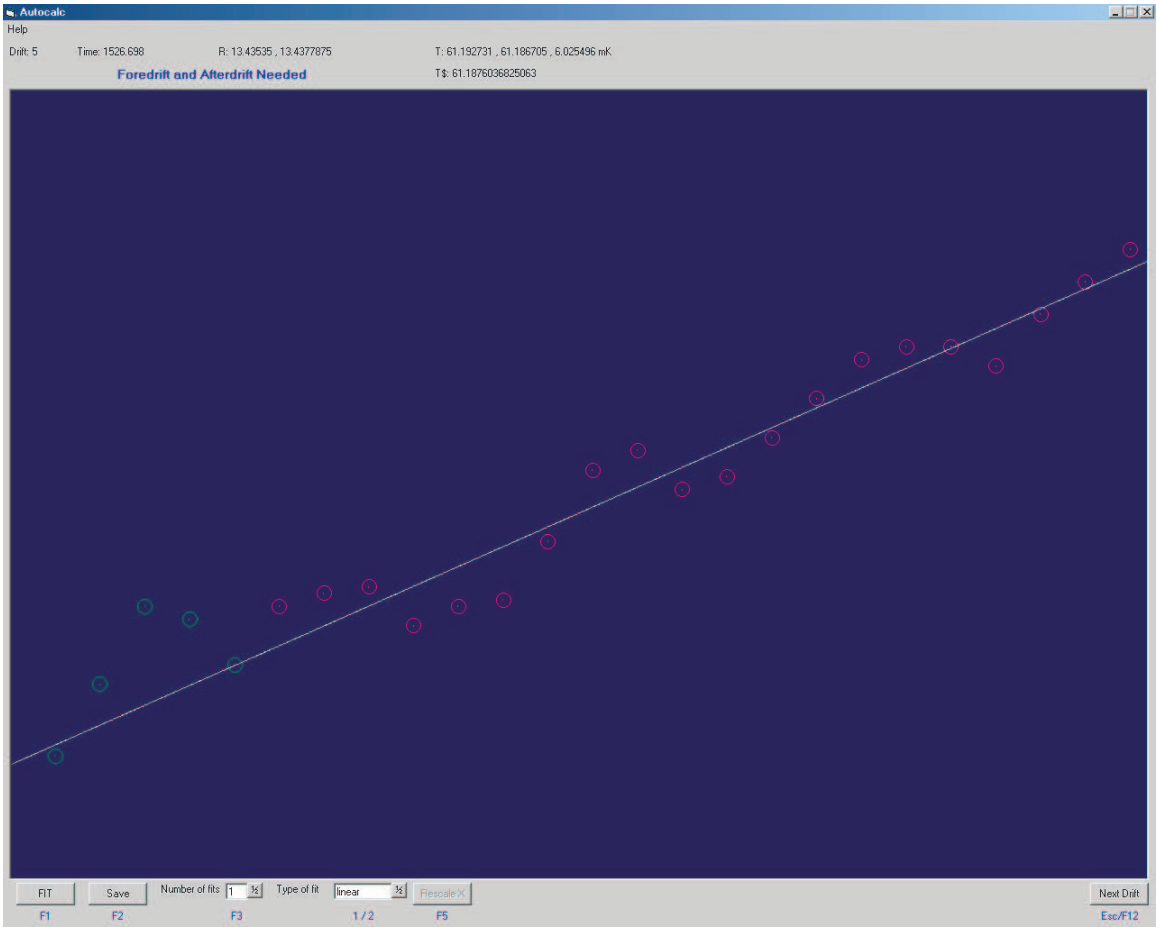

Figure B.5. Drift screen for the Autocalc program.

Type of Fit, 1/2 Allows the user to fit the drift to either a linear or a quadratic equation, using number keys **1** and **2** respectively. The default is a linear equation.

Rescale X Allows the user to re-scale the x-axis if points on the far-left or far-right have been deleted. (The y-axis is scaled automatically) [**F5**]

Next Drift Indicates to the program that the user has finished analyzing the current drift, and then displays the data points for the subsequent drift. On the final drift, the specific heats are calculated and the output window is opened. **ESC,** [**F12**]

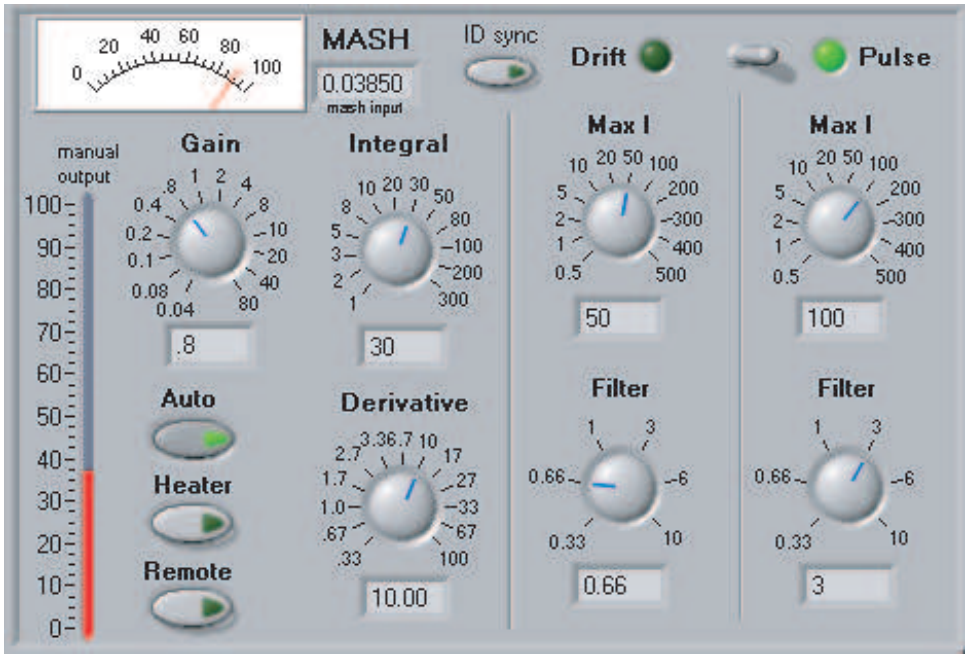

Figure B.6. A sample front panel for the PID control program

B.3 PID Control Program

This section details the Labview PID control program in terms of the front panel operations and other functions accessible to the user. Following this will be a description of some of the main elements of the Labveiw wiring structure, their purpose and other technical notes.

The front panel interface for the PID control program can be seen in figure B.6. At the top left of the control panel is an analog display of the percent output gain sent to the respective adiabatic shield heater, and adjacent to this is a digital display showing the voltage input into the PID algorithm. Below is a description of the function of buttons, dials, etc. on the virtual interface. The digital indicators below each of the dials display the current setting for the respective dial, this is especially important in remote operations.

Auto The Auto button allows the user to switch between automatic and manual

mode. When the Auto button is selected, the program uses the PID *sub vi* to determine the output gain, and when it is deselected, the user is able to set the output gain with the manual output slider.

Heater When the Heater button is selected, the program instructs the heater power supply for the respective shield to turn on, otherwise the power supply is turned off (the maximum current is set to zero).

Remote The Remote button toggles between remote and local operations. In the remote mode (button selected), commands from the data collection override any settings from from the front panel except for the Auto and Heater buttons. Any other changes to the front panel PID settings will not be implemented until the Remote button is deselected.

Manual Output This slider allows the user to adjust the percent output gain manually when the Auto button is deselected.

Gain Sets the proportional gain constant for the PID algorithm.

Integral Sets the integral time constant (in seconds) for the PID algorithm.

Derivative Sets the derivative time constant (in seconds) for the PID algorithm.

ID sync When selected, this button overrides the derivative setting and sets the derivative time constant as one-third of the integral time constant.

Drift/Pulse Switches between the drift and pulse settings for Max I and the Filter, and uses the respective setting on the dials below the Drift or Pulse indicators. In remote operations, the indicator light shows which settings are being used.

Max I Selects the maximum current output for the heater power supply. The Drift/Pulse switch determines which one of the two Max I settings is sent to the power supply.

Filter Selects the filter time (in seconds) for the moving boxcar average. The Drift/Pulse switch determines which one of the two filter settings is used.

B.3.1 Labview code structure

This section will describe the the main sub-units of the Labview code structure, their purpose, and other pertinent information.

The bulk of the Labview code structures are nested inside a single loop that continues indefinitely until the program is halted. Before the loop begins, there are

three main elements to the code that run. The first prepares the NI 4351 card for taking measurements; defining the channels to be read, and setting up parameters such as the digital filter. The second process initializes the (virtual) serial port, the RS-232/USB connection, and clears all the data in the buffer. The final process initializes three sets of arrays that are used in the boxcar filters.

Thermocouple voltage reading

The first part of the PID control program is the reading of the thermocouple voltages for all of the shields. This process is illustrated in figure **??**. In each iteration of the loop, the NI345x CHECKREAD *sub vi* reads all of the input voltages from the NI 4351 card and outputs the numeric values as a two-dimensional array (this includes time information as well). Following this, an Index Array *sub vi* extracts the zeroth component of the index array, which is a one-dimensional array containing just the voltage values. This signal is split to each of the individual PID algorithms, and a second Index Array *sub vi* extracts the voltage for the appropriate shield. The MASH thermocouple voltage is 0^{th} item in the array, the Ring voltage is the 1^{st} item, and the GASH voltage is the 2^{nd} item in the array. Once the thermocouple voltage has been extracted, the signal is processed by another *sub vi* that takes a maximum and a minimum input values (± 1) and converts the voltage into a percentage (-1 V is 0%, 1 V is 100%, and 0 V is 50%). This signal is sent to the Boxcar Filter *sub vi*.

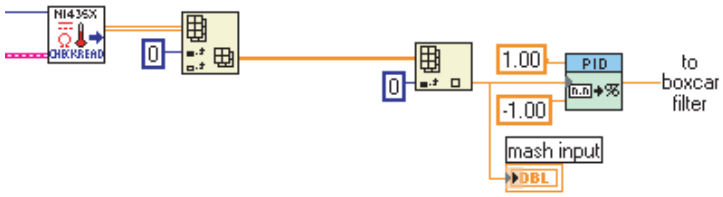

Figure B.7. Labview structural components used to acquire the thermocouple voltage from the NI-4351 card and then convert these values to a percentage.

Boxcar Filter

The Boxcar Filter *sub vi* was designed to average the percentage signal using a variable walking window to help filter some of the noise of the signal. The filter algorithm first determines the walking window size by dividing the filter time by the loop time, and then adds the current value of the percent span to an array containing the previous data. The values of points in the array are added together, and then divided by the number of points in the array to obtain the average value of the input data. The algorithm also compares its value to the previous walking window size (the Numeric In variable; see figure B.8) and incrementally increases the number of points averaged in the one-dimensional array, which is necessary to avoid sudden changes in the average when the filter time is increased. A final part of the algorithm removes the last data point in the algorithm and increases the index of the remaining data points to prepare for the next data point (this is effectively the walking window). An important part of this algorithm is that the Output Array, Input Array, Numeric Out, and Numeric In data terminals must be linked to the sides of the main do loop with a Labview structure called a shift register, which allows the data in the array to remain in memory from one iteration of the loop to the next.

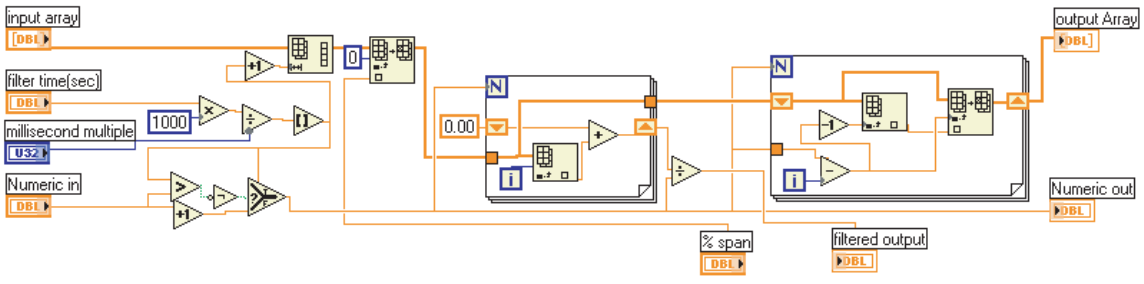

Figure B.8. Labview structural components of the boxcar filter.

PID *sub vi*

The heart of the shield control program uses the PID advanced *sub vi* packaged with the Labview PID toolkit that takes several inputs into the *sub vi* and produces the appropriate PID response. The primary inputs are the averaged voltage signal from the boxcar filter (which has a code structure that allows one to switch the input from positive to negative response using a true false constant if experimental conditions warrant), and the PID constants that are input from the front panel of the Labview program. Additional inputs include the setpoint (set at 50%), the output range (0 to 100 percent), and the switch from auto to manual control, which in the manual mode uses inputs from the manual slider on the front panel to set the percent maximum of the output current. The output from the PID advanced *sub vi* is sent to a second *sub vi* that converts the output percentage to a voltage between 0 and 10 V, which is then output to the PCI-6703 card and then to the shield control heater.

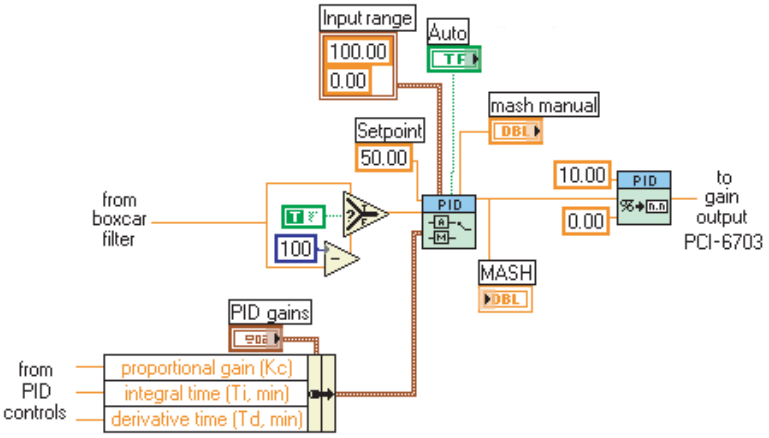

Figure B.9. Inputs into the Labview PID *sub vi*.

PID constant controls

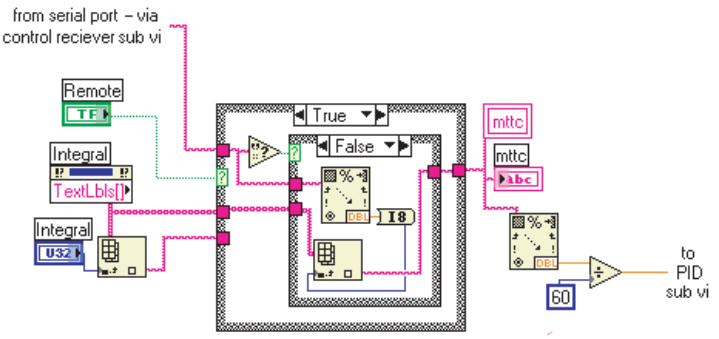

Figure B.10. Components of the PID constant controls.

The inputs for the PID control parameters are text controls changed by knobs on the front panel using an index array *sub vi* to extract the numeric value of the index corresponding to the front panel control.The index values of the PID variables correspond to the inputs of the PID controls from the data collection computer. The data from the PID variables goes through a logic gate used to evaluate the PID control parameters from the front panel and from the data collection computer. The first part of the logic gate tests if the individual PID control is in the remote mode or not. If the PID system is not in the remote mode (the remote switch is off), the remote switch sends a boolean string of false to the logic gate that simply sends the value of the PID control through the gate and to the PID algorithm. When the PID control is in the remote mode, the remote switch sends a boolean string of true to the logic gate that sends the value of the PID constant signal to a second logic gate. This logic gate tests for a change in the PID constant from the data collection computer, and if a signal has been sent, the gate sets the PID constant to the new value; otherwise, the current value for the PID constant is used. For the integral and derivative values, the numeric constants are divided by 60, to convert the gain values from seconds to minutes since the PID algorithm uses values of minutes. There is an additional logic gate for when the ID sync button is selected that overrides the derivative setting and sets the derivative time constant as one-third of the integral time constant.

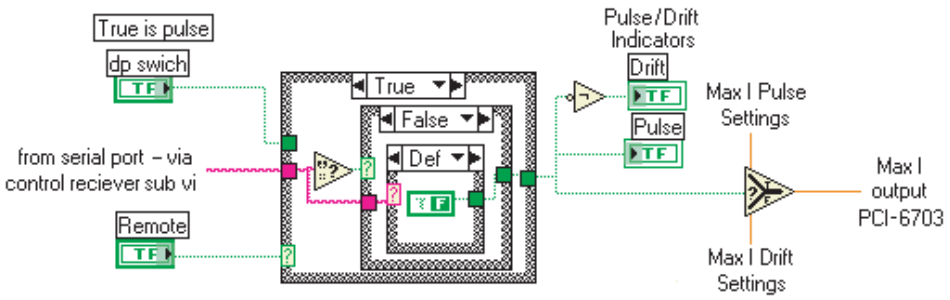

Figure B.11. Pulse/drift switch logic gate components

Pulse/Drift controls

To switch between the pulse and drift mode there is a toggle switch on the front panel that sends a true/false boolean string out to a logic gate. The logic gate tests if the PID control is in the remote mode, a nested gate checks for signals from the data collection computer. The output from this logic gate is a true/false boolean string that is sent to two true/false test switches that regulate which filter and maximum current control settings should be used. A boolean string of true corresponds to pulse control settings, and a string of false corresponds to drift control settings.

Maximum current and filter controls

The maximum current and filter controls are similar to the PID constant controls in that the data output from the front panel passes though the same type of logic gate as the PID controls. The outputs from both sets of logic gates pass though a true/false test switch, which regulates the pulse/drift settings (see previous section). The output for the filter time is directed to the boxcar filter, and the heater maximum current output is sent to the PCI-6703 card.

Remote PID inputs

As discussed before, the PID inputs from the data collection computer are sent to the PID computer via a virtual RS-232 interface. During each iteration of the loop, the program checks for any data in the serial port buffer and reads in the data as a string. The string length read in is a multiple of 5, since each PID command sent from the data collection computer is a string of four characters and a semicolon that is used as a separator. Each five character packet of information is sent to a *sub vi* (Control Router) that reads in the fist letter of the string that is used to direct the remaining part of the signal to the appropriate PID loop. At the PID loop, the string is sent to a second *sub vi* (Control Receiver) that reads in the second letter of the string and routes the command to the one of the logic gates in the PID algorithm. The last two characters in the string are commands to change the selected variable.

B.4 Miscellaneous Programs

B.4.1 Bridgecal 16

This program is for calibrating the AC resistance bridge, in order to obtain better resistance measurements for the thermometer. It measures the resistance of 5 standard resistors (0.1 Ω, 1.0 Ω, 10 Ωs, 100 Ωs, and 1000 Ω) over several of the bridge's resistance ranges (0.2 Ωs, 2.0 Ωs, 20 Ωs, 200 Ωs, and 2000 Ωs). The program then outputs a *.dat file that records the measured resistances of the standards and is used in conjunction with the Autocalc v2b program to calculate the thermometer resistances and temperatures. A second *.raw file is generated with all of the measured data, while the *.dat file is an averaged summary of the output. All resistances are referenced to the 10 Ω standard resistor, which has been measured very accurately

and is well known and characterized (see section 2.3.4).

Upon running this program, the user is prompted to choose an excitation voltage (either 20 mV or 2 mV) and to give an output file name. Generally, the user will want to use the 20 mV excitation setting; thus, it is the default. The user is required to input the file name with no extension (generally the numeric form of the date), and the output files are written to the *C:\workdata\bridgecal16* directory with the appropriate file extensions. If the user does not input a file name, acal.dat and acal.raw are written to the *bridgecal16* directory.